Stochastic modelling and analysis of homogeneous hyperelastic solids

Danielle Fitt

Thesis submitted in candidature for the degree of

Doctor of Philosophy

School of Mathematics

Cardiff University

October 19, 2020

Abstract

Combining finite elasticity and information theory, a stochastic method is developed in order to accurately predict and assess the behaviour of materials, and also to model experimental data. An explicit strategy to calibrate homogeneous isotropic hyperelastic models to mean values and the standard deviation of either the stress-strain function or the nonlinear shear modulus is devised, and the technique of using Bayes Theorem to select the optimal model to represent the material or data in question is presented, specifically here in relation to manufactured silicone specimens. An analysis of the behaviour of solid materials under various deformations, including necking instability, the inflation of cylindrical tubes and spheres, and the cavitation of spherical shells, when the material is stochastic, is demonstrated, before an extension to the dynamic finite deformations of stochastic hyperelastic solids, including the shear motion of a cuboid, the quasi-equilibrated radial-axial motion of a cylindrical tube, and the quasi-equilibrated radial motion of a spherical shell, is explored. Ultimately, it is determined that the amplitude and period of oscillation of stochastic bodies are characterised by probability distributions. Overall, the aim is to highlight the need for mathematical modelling to consider the variability obtained in experimental data, in the mechanical responses of materials, or in testing protocols, with a view to enhancing the accuracy of the mathematical modelling techniques employed, and, as a result, to provide an improved assessment or prediction of the behaviour of the materials in question.

Acknowledgements

This work would not have been possible had it not been for the support and encouragement of many people.

Firstly, I would like to thank my academic supervisor, Dr Angela Mihai, who believed in my ability to complete this research long before I believed in myself. For her continual support, encouragement, and care over the last three years, I will be eternally grateful. Also, thanks must go to my second supervisor, Dr Thomas Woolley, for his useful input and support over the course of my research, and to Dr Hayley Wyatt and Richard Thomas of Cardiff School of Engineering, for their help and guidance in conducting the experiments performed as part of this work.

Without the financial support of my incredible family, this venture would not have been possible in the first place. As such, I would like to formally thank my parents, Anthony and Christine Fitt, my grandparents, Alan and Lynne Fitt, and my great-grandmothers, Joan Rees and Maisie Fitt, for their generosity over the last three years. I am also exceedingly grateful to both The Sir Richard Stapley Educational Trust and The Sidney Perry Foundation for their kind gifts towards the cost of my studies. Their support helped to ease the financial burden off of my family, and for that I am truly thankful.

I would like to take this opportunity to slightly-less-formally thank my best friend and grandfather, Alan Fitt, for the support he's given me over the years. From taking me to school every day from day one, to being on the frontline before and after every exam I've ever taken, to getting me to and from university each day (without ever being late for a lecture!), not to mention the endless games of school with my dolls as pupils, football in the street in the evenings, and helping with my homework. Grandad, you're one in a million!

As well as financially, my family have been a constant source of support and encouragement throughout my education. Mum and Dad, without you both I couldn't have dreamed of being anywhere near where I am now, and I hope I've

done you proud! Thank you for getting me through my worst so that I had a chance to be my best. Nana and Grandad, you're amazing (and I'm not just saying that because I want something!), and without your backing I couldn't have achieved even half of what I have. Gu and Nan, you've both been pillars of support for me over the course of my education, keeping my feet on the ground by taking the mickey out of me for choosing to study maths, a concept which neither of you could get your head around (it's more fun than it sounds, I promise you!). Nan and Grandad, although I don't get to see you as often because of the distance between our homes, the time I've spent with you has always been filled with questions about my progress, updates on the state of my thesis, and encouraging comments of support for my studies, which have meant the world to me. To all of you, it honestly doesn't feel like enough, but thank you for everything!

My friends have also played a vital role in getting me through my education, particularly so through the course of my PhD, and so lots of "thank yous" are in order. Firstly, to my best friend Nanci, for constantly having my back over the last seven years, and listening to my ranting about anything and everything without judgement. Thanks mate! Thanks also to my office mates, Asyl and Hayley, for putting up with me for the last couple of years. To my many other friends and colleagues in Cardiff School of Mathematics, but particularly to Emily, Emma, Nikoleta, Manal and Ambrose, for all the conversations that weren't directly related to work, and which reminded me constantly that there is a world outside of maths! Lastly, to my friends away from university; Adam, Beth, Jade, Jasmine, Matthew and Stacey, for being there to listen whenever I've needed them. Thanks guys, much appreciated!

Finally, I'd like to dedicate this work to my great-grandmother, Maisie Fitt, and my grandfather, Ronald Feist, both of whom we lost during the course of my PhD. I know you're both watching over me with pride, so this is for you!

Contents

Chapter 1

Introduction

1.1 Motivation and background

The use of mathematical models in predicting the behaviour of materials in numerous different applications has been fundamental to scientific research for many years [146–148, 222]. Within nonlinear elasticity field theory, which is based on average data values and covers the simplest case where internal forces only depend on the current deformation of the material and not on its history, hyperelastic materials are the class of material models described by a strain-energy function with respect to the reference configuration [70, 151, 209]. In general, hyperelastic models are used to capture the physical responses of many manufactured or biological systems at a macroscopic (non-molecular) level. Ideally, these models are calibrated and validated on multiaxial test data [126, 127, 135, 192]. For these materials, boundary value problems can be cast as variational problems, providing powerful methods for obtaining approximate solutions, and can also be used to generate finite element methods for computer simulations.

In terms of the mathematical modelling of biological materials, in [40], a comprehensive evaluation of the hyperelastic constitutive equations that are the basis of the model used in the context of the behavioural analysis of soft biological tissues is presented. Further developments within this paper led to a review of the

constitutive equations that are based on statistical modelling. A non-deterministic approach to model the inhomogeneity of liver tissue when it is subject to compression is developed in [61], and its feasibility is demonstrated. The method in question allows the inherent stiffness variations arising in biological soft tissues to be taken into account in a statistical model. The liver tissue was modelled using a Mooney-Rivlin hyperelastic constitutive equation, thus allowing its material parameters to be represented by a statistical function with a normal distribution. In [194–196], experimental data was analysed and stochastic hyperelastic models were developed to represent both compressible and incompressible hyperelastic materials in a probabilistic framework. The physics of growing biological tissues was investigated in [26]. A stochastic approach is used in [196] to analyse the calibration of an Ogden-type model for various different hyperelastic biological tissues. These Ogden-type strain energy functions were first introduced in [194] within a stochastic framework, developed further with the extension to compressible materials in [195]. The use of Bayesian statistics, both in the context of model selection and calibration, with regard to the hyperelastic modelling of soft tissue, was investigated in [33, 85, 117, 118]. The nature of the applications in which these techniques are being applied demands the utmost precision of the calibration of the models using the data that is available, and also the quantification of uncertainties in the model parameters.

Motivated by the ability of using a mathematical model to investigate the behaviour of both engineered and biological structures, models of an internally pressurised hollow cylinders and spheres were investigated in [70, 212]. These configurations are instructive as they apply to many structures, from living cells, to blood vessels, to aircraft fuselages. For these structures to be serviceable, they must be able to withstand and function at a certain level of internal pressure without damage. The finite symmetric inflation and stretching of a cylindrical tube of homogeneous isotropic incompressible hyperelastic material was first investigated

in the mid-twentieth century by Rivlin (1949) [169], while the finite radially symmetric inflation of an elastic spherical shell was studied in [72]. A general theory of possible qualitative behaviours for both the elastic tubes and the spherical shells was developed in [38], which then formed the basis for further studies where these deformations were examined for different material constitutive laws [69, 221], and opened the way to the modelling of more complex phenomena [79]. Experiments carried out in [64] on rubber cylinders first revealed that there was internal rupture under relatively small tensile dead loads. Following this, in [19], it was determined that a spherical cavity forms at the centre of a sphere of isotropic hyperelastic material in radially symmetric tension under prescribed surface displacements or dead loads, in both the static and dynamic cases. Experimental results on the onset, healing and growth of cavities in elastomers were reported in [159, 160]. In engineering applications, there is a need to understand and reduce uncertainties in materials or data to achieve repeatability between experiments and to increase the potential for a material to obtain optimal performance.

Oscillatory motions of cylindrical and spherical shells made of linear elastic material [109, 115, 116, 165] have generated a wide range of experimental, theoretical, and computational studies [6–8, 31, 50]. In contrast, time-dependent finite oscillations of cylindrical tubes and spherical shells of nonlinear hyperelastic material, relevant to the modelling of physical responses in many biological and synthetic systems [3, 10, 47, 79, 81, 83, 110], have been less investigated, and much of the work in finite nonlinear elasticity has focused on the static stability of pressurised shells [2, 28, 34, 35, 38, 62, 68, 69, 72, 119, 139, 169, 181, 221], or on wave-type solutions in infinite media [92, 154]. The governing equations for large amplitude oscillations of cylindrical tubes and spherical shells of homogeneous isotropic incompressible nonlinear hyperelastic material, formulated as special cases of quasi-equilibrated motions [208], were reviewed in [209]. These are the class of motions for which the deformation field is circulation preserving, and at every time instant, the current

configuration is a possible static configuration under the given forces. The free and forced axially symmetric radial oscillations of infinitely long, isotropic incompressible circular cylindrical tubes, with arbitrary wall thickness, were described for the first time in [106, 107]. In [86, 108, 213], free and forced oscillations of spherical shells were derived analogously. The dynamic deformation of cylindrical tubes of Mooney-Rivlin material in finite amplitude radial oscillation was obtained in [175, 176, 178], while the oscillatory motion caused by the dynamic cavitation of a neo-Hookean sphere was considered in [41]. For a hyperelastic sphere of Mooney-Rivlin material with a cavity, the solution to the nonlinear problem of large amplitude oscillations was computed numerically in [18]. Theoretical and experimental studies of cylindrical and spherical shells of rubberlike material under external pressure were presented in [215]. In [37], the finite amplitude radial oscillations of homogeneous isotropic incompressible hyperelastic spherical and cylindrical shells under a constant pressure difference between the inner and the outer surface were studied theoretically. The finite longitudinal, or telescopic, oscillations of infinitely long cylindrical tubes were investigated in [144], whilst the oscillatory motions of cylindrical and prismatic bodies of incompressible hyperelastic material under dynamic finite shear deformation were analysed in [143]. Other dynamic shear deformations were considered in [214], where it was emphasised that such shear motions were not quasi-equilibrated. The dynamic problem of axially symmetric oscillations of cylindrical tubes of transversely isotropic incompressible material, with radial transverse isotropy, was treated in [91], whilst in [177], the dynamic deformation of a longitudinally anisotropic thin-walled cylindrical tube under radial oscillations was obtained. Radial oscillations of non-homogeneous thick-walled cylindrical and spherical shells of neo-Hookean material, with a material constant varying continuously along the radial direction, were explored in [54]. In [4], for pressurised homogeneous isotropic compressible hyperelastic tubes of arbitrary wall thickness under uniform radial dead-load traction, the stability of the finitely

deformed state and small radial vibrations about this state were treated, using the theory of small deformations superposed on large elastic deformations. Here, the governing equations were solved numerically. The dynamic inflation of hyperelastic spherical membranes of Mooney-Rivlin material subjected to a uniform step pressure was studied in [211], and the absence of damping in these models was discussed. As the amplitude and period of oscillations are strongly influenced by the rate of internal pressure, it was concluded that, if the pressure was suddenly imposed and the inflation process was short, then sustained oscillations due to the dominant elastic effects could be observed. In general, however, for many systems under slowly increasing pressure, strong damping would delay, or even prevent, oscillations [46]. More recently, the dynamic response of incompressible hyperelastic cylindrical and spherical shells subjected to periodic loading was discussed in [166, 167]. Radial oscillations of cylindrical tubes and spherical shells of neo-Hookean [205], Mooney-Rivlin [137,168], and Gent [66] hyperelastic materials were analysed in [23,25], where it was deduced that, in general, both the amplitude and period of oscillations decrease when the stiffness of the material increases. The influence of the material constitutive law on the dynamic behaviour of cylindrical and spherical shells was also examined in [9, 11, 173, 220], where the results for Yeoh [219] and Mooney-Rivlin material models were compared. In [32], the static and dynamic behaviour of circular cylindrical shells of homogeneous isotropic incompressible hyperelastic material modelling arterial walls were considered. The nonlinear static and dynamic behaviour of a spherical membrane of neo-Hookean or Mooney-Rivlin material, subjected to a uniformly distributed radial pressure on its inner surface, was studied in [185], and a parametric analysis of the influence of the material constants was presented.

The use of stochastic processes within the broad field of elasticity is a fairly young, but ever-expanding, area of research. These processes can be used within the mathematical modelling of solid materials to fully account for the uncertain-

ties arising within the obtained experimental data, and the randomness in the mathematical models that follows as a result [128, 129, 146, 147, 188, 196]. Pioneering the use of stochastic processes for this purpose was Huet (1990) [90], whose proposed strategies regarding the use of stochastic processes for the study of mesoscopic material effects in random materials were based within the field of linear elasticity. In [153], the use of stochastic modelling within the context of heterogeneous solids was investigated. More recently, in [56], techniques that are useful for making optimal decisions and constructing control policies relating to the mathematical modelling of a variety of situations were analysed, but with particular emphasis on the application to the oil industry. Improving the potential of mathematical models to make more meaningful, accurate predictions was also explored in [56], leading to the conclusion that taking data dispersion into consideration in the stochastic models yields a significant improvement in model predictions [129]. Stochastic processes can also be applied to machine learning and multiscale modelling, particularly within the fields of biological, biomedical and behavioural sciences [5].

Depending on the type of material under investigation, uncertainties in the experimental observations can arise from the inherent stiffness and inhomogeneity of the material in question, sample-to-sample intrinsic variability, or when the data extracted from viscoelastic mechanical tests is elastic [40, 56, 61, 67, 89, 103, 105, 127, 149, 153, 202]. Typically, these uncertainties arise in both natural and engineered materials [194]. Stochastic models take into account not only the inevitable uncertainties arising in experimental observations, but also the dispersion of the obtained data [75, 76, 129, 164, 194–196]. In [105], statistical approaches which can, in terms of rubberlike networks, be applied to the mechanical analysis of these materials were explored. Further developments in this area were provided in [84], where a Monte-Carlo estimator was used to evaluate uncertainties. Additionally, Monte-Carlo simulations were used in the context of modelling

visco-elastic structures with random material properties in [102]. A numerical method using Monte-Carlo markov chains and Bayesian statistics was also followed in [33, 117, 118]. Due to the quantification of uncertainties, many challenges have to be dealt with regarding the use of the mathematical models in question, such as the verification and validation of the models [15, 16], and also the rational selection of these models, model calibration, and plausibility using Bayesian inference [146–148].

Further, it is possible to invoke information theory to calibrate material models using the standard data available, such as the mean and standard deviation, for isotropic elastic solids, thus allowing experiments to be reproduced precisely, and the behaviour of the materials in question to be accurately represented [196]. Strategies of a similar nature were employed in [75, 76] to construct stochastic models for fourth-order random elasticity tensors, and to investigate the statistical dependence between the components of these random elasticity tensors exhibiting some material symmetries. The characterisation of the statistical dependence here relies on the Maximum Entropy Principle for a discrete probability distribution. First described by Jaynes (1957) [94–96], the Maximum Entropy Principle is based on the concept of entropy (or uncertainty) introduced by Shannon (1948) [179], further investigated in [186], within the framework of information theory (for further information, see Appendix B). These concepts allow for the propagation of uncertainties from input data to output quantities of interest [190]. They are also suitable for incorporation into Bayesian methodologies [22, 122] for model selection or updates [129, 149, 172].

To investigate the effect of probabilistic model parameters on predicted mechanical responses, for different bodies with simple geometries at finite strain deformations, it has been explicitly demonstrated that, for the stochastic problem, a probabilistic interval exists where the stable and unstable states always compete [130–134]. In other words, both the stable and unstable states have a

quantifiable chance to be found. This is in contrast to the deterministic elastic problem, in which the stable and unstable cases are strictly separated by a single critical value. To date, specific case studies include the cavitation of a sphere under uniform tensile dead load [131], the inflation of pressurised spherical and cylindrical shells [130], the oscillatory motions of stochastic hyperelastic solids [134], the classical problems of the Rivlin cube [133], and the rotation and perversion of anisotropic hyperelastic cylindrical tubes [132].

This now leads to the following conundrum; which approach, deterministic or stochastic, provides the superior representation of the solid materials in question, both in terms of the amount of detail potentially obtainable and how realistic the representation is, in practical applications?

1.2 Deterministic versus stochastic approaches

Traditionally, hyperelastic materials, the class of material models described by a strain-energy function, characterised by a set of *deterministic* (or definite) model parameters, and based on ensemble averages, have been used to represent the mechanical responses of various types of natural or manufactured materials, and to quantify constitutive parameters [127]. In practice, these parameters can meaningfully take on different values corresponding to possible outcomes of experiments. Whilst a deterministic approach provides a good starting point in material modelling [56, 118, 123], in general, it has no stochastic elements, the model parameters are either known or assumed, and no account is taken of any uncertainties which potentially arise during experiments, or while observing data [138, 164], thus rendering the accuracy of the material model questionable. In many disciplines, such as materials science, engineering and biomechanics, understanding the variability in the mechanical behaviour of the materials in question is of the utmost importance, as any slight variation could have significant, or even catastrophic, consequences if not fully accounted for. For these materials, the traditional, widely

accepted deterministic approaches, based on average data values, can greatly underestimate or overestimate their properties. Further, for the assessment and prediction of the mechanical responses of engineered and natural materials, additional challenges arise from; the uncertainties in their elastic properties inferred from sparse and approximate observational data, variation in testing protocols, indirect measurements, data contaminated by noise, the inherent micro-structural inhomogeneity, and sample-to-sample intrinsic variability [22, 56, 67, 89, 103, 149, 153, 202]. For these materials, mathematical representations that account for data dispersion are needed to significantly improve assessment and predictions of the behaviour of the material, to achieve repeatability between experiments, and to provide a more accurate representation of experimental data [129]. For this reason, *stochastic* elasticity is a field that is very quickly evolving and developing.

Stochastic elasticity combines nonlinear elasticity and stochastic theories to significantly improve model predictions by accounting for uncertainties in the mechanical responses of materials, a crucial part of assessing the elasticity of materials. As a result of these uncertainties, stochastic homogeneous hyperelastic materials, which can be described using advanced phenomenological models within the stated framework, and characterised by strain-energy densities where the parameters are random variables defined by probability density functions, can be used to represent the behaviour of a material, or the experimental data obtained [129, 194–196, 198, 199]. Stochastic models rely on finite elasticity theory [70, 151, 209] and on the notion of uncertainty (or entropy) [94–96, 179, 186], and have the ability to incorporate at least one probabilistic element into the model, leading to an enhanced insight into the mechanics of the problem in question, thus generating significant improvements in model predictions. This technique also allows for the propagation of uncertainties from input data to output quantities of interest [190]. Additionally, stochastic techniques have the potential to be incorporated into Bayesian approaches for model selection and

updates [22, 122, 129, 149, 172]. Although this approach incorporates stochastic elements, very little of the mechanical aspect of the problem is addressed.

There is a growing interest in the use of stochastic modelling techniques in engineering and biomedical applications, where a central challenge is the quantification of uncertainties in the model parameters calibrated to observational data, and in the material responses predicted by them. In particular, from an engineering perspective, a central challenge in material modelling is to identify uncertainties within data, and to reduce them to achieve repeatability between experiments. As a result, stochastic representations are essential to fully account for this data dispersion [53, 67, 89, 103, 149, 153, 191, 202]. For rubber-like materials, the first experimental data exhibiting variability in the load-deformation responses between the tested samples were reported on by Rivlin and Saunders [170]. Exploiting the variability in those data, the first probability distributions for the random shear modulus of the material under relatively small strains were obtained in [131]. For rubber and soft tissues under large strain, explicit stochastic hyperelastic models based on data sets consisting of mean values and standard deviations were developed in [129], while statistical models derived from numerically generated data were presented in [39, 142]. In [102], from a manufactured materials point of view, the modelling of visco-elastic structures with random material properties was investigated using time-separated stochastic mechanics. From a biomedical perspective, in [44], the modelling of tracer distributions in the brain was explored, and uncertainties were accounted for to obtain an accurate representation of the problem at hand.

Generally, for non-deterministic material models, two important questions arise, namely; "what influence do material constitutive laws have on possible equilibrium states and their stability?" and "what effect do the probabilistic parameters have on the predicted elastic responses?". Recently, theoretical approaches have been able to successfully contend with cases of simple geometry,

such as cubes, spheres, shells and tubes [130–134]. These problems offer important insight into how stochastic-elastic models can be integrated into the nonlinear field theory. To investigate the effect of probabilistic parameters in the case of more realistic geometries and loading conditions, computational approaches were proposed in [198, 199]. Similar stochastic approaches can be developed for other mechanical systems, and may lead to more accurate assessment and prediction in many application areas. However, for real materials, most available data consist of mean values, from which deterministic models are usually derived [206], and there is a lack of experimental data reported in the literature that are directly suitable for stochastic modelling.

By revisiting well-known problems from the stochastic perspective, an opportunity arises to potentially gain new insights into the fundamental elastic solutions, and to address some inconsistencies found in previous works. Due to this, a stochastic approach similar to that in [75, 76] will be developed during this study, with the aim of providing the most accurate and realistic representation of the problems in question [15, 138, 146, 147]. Here, stochastic hyperelastic models, characterised by strain-energy functions where the parameters are random variables satisfying standard probability distributions, and directly amenable to standard finite elasticity approaches, will be introduced. These models have the ability to propagate uncertainties from input data to output mechanical responses. An explicit approach will be developed, thus providing a clear method and enriching our knowledge of the mechanics of the problems in question by taking into account material uncertainties.

1.3 Aims and outline of this thesis

The overall objective of this research is to highlight the need for mathematical models to consider the variability in the mechanical responses of materials, and to advocate for the use of stochastic modelling techniques for this purpose. To

achieve this, an explicit strategy will be devised to calibrate homogeneous isotropic hyperelastic models, generally used to capture the elastic responses of many biological systems (plants, tissues and organs), and whose random field parameters follow probability laws, to the mean values and standard deviation of either the stress-strain function, or the nonlinear shear modulus, which is a function of the deformation under large strain, coinciding with the classical shear modulus under small strain. Ideally, these models are calibrated and validated on multiaxial test data [126, 127, 135, 192]. A review of the formal derivation of the key nonlinear elastic parameters for isotropic hyperelastic materials is provided in [128]. The parameters in question can take on different values, with each value corresponding to each potential outcome of the experiments. As a result, in general terms, the behaviour of materials can be determined by more than one parameterised model, thus provoking the question of the selection of the optimal model for this purpose, which will be addressed. The modelling framework that will be employed here is a combination of finite elasticity and information theory [94–96, 196], and the stochastic method developed in [129] can be employed to construct constitutive models similar to those illustrated throughout this work. Numerical computations were carried out in MATLAB, where specific use was made of inbuilt functions for random number generation. Namely, "gamrnd" was used to generate the Gamma distributed random variables and "gamcdf" to generate the Gamma cumulative distribution function.

We begin in Chapter 2 with an outline of the prerequisite knowledge required, firstly from finite elasticity in Section 2.1, and then from probability theory in Section 2.3. A brief exploration of important results within the field of quasi-equilibrated motion is presented in Section 2.2, providing the foundations for the analysis to follow in Chapter 6. Chapter 3 explores the calibration procedure for stochastic isotropic incompressible hyperelastic models. A set of model assumptions is presented in Section 3.1, followed by a practical example of applying the

calibration procedure to rubberlike materials, using data obtained in [170], to obtain the probability distribution of the random shear modulus μ (Section 3.2). The calibration procedure is then applied theoretically to models with multiple terms in Section 3.3, before being applied to the more specific cases of models with both two terms and one term, in Sections 3.4 and 3.5, respectively.

In Chapter 4, simple experiments are performed on manufactured silicone specimens to observe variations arising in the data. Full details of the manufactured material are found in Section 4.2.1, while specific descriptions of the experimental set up and techniques used are given in Sections 4.2.2 and 4.2.3, respectively. Section 4.3 contains information regarding the assumptions and ideas we are required to adopt in order to use stochastic modelling to represent the data obtained in the experiments (Section 4.3.1), the statistical tests that were applied to verify how the data sets obtained in the experiments should be treated in terms of the material modelling (Section 4.3.2), the calibration of the random Piola-Kirchhoff shear stress of three different material models to the experimental data obtained for the rubber material under uniaxial stretch (Section 4.3.3), and details of how to use *Bayes' theorem* to select the best performing model to represent the obtained data (Section 4.3.4).

Building on the general model calibration procedure outlined in Chapter 3, some specific examples of deformations and instabilities of stochastic hyperelastic bodies are explored in Chapter 5. Firstly, in Section 5.1, the conditions under which a necking instability occurs for materials characterised by two-term Ogden type models (Section 5.1.1), the Carroll model (Section 5.1.2), and the Gent-Thomas model (Section 5.1.3), are determined. Section 5.2 then investigates the behaviour observed in the inflation of spheres (Section 5.2.1) and cylinders (Section 5.2.2), both in the deterministic case and stochastic case, respectively. The limit-point instability criterion for both the spherical shells and cylindrical tubes is also discussed within this chapter. This occurs when there is a change in the

monotonicity of the internal pressure, in both the shells and tubes. Ultimately, it is determined that, in an interval surrounding the deterministic critical value, there is a percentage chance of the inflation that occurs being stable or unstable. It is possible to increase the probability of stable inflation by considering sufficiently small values of the random parameter, below the deterministic critical value obtained within the analysis presented. An examination of the cavitation problems of incompressible spheres of stochastic isotropic hyperelastic material under radial tensile dead loads is then presented in Section 5.3, with the stability of the cavitation in both the deterministic and stochastic cases being the main topic of discussion. In the case of a stochastic material, there is a probabilistic interval, containing the deterministic critical value found during the analysis, in which there is always a competition between the stable and unstable states, as they both have a quantifiable chance of being found. Within this interval a cavity may form, with a given probability, under smaller or greater loads than the expected critical value.

The techniques developed throughout Chapter 5 are then extended and applied to dynamic finite deformations of stochastic hyperelastic solids in Chapter 6. The likely oscillation of stochastic hyperelastic solids is explored, then applied to investigate the generalised shear motion of stochastic hyperelastic cuboids (Section 6.1), the quasi-equilibrated radial-axial motion of a stochastic hyperelastic cylindrical tube (Section 6.2), with applications to a cylindrical tube made of stochastic Mooney-Rivlin material, and the quasi-equilibrated radial motion of a stochastic hyperelastic spherical shell (Section 6.3), with applications to a spherical shell made of stochastic neo-Hookean material. The dynamic radial and radial-axial deformations of the spherical shells and cylindrical tubes, respectively, are also presented within these sections and, ultimately, it is determined that the amplitude and period of the oscillation of these stochastic bodies are characterised by probability distributions.

Potential directions for future research within the area of stochastic modelling are discussed in Chapter 7, whilst a formal conclusion to this research is provided in Chapter 8.

Chapter 2

Prerequisites

We begin by introducing some well-known results from finite elasticity theory, probability and statistics, in Sections 2.1 and 2.3, respectively, that will be relied upon in the upcoming chapters, and also some background material on quasi-equilibrated motion (Section 2.2), providing a foundation for the analysis presented in Chapter 6.

2.1   Finite elasticity theory

In general terms, the main objective of finite elasticity theory is to predict changes that occur in the geometry of solid bodies upon the addition of forces. Finite elasticity theory covers the simplest case where forces only depend on the current deformation of the material and not on its history, and is based on average data values. Here, as previously presented in [151], some of the key results relied upon throughout this work are introduced.

A one-to-one mapping, χ, takes place between the reference (Lagrangian, material) configuration, $\mathcal{B}_0$, with Cartesian coordinates (X_1, X_2, X_3), and the current (Eulerian, spatial) configuration, $\mathcal{B}$, with Cartesian coordinates (x_1, x_2, x_3), which defines the deformation of the body in question [129]. This concept is demonstrated in Figure 2.1.
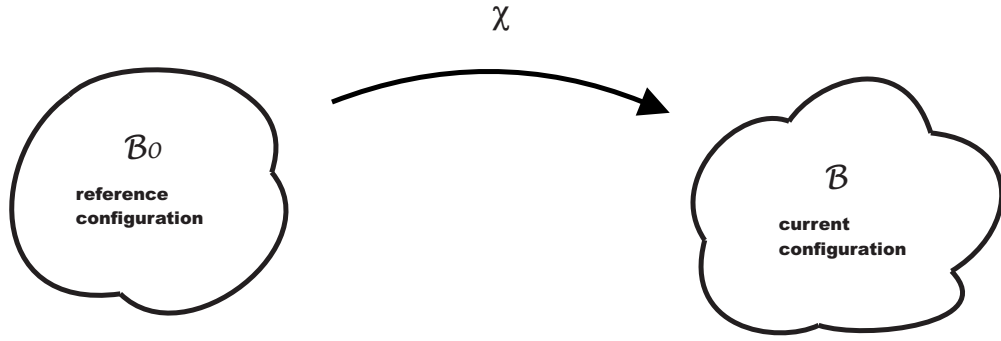
Figure 2.1: A typical deformation diagram representing a one-to-one mapping between the reference configuration and the current configuration.

Consider a unit cube of homogeneous isotropic incompressible hyperelastic material. In this context, the following definitions apply:

Definition 2.1.1 *A material is said to be **homogeneous** if there exists a reference configuration such that all of the material particles respond in the same way to the deformations described with respect to this configuration. In other words, it is a deformation for which all measures of strain and rotation are constant.*

Definition 2.1.2 *A material is said to be **isotropic** if it has the same mechanical properties in all directions.*

Definition 2.1.3 *A material is said to be **incompressible** if it can undertake only volume preserving (**isochoric**) deformations.*

Definition 2.1.4 *The **gradient tensor** governs the deformation χ (see Figure 2.1), and is defined as:*

$$\boldsymbol{F} = \nabla\chi = \begin{bmatrix} \frac{\partial\chi_1}{\partial X_1} & \frac{\partial\chi_1}{\partial X_2} & \frac{\partial\chi_1}{\partial X_3} \\[2mm] \frac{\partial\chi_2}{\partial X_1} & \frac{\partial\chi_2}{\partial X_2} & \frac{\partial\chi_2}{\partial X_3} \\[2mm] \frac{\partial\chi_3}{\partial X_1} & \frac{\partial\chi_3}{\partial X_2} & \frac{\partial\chi_3}{\partial X_3} \end{bmatrix}. \tag{2.1.1}$$

The transpose of $\boldsymbol{F}$ is

$$\boldsymbol{F}^T = \begin{bmatrix} \frac{\partial \chi_1}{\partial X_1} & \frac{\partial \chi_2}{\partial X_1} & \frac{\partial \chi_3}{\partial X_1} \\[2mm] \frac{\partial \chi_1}{\partial X_2} & \frac{\partial \chi_2}{\partial X_2} & \frac{\partial \chi_3}{\partial X_2} \\[2mm] \frac{\partial \chi_1}{\partial X_3} & \frac{\partial \chi_2}{\partial X_3} & \frac{\partial \chi_3}{\partial X_3} \end{bmatrix}. \tag{2.1.2}$$

Definition 2.1.5 *$\boldsymbol{Hyperelastic\ materials}$ are a class of material models that are described by a strain energy density, $W(\mathbf{F})$, that depends on the deformation gradient tensor, $\mathbf{F}$, with respect to a fixed reference configuration, and is characterised by a set of deterministic model parameters [70, 151, 209].*

Definition 2.1.6 *The $\boldsymbol{right\ Cauchy\text{-}Green\ tensor\ C = F^T F}$ is a measure of the deformation in the reference configuration. The $\boldsymbol{left\ Cauchy\text{-}Green\ tensor}$ $\boldsymbol{B = F F^T}$ is a measure of the deformation in the current configuration.*

Definition 2.1.7 *The $\boldsymbol{principal\ invariants}$ satisfy*

$$I_1(\boldsymbol{B}) = tr\ \boldsymbol{B} = I_1(\boldsymbol{C}), \tag{2.1.3}$$

$$I_2(\boldsymbol{B}) = \frac{1}{2}[(tr\ \boldsymbol{B})^2 - tr\ (\boldsymbol{B}^2)] = tr\ (Cof\ \boldsymbol{B}) = I_2(\boldsymbol{C}), \tag{2.1.4}$$

$$I_3(\boldsymbol{B}) = \det\ \boldsymbol{B} = I_3(\boldsymbol{C}). \tag{2.1.5}$$

Definition 2.1.8 *The principal invariants can be equivalently expressed in terms of the principal stretches:*

$$I_1(\boldsymbol{B}) = \lambda_1^2 + \lambda_2^2 + \lambda_3^2, \qquad I_2(\boldsymbol{B}) = \lambda_1^2 \lambda_2^2 + \lambda_2^2 \lambda_3^2 + \lambda_3^2 \lambda_1^2, \qquad I_3(\boldsymbol{B}) = \lambda_1^2 \lambda_2^2 \lambda_3^2.$$
$$\tag{2.1.6}$$

Definition 2.1.9 *The deformation of the area is described in terms of the cofactor $Cof\ \boldsymbol{F} = \det\ (\boldsymbol{F}) \boldsymbol{F}^{-T}$.*

Definition 2.1.10 *The **Jacobian** J describes the deformation of the volume, and is defined as $J = \det \boldsymbol{F}$. It is related to the Cauchy-Green tensors as follows;*

$$\det \boldsymbol{C} = \det \boldsymbol{B} = J^2. \tag{2.1.7}$$

Definition 2.1.11 *The **Cauchy stress tensor** describes the force per unit area in the current configuration, and for an incompressible material is given by*

$$\boldsymbol{\sigma} = -pI + \beta_1 \boldsymbol{B} + \beta_{-1} \boldsymbol{B}^{-1}, \tag{2.1.8}$$

where I is the identity tensor, p is the Lagrange multiplier associated with the in-compressibility condition ($\det \boldsymbol{F} = 1$), and the constitutive coefficients are given by

$$\beta_1 = \frac{1}{\lambda_1^2 - \lambda_2^2}\left(\frac{\lambda_1^2 + \lambda_3^2}{\lambda_1}\frac{\partial \mathcal{W}}{\partial \lambda_1} - \frac{\lambda_2^2 + \lambda_3^2}{\lambda_2}\frac{\partial \mathcal{W}}{\partial \lambda_2}\right) \tag{2.1.9}$$

and

$$\beta_{-1} = \frac{1}{\lambda_1^2 - \lambda_2^2}\left(\frac{1}{\lambda_1}\frac{\partial \mathcal{W}}{\partial \lambda_1} - \frac{1}{\lambda_2}\frac{\partial \mathcal{W}}{\partial \lambda_2}\right), \tag{2.1.10}$$

where, in the case of isotropic materials, $W(\boldsymbol{F}) = \mathcal{W}(\lambda_1, \lambda_2, \lambda_3)$.

Definition 2.1.12 *The **1st Piola-Kirchhoff stress tensor** represents the in-ternal force per unit area acting within the deformed solid (in other words, within the reference configuration):*

$$\boldsymbol{P} = \frac{\boldsymbol{F}}{A} = \boldsymbol{\sigma}\frac{a}{A}, \tag{2.1.11}$$

where A is the cross-sectional area in the reference configuration.

The way in which these definitions are applied to a practical problem will now be demonstrated in the following example:

Consider a unit cube of an isotropic incompressible material, subject to the following homogeneous deformation, consisting of a simple shear superposed on a

finite axial stretch [48, 163]:

$$x_1 = \frac{X_1}{\sqrt{a}} + kaX_2, \qquad x_2 = aX_2, \qquad x_3 = \frac{X_3}{\sqrt{a}}, \qquad (2.1.12)$$

where (X_1, X_2, X_3) and (x_1, x_2, x_3) are the Cartesian coordinates for the reference and the current configuration, respectively, and $k > 0$ and $a > 0$ are positive constants representing the shear parameter and the axial stretch. In the case of axial compression, we have $0 < a < 1$, and in the case of axial tension, we have $a > 1$.

Ericksen's Theorem [180] states that a deformation of an arbitrary homogeneous isotropic hyperelastic body can be maintained by the application of surface tractions only, or without body forces, if and only if it is a homogeneous deformation in the Cartesian coordinates. In this coordinate system also, the deformation gradient $\mathbf{F}$ is constant. Figure 2.2 serves to demonstrate this concept.
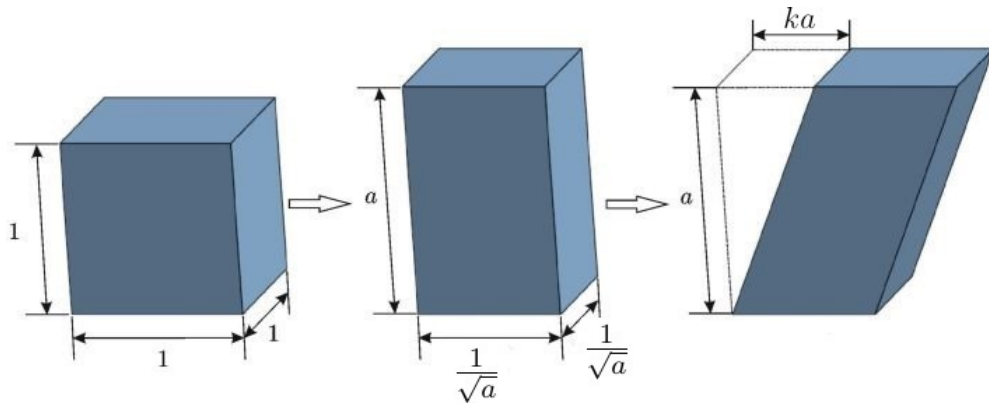
Figure 2.2: A demonstration of the stretching and shearing of a unit cube.

For the homogeneous deformation (2.1.12), the constant deformation gradient tensor is given by

$$\mathbf{F} = \begin{bmatrix} 1/\sqrt{a} & ka & 0 \\ 0 & a & 0 \\ 0 & 0 & 1/\sqrt{a} \end{bmatrix}, \qquad (2.1.13)$$

and the corresponding left Cauchy-Green tensor is then

$$
\mathbf{B} = \begin{bmatrix} k^2a^2 + 1/a & ka^2 & 0 \\ ka^2 & a^2 & 0 \\ 0 & 0 & 1/a \end{bmatrix}. \tag{2.1.14}
$$

The stretches $\{\lambda_i\}_{i=1,2,3}$, such that $\{\lambda_i^2\}_{i=1,2,3}$ are the eigenvalues of the left Cauchy-Green tensor $\mathbf{B}$, satisfy

$$
\lambda_1^2 = \frac{1 + a^3(1+k^2) + \sqrt{[1+a^3(1+k^2)]^2 - 4a^3}}{2a}, \tag{2.1.15}
$$

$$
\lambda_2^2 = \frac{1 + a^3(1+k^2) - \sqrt{[1+a^3(1+k^2)]^2 - 4a^3}}{2a}, \tag{2.1.16}
$$

$$
\lambda_3^2 = \frac{1}{a}. \tag{2.1.17}
$$

The constitutive coefficients of the Cauchy stress tensor (2.1.8) are given in (2.1.9) and (2.1.10) where, in the case of isotropic materials, $W(\mathbf{F}) = \mathcal{W}(\lambda_1, \lambda_2, \lambda_3)$, i.e. the strain-energy function is a symmetric function of the principal stretches $\{\lambda_i\}_{i=1,2,3}$ of $\mathbf{F}$. Then the nonzero components of the Cauchy stress tensor in Cartesian coordinates are

$$
\sigma_{11} = \sigma_{33} + k^2a^2\beta_1, \tag{2.1.18}
$$

$$
\sigma_{12} = ka^2\left(\beta_1 - \frac{\beta_{-1}}{a}\right), \tag{2.1.19}
$$

$$
\sigma_{22} = \sigma_{33} + \left(a^2 - \frac{1}{a}\right)\left(\beta_1 - \frac{\beta_{-1}}{a}\right) + k^2a\beta_{-1}, \tag{2.1.20}
$$

$$
\sigma_{33} = -p + \frac{\beta_1}{a} + a\beta_{-1}. \tag{2.1.21}
$$

The principal components (or principal eigenvalues) of the Cauchy stress tensor are given by [209]

$$
\sigma_i = -p + \beta_1\lambda_i^2 + \beta_{-1}\lambda_i^{-2}, \qquad i = 1, 2, 3. \tag{2.1.22}
$$

There are two points to make before proceeding to develop an expression for the nonlinear shear modulus. Firstly, the stresses in the material body are constant given a homogeneous deformation of the form defined in (2.1.12). Secondly, the 1st Piola-Kirchhoff stress tensor associated with the Cauchy stress tensor (2.1.22), representing the force per unit area in the reference configuration, is defined as [209]

$$\mathbf{P} = \mathbf{J}\boldsymbol{\sigma}\mathbf{F}^{-T}, \tag{2.1.23}$$

where J is the Jacobian. A demonstration of the practical application of the 1st Piola-Kirchoff stress tensor will be presented in Chapter 4, in terms of the modelling of data obtained in simple experiments on silicone. The important point to note here is that the shear component of the 1st Piola-Kirchhoff stress tensor;

$$\mathbf{P}_{12} = \frac{\sigma_{12}}{a}, \tag{2.1.24}$$

is proportional to the shear strain ka.

The above observations justify the introduction of the nonlinear shear modulus [128];

$$\mu(a, k) = \frac{\mathbf{P}_{12}}{ka} = \frac{\sigma_{12}}{ka^2} = \beta_1 - \frac{\beta_{-1}}{a}. \tag{2.1.25}$$

This modulus is a function of the deformation, is independent of the Lagrange multiplier p, and can be estimated directly from experimental observations if the shear force is known. Equivalently, by the representation (2.1.22) of the principal Cauchy stresses, the nonlinear shear modulus (2.1.25) can be expressed as [128]

$$\mu(a, k) = \frac{\sigma_1 - \sigma_2}{\lambda_1^2 - \lambda_2^2}. \tag{2.1.26}$$

This modulus is always positive, assuming that the following Baker-Ericksen inequalities hold [209];

$$(\sigma_i - \sigma_j)(\lambda_i - \lambda_j) > 0 \quad \text{if} \quad \lambda_i \neq \lambda_j, \quad i, j = 1, 2, 3. \tag{2.1.27}$$

(See Section 3.1 for further details).

When $a \to 1$ in the deformation (2.1.12), simple shear is superposed on an infinitesimal axial stretch. Consequently, the nonlinear shear modulus (2.1.25) converges to the nonlinear shear modulus for simple shear,

$$\hat{\mu}(k) = \lim_{a \to 1} \mu(a, k) = \hat{\beta}_1 - \hat{\beta}_{-1}, \tag{2.1.28}$$

where $\hat{\beta}_1 = \lim_{a \to 1} \beta_1$ and $\hat{\beta}_{-1} = \lim_{a \to 1} \beta_{-1}$, and the corresponding principal stretches are $\hat{\lambda}_i = \lim_{a \to 1} \lambda_i, \quad i = 1, 2, 3$.

Similarly, when $k \to 0$, the deformation (2.1.12) becomes an infinitesimal shear superposed on a finite axial stretch. In this case, the nonlinear shear modulus (2.1.25) converges to

$$\tilde{\mu}(a) = \lim_{k \to 0} \mu(a, k) = \tilde{\beta}_1 - \frac{\tilde{\beta}_{-1}}{a}, \tag{2.1.29}$$

where $\tilde{\beta}_1 = \lim_{k \to 0} \beta_1$ and $\tilde{\beta}_{-1} = \lim_{k \to 0} \beta_{-1}$, and the principal stretches are $\tilde{\lambda}_i = \lim_{k \to 0} \lambda_i, \quad i = 1, 2, 3$.

Assuming that limits can be taken independently and, thus, orderings can be swapped, the linear elastic limit (i.e. $k \to 0$ and $a \to 1$) is considered. In this case, the moduli defined by (2.1.25), (2.1.28) and (2.1.29) converge to the classical shear modulus from the infinitesimal theory [209];

$$\bar{\mu} = \lim_{a \to 1} \lim_{k \to 0} \mu(a, k) = \lim_{k \to 0} \hat{\mu}(k) = \lim_{a \to 1} \tilde{\mu}(a) = \bar{\beta}_1 - \bar{\beta}_{-1}, \tag{2.1.30}$$

where $\bar{\beta}_1 = \lim_{a \to 1} \lim_{k \to 0} \beta_1$ and $\bar{\beta}_{-1} = \lim_{a \to 1} \lim_{k \to 0} \beta_{-1}$, and the principal stretches are given by $\bar{\lambda}_i = \lim_{k \to 0} \lambda_i, \quad i = 1, 2, 3$.

For the shear moduli $\hat{\mu}(k)$, $\tilde{\mu}(a)$ and $\bar{\mu}$, the nonlinear shear modulus at small

shear superposed on finite axial stretch can be written as

$$\tilde{\mu}(a) = \sum_{p=1}^{n} C_p g_p(a), \tag{2.1.31}$$

where C_p, $p = 1, \cdots, n$, are the coefficients independent of the deformation, and $g_p(a)$, $p = 1, \cdots, n$, are functions of the stretch parameter $a > 0$. Similarly, under simple shear, the nonlinear shear modulus is of the form

$$\hat{\mu}(k) = \sum_{p=1}^{n} C_p h_p(k), \tag{2.1.32}$$

where $h_p(k)$, $p = 1, \cdots, n$, are functions of the shear parameter $k > 0$.

This background knowledge of finite elasticity theory will provide the foundations for the analysis of stochastic material modelling presented in later chapters.

2.2 Quasi-equilibrated motion

In this section, the concept of (universal) quasi-equilibrated motion in finite elasticity, introduced in [208] and reviewed in [209], is evoked, and an outline of the stochastic finite elasticity framework developed in [129], and applied to various static stability problems in [130, 132, 133], is presented.

For the large strain time-dependent behaviour of an elastic solid, Cauchy's laws of motion (balance laws of linear and angular momentum) are governed by the following Eulerian field equations [209, p. 40];

$$\rho \ddot{\boldsymbol{x}} = \text{div } \boldsymbol{\sigma} + \rho \mathbf{b}, \tag{2.2.1}$$

$$\boldsymbol{\sigma} = \boldsymbol{\sigma}^T, \tag{2.2.2}$$

where $\boldsymbol{x} = \chi(\boldsymbol{X}, t)$ is the motion of the elastic solid, ρ is the material density, which is assumed to be constant, $\mathbf{b} = \mathbf{b}(\boldsymbol{x}, t)$ is the body force, and $\boldsymbol{\sigma} = \boldsymbol{\sigma}(\boldsymbol{x}, t)$

is the Cauchy stress tensor. In order to obtain possible dynamical solutions, Cauchy's equation for particular motions can be solved, or known static solutions to dynamical forms can be generalised, using *quasi-equilibrated motion*, a concept which can formally be defined as follows:

Definition 2.2.1 *[209, p. 208] A quasi-equilibrated motion, $\boldsymbol{x} = \chi(\boldsymbol{X}, t)$, is the motion of an incompressible homogeneous elastic solid subject to a given body force, $\boldsymbol{b} = \boldsymbol{b}(\boldsymbol{x}, t)$, whereby, for each value of t, $\boldsymbol{x} = \chi(\boldsymbol{X}, t)$ defines a static deformation that satisfies the equilibrium conditions under the body force $\boldsymbol{b} = \boldsymbol{b}(\boldsymbol{x}, t)$.*

The subsequent theorem then follows:

Theorem 2.2.2 *[209, p. 208] A quasi-equilibrated motion, $\boldsymbol{x} = \chi(\boldsymbol{X}, t)$, of an incompressible homogeneous elastic solid subject to a given body force, $\boldsymbol{b} = \boldsymbol{b}(\boldsymbol{x}, t)$, is dynamically possible, subject to the same body force, if and only if the motion is circulation preserving with a single-valued acceleration potential ξ, i.e.*

$$\ddot{\boldsymbol{x}} = -\text{grad } \xi. \tag{2.2.3}$$

For the condition (2.2.3) to be satisfied, it is necessary that

$$\text{curl } \ddot{\boldsymbol{x}} = \boldsymbol{0}. \tag{2.2.4}$$

Then the Cauchy stress tensor takes the form

$$\boldsymbol{\sigma} = -\rho \xi \boldsymbol{I} + \boldsymbol{\sigma}^{(0)}, \tag{2.2.5}$$

where $\boldsymbol{\sigma}^{(0)}$ is the Cauchy stress for the equilibrium state at time t and $\boldsymbol{I} = diag(1, 1, 1)$ is the identity tensor. In this case, the stress field is determined by the present configuration alone. In particular, the shear stresses in the motion are the same as those of the equilibrium state at time t.

Proof: The Cauchy stress $\boldsymbol{\sigma}^{(0)}$ for the equilibrium state under the body force $\mathbf{b} = \mathbf{b}(\boldsymbol{x}, t)$ at time t satisfies

$$-\mathrm{div}\, \boldsymbol{\sigma}^{(0)} = \rho \mathbf{b}. \tag{2.2.6}$$

Firstly, we make the assumption that the motion $\boldsymbol{x} = \chi(\boldsymbol{X}, t)$ is quasi-equilibrated under the body force $\mathbf{b} = \mathbf{b}(\boldsymbol{x}, t)$, and deduce that there is a single-valued function, ξ, such that (2.2.3) holds. If the motion is quasi-equilibrated, then Definition 2.2.1 implies that, at any fixed time-instant t, the Cauchy stress takes the form (2.2.5), where $\xi = \xi(t)$ is a single-valued function of t. If we then substitute (2.2.5) into (2.2.1), we obtain

$$\rho \ddot{\boldsymbol{x}} = -\rho\, \mathrm{grad}\, \xi + \mathrm{div}\, \boldsymbol{\sigma}^{(0)} + \rho \mathbf{b}. \tag{2.2.7}$$

Then the equation stated in (2.2.3) follows from (2.2.6) and (2.2.7).

On the other hand, if (2.2.3) holds, with ξ a single-valued function, then substituting (2.2.3) and (2.2.6) into (2.2.1) yields the following result:

$$-\rho\, \mathrm{grad}\, \xi = \mathrm{div}\, \left(\boldsymbol{\sigma} - \boldsymbol{\sigma}^{(0)}\right), \tag{2.2.8}$$

at any time-instant t. Following from (2.2.8), it can be observed that the Cauchy stress $\boldsymbol{\sigma}$ takes the form (2.2.5). Hence, according to Definition 2.2.1, the motion is quasi-equilibrated. $\square$

The theorem presented above may only be applicable to specific quasi-equilibrated motions of specific materials. Regardless of this, in all elastic materials, for a quasi-equilibrated motion to be dynamically possible under a given body force, it is necessary, by Theorem 2.2.2, that the deformation is a possible equilibrium state under that body force in all those materials, at every time instant. In order to obtain quasi-equilibrated motions of isotropic materials subject only to surface

tractions, we take the arbitrary constant in those deformations to be an arbitrary function of time. Examples of this are the homogeneous motions that are possible in all homogeneous incompressible materials, and also those considered in Sections 6.2 and 6.3 (for further information, see [209, p. 209]).

2.3 Probability and statistics

Some of the main concepts of probability and statistics that form the basis of the analysis presented in later sections regarding the stochastic modelling of materials will now be defined. For further details, see [74, 96, 101].

Definition 2.3.1 *A **random variable** is a function $X : \Omega \to \mathbb{R}$ with the property that $\{\omega \in \Omega : X(\omega) \leq x\} \in \mathcal{F}$, where $\mathcal{F}$ is the event space, for each $x \in \mathbb{R}$. Such a function is said to be $\mathcal{F}$-measurable.*

Definition 2.3.2 *The random variable X is called **discrete** if it takes values in some countable subset $\{x_1, x_2, ...\}$, only, of $\mathbb{R}$. The discrete random variable X has **probability mass function** $f : \mathbb{R} \to [0, 1]$ given by $f(x) = \mathbb{P}(X = x)$.*

Definition 2.3.3 *The random variable X is called **continuous** if its distribution function can be expressed as*

$$F(x) = \int_{-\infty}^{x} f(u)\mathrm{d}u, \qquad x \in \mathbb{R},$$

for some integrable function $f : \mathbb{R} \to [0, \infty)$.

Definition 2.3.4 *The integrable function $f : \mathbb{R} \to [0, \infty)$ is called the **probability density function** of X.*

Definition 2.3.5 *The **expectation** of a random variable X (also called the **mean***

value of X) can be defined as follows;

$$E[X] = \begin{cases} \sum_{x \in S} x f(x), & X \text{ discrete}; \\ \int_{-\infty}^{\infty} x f(x) \, \mathrm{d}x, & X \text{ continuous}, \end{cases}$$

where S is the sample space and $f(x)$ is the probability mass function in the case where X is discrete, and the probability density function in the case where X is continuous.

Definition 2.3.6 *The **variance** of a random variable X is defined as;*

$$Var\ (X) = E[X^2] - E[X]^2.$$

Definition 2.3.7 *The **standard deviation** of a random variable X is defined to be the square root of the variance;*

$$\|X\| = \sqrt{Var\ (X)}.$$

Definition 2.3.8 *The **covariance** of random variables X and Y intuitively describes how X and Y vary together, and is mathematically defined as*

$$Cov\ [X, Y] = E[(X - E[X])(Y - E[Y])].$$

Definition 2.3.9 *The **correlation coefficient**, defined as*

$$corr\ [X, Y] = \frac{Cov\ [X, Y]}{\sqrt{Var\ (X)\, Var\ (Y)}},$$

is a scale invariant measure of how X and Y co-vary.

Definition 2.3.10 *The **coefficient of variation** is defined as the ratio of the*

standard deviation of a random variable X to its expectation;

$$C_v = \frac{\|X\|}{E[X]}.$$

All of the definitions presented here will be of various degrees of use within the analysis presented in the sections comprising Chapter 3, and provide a foundation for the investigations outlined in later chapters of this work.

Chapter 3

Stochastic isotropic incompressible hyperelastic models: explicit calibration

In this chapter, an explicit calibration procedure for stochastic isotropic incompressible hyperelastic models is presented. A set of model assumptions is given in Section 3.1, with an outline of the strain-energy function the material in question follows, and also various constraints on the parameters in the expression for the random shear modulus and auxiliary random variables. Following this, in Section 3.2, an application of the calibration procedure is demonstrated in terms of rubberlike materials. Using data obtained in [170], explicitly stated in Table 3.1, the probability distribution of the random shear modulus μ is established.

The assumptions stated in Section 3.1 provide the foundation for the two-step calibration procedure developed in Section 3.3 for models with multiple terms, which is then specialised in Sections 3.4 and 3.5, for models with two terms and one term, respectively. In the first step of the calibration procedure, the mean value of the nonlinear shear modulus is determined. Then, in step two, the probability distribution followed by the nonlinear shear modulus is found, using the mean value of the nonlinear shear modulus determined in the previous step. In the

case of models with multiple-terms, this process is extended in order to determine expressions for the variance and covariance of the random coefficients C_1 and C_2, in terms of the parameters of the Gamma and Beta distributions.

3.1 Model assumptions

Firstly, it is of fundamental importance to recall that a hyperelastic model is described by a strain-energy function $W(\mathbf{F})$ that depends on the deformation gradient tensor, $\mathbf{F}$, with respect to a fixed reference configuration, and is characterised by a set of deterministic model parameters (see Section 2.1) [70, 151, 209]. In contrast to this, a stochastic hyperelastic model is defined by a stochastic strain-energy function, for which the model parameters are random variables that satisfy standard probability laws [129, 194–196]. Notably, each model parameter is described in terms of the first and second statistical moments, namely, the mean value and the variance, respectively, which are usually adequate for the approximation in numerous practical circumstances [39, 89, 121] (see Section 2.3). Here, a combination of finite elasticity and information theory will be relied upon, along with the following general hypotheses [129, 130, 133]:

(A1) Material objectivity: The principle of material objectivity (or frame indifference) states that constitutive equations must be invariant under changes of frame of reference. It requires that the scalar strain-energy function, $W = W(\mathbf{F})$, depending only on the deformation gradient $\mathbf{F}$, with respect to the reference configuration, is unaffected by a superimposed rigid-body transformation (which involves a change of position) after deformation, i.e. $W(\mathbf{R}^T\mathbf{F}) = W(\mathbf{F})$, where $\mathbf{R} \in SO(3)$ is a proper orthogonal tensor (rotation). Material objectivity is guaranteed by considering strain-energy functions defined in terms of invariants.

(A2) Material isotropy: The principle of isotropy requires that the strain-energy

function is unaffected by a superimposed rigid-body transformation prior to deformation, i.e. $W(\mathbf{F}\mathbf{Q}) = W(\mathbf{F})$, where $\mathbf{Q} \in SO(3)$. For isotropic materials, the strain-energy function is a symmetric function of the principal stretches $\{\lambda_i\}_{i=1,2,3}$ of $\mathbf{F}$, i.e. $W(\mathbf{F}) = \mathcal{W}(\lambda_1, \lambda_2, \lambda_3)$.

(A3) Baker-Ericksen inequalities: In addition to the fundamental principles of objectivity and material symmetry, in order for the behaviour of a hyperelastic material to be physically realistic, there are some universally accepted constraints on the constitutive equations. Specifically, for a hyperelastic body, the Baker-Ericksen (BE) inequalities are [17, 120];

$$(\sigma_i - \sigma_j)(\lambda_i - \lambda_j) > 0 \quad \text{if} \quad \lambda_i \neq \lambda_j, \quad i, j = 1, 2, 3, \tag{3.1.1}$$

where $\{\lambda_i\}_{i=1,2,3}$ and $\{\sigma_i\}_{i=1,2,3}$ denote the principal stretches and the principal Cauchy stresses, respectively, and the strict inequality ">" is replaced by "$\geq$" if any two principal stretches are equal [17, 120]. In other words, these inequalities state that *the greater principal (Cauchy) stress occurs in the direction of the greater principal stretch*. Under these mechanical constraints, the shear modulus of the material, under finite strains, is positive [127]. Furthermore, either the positive or the negative *Poynting effect* can occur in a material for which the BE inequalities hold [124, 125, 127, 133]. Concisely, the Poynting effect is a nonlinear elastic effect observed when an elastic cube is sheared between two plates and stress is developed in the direction normal to the sheared faces, or when a cylinder is subjected to torsion and the axial length changes [93, 136, 158, 171, 207].

(A4) Finite mean and variance for the random shear modulus: For any given deformation, the random shear modulus, μ, and its inverse, $1/\mu$, are assumed to be second-order random variables. In other words, this means that they have a finite mean value and finite variance [194–196].

Assumptions (A1)-(A3) are well-known principles in isotropic finite elasticity [70, 151, 209], while (A4) contains physically realistic expectations on the random shear modulus, which will be drawn from a probability distribution.

Specifically, attention here is focused on stochastic incompressible hyperelastic materials characterised by the following strain-energy function [129, 194, 196];

$$\mathcal{W}(\lambda_1, \lambda_2, \lambda_3) = \frac{\mu_1}{2m^2} \left(\lambda_1^{2m} + \lambda_2^{2m} + \lambda_3^{2m} - 3 \right) + \frac{\mu_2}{2n^2} \left(\lambda_1^{2n} + \lambda_2^{2n} + \lambda_3^{2n} - 3 \right),$$

(3.1.2)

with distributions to be defined, where m and n are deterministic constants, and μ_1 and μ_2 are random parameters. The random shear modulus for infinitesimal deformations of these stochastic models is defined as $\mu = \mu_1 + \mu_2$, which is consistent with the purely elastic theory [127]. In this case, the BE inequalities (3.1.1) are equivalent to

$$\left(\lambda_1 \frac{\partial \mathcal{W}}{\partial \lambda_1} - \lambda_2 \frac{\partial \mathcal{W}}{\partial \lambda_2} \right) (\lambda_1 - \lambda_2) > 0 \quad \text{if} \quad \lambda_i \neq \lambda_j, \quad i, j = 1, 2, 3, \qquad (3.1.3)$$

with the strict inequality ">" being replaced by "≥" if any two principal stretches are equal.

For the stochastic materials described by (3.1.2), condition (A4) is guaranteed by the following constraints on the expected values [129, 133, 194–196]:

$$\begin{cases} E\left[\mu\right] = \underline{\mu} > 0, \\ E\left[\log \mu\right] = \nu, \quad \text{such that } |\nu| < +\infty, \end{cases} \qquad (3.1.4)$$

i.e. the mean value $\underline{\mu}$ of the shear modulus, μ, is fixed and greater than zero, and the mean value of $\log \mu$ is fixed and finite, implying that both μ and $1/\mu$ are second-order random variables, i.e. they have finite mean and finite variance [187, 188]. These expected values are then used to find the maximum likelihood probability for the random shear modulus, μ, with mean value $\underline{\mu}$, and standard

deviation $\|\mu\| = \sqrt{\mathrm{Var}[\mu]}$, defined as the square root of the variance, $\mathrm{Var}[\mu]$. Critically, under the constraints (3.1.4), and by the Maximum Entropy Principle (see Appendix B), μ follows a Gamma probability distribution [187, 188], with hyperparameters $\rho_1 > 0$ and $\rho_2 > 0$ satisfying

$$\underline{\mu} = \rho_1 \rho_2 \quad \text{and} \quad \|\mu\| = \sqrt{\rho_1} \rho_2. \tag{3.1.5}$$

The corresponding probability density function takes the form [1, 100]

$$g(\mu; \rho_1, \rho_2) = \frac{\mu^{\rho_1 - 1} e^{-\mu/\rho_2}}{\rho_2^{\rho_1} \Gamma(\rho_1)}, \qquad \text{for } \mu > 0 \text{ and } \rho_1, \rho_2 > 0, \tag{3.1.6}$$

where $\Gamma : \mathbb{R}_+^* \to \mathbb{R}$ is the complete Gamma function

$$\Gamma(z) = \int_0^{+\infty} t^{z-1} e^{-t} \mathrm{d}t. \tag{3.1.7}$$

Setting a constant deterministic value $b > -\infty$, such that $\mu_i > b$, $i = 1, 2$ (for example, $b = 0$ if $\mu_1 > 0$ and $\mu_2 > 0$, although b is not unique in general), the auxiliary random variable can be defined as follows [129]:

$$R_1 = \frac{\mu_1 - b}{\mu - 2b}, \tag{3.1.8}$$

where $0 < R_1 < 1$, and the set $\{R_1, 1 - R_1\}$ forms a complete probability distribution. The random model parameters can then be expressed equivalently as

$$\mu_1 = R_1(\mu - 2b) + b, \qquad \mu_2 = \mu - \mu_1 = (1 - R_1)(\mu - 2b) + b. \tag{3.1.9}$$

Under the following constraints [129, 194–196]

$$\begin{cases} E\left[\log R_1\right] = \nu_1, & \text{such that } |\nu_1| < +\infty, \\ E\left[\log (1 - R_1)\right] = \nu_2, & \text{such that } |\nu_2| < +\infty, \end{cases} \tag{3.1.10}$$

and by the Maximum Entropy Principle (see Appendix B), the random variable R_1, with mean value $\underline{R}_1$ and standard deviation $\|R_1\| = \sqrt{\text{Var}\,[R_1]}$, follows a standard Beta distribution $[1, 100]$, with hyperparameters $\xi_1 > 0$ and $\xi_2 > 0$ satisfying

$$\underline{R}_1 = \frac{\xi_1}{\xi_1 + \xi_2} \qquad \text{and} \qquad \|R_1\|^2 = \text{Var}\,[R_1] = \frac{\xi_1 \xi_2}{(\xi_1 + \xi_2)^2\,(\xi_1 + \xi_2 + 1)}. \qquad (3.1.11)$$

The corresponding probability density function takes the form

$$\beta(r; \xi_1, \xi_2) = \frac{r^{\xi_1 - 1}(1 - r)^{\xi_2}}{B(\xi_1, \xi_2)}, \qquad \text{for } r \in (0, 1) \text{ and } \xi_1, \xi_2 > 0, \qquad (3.1.12)$$

where $B : \mathbb{R}_+^* \times \mathbb{R}_+^* \to \mathbb{R}$ is the Beta function

$$B(x, y) = \int_0^1 t^{x-1}(1 - t)^{y-1}\mathrm{d}t. \qquad (3.1.13)$$

For the random parameters given by (3.1.9), the corresponding mean values then take the form

$$\underline{\mu}_1 = \underline{R}_1(\underline{\mu} - 2b) + b, \qquad \underline{\mu}_2 = \underline{\mu} - \underline{\mu}_1 = (1 - \underline{R}_1)(\underline{\mu} - 2b) + b, \qquad (3.1.14)$$

and the variances and covariance are, respectively,

$$\text{Var}\,[\mu_1] = (\underline{\mu} - 2b)^2\,\text{Var}\,[R_1] + (\underline{R}_1)^2\,\text{Var}\,[\mu] + \text{Var}\,[\mu]\,\text{Var}\,[R_1], \qquad (3.1.15)$$

$$\text{Var}\,[\mu_2] = (\underline{\mu} - 2b)^2\,\text{Var}\,[R_1] + (1 - \underline{R}_1)^2\,\text{Var}\,[\mu] + \text{Var}\,[\mu]\,\text{Var}\,[R_1], \qquad (3.1.16)$$

$$\text{Cov}\,[\mu_1, \mu_2] = \frac{1}{2}\left(\text{Var}\,[\mu] - \text{Var}\,[\mu_1] - \text{Var}\,[\mu_2]\right). \qquad (3.1.17)$$

When $\rho_1 \approx 1$, the probability distribution (3.1.6) reduces to an exponential

distribution;

$$g_2(\mu; \rho_2) = \frac{e^{-\mu/\rho_2}}{\rho_2}, \qquad \text{for} \quad \mu > 0 \quad \text{and} \quad \rho_2 > 0. \qquad (3.1.18)$$

In this case, the mean value, $\underline{\mu}$, and standard deviation, $\|\mu\|$ (3.1.5), take comparable values. In practical applications, a situation of this kind may arise, for example, when the sampled data contain a lot of noise.

3.2 Rubberlike materials

We now apply the above theory to the specific example of materials of a rubberlike nature, based on the data obtained in [170].

Pioneering the research in this area were Rivlin and Saunders (1951) [170], who reported the first experimental data in large deformations for a material of a rubberlike nature. Taking these data into consideration, and making the assumption that such a material can be described by the stochastic hyperelastic model (3.1.2) under sufficiently small deformations, the probability distribution for the random shear modulus, $\mu = \mu_1 + \mu_2$, for this material is derived (see Figure 3.1). The assumption stated above is made in order to provide examples of probability distributions based on real data measurements, without attempting to optimise a specific hyperelastic strain-energy function to the given data. As further examples, deterministic hyperelastic models calibrated to mean data values for rubberlike materials under finite deformations were put forward in [49, 82, 126, 152, 200, 210], statistical models were derived computationally from artificially generated data in [39, 142], while explicit stochastic hyperelastic models based on available data sets consisting of mean values and standard deviations were detailed in [129].

The chosen data values are recorded in Table 3.1, with the Gamma probability distribution fitted to the shear modulus data, together with the normal distribution derived from the Gamma distribution, and also the standard normal
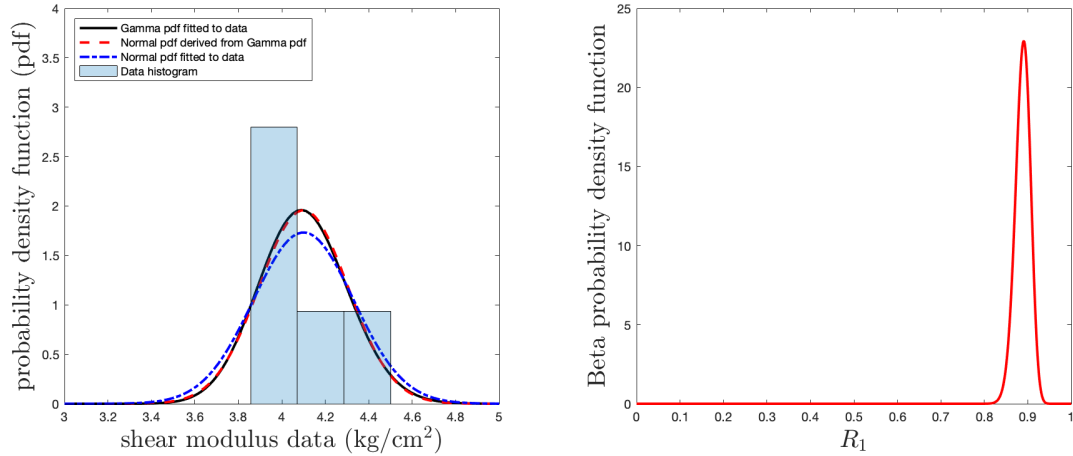
Figure 3.1: Probability distributions derived from the data values for the random shear modulus, $\mu = \mu_1 + \mu_2$, given in Table 3.1. Left: the Gamma distribution takes the form (3.1.6). The parameters for this distribution, along with the normal distributions presented here, are recorded in Table 3.2. Right: the Beta distribution takes the form (3.1.12), with parameters recorded in Table 3.3.

distribution fitted to the data, represented in Figure 3.1. Examining these distributions, it is noticeable that there is a distinct similarity between the Gamma and normal distributions in this case. For each probability distribution, the mean value $\underline{\mu}$ and standard deviation $\|\mu\|$ are recorded in Table 3.2. For the normal distribution derived from the Gamma distribution, the mean value and standard deviation are given by (3.1.5), as for the Gamma distribution. For the auxiliary random variable $R_1 = \mu_1/\mu$, the mean value $\underline{R_1}$ and standard deviation $\|R_1\|$ are provided in Table 3.3.

Table 3.1: Experimental data for rubberlike material under sufficiently small deformations, with the values of $\mu_1/2$ and $\mu_2/2$ selected from Tables 1 and 2 of [170].

λ_1	1.90	1.80	1.70	1.90	1.80
λ_2	1.07	1.25	1.39	1.02	1.09
$\mu_1/2$ (kg/cm^2)	1.77	1.89	2.01	1.68	1.76
$\mu_2/2$ (kg/cm^2)	0.20	0.23	0.21	0.29	0.21
$\mu = \mu_1 + \mu_2$ (kg/cm^2)	3.94	4.24	4.44	3.94	3.94

Page 38

Table 3.2: Parameters of the probability distributions derived from the data values for the random shear modulus, $\mu = \mu_1 + \mu_2$, given in Table 3.1.

Probability density function (pdf)	$\underline{\mu}$	$\|\mu\|$	ρ_1	ρ_2
Gamma pdf fitted to data	4.0907	0.2037	405.0214	0.0101
Normal pdf derived from Gamma pdf	4.0907	0.2037	-	-
Normal pdf fitted to data	4.0907	0.2302	-	-

Table 3.3: Parameters of the probability distribution for the random variable $R_1 = \mu_1/\mu$ derived from the data values provided in Table 3.1.

Probability density function (pdf)	$\underline{R_1}$	$\|R_1\|$	ξ_1	ξ_2
Beta pdf fitted to data	0.8883	0.0175	287.2297	36.1194

3.3   Multiple-term models

The calibration procedure for models with n terms, where $n > 2$, will now be presented [129]. In stochastic modelling, the measured standard deviation is considered, as well as the mean value of the modulus provided for each of the m stretches. This differs from the deterministic approach, in which only one mean value of the modulus for each of the stretches would be required. As a result, we assume that the given data consist of mean values $\{\tilde{\underline{\mu}}_s\}_{s=1,\cdots,m}$, and the associated standard deviations $\{d_s\}_{s=1,\cdots,m}$ of the nonlinear shear modulus (2.1.29) at the prescribed stretches $\{a_s\}_{s=1,\cdots,m}$. Here, a two-step procedure used to calibrate these models is presented, with the objectives of each step outlined at the outset.

Step 1: We begin by approaching the problem from the traditional deterministic angle [36, 126, 127, 152]. The objective here is to determine the mean value of the nonlinear shear modulus (2.1.29), and any other unknown constant parameter which appears in the expression for the strain-energy function, by minimising the

residual function

$$\mathcal{R}_{mean} = \sqrt{\sum_{s=1}^{m} \left(\tilde{\mu}(a_s) - \underline{\tilde{\mu}}_s \right)^2}, \tag{3.3.1}$$

between the mean nonlinear shear modulus $\underline{\tilde{\mu}}$ and the mean data values $\{\underline{\tilde{\mu}}_s\}_{s=1,\cdots,m}$ at the prescribed stretches $\{a_s\}_{s=1,\cdots,m}$, resulting in the determination of the mean values $\{\underline{C}_p\}_{p=1,\cdots,n}$ of the random constant coefficients $\{C_p\}_{p=1,\cdots,n}$, for the mean value of the nonlinear shear modulus

$$\tilde{\mu}(a) = \lim_{k \to 0} \mu(a, k). \tag{3.3.2}$$

The mean value of the random shear modulus (3.3.2) is defined as

$$\underline{\tilde{\mu}}(a) = \sum_{p=1}^{n} \underline{C}_p g_p(a), \tag{3.3.3}$$

where $g_p(a)$, $p = 1, \cdots, n$, are functions of the stretch parameter $a > 0$, and are defined in (2.1.31).

The mean shear modulus in the linear elastic limit is given by

$$\underline{\mu} = \lim_{a \to 1} \underline{\tilde{\mu}}(a) = \underline{\tilde{\mu}}(1). \tag{3.3.4}$$

Step 2: The aim in this step is to determine the probability distribution that the nonlinear shear modulus $\tilde{\mu}$ follows, using the mean value of $\tilde{\mu}$ established in the first step. To achieve this, we need to calibrate the variance of the nonlinear shear modulus (2.1.29), which is defined as

$$\text{Var}\left[\tilde{\mu}(a)\right] = \sum_{p=1}^{n} \text{Var}\left[C_p\right] g_p(a)^2 + 2 \sum_{p_1=1}^{n} \left(\sum_{p_2=p_1+1}^{n} \text{Cov}\left[C_{p_1}, C_{p_2}\right] g_{p_1}(a) g_{p_2}(a) \right), \tag{3.3.5}$$

where $\text{Var}\left[C_p\right]$ denotes the variance of C_p, and $\text{Cov}\left[C_{p_1}, C_{p_2}\right]$ denotes the covariance between C_{p_1} and C_{p_2}. Consequently, (3.3.5) and the nonlinear shear modulus

(3.3.2) lead to an expression for the standard deviation of $\tilde{\mu}$;

$$\|\tilde{\mu}(a)\| = \sqrt{\text{Var } [\tilde{\mu}(a)]}. \tag{3.3.6}$$

Next, the optimal coefficients Var $[C_p]$ are computed by minimising the residual

$$\mathcal{R}_{std} = \sqrt{\sum_{s=1}^{m} \left(\|\tilde{\mu}(a_s)\| - d_s \right)^2}, \tag{3.3.7}$$

between the standard deviation (3.3.6) and the associated data $\{d_s\}_{s=1,\cdots,m}$, at the prescribed data $\{a_s\}_{s=1,\cdots,m}$. We seek to determine the probability distribution for the coefficients C_p given the variance. The stretch parameter is then fixed to a convenient value, $a_0 > 0$, that is used for calibration.

Our attention is now restricted to the linear case, described by the nonlinear shear modulus $\tilde{\mu}(a_0) = \bar{\mu}$, which is a random variable. It is assumed that each random coefficient $C_p > 0$, $p = 1, \cdots, n$, has the form $C_p = \bar{\mu} R_p$, $p = 1, \cdots, n$, where the random variable R_p, $p = 1, \cdots, n$, follows a Beta distribution, $\beta(\xi_p, \chi_p)$, with $\xi_p > 0$ and $\chi_p = \sum_{q=1,q\neq p}^{n} \xi_p > 0$, $p = 1, \cdots, n$. The expressions for the mean value and the variance of R_p, denoted by $\underline{R}_p$ and Var $[R_p]$, $p = 1, \cdots, n$, respectively, then satisfy

$$\underline{R}_p = \frac{\xi_p}{\xi_p + \chi_p} \tag{3.3.8}$$

and

$$\text{Var } [R_p] = \frac{\underline{R}_p^2 \chi_p}{\xi_p(\xi_p + \chi_p + 1)}, \tag{3.3.9}$$

where

$$\chi_p = \sum_{q=1,\ q\neq p}^{n} \xi_q, \tag{3.3.10}$$

respectively. For each random coefficient C_p, $p = 1, \cdots, n$, the mean value is given by the expression

$$\underline{C}_p = \underline{\mu} \underline{R}_p = \frac{\rho_1 \rho_2 \xi_p}{\xi_p + \chi_p}, \tag{3.3.11}$$

and the variance of C_p, $p = 1, \cdots, n$, is given by

$$
\begin{aligned}
\mathrm{Var}\,[C_p] &= \bar{\underline{\mu}}^2\,\mathrm{Var}\,[R_p] + \underline{R}_p^2\,\mathrm{Var}\,[\bar{\mu}] + \mathrm{Var}\,[\bar{\mu}]\,\mathrm{Var}\,[R_p] \\
&= \frac{\rho_1\rho_2^2\xi_p(\xi_p^2 + \xi_p + \chi_p + \xi_p\chi_p + \chi_p\rho_1)}{(\xi_p + \chi_p)^2(\xi_p + \chi_p + 1)}.
\end{aligned} \tag{3.3.12}
$$

The following mathematical expectations are then set [133, 194–196];

$$
E[\bar{\mu}] = \sum_{p=1}^{n} \underline{C}_p g_p(a_0), \quad \bar{\underline{\mu}} > 0, \tag{3.3.13}
$$

$$
E[\log\ \bar{\mu}] = \nu, \quad |\nu| < +\infty, \tag{3.3.14}
$$

where, by the constraint (3.3.13), the mean value of the nonlinear shear modulus, given by $\bar{\underline{\mu}} > 0$, is fixed, and the logarithmic constraint (3.3.14) implies that both the nonlinear shear modulus and its inverse, denoted by $\bar{\mu}$ and $\bar{\mu}^{-1}$, respectively, are second-order random variables, so they have a finite mean and variance. The expectations (3.3.13) and (3.3.14) can now be implemented to determine the type of probability distribution that the nonlinear shear modulus $\bar{\mu}$ follows. For the sake of simplicity, an assumption is made that the shear modulus is equal to

$$
\bar{\mu} = \sum_{p=1}^{n} C_p, \tag{3.3.15}
$$

and that it follows a **Gamma distribution**, $\Gamma(\rho_1, \rho_2)$, with $\rho_1, \rho_2 > 0$ satisfying

$$
\bar{\underline{\mu}} = \rho_1\rho_2 \tag{3.3.16}
$$

and

$$
\mathrm{Var}\,[\bar{\mu}] = \rho_1\rho_2^2, \tag{3.3.17}
$$

where $\bar{\underline{\mu}}$ denotes the mean value of the shear modulus $\bar{\mu}$, and $\mathrm{Var}\,[\bar{\mu}]$ is the variance of $\bar{\mu}$.

Extending this further, it can be determined that

$$\text{Var}\,[\bar{\mu} - C_p] = \frac{\rho_1 \rho_2^2 \chi_p (\chi_p^2 + \xi_p + \chi_p + \xi_p \chi_p + \xi_p \rho_1)}{(\xi_p + \chi_p)^2 (\xi_p + \chi_p + 1)}, \qquad p = 1, \cdots, n, \quad (3.3.18)$$

and the covariance of C_p and $\bar{\mu} - C_p$, $p = 1, \cdots, n$, is

$$\begin{aligned}
\text{Cov}\,[C_p, \bar{\mu} - C_p] &= \frac{1}{2}(\text{Var}\,[\bar{\mu}] - \text{Var}\,[C_p] - \text{Var}\,[\bar{\mu} - C_p]) \\
&= \frac{\rho_1 \rho_2^2 \xi_p \chi_p (\xi_p + \chi_p - \rho_1)}{(\xi_p + \chi_p)^2 (\xi_p + \chi_p + 1)}.
\end{aligned} \qquad (3.3.19)$$

Letting $\xi_{ij} = \xi_i + \xi_j$ and $\chi_{ij} = \sum_{q=1, q \neq i,j}^{n} \xi_q$, the expressions for the variance of $C_i + C_j$ and the covariance of C_i and C_j are

$$\text{Var}\,[C_i + C_j] = \frac{\rho_1 \rho_2^2 \xi_{ij} (\xi_{ij}^2 + \xi_{ij} + \chi_{ij} + \xi_{ij}\chi_{ij} + \chi_{ij}\rho_1)}{(\xi_{ij} + \chi_{ij})^2 (\xi_{ij} + \chi_{ij} + 1)}, \qquad (3.3.20)$$

and

$$\text{Cov}\,[C_i, C_j] = \frac{1}{2}(\text{Var}\,[C_i + C_j] - \text{Var}\,[C_i] - \text{Var}\,[C_j]), \qquad (3.3.21)$$

respectively.

For the random vector $\underline{R}$, the following constraints are used [194, 196]:

$$E[\log\,R_p] = \nu_p, \qquad |\nu_p| < +\infty, \qquad p = 1, \cdots, n. \qquad (3.3.22)$$

Subsequently, $\underline{R}$ follows a **Beta distribution** [1, 100], $\beta(\xi_1, \xi_2)$, with parameters $\xi_p > 1$, $p = 1, \cdots, n$, satisfying

$$E[R_p] = \frac{\xi_p}{\sum\limits_{q=1}^{n} \xi_q}, \qquad p = 1, \cdots, n. \qquad (3.3.23)$$

The expected values are then given by

$$E[R_p] = \underline{R}_p, \qquad p = 1, \cdots, n, \qquad (3.3.24)$$

with $\underline{R}_p$, $p = 1, \cdots, n$, defined as in (3.3.8).

Further to this, it can also be determined that

$$\text{Var}\,[C_i C_j] = \underline{C}_i^2\,\text{Var}\,[C_j] + \underline{C}_j^2\,\text{Var}\,[C_i] + \text{Var}\,[C_i]\,\text{Var}\,[C_j] \tag{3.3.25}$$

and

$$\text{Var}\,\left[\frac{C_i}{C_j}\right] = \frac{\underline{C}_i^2}{\underline{C}_j^2}\left(\frac{\text{Var}\,[C_i]}{\underline{C}_i^2} + \frac{\text{Var}\,[C_j]}{\underline{C}_j^2} - \frac{2\,\text{Cov}\,[C_i, C_j]}{\underline{C}_i \underline{C}_j}\right). \tag{3.3.26}$$

The results presented here provide general expressions that can be employed in the explicit calibration of stochastic isotropic hyperelastic models with multiple terms. We now specialise to the specific case of models with two terms.

3.4 Two-term models

Following the method structure set out in Section 3.3 for models with multiple terms, in the more specific case of models with two terms, the procedure is as follows:

Step 1: Here, we once again aim to determine the mean value of the nonlinear shear modulus (2.1.29), and any other unknown constant parameter which appears in the expression for the strain-energy function, by minimising the residual function (3.3.1), where $m = 2$ in this case, between the mean nonlinear shear modulus $\tilde{\underline{\mu}}$ and the mean data values $\{\tilde{\underline{\mu}}_s\}_{s=1,2}$, at the prescribed stretches $\{a_s\}_{s=1,2}$. The mean values $\{\underline{C}_p\}_{p=1,2}$ of the random constant coefficients $\{C_p\}_{p=1,2}$ can then be determined for the mean value of the nonlinear shear modulus (3.3.2). We begin by approaching this from the deterministic perspective [36, 126, 127, 152].

The mean shear modulus in the linear elastic limit (3.3.4), in this case, takes the form

$$\bar{\mu} = \sum_{p=1}^{2} \underline{C}_p g_p(1) = \underline{C}_1 g_1(1) + \underline{C}_2 g_2(1) = \underline{C}_1 + \underline{C}_2, \tag{3.4.1}$$

where the functions $g_p(1)$, $p = 1, 2$, are defined in the expression for the nonlinear shear modulus (2.1.31), which here yields

$$\tilde{\mu} = C_1 g_1(1) + C_2 g_2(1). \tag{3.4.2}$$

Step 2: The probability distribution that the nonlinear shear modulus $\bar{\mu}$ follows in this case will now be determined, using the mean value of $\bar{\mu}$ established in step one. An expression for the variance of $\bar{\mu}$ after defining the variance of the nonlinear shear modulus is then determined.

For a two-term model, the expression for the variance (3.3.5) can be simplified to give

$$\text{Var}\,[\tilde{\mu}(a)] = \text{Var}\,[C_1]\,g_1(a)^2 + \text{Var}\,[C_2]\,g_2(a)^2 + 2\,\text{Cov}\,[C_1, C_2]\,g_1(a)g_2(a). \tag{3.4.3}$$

Equations (3.4.2) and (3.4.3) then lead to the following expression for the standard deviation of $\tilde{\mu}$;

$$\|C_1 g_1(a) + C_2 g_2(a)\| = \sqrt{\text{Var}\,[C_1]\,g_1(a)^2 + \text{Var}\,[C_2]\,g_2(a)^2 + 2\,\text{Cov}\,[C_1, C_2]\,g_1(a)g_2(a)}. \tag{3.4.4}$$

Next, the optimal coefficients $\text{Var}\,[C_p]$, $p = 1, 2$, are computed by minimising the residual (3.3.7), with $m = 2$, between the standard deviation (3.4.4) and the associated data $\{d_s\}_{s=1,2}$, at the prescribed stretches $\{a_s\}_{s=1,2}$. In the case of two-term models, we aim to determine the probability distribution for the coefficients C_p, $p = 1, 2$, given the variance. To proceed, we fix the stretch parameter to a convenient value, $a_0 > 0$, to be used for calibration. Here, $a_0 = 1$ is chosen. For this chosen value of a_0, the random shear modulus (3.4.2) is equal to

$$\bar{\mu} = \sum_{p=1}^{2} C_p g_p(1) = C_1 + C_2. \tag{3.4.5}$$

For the case in question, we have $a_0 = 1$, and so

$$R_p(1) = g_p(1)C_p(\bar{\mu})^{-1} = C_p(\bar{\mu})^{-1}, \qquad p = 1, 2. \tag{3.4.6}$$

Now (3.4.6) can be rewritten in terms of the random coefficients C_1 and C_2 using (3.4.5). Thus, we obtain

$$R_p = C_p(C_1 + C_2)^{-1}, \qquad p = 1, 2, \tag{3.4.7}$$

and so the auxiliary random parameters can be expressed, at $p = 1, 2$, in terms of the random coefficients C_1 and C_2, as

$$R_1 = \frac{C_1}{C_1 + C_2} \qquad \text{and} \qquad R_2 = \frac{C_2}{C_1 + C_2}. \tag{3.4.8}$$

Note, here we have that $R_2 = 1 - R_1$, and so in this case, it is not necessary to calculate R_2 specifically, as it can be determined through the computation of R_1. These parameters are such that $R_p > 0$, $p = 1, 2$, and satisfy

$$\sum_{p=1}^{2} R_p(a_0) = 1, \tag{3.4.9}$$

where $a_0 = 1$. By (3.4.7), the random coefficients are

$$C_p = R_p(C_1 + C_2), \qquad p = 1, 2. \tag{3.4.10}$$

Using (3.4.5), expression (3.4.10) can be rewritten as

$$C_p = R_p\bar{\mu}, \qquad p = 1, 2. \tag{3.4.11}$$

Therefore, the random coefficients can be expressed as

$$C_1 = R_1\bar{\mu} \qquad \text{and} \qquad C_2 = (1 - R_1)\bar{\mu}. \tag{3.4.12}$$

For the random nonlinear shear modulus $\tilde{\mu}(a_0) = \bar{\mu}$, the mathematical expectations (3.3.13) and (3.3.14), for $n = 2$ and $a_0 = 1$, become

$$E[\bar{\mu}] = \underline{C}_1 + \underline{C}_2, \quad \bar{\mu} > 0, \tag{3.4.13}$$

and

$$E[\log \bar{\mu}] = \nu, \quad |\nu| < +\infty, \tag{3.4.14}$$

respectively, where, by the constraint (3.4.13), the mean value of the nonlinear shear modulus, given by $\bar{\mu} = \underline{C}_1 + \underline{C}_2 > 0$, is fixed, and the logarithmic constraint (3.4.14) implies that both the nonlinear shear modulus and its inverse, denoted by $\bar{\mu}$ and $\bar{\mu}^{-1}$ respectively, are second-order random variables, so they have a finite mean and variance. The expectations (3.4.13) and (3.4.14) imply that the nonlinear shear modulus $\bar{\mu}$ follows a Gamma distribution, $\Gamma(\rho_1, \rho_2)$, with parameters $\rho_1 > 0$ and $\rho_2 > 0$ [1, 100, 187, 188]. Hence, the expressions for the mean shear modulus in the linear elastic limit, and the variance of this mean shear modulus, are given by (3.3.16) and (3.3.17), respectively.

Now (3.3.17) can be rewritten in terms of the random coefficients, C_1 and C_2, and the mean values of these random coefficients, $\underline{C}_1$ and $\underline{C}_2$, using (3.4.1). Hence, after substitution and some minor rearrangement, we obtain the following;

$$\underline{C}_1 + \underline{C}_2 = \rho_1 \rho_2 \tag{3.4.15}$$

and

$$\text{Var}\,[C_1 + C_2] = \rho_1 \rho_2^2. \tag{3.4.16}$$

For the random vector $\underline{R} = (R_1, 1 - R_1)^T$, the constraint (3.3.14) becomes [194, 196]:

$$E[\log R_p] = \nu_p, \quad |\nu_p| < +\infty, \quad p = 1, 2.$$

$\underline{R}$ then follows a Beta distribution [1, 100], $\beta(\xi_1, \xi_2)$, with parameters $\xi_p > 1$,

$p = 1, 2$, satisfying (3.3.22) with $n = 2$, or explicitly in terms of the values of p,

$$E[R_1] = \frac{\xi_1}{\xi_1 + \xi_2} > 0 \qquad (3.4.17)$$

and

$$E[1 - R_1] = \frac{\xi_2}{\xi_1 + \xi_2} > 0. \qquad (3.4.18)$$

The expected values are given by (3.3.24) with $p = 1, 2$. Using (3.4.17) and (3.4.18), it can then be deduced that

$$\underline{R}_p = \frac{\xi_p}{\xi_1 + \xi_2}, \qquad p = 1, 2, \qquad (3.4.19)$$

with $\underline{R}_p = \underline{C}_p / \bar{\mu}$, $p = 1, 2$. In this case, every random variable R_p, $p = 1, 2$, follows a standard Beta distribution, $\beta(\xi_1, \xi_2)$, with parameters ξ_1 and ξ_2.

The variance of R_p (3.3.9) can be explicitly written in terms of the values of p as

$$\text{Var}\,[R_1] = \frac{\underline{R}_1{}^2 \xi_2}{\xi_1(\xi_1 + \xi_2 + 1)} \qquad (3.4.20)$$

and

$$\text{Var}\,[1 - R_1] = \frac{(1 - \underline{R}_1)^2 \xi_1}{\xi_2(\xi_1 + \xi_2 + 1)}, \qquad (3.4.21)$$

with the corresponding standard deviations of (3.4.20) and (3.4.21) given by

$$\|R_1\| = \sqrt{\frac{\underline{R}_1{}^2 \xi_2}{\xi_1(\xi_1 + \xi_2 + 1)}} \qquad (3.4.22)$$

and

$$\|1 - R_1\| = \sqrt{\frac{(1 - \underline{R}_1)^2 \xi_1}{\xi_2(\xi_1 + \xi_2 + 1)}}, \qquad (3.4.23)$$

respectively.

The hyperparameter vectors (ρ_1, ρ_2) and (ξ_1, ξ_2) are identified by minimising the residual for the standard deviation, given by (3.3.7), with $m = 2$.

In (3.4.8), the expression for the random auxiliary parameters R_p was defined

in terms of the random constant coefficients C_p, where we have $p = 1, 2$ in this case. Previously, it was stated that $\bar{\mu} = C_1 + C_2$, and so $C_1 = R_1\bar{\mu}$ and $C_2 = (1 - R_1)\bar{\mu}$. Hence, (3.3.16) and (3.3.17) then lead to

$$\underline{\bar{\mu}} = \rho_1\rho_2 \tag{3.4.24}$$

and

$$\|\bar{\mu}\|^2 = \rho_1\rho_2^2. \tag{3.4.25}$$

Further, from $C_1 = R_1\bar{\mu}$, it can be determined that the mean value of C_1 is $\underline{C}_1 = \underline{R}_1\underline{\bar{\mu}}$. An expression for $\underline{R}_1$ was stated in (3.4.19) and so, using (3.4.22),

$$\|R_1\| = \frac{1}{\xi_1 + \xi_2}\sqrt{\frac{\xi_1\xi_2}{\xi_1 + \xi_2 + 1}}. \tag{3.4.26}$$

The variance of C_1 is then given by the expression

$$\text{Var}\,[C_1] = \underline{\bar{\mu}}^2\|R_1\|^2 + \|\bar{\mu}\|^2\underline{R}_1^2 + \|\bar{\mu}\|^2\|R_1\|^2. \tag{3.4.27}$$

Similarly, in (3.4.12), the expression for C_2 is given by $C_2 = (1 - R_1)\bar{\mu}$, and so, as in the case of C_1, it can be observed that $\underline{C}_2 = (1 - \underline{R}_1)\underline{\bar{\mu}}$. Once again, from (3.4.19), an expression for $(1 - \underline{R}_1)$ can be obtained, and so, using (3.4.23), it is clear that

$$\|1 - R_1\| = \frac{1}{\xi_1 + \xi_2}\sqrt{\frac{\xi_1\xi_2}{\xi_1 + \xi_2 + 1}}. \tag{3.4.28}$$

A comparison between expressions (3.4.26) and (3.4.28) leads to the conclusion that the standard deviations of both R_1 and $1 - R_1$ are equal, so

$$\|R_1\| = \|1 - R_1\|. \tag{3.4.29}$$

The variance of C_2 is then given by the expression

$$\text{Var}\,[C_2] = \underline{\bar{\mu}}^2 \|R_1\|^2 + \|\bar{\mu}\|^2 (1 - \underline{R_1})^2 + \|\bar{\mu}\|^2 \|1 - R_1\|^2, \qquad (3.4.30)$$

which, using (3.4.29), yields

$$\text{Var}\,[C_2] = \underline{\bar{\mu}}^2 \|R_1\|^2 + \|\bar{\mu}\|^2 (1 - \underline{R_1})^2 + \|\bar{\mu}\|^2 \|R_1\|^2. \qquad (3.4.31)$$

To proceed, each term in (3.4.27) and (3.4.31) must be evaluated. The first term in both of these expressions is $\underline{\bar{\mu}}^2 \|R_1\|^2$. Using (3.4.24) and (3.4.26), it can be deduced that

$$\underline{\bar{\mu}}^2 \|R_1\|^2 = \frac{\rho_1^2 \rho_2^2}{(\xi_1 + \xi_2)^2} \frac{\xi_1 \xi_2}{\xi_1 + \xi_2 + 1}. \qquad (3.4.32)$$

For the second term $\|\bar{\mu}\|^2 \underline{R_1}^2$, (3.4.19) and (3.4.25) lead to

$$\|\bar{\mu}\|^2 \underline{R_1}^2 = \frac{\rho_1 \rho_2^2}{(\xi_1 + \xi_2)^2} \xi_1^2 = \frac{\rho_1 \rho_2^2}{(\xi_1 + \xi_2)^2} \frac{\xi_1^2 (\xi_1 + \xi_2 + 1)}{\xi_1 + \xi_2 + 1}. \qquad (3.4.33)$$

Thirdly, for $\|\bar{\mu}\|^2 \|R_1\|^2$, using (3.4.25) and (3.4.26),

$$\|\bar{\mu}\|^2 \|R_1\|^2 = \frac{\rho_1 \rho_2^2}{(\xi_1 + \xi_2)^2} \frac{\xi_1 \xi_2}{\xi_1 + \xi_2 + 1}. \qquad (3.4.34)$$

The final term is given by $\|\bar{\mu}\|^2 (1 - \underline{R_1})^2$. Once again, using (3.4.19) and (3.4.25), it can be determined that

$$\|\bar{\mu}\|^2 (1 - \underline{R_1})^2 = \frac{\rho_1 \rho_2^2}{(\xi_1 + \xi_2)^2} \xi_2^2 = \frac{\rho_1 \rho_2^2}{(\xi_1 + \xi_2)^2} \frac{\xi_2^2 (\xi_1 + \xi_2 + 1)}{\xi_1 + \xi_2 + 1}. \qquad (3.4.35)$$

Substituting (3.4.32)-(3.4.35) into (3.4.27) leads to the following expression for the variance of C_1;

$$\text{Var}\,[C_1] = \frac{\rho_1 \rho_2^2}{(\xi_1 + \xi_2)^2} \frac{\xi_1 (\rho_1 \xi_2 + \xi_1^2 + \xi_1 \xi_2 + \xi_1 + \xi_2)}{\xi_1 + \xi_2 + 1}. \qquad (3.4.36)$$

In a similar manner, the expression for the variance of C_2 (3.4.31) becomes

$$\text{Var}\,[C_2] = \frac{\rho_1 \rho_2^2}{(\xi_1 + \xi_2)^2} \frac{\xi_2(\xi_1 \rho_1 + \xi_1 \xi_2 + \xi_2^2 + \xi_2 + \xi_1)}{\xi_1 + \xi_2 + 1}. \tag{3.4.37}$$

The covariance of C_1 and C_2 is given by

$$\text{Cov}\,[C_1, C_2] = \frac{1}{2}(\text{Var}\,[C_1 + C_2] - \text{Var}\,[C_1] - \text{Var}\,[C_2]). \tag{3.4.38}$$

Following a similar procedure to that which was carried out to obtain the expressions for the variance of C_1 and C_2 above, each term in (3.4.38) will be explicitly evaluated. Firstly, we have the term $\text{Var}\,[C_1 + C_2]$. Using (3.4.24) and the fact that $\mu = C_1 + C_2$, it can be deduced that

$$\text{Var}\,[C_1 + C_2] = \text{Var}\,[\bar{\mu}] = \|\bar{\mu}\|^2 = \rho_1 \rho_2^2. \tag{3.4.39}$$

The second and third terms in (3.4.38) are given in (3.4.36) and (3.4.37), respectively. Substituting (3.4.36), (3.4.37) and (3.4.39) into (3.4.38), the expression for the covariance of C_1 and C_2 is

$$\text{Cov}\,[C_1, C_2] = \frac{\rho_1 \rho_2^2}{(\xi_1 + \xi_2)^2} \left[\frac{\xi_1 \xi_2 (\xi_1 + \xi_2 - \rho_1)}{\xi_1 + \xi_2 + 1} \right]. \tag{3.4.40}$$

Further, note that, when $\rho_1 \to \infty$, assuming that the standard deviation, $\|\mu\|$, is constant, by (3.1.5),

$$\rho_2 = \frac{\|\mu\|}{\sqrt{\rho_1}}. \tag{3.4.41}$$

Next, defining $u = \mu + \|\mu\|/\sqrt{\rho_1} > \|\mu\|/\sqrt{\rho_1}$, the probability density function (3.1.6) takes the form

$$g_1(u - \|\mu\|/\sqrt{\rho_1}; \rho_1, \|\mu\|/\sqrt{\rho_1}) = \frac{(u - \|\mu\|/\sqrt{\rho_1})^{\rho_1 - 1} e^{-(u - \|\mu\|/\sqrt{\rho_1})/(\|\mu\|/\sqrt{\rho_1})}}{(\|\mu\|/\sqrt{\rho_1})^{\rho_1} \Gamma(\rho_1)}. \tag{3.4.42}$$

The limit of the above function as $\rho_1 \to \infty$ is then equal to

$$\lim_{\rho_1 \to \infty} g_1(u - \|\mu\|/\sqrt{\rho_1}; \rho_1, \|\mu\|/\sqrt{\rho_1}) = \frac{e^{-(u-\underline{\mu})^2/(2\|\mu\|^2)}}{\sqrt{2\pi}\|\mu\|}. \tag{3.4.43}$$

Hence, the Gamma probability density function (3.1.6) is approximated by a normal (Gaussian) density function

$$h(u; \underline{\mu}, \|\mu\|) = \frac{e^{-(u-\underline{\mu})^2/(2\|\mu\|^2)}}{\sqrt{2\pi}\|\mu\|}, \tag{3.4.44}$$

where u is a random normal variable with mean value $\underline{\mu}$ and standard deviation $\|\mu\|$.

When $\rho_1 \approx 1$, the probability distribution (3.1.6) reduces to an exponential distribution (3.1.18), where the mean value $\underline{\mu}$ and standard deviation $\|\mu\|$ (3.1.5) take comparable values.

The strategy applied during this analysis can now be applied to investigate the calibration of models with just one term.

3.5 One-term models

Further specialising the method set out in Section 3.3, the calibration procedure for models with one term will now be demonstrated. For these models, there is only one random coefficient, C_1, which needs to be determined, and one random auxiliary parameter, $R_1 = 1$. To proceed, the two-step procedure demonstrated in Section 3.3 is implemented [129].

Step 1: Here, the mean coefficient $\underline{C}_1$, and any other unknown constant parameter which appears in the expression for the strain-energy function are determined by minimising the residual function for the mean value (3.3.2), with $m = 1$. As in Section 3.3, we firstly implement a deterministic method [36, 126, 127, 152].

In the case of one-term models, the mean value of expression (3.3.3) is

$$\underline{\tilde{\mu}}(a) = \underline{C}_1 g_1(a). \tag{3.5.1}$$

The linear elastic limit here is

$$\underline{\bar{\mu}} = \lim_{a \to 1} \underline{\tilde{\mu}}(a) = \lim_{a \to 1} \underline{C}_1 g_1(a) = \underline{C}_1. \tag{3.5.2}$$

Hence, combining (3.5.1) and (3.5.2) yields

$$\underline{\tilde{\mu}}(a) = \underline{\bar{\mu}} g_1(a). \tag{3.5.3}$$

Step 2: Now the probability distribution that the nonlinear shear modulus $\tilde{\mu}$ follows will be identified.

In this specific case of one-term models, (3.3.5) reduces to

$$\text{Var} \ [\tilde{\mu}(a)] = \text{Var} \ [\bar{\mu} g_1(a)] = \text{Var} \ [C_1] g_1(a)^2. \tag{3.5.4}$$

The corresponding standard deviation is

$$\|\tilde{\mu}(a)\| = \|\bar{\mu} g_1(a)\| = \sqrt{\text{Var} \ [C_1] g_1(a)^2} = \|C_1\| g_1(a), \tag{3.5.5}$$

where $\|C_1\| = \sqrt{\text{Var} \ [C_1]}$ is the standard deviation of C_1.

In this case, using (3.5.3), the random shear modulus (2.1.31) becomes

$$\tilde{\mu}(a) = \bar{\mu} g_1(a) = C_1 g_1(a). \tag{3.5.6}$$

At any stretch $a = a_0$, (3.5.6) satisfies

$$\tilde{\mu}(a_0) = \bar{\mu} g_1(a_0) = C_1 g_1(a_0). \tag{3.5.7}$$

For the random nonlinear shear modulus $\tilde{\mu}(a_0)$, the mathematical expectations (3.3.13) and (3.3.14) can be rewritten, using (3.5.7), as

$$E[\bar{\mu}] = \underline{\mu}, \qquad \underline{\mu} > 0 \qquad (3.5.8)$$

and

$$E[\log \, \bar{\mu}] = \nu, \qquad |\nu| < +\infty, \qquad (3.5.9)$$

respectively. It can then be observed that $\bar{\mu}$ follows a Gamma distribution, $\Gamma(\rho_1, \rho_2)$, with parameters $\rho_1, \rho_2 > 0$ [1, 100, 187, 188]. Using (3.5.3) and (3.5.5), and choosing $a_0 = 1$ for calibration, we observe that

$$\|\bar{\mu}\| = \|C_1\| = \frac{\underline{C_1}}{\sqrt{\rho_1}} \qquad (3.5.10)$$

and

$$\underline{C_1} = \underline{\mu} = \underline{C_1} g_1(1) = \rho_1 \rho_2. \qquad (3.5.11)$$

After the optimal value of $\|C_1\|$ is computed by minimising the residual (3.3.7) for the standard deviation, the hyperparameters (ρ_1, ρ_2) are obtained from equations (3.5.10) and (3.5.11), respectively.

3.6 Summary

In this chapter, the calibration procedure of stochastic isotropic incompressible hyperelastic models was explicitly detailed. To provide a foundation for the analysis that will follow in later sections, a set of model assumptions was given in Section 3.1. A specific example of an application of the calibration procedure to the data obtained in [170] to establish the probability distribution of the random shear modulus μ was explored in Section 3.2. Based on the assumptions presented in Section 3.1, a two-step calibration procedure was presented in Sections 3.3 for models with multiple terms, before the more specific cases of models with two

terms and models with one term were investigated in Sections 3.4 and 3.5, respectively. The process in each case involved determining the mean value of the nonlinear shear modulus, and subsequently identifying the probability distribution that it follows using the mean value obtained in the previous step. For the two-term and multiple-term models, this process was extended by determining expressions for the variance and covariance of the random coefficients in terms of the parameters of the Gamma and Beta distributions.

The calibration procedure of stochastic isotropic incompressible hyperelastic materials outlined in this chapter will provide a mathematical foundation to the model selection process, based on experimental data, which follows in Chapter 4, and will also form the basis for the investigations into the likely deformations and instabilities of stochastic hyperelastic bodies presented in Chapter 5.

While the calibration procedure presented here was first demonstrated in [129], the work in the following chapters is based on original work published in [130, 131, 134].

Chapter 4

Uncertainty quantification of elastic material responses: testing, stochastic calibration and Bayesian model selection

4.1   Introduction

To apply the theory presented in Chapter 3 to a real world example, and to support the argument for the use of stochastic models over deterministic in the modelling of solid materials, it was of the utmost importance to demonstrate the variation arising within experimental data. As such, simple experimental tests were performed on manufactured silicone specimens in uniaxial tension, and any variations observed in the test data were taken into account within the mathematical modelling. The tests performed contain critical information regarding the variability in the constitutive responses between different specimens. Full details of the manufactured material are found in Section 4.2.1, while Sections 4.2.2 and 4.2.3 contain specific descriptions of the experimental set up and techniques used, respectively.

Employing the stochastic calibration method proposed in Section 3.3, homogeneous stochastic hyperelastic models are constructed from the experimental data at a continuum level (Section 4.3). This section also contains information of the assumptions and ideas adopted in order to use stochastic modelling to represent the data obtained in the experiments, and the calibration of the random Piola-Kirchhoff shear stress of three different material models to the experimental data obtained for the rubber material under uniaxial stretch (Section 4.3.3), followed by details of how to employ *Bayes' theorem* to select the best performing model to represent the obtained data (Section 4.3.4). The assumptions and ideas that are relied upon for the stochastic modelling are discussed in Section 3.1. The results presented here demonstrate that the data are more likely with the computations performed by the Ogden model than with either the Mooney-Rivlin or Gent-Gent models, advocating for its use in mathematically modelling this type of material.

4.2 Experimental measurements

In this section, the experimental set-up and techniques used to measure large elastic deformations of manufactured silicone rubber specimens are described. The experimental results obtained capture the inherent variability in the acquired data between different specimens during tensile tests.

4.2.1 Specimen manufacture

Two batches of silicone were manufactured to investigate the consistency of the specimen behaviour within the same batch, and within different batches. Each sample was a simple rectangular shape with rounded edges, made using a standard mould for this type of material. The approximate geometric parameters of each tested specimen were: height 100mm, width 10mm, and depth 4mm. Examples of undeformed specimens are illustrated in Figure 4.1.

- For Batch 1, tensile testing specimens were cast using Tech-Sil 25 Silicone (Technovent). This is a two part silicone, with a standard mixture ratio of 9:1 for Part A:Part B, respectively, as per the manufacturer's recommendation, and is generally allowed to cure at room temperature for at least 24 hours. The silicone was mixed and de-gassed prior to casting, ensuring an even mixture, and no air bubbles were present in the tensile specimens. Testing specimens of equal dimensions were made within a mould that is typically used for this purpose. The silicone was removed from the mould for testing after 4 weeks.

- For Batch 2, the same make of silicone as in Batch 1 was used, with slight variations in the mixture components to simulate an error that would be within a realistic experimental range. Namely, the mixture ratio was 8.96:1. Tensile testing specimens with the specified geometry were created using this mixture. The silicone was also left to cure at room temperature, and taken out of the mould for testing after 2 weeks.

The full details of the silicone mixture for the two batches are recorded in Table 4.1.

(a)   (b)
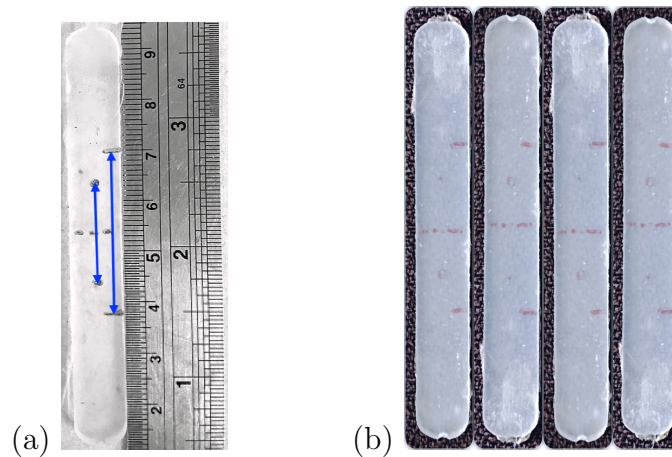
Figure 4.1: Marked undeformed specimens, with height 100mm, width 10mm, and depth 4mm: (a) A single specimen where the longer double arrow shows the grip length, which was 30mm as standard, and reduced to 20mm for some tests, while the shorter arrow indicates the gauge length, which was 20mm as standard and 10mm when using the reduced grip length; (b) Multiple specimens.

Table 4.1: Full details of the silicone mixture for the two batches of tensile testing specimens.

Batch number	1	2
Part A weight (g)	180	92.3
Part B weight (g)	20	10.3
Mixing ratio	9:1	8.96:1
Curing period	4 weeks	2 weeks
Number of specimens tested	6	2

4.2.2 Experimental set up

Two testing sessions were conducted to allow for variability in the experimental results due to degradation of silicone properties over different testing days. To conduct uniaxial tests on each silicone specimen, a bespoke fixture was designed [217]. Uniaxial tests were conducted on the Zwick Roel Z050 testing machine, with a 1KN load cell to measure tensile force. Specimens were mounted using a set of roll clamps, and the general experiment set-up can be observed in Figure 4.2. The standard test method used consisted of a pre-load of 2N, 30mm grip length of the specimens, and loading at a speed of 30mm/min. However, testing parameters, such as the grip length and testing speed, were varied between specimens, as detailed in Table 4.2. Tests were stopped once specimens reached approximately 100% strain measured optically (see Section 4.2.3 for details). All specimens were tested with the same technician loading the test specimens and using the test machine.

4.2.3 Optical strain measurement

A video strain gauge system (Imetrum) was used to capture the global deformation of the specimen during tensile tests. The system works by imaging the specimen
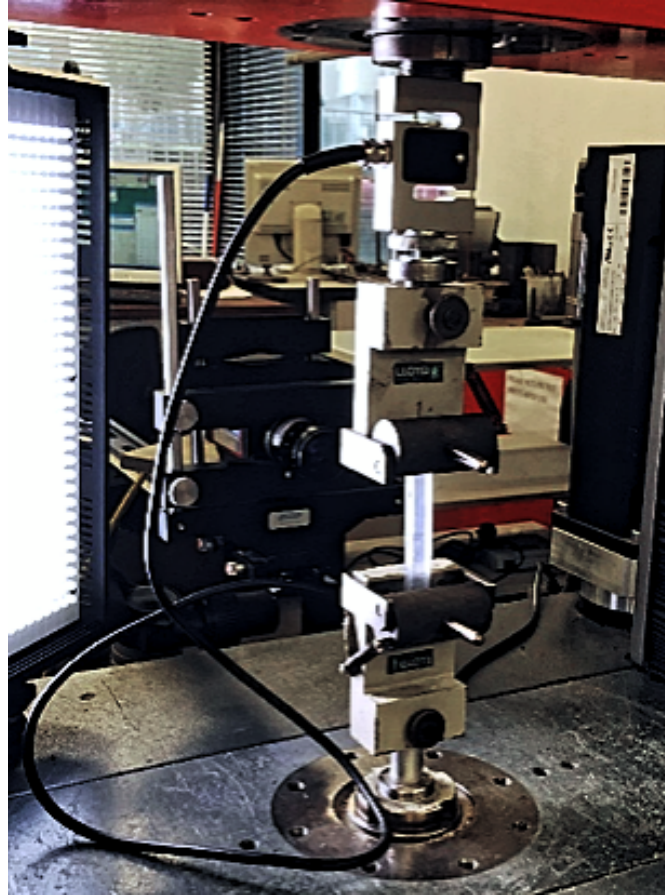
Figure 4.2: Experimental set-up for uniaxial tensile testing of silicone specimens mounted in roll grips, with lights and cameras for optical strain measurement.

Table 4.2: Specimen details and testing parameters.

Specimen number	Silicone batch	Testing session	Testing speed (mm/min)	Grip length (mm)	Number of tests
1	1	1	30	30	3
2	1	1	30	30	3
3	1	1	30	30	3
4	1	1	30	20	2
5	1	2	30	30	3
6	1	2	30	20	3
7	2	2	30	30	3
8	2	2	30	20	3

in an unloaded state, and then tracking the position of markers on the surface of the specimen throughout loading to measure displacements [55, 203, 216, 217]. The system was used with a single camera with a general purpose lens, and calibrated using markers of a known distance apart within the field of view, as per the manufacturer's instructions. When processing the captured video, a digital strain gauge was placed between two marker points. Specimens were marked using a permanent marker in the positions indicated in Figure 4.3, so the digital gauge length could vary. An example of a marked silicone specimen is shown in Figure 4.1.
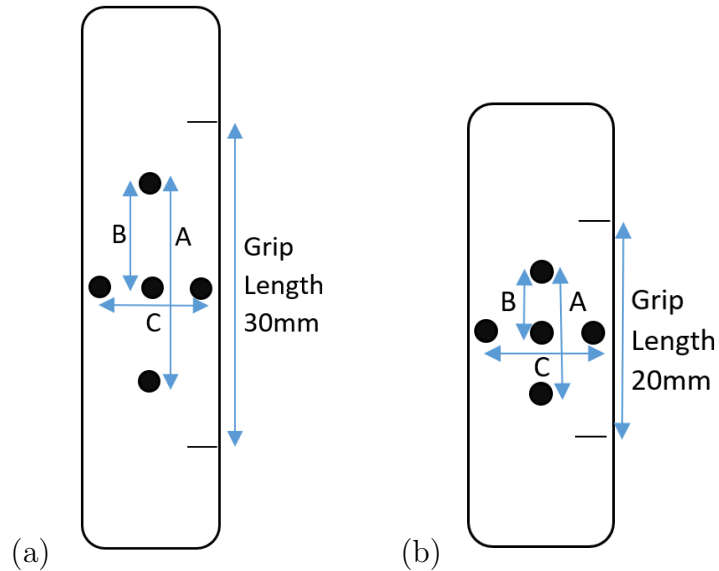
Figure 4.3: Schematic of silicone specimens with marker positions for: (a) 30mm grip length, where A is 20mm, B is 10mm and C is 7mm, and (b) 20mm grip length, where A is 10mm, B is 5mm, and C is 7mm.

Table 4.3: Post-processing parameters for the optical strain measurement system, with the gauge lengths as indicated in Figure 4.3.

	Settings 1	Settings 2	Settings 3	Settings 4
Tracking Algorithm	Deform only	Stretch, rotate and deform	Deform only	Deform only
Target 1 Size	Random (based on user)	Random (based on user)	45×45 pixels	45×45 pixels
Target 2 Size	Random (based on user)	Random (based on user)	45×45 pixels	45×45 pixels
Gauge Length	A	A	A	B

When processing the data, the target size for each marker was varied. The target area defines the area in which the software locates the surface marker. Within the software, the user also has the option to control certain elements of the tracking algorithm, for example, to account for the stretch and rotation in specimens subjected to large deformations. The post-processing variations are outlined in Table 4.3, and were allowed for the purpose of accounting for varying user preferences.

The data values measured and recorded during the experimental tests capture the inherent variation between the constitutive behaviour of the different specimens listed in Table 4.2. The values for the applied force versus maximum vertical displacement in tensile loading for each individual specimen are shown in Figure 4.4. The data collected and supplied by the experimental team was given in this format. For the specimens in each batch, the data are represented together in Figure 4.5, where the average values, which are typically used for the calibration of deterministic models, are marked by red lines. This was the first processing of the experimental data. In this figure, different quantities of interest are also illustrated. Specifically, in addition to the applied force versus maximum vertical displacement observed experimentally, the following nonlinear quantities have been calculated:

- The first Piola-Kirchhoff (PK) tensile stress (2.1.11), representing the force per unit area in the reference configuration, where $\mathbf{F}$ is the applied tensile force and $A = 40\text{mm}^2$ is the cross-sectional area.

- The nonlinear stretch modulus [127]

$$E = \frac{\boldsymbol{\sigma}}{\ln \lambda} = \frac{\lambda \mathbf{P}}{\ln \lambda},\qquad(4.2.1)$$

where λ is the stretch ratio and $\boldsymbol{\sigma} = \lambda \mathbf{P}$ is the Cauchy stress (representing the force per unit area in the current configuration), with $\mathbf{P}$ the first Piola-
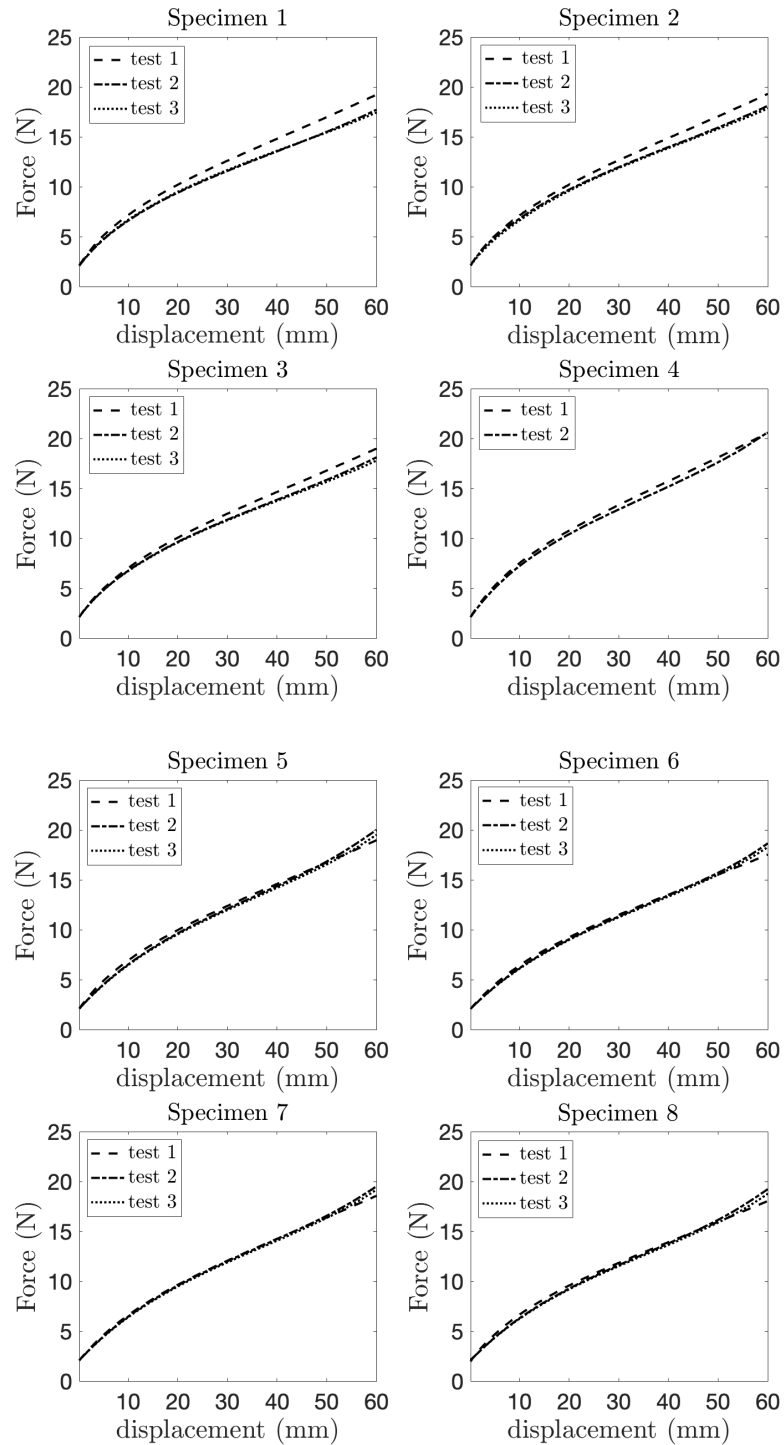
Figure 4.4: Experimental data for applied force versus maximum vertical displacement in tensile loading of individual silicone specimens listed in Table 4.2.
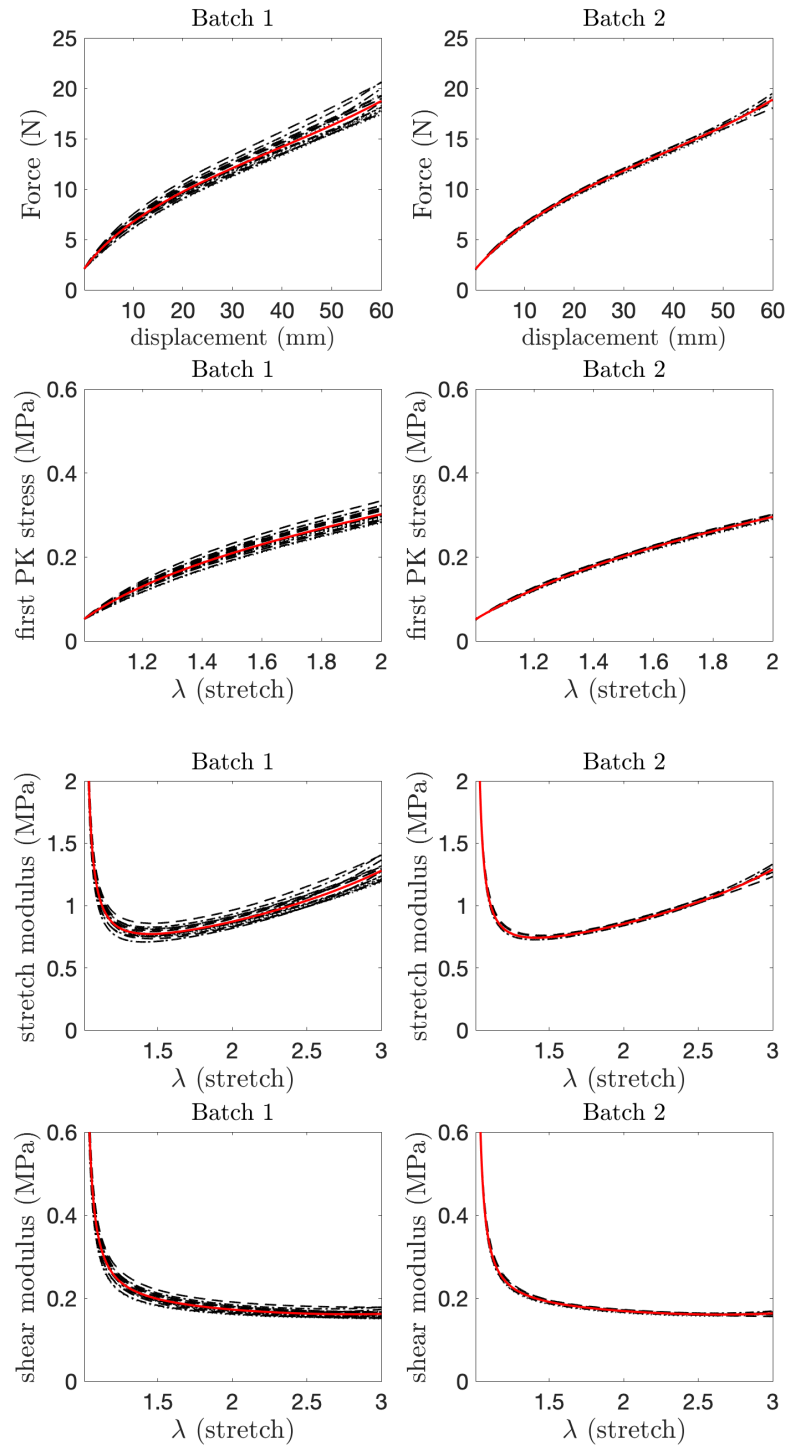
Figure 4.5: Experimental data for applied force versus maximum vertical displacement in tensile loading of the two batches of silicone specimens listed in Table 4.2, together with the first Piola-Kirchhoff (PK) tensile stress given by (2.1.11), and the nonlinear stretch and shear moduli defined by (4.2.1) and (4.2.2), respectively. The red lines indicate the mean data values.

Kirchhoff stress defined by (2.1.11).

- The nonlinear shear modulus, given by the universal formula [127]

$$\mu = \frac{E \ln \lambda}{\lambda^2 - \lambda^{-1}} = \frac{\lambda \mathbf{P}}{\lambda^2 - \lambda^{-1}}, \qquad (4.2.2)$$

where λ is the stretch ratio and E is the stretch modulus defined by (4.2.1).

Formal definitions and explicit derivations of key nonlinear elastic moduli in homogeneous isotropic finite elasticity, and their universal relations under large strains, can be found in [127].

4.3 Stochastic modelling

In this section, specific stochastic homogeneous hyperelastic models are constructed, where the parameters are characterised by probability distributions and optimised to the collected data. Deterministic hyperelastic models calibrated to mean data values of rubberlike material under finite deformations can be found, for example, in [43, 49, 82, 127, 152, 200, 210]. Statistical models derived from numerically generated data are proposed in [39, 142], while explicit stochastic hyperelastic models based on data sets consisting of mean values and standard deviations are presented in [129].

4.3.1 Stochastic isotropic incompressible hyperelastic models

As stated in earlier chapters, a homogeneous hyperelastic material is defined by a strain-energy function $W(\mathbf{F})$ with respect to a reference configuration [70, 151, 209], and characterised by a set of deterministic model parameters, which contribute to the constant elastic moduli under small strains, or to the nonlinear elastic moduli, which are functions of the deformation under large strains [127]. In contrast, a

stochastic hyperelastic model has parameters which are defined by probability density functions [129, 194–196] where, typically, each model parameter is described in terms of its mean value and its variance, which hold information regarding the range of values about the mean value [33,39,89,121,142]. Here, stochastic homogeneous isotropic incompressible hyperelastic models are constructed. These rely on the assumptions outlined in Section 3.1 [129–134]. The principle of maximum entropy is employed, which then enables the construction of their probability distributions based on the available information. Approaches for the explicit derivation of probability distributions for the elastic parameters of stochastic homogeneous isotropic hyperelastic models calibrated to experimental data for rubber-like material and soft tissues were proposed in [129, 196].

4.3.2 Hypothesis testing

Prior to attempting to construct models based on the collected data, standard statistical tests [59] were applied to verify whether the entire data set can be treated as one, or whether the data set of each batch must be modelled separately. In general, a goodness of fit test will demonstrate how well the data fits the model. Specifically, it is desirable that the data here is normally distributed, and so a goodness of fit test in this case will allow the rejection of the hypothesis that other distributions are behind the data.

Firstly, an unpaired t-test [201] was used to compare the shear modulus data at small strain for the two batches. In general terms, an unpaired t-test is useful as a technique to compare the means of two samples of data, with both samples containing distinct test subjects. The idea here was to generate a probability for how likely it is that the moduli of the two batches come from the same distribution. This test provided a p-value (or probability) of approximately 10^{-12}. The 'standard' significance level is 0.05, meaning that if the p-value is less than this standard threshold, we can be 95% certain that the data does not come from the

distribution, and thus the hypothesis that the distribution is behind the data can be rejected. In the specific case here, we have $p \approx 10^{-12}$, which is clearly less than the 0.05 significance level, and therefore enables the rejection of the null hypothesis that the moduli of the two batches come from the same distribution. As a result, the distributions had to be calibrated to the different batches separately. The significant differences between the data corresponding to the two batches are illustrated in Figure 4.6.

Further, a χ^2 (chi-square) goodness-of-fit test [184] was employed to check whether or not the null hypothesis that the shear modulus data of each batch come from a Gamma distribution can be rejected. A chi-square goodness-of-fit test is used to determine how well a theoretical distribution fits to an empirical distribution, where an empirical distribution is derived from the sample, and the theoretical distribution is constructed based on the prior knowledge of the distribution and its parameters. In the current case, the p-values for the Batch 1 and 2 fits were 0.1 and 0.07, respectively, which are both greater than the 0.05 significance level, and thus the hypothesis that the shear moduli are Gamma-distributed could not be rejected.

Table 4.4: Parameters of the probability distributions derived from the data values for the random shear modulus at small strain.

Probability density function (pdf)	$\underline{\mu}$	$\|\mu\|$	ρ_1	ρ_2
Gamma pdf fitted to Batch 1 data	0.2837	0.0171	275.4403	0.0010
Normal pdf fitted to Batch 1 data	0.2837	0.0170	-	-
Gamma pdf fitted to Batch 2 data	0.2663	0.0083	1029.4047	0.0003
Normal pdf fitted to Batch 2 data	0.2663	0.0084	-	-

Figure 4.7 illustrates the Gamma and normal (Gaussian) probability distributions fitted to the shear modulus data at small strain. Note here the similarity between the represented Gamma and normal distributions [131]. This is to be
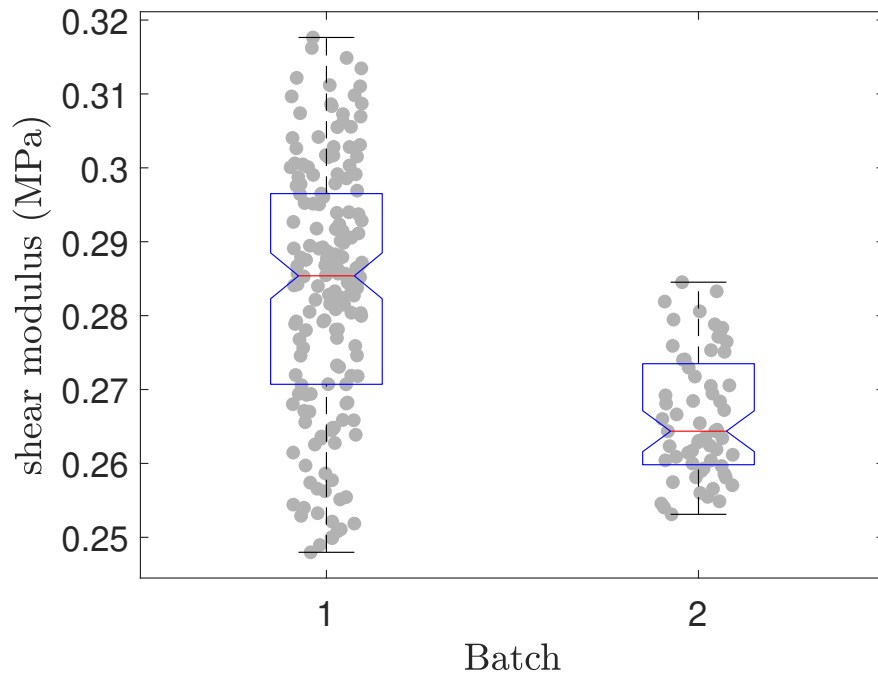
Figure 4.6: Box plots of the shear modulus at small strain data of the two batches. On each box, the grey dots represent the data, the central mark indicates the median, and the bottom and top edges of the box indicate the 25th and 75th percentiles, respectively. The whiskers extend to the most extreme data points. Critically, these distributions are significantly different.
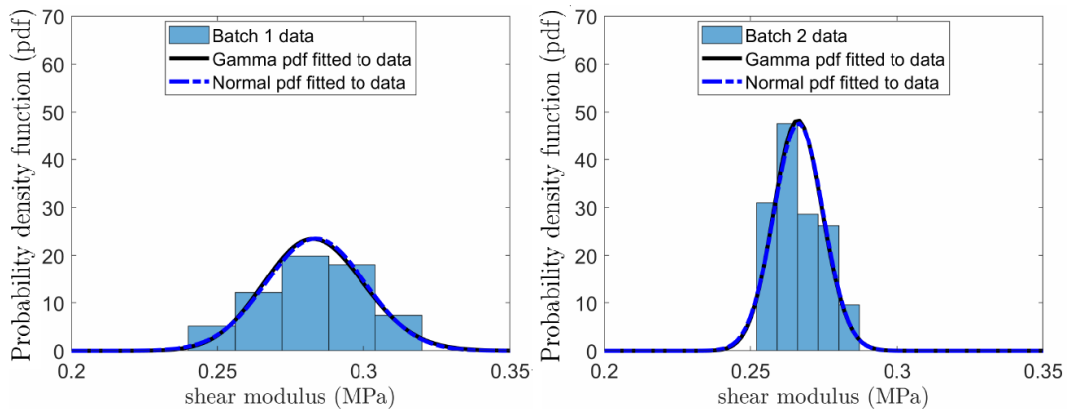
Figure 4.7: Probability distributions derived from the data values for the random shear modulus at small strain. The parameters for these distributions are recorded in Table 4.4.

expected in this case because, when $\rho_1 \to \infty$, the Gamma probability distribution (3.1.6) is approximated by a normal distribution (see Appendix D for a detailed proof). Table 4.4 provides the fitted variables for both distributions. It can be observed that ρ_1 is very large compared to ρ_2, justifying the similarity between the two distributions. The fitted values for the shear modulus are also comparable to those recorded in Tables 4.6 and 4.7, corresponding to the three hyperelastic models for which the shear modulus satisfies a Gamma distribution. However, elastic moduli cannot be characterised by the normal distribution since this distribution is defined on the entire real line, whereas elastic moduli are typically positive.

4.3.3 Stochastic calibration

Applying the stochastic method developed in Section 3.3, the analysis is now specialised to three different stochastic hyperelastic strain-energy functions which are then calibrated to the collected experimental data. These strain-energy functions are presented in Table 4.5, while their constitutive parameters fitted to the experimental measurements for Batch 1 and Batch 2 are recorded in Tables 4.6 and 4.7, respectively. Specifically, in the case of the Ogden model, the calibration procedure presented in Chapter 3 was followed, and the parameters here provided the most stable solution. The load-deformation results are plotted in Figures 4.8 and 4.9, demonstrating that all three models perform well, but exhibit different levels of accuracy when compared to the actual data.

4.3.4 Bayesian model selection

In this section, Bayes' theorem [22, 122] is employed to select a model among competing models calibrated to the given data. Bayes' theorem is used to describe the probability of an event occurring, based on the prior knowledge of conditions that are potentially related to the event in question. In practical applications, Bayes' theorem is relied upon in many machine learning techniques, and also

Table 4.5: Incompressible isotropic hyperelastic models, $\mathcal{W}(\lambda_1, \lambda_2, \lambda_3)$, their non-linear shear modulus $\mu(\lambda)$ at a given stretch $\lambda = a$, and the shear modulus at infinitesimal deformation, $\lim_{\lambda \to 1} \mu(\lambda) = \overline{\mu}$.

Material Model	Strain-Energy Density	Shear Moduli
	$\mathcal{W}(\lambda_1, \lambda_2, \lambda_3)$	
Mooney-Rivlin	$\frac{C_1}{2}\left(\lambda_1^2 + \lambda_2^2 + \lambda_3^2 - 3\right) + \frac{C_2}{2}\left(\lambda_1^{-2} + \lambda_2^{-2} + \lambda_3^{-2} - 3\right)$	$\mu(a) = C_1 + \frac{C_2}{a}$
[137, 168]	C_1, C_2 independent of deformation	$\overline{\mu} = C_1 + C_2$
Gent-Gent	$-\frac{C_1}{2\beta}\ln\left[1 - \beta\left(\lambda_1^2 + \lambda_2^2 + \lambda_3^2 - 3\right)\right] + \frac{3C_2}{2}\ln\frac{\lambda_1^{-2} + \lambda_2^{-2} + \lambda_3^{-2}}{3}$	$\mu(a) = \frac{C_1}{1 - \beta(a^2 + 2/a - 3)} + \frac{3C_2}{2a^2 + 1/a}$
[152, 161]	C_1, C_2, β independent of deformation	$\overline{\mu} = C_1 + C_2$
Ogden	$\sum_{p=1}^{3} \frac{C_p}{2\alpha_p^2}\left(\lambda_1^{2\alpha_p} + \lambda_2^{2\alpha_p} + \lambda_3^{2\alpha_p} - 3\right)$	$\mu(a) = \sum_{p=1}^{3} \frac{C_p}{\alpha_p}\frac{a^{1-\alpha_p}\left(1 - a^{3\alpha_p}\right)}{1 - a^3}$
[150]	C_p independent of deformation; $\alpha_1 = 1$, $\alpha_2 = -1$, $\alpha_3 = -2$,	$\overline{\mu} = \sum_{p=1}^{3} C_p$

Table 4.6: Parameters of the stochastic constitutive models given in Table 4.5, calibrated to Batch 1 data, and the corresponding random nonlinear shear modulus $\mu = \mu(\lambda)$ at $\lambda = 1.15$.

Stochastic Model	Calibrated Parameters	Shear Modulus (MPa)
	(mean value $\pm$ std deviation)	(mean value $\pm$ std deviation)
Mooney-Rivlin	$C_1 = 0.0936 \pm 0.0030$	$\mu = 0.2411 \pm 0.0130$
	$C_2 = 0.1696 \pm 0.0115$	
Gent-Gent	$C_1 = 0.0971 \pm 0.0042$	$\mu = 0.2532 \pm 0.0136$
	$C_2 = 0.1826 \pm 0.0110$	
	$\beta = 0.0434$	
Ogden	$C_1 = -0.0645 \pm 0.0143$	$\mu = 0.2719 \pm 0.0720$
	$C_2 = -0.0764 \pm 0.0155$	
	$C_3 = 0.4861 \pm 0.0534$	
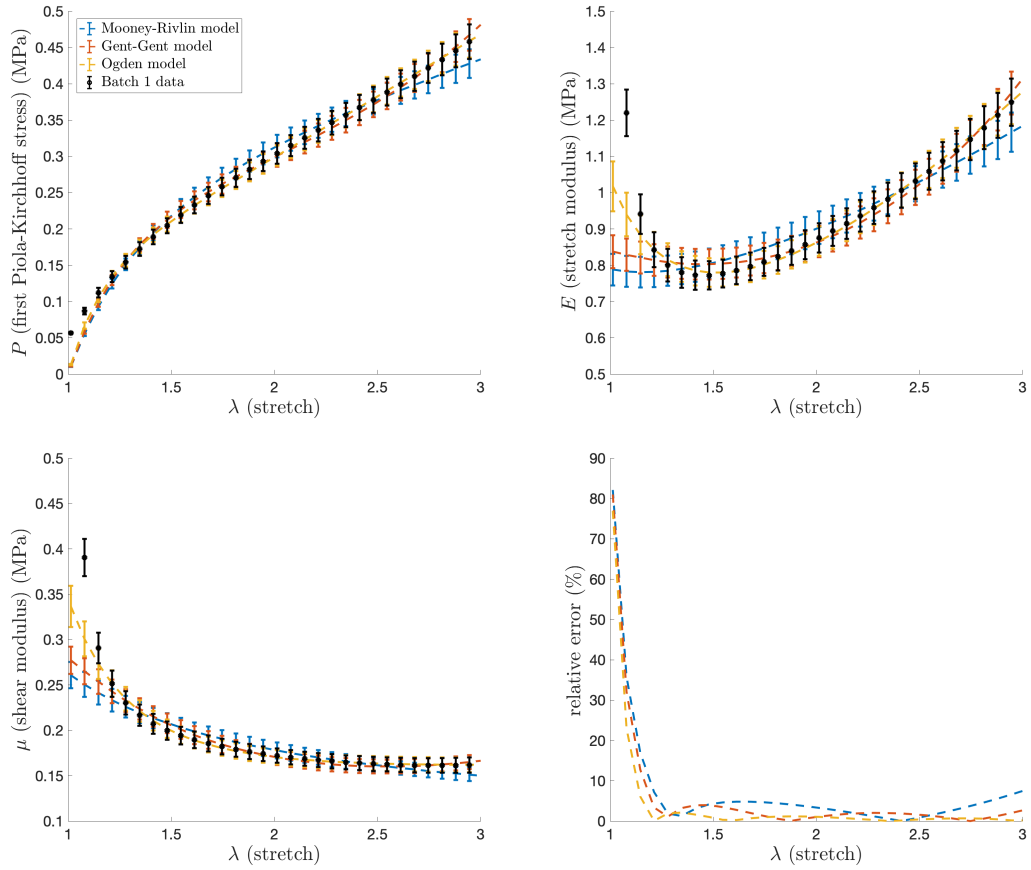
Figure 4.8: Stochastic models calibrated to the Batch 1 data, with the parameters recorded in Table 4.6, showing: (a) the first Piola-Kirchhoff tensile stress, (b) the nonlinear stretch modulus, (c) the nonlinear shear modulus, and (d) the relative error for the shear modulus mean values.
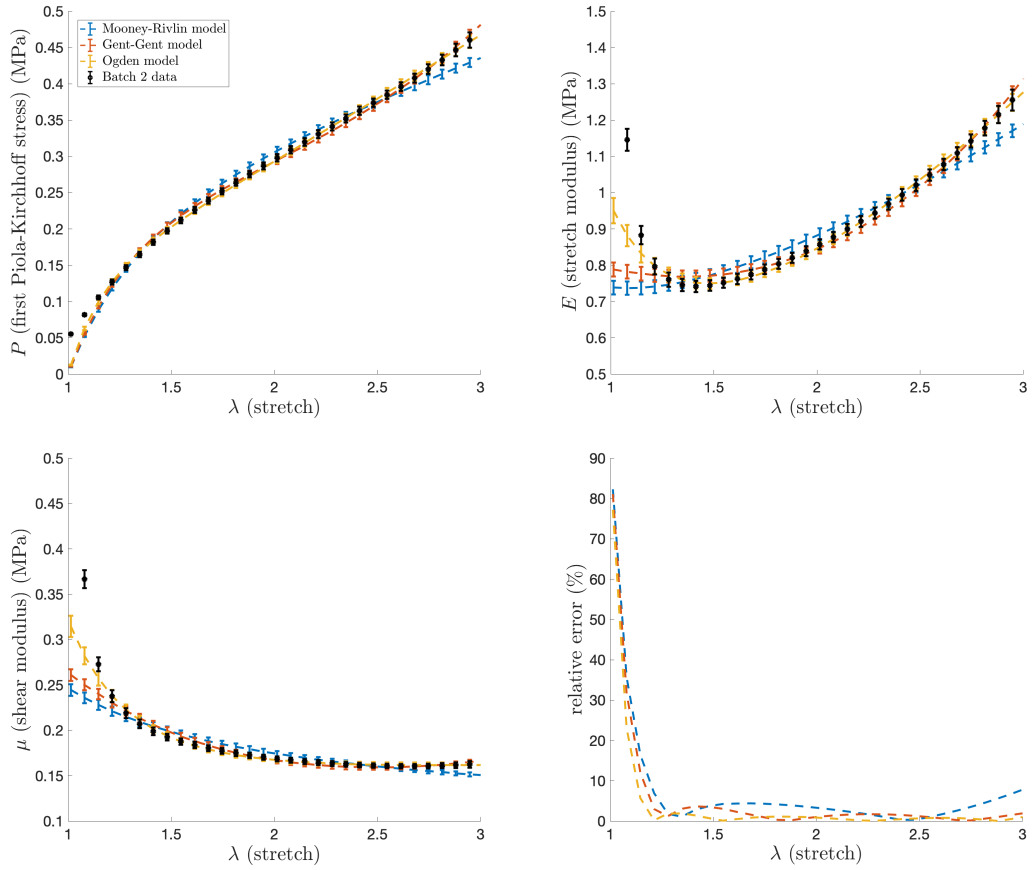
Figure 4.9: Stochastic models calibrated to the Batch 2 data, with the parameters recorded in Table 4.7, showing: (a) the first Piola-Kirchhoff tensile stress, (b) the nonlinear stretch modulus, (c) the nonlinear shear modulus, and (d) the relative error for the shear modulus mean values.

Table 4.7: Parameters of the stochastic constitutive models given in Table 4.5, calibrated to Batch 2 data, and the corresponding random nonlinear shear modulus $\mu = \mu(\lambda)$ at $\lambda = 1.15$.

Stochastic Model	Calibrated Parameters (mean value $\pm$ std deviation)	Shear Modulus (MPa) (mean value $\pm$ std deviation)
Mooney-Rivlin	$C_1 = 0.1029 \pm 0.0001$	$\mu = 0.2277 \pm 0.0056$
	$C_2 = 0.1435 \pm 0.0063$	
Gent-Gent	$C_1 = 0.1007 \pm 0.0011$	$\mu = 0.2397 \pm 0.0056$
	$C_2 = 0.1625 \pm 0.0053$	
	$\beta = 0.0421$	
Ogden	$C_1 = -0.0437 \pm 0.0111$	$\mu = 0.2563 \pm 0.0272$
	$C_2 = -0.0844 \pm 0.0112$	
	$C_3 = 0.4505 \pm 0.0345$	

within the biomedical field in medical testing.

Here, $P(M)$ denotes the prior probability of choosing a model M before the data values D are taken into account, and $P(D|M)$ denotes the likelihood, or the probability, of obtaining the data values D from the model M. Bayes' theorem states that

$$P(M|D) = \frac{P(M)P(D|M)}{P(D)}, \qquad (4.3.1)$$

where $P(M|D)$ is the posterior probability of the model M, or in other words, the probability that the hypothesis is true after taking the relevant data into consideration, and $P(D)$ is the normalisation value, known as the marginal likelihood, which is a likelihood function as described above, where, as the name suggests, some parameter variables have been marginalised. In addition, this theorem supplies a methodology for estimating the odds for a model $M^{(i)}$ to another model

$M^{(j)}$, in light of the data D;

$$O_{ij} = \frac{P(M^{(i)}|D)}{P(M^{(j)}|D)} = \frac{P(M^{(i)})P(D|M^{(i)})}{P(M^{(j)})P(D|M^{(j)})} = \frac{P(M^{(i)})}{P(M^{(j)})}B_{ij}, \qquad (4.3.2)$$

where

$$B_{ij} = \frac{P(D|M^{(i)})}{P(D|M^{(j)})} \qquad (4.3.3)$$

is the *Bayes factor*. The objective of the Bayes factor in this context is to appraise the support for the use of one material model over another. Formula (4.3.2) states that the posterior odds O_{ij} for the model $M^{(i)}$ against the model $M^{(j)}$, given the data D, are equal to the prior odds multiplied by the Bayes factor. In particular, if the models have equal prior probabilities, $P(M^{(i)}) = P(M^{(j)})$, so there is no prior favourite, then, by (4.3.2), the posterior odds are equal to the Bayes factor, i.e. $O_{ij} = B_{ij}$.

If, however, the Bayes factor is equal to 1, then *Occam's razor* [97–99, 204] would imply that a larger prior probability should be assigned to the simpler model, rather than to the more complex one, purely for frugal reasoning.

Maintaining a general framework, it is assumed that $P(D|M)$ is an arbitrary probability that is symmetric about the mean value $D = 0$ and decreasing in the absolute value of D. In this case, the Bayes factor B_{ij} satisfies the inequality [27]

$$B_{ij} \geq \frac{\|D^{(j)}\| + \sqrt{2\ln\left(\|D^{(j)}\| + 1.2\right)}}{e^{\|D^{(i)}\|^2/2}}\sqrt{\frac{2}{\pi}}, \qquad (4.3.4)$$

where $\|D^{(i)}\|$ and $\|D^{(j)}\|$ designate the standard deviation that the predicted quantity of interest computed with the model $M^{(i)}$ and $M^{(j)}$, respectively, deviates from the observed data value D. The formula for calculating $\|D^{(i)}\|$, for example, is as follows

$$\|D^{(i)}\| = \frac{|Q^{(i)} - D|}{\|D\|}, \qquad (4.3.5)$$

where, for the quantity of interest, $Q^{(i)}$ is the expected value computed with the

model $M^{(i)}$, while $\underline{D}$ and $\|D\|$ represent the experimentally observed mean value and standard deviation, respectively. The expression on the right-hand side of (4.3.4) provides an explicit lower bound on the Bayes factor B_{ij}. Hence, assuming that the prior probabilities are equal, the lower bound on the Bayes factor, given by (4.3.4), represents a lower bound on the posterior odds. This lower bound on B_{ij} is an estimate of the amount of evidence against the model $M^{(i)}$, or alternatively, the maximum support for the model $M^{(j)}$, provided by the data.

These bounds are now applied to select the best performing model among the models calibrated to the experimental data. For example, at $\lambda = 1.15$, for each model recorded in Table 4.6, the standard deviations that the mean shear modulus μ deviates from the experimental mean data value 0.2909, given that the experimental standard deviation is 0.0170, are calculated. Applying formula (4.3.5) yields the following:

$$\|D^{(1)}\| = \frac{|0.2411 - 0.2909|}{0.0170} = 2.9294 \qquad \text{for Mooney-Rivlin model,}$$

$$\|D^{(2)}\| = \frac{|0.2532 - 0.2909|}{0.0170} = 2.2176 \qquad \text{for Gent-Gent model,}$$

$$\|D^{(3)}\| = \frac{|0.2719 - 0.2909|}{0.0170} = 1.1176 \qquad \text{for Ogden model.}$$

Assuming no prior favourite model, so equal prior probabilities, by (4.3.4), it follows that the Bayes factors, or the odds, for the Ogden model against each of the other two models satisfy $B_{31} \geq 1.9713$ and $B_{32} \geq 1.6174$, respectively. Now, taking $P(D|M^{(1)}) = 1 - P(D|M^{(3)})$, by the lower bound on the Bayes factor B_{31}, the likelihood of obtaining the data with the Ogden model is $P(D|M^{(3)}) \geq 0.6634$. Similarly, assuming equal prior probabilities and taking $P(D|M^{(2)}) = 1 - P(D|M^{(3)})$, the lower bound on B_{32} implies $P(D|M^{(3)}) \geq 0.6179$. Therefore, for uniaxial tension, the data at $\lambda = 1.15$ are more likely to be reproduced with the Ogden model than with any of the other two models.

The lower bounds on the Bayes factors B_{ij} for each model $M^{(i)}$ against another model $M^{(j)}$ at various stretch ratios are illustrated in Figure 4.10. From these
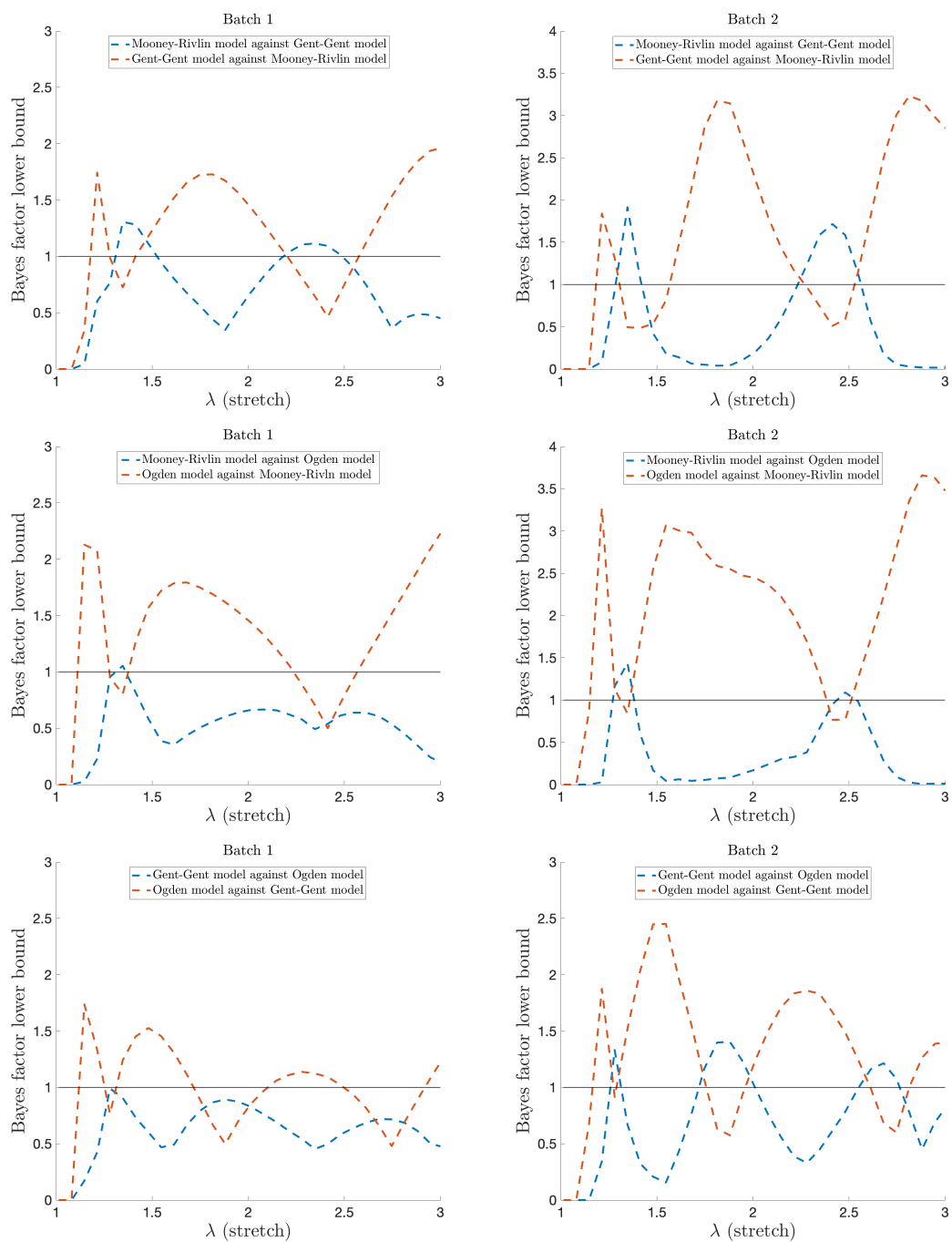
Figure 4.10: Lower bounds on the Bayes factors for each model against the other at various stretch ratios.

bounds, it can be understood that the Gent-Gent model is generally more likely to represent the data than the Mooney-Rivlin model, and the Ogden model is more likely than both the Mooney-Rivlin and the Gent-Gent models. These results are consistent with those in Figures 4.8(d) and 4.9(d), where the relative errors for the mean values of the shear modulus are shown. The relative error (a measure of the uncertainty of the measurement compared to the size of the measurement) was calculated using $|\underline{\mu}_{model} - \underline{\mu}_{data}|/\underline{\mu}_{data}$, where $\underline{\mu}_{model}$ is the mean value of the shear modulus for the respective model and $\underline{\mu}_{data}$ is the mean value of the shear modulus obtained from the experimental data.

4.4 Summary

Motivated by the need to quantify uncertainties in the mechanical responses of solid materials to achieve repeatability between experiments in engineering applications, in this chapter, experimental tests were performed on different samples of a manufactured rubber-like material under tensile loading, and a stochastic modelling strategy was employed to derive constitutive models that account for the variability in the collected data. Specifically, isotropic incompressible hyperelastic models with model parameters defined as spatially-independent random variables characterised by probability density functions were constructed. Furthermore, a methodology to compare different models using an explicit lower bound on the Bayes factor was applied in order to select the model that was most likely to reproduce the experimental data.

The objective of this chapter is to highlight the need for continuum models to consider the variability in the elastic behaviour of materials at large strains, complementing the theoretical investigations of how elastic solutions of fundamental problems in nonlinear elasticity can be extended to stochastic hyperelastic models, which will be presented in Chapters 5 and 6. Overall, it is the hope that the results presented in this chapter will motivate and inspire others to collect and

report on their data in a similar manner.

Chapter 5

Likely deformations and instabilities of stochastic hyperelastic bodies

Extending the more general concepts discussed in Chapter 3, the likely deformations and instabilities of stochastic hyperelastic bodies are now discussed for a variety of material models. Firstly, in Section 5.1, an in-depth analysis into the occurrence of a necking instability in materials modelled by four different stain-energy functions, namely, two-term Ogden-type models (Section 5.1.1), the Carroll model (Section 5.1.2), and the Gent-Thomas model (Section 5.1.3), is presented. The purpose of this is to apply stochastic modelling techniques to a simpler deformation to aid understanding, before extending the analysis of the more complex material deformations from the traditional deterministic approach to the novel stochastic perspective in later sections and chapters. The conditions under which a necking instability occurs for a particular material are outlined, followed by a deterministic analysis which allows a critical point to be established. Traditionally, any value below this critical point would be unstable, and anything above would be stable, thus implying the occurrence of necking. A stochastic analysis is then presented, in which the stability of points within an interval surrounding

the deterministic critical value is analysed, allowing the probability of necking occurring at points within this interval to be realised.

The inflation of stochastic spheres and circular cylinders is discussed in Sections 5.2.1 and 5.2.2, respectively. In both cases, an approach based on the procedures outlined in both [38] and [151] is developed, and the behaviour of the spheres and cylinders is analysed. Firstly, the purely elastic case is investigated, with a description of the qualitative behaviour of the pressure in both the spheres and cylinders during inflation in terms of the uniaxial compressive stress response of the material being presented. As in [38], three types of behaviour are established; either the pressure increases monotonically, it increases to a maximum value then decreases, or it increases, decreases, then increases again. The three types of behaviour are then demonstrated using the well-known Mooney-Rivlin model. The limit-point instability criterion for both spherical shells and cylindrical tubes is discussed, and the critical value where a limit-point instability occurs is established in both scenarios. A limit-point instability implies the existence of a localised bulging in the material (for further details on this, see [62, 218]). Following this, a stochastic approach is presented, and a description of the criteria for instability is suggested for both spheres and cylinders in this probabilistic case.

In Section 5.3, explicit solutions to the cavitation problems of incompressible spheres of stochastic isotropic hyperelastic material under radial tensile dead loads are investigated. The question of the influence of the stochastic model parameters on the predicted nonlinear elastic response of the material is addressed by presenting explicit solutions to the cavitation problems of incompressible spheres made of a class of stochastic isotropic hyperelastic materials, described by a two-term Ogden-type model [129, 194, 196], under uniform radial tensile dead loads. For the purely elastic problem, involving isotropic incompressible materials, there is a critical tensile traction that strictly separates the cases where cavitation can or cannot occur. The stability of the cavitated solution is analysed, followed by

distinguishing between a supercritical cavitation, and a subcritical, or snap, cavitation. Attention is then refocused on the stochastic problem where, in addition to the mean critical traction, the probability distribution of stable deformation under radially symmetric tension is also derived. It is established that, due to the probabilistic nature of the material parameters, there is always competition between the two cases. Therefore, cavitation can no longer be discussed as a certainty, but now in terms of 'likely cavitation', obtained under a given tensile traction with a given probability. In this case, equivalent material behaviour is found when the model parameters are drawn from probability distributions.

By approaching these varying deformations from the stochastic perspective, we are able to gain further insight into the behaviour of the materials in question, and to develop enhanced mathematical models to be used in many practical applications.

5.1 Necking instability

To begin, the conditions under which a necking instability occurs for a particular material are discussed. Necking instability is a well-known material deformation, occurring in materials which undergo a maximum load in testing, and deformation localises in an area on the order of the thickness of the material specimen, at some location along the specimen length. Necking instabilities are highly nonlinear due to material and geometric nonlinearities. The full necking response, including bifurcation from the uniform deformation, is analysed in [13].

By considering first this simple deformation, an enhanced understanding of extending the analysis from the traditional deterministic viewpoint to the stochastic perspective can be well understood, before the stochastic approach is presented for the more complex material deformations discussed in Sections 5.2, 5.3 and Chapter 6.

The onset of necking for four different material models is investigated within

Sections 5.1.1, 5.1.2, and 5.1.3. The conditions for instability are unique for each material model. A deterministic analysis is presented, in which a critical value is found. In this traditional analysis, values below the critical value would be unstable, and anything above this value would be stable. This problem is then approached from a stochastic perspective, where an interval surrounding the deterministic critical point is observed, and the probability of necking occuring for values within this interval is obtained, providing a clearer, enhanced understanding of the conditions under which a necking instability occurs in each model presented.

5.1.1 Two-term Ogden-type models

Firstly, the situation considering the conditions under which a necking instability may occur in a Mooney-Rivlin material is addressed.

The Mooney-Rivlin model is characterised by the strain-energy function

$$\mathcal{W}(\lambda_1, \lambda_2, \lambda_3) = \frac{C_1}{2}(\lambda_1^2 + \lambda_2^2 + \lambda_3^2 - 3) + \frac{C_2}{2}(\lambda_1^{-2} + \lambda_2^{-2} + \lambda_3^{-2} - 3), \qquad (5.1.1)$$

where C_1 and C_2 are constants, with $C_1, C_2 > 0$. Assuming that this material is subject to the normal tension

$$\lambda_1 = \lambda > 1, \qquad \lambda_2 = \lambda_3 = \frac{1}{\sqrt{\lambda}} < 1, \qquad (5.1.2)$$

the strain energy function takes the equivalent form

$$W(\lambda) = \frac{C_1}{2}(\lambda^2 + 2\lambda^{-1} - 3) + \frac{C_2}{2}(\lambda^{-2} + 2\lambda - 3). \qquad (5.1.3)$$

For a model to have an instability, at some point, we must have $W''(0) < 0$. Alternatively, we can find a critical point where $W''(\lambda) = 0$, and observe that a

change of sign occurs. The second derivative of (5.1.3) is

$$W''(\lambda) = C_1(1 + 2\lambda^{-3}) + 3C_2\lambda^{-4}, \tag{5.1.4}$$

where, since $C_1, C_2 > 0$ and $\lambda > 1$, we have $W''(\lambda) > 0$, and so this model is always stable. Hence, necking does not occur in the Mooney-Rivlin model.

Let

$$f(\lambda) = \frac{3\lambda^{-4}}{1 + 2\lambda^{-3}}. \tag{5.1.5}$$

Defining $g(\lambda) = f'(\lambda)$, we have

$$g(\lambda) = \frac{-6(\lambda^{-8} + 2\lambda^{-5})}{(1 + 2\lambda^{-3})^2}. \tag{5.1.6}$$

Expressions (5.1.5) and (5.1.6) are depicted in Figure 5.1(a) and (b), for small and large values of λ, respectively. A plot demonstrating that a necking instability does not occur in the Mooney-Rivlin model discussed above is then given in Figure 5.2.

Next, the model in question is characterised by the strain-energy function

$$\mathcal{W}(\lambda_1, \lambda_2, \lambda_3) = \frac{C_1}{2}(\lambda_1^2 + \lambda_2^2 + \lambda_3^2 - 3) + \frac{C_2}{2}(\lambda_1^{-1} + \lambda_2^{-1} + \lambda_3^{-1} - 3), \tag{5.1.7}$$

where C_1 and C_2 are constants, with $C_1, C_2 > 0$. As before, we assume that this material is subject to the normal tension (5.1.2), so the strain-energy function (5.1.7) takes the equivalent form

$$W(\lambda) = \frac{C_1}{2}(\lambda^2 + 2\lambda^{-1} - 3) + \frac{C_2}{2}(\lambda^{-1} + 2\sqrt{\lambda} - 3), \tag{5.1.8}$$

with

$$W''(\lambda) = C_1(1 + 2\lambda^{-3}) + \frac{C_2}{2}\left(2\lambda^{-3} - \frac{1}{2}\lambda^{-\frac{3}{2}}\right). \tag{5.1.9}$$

(a)

(b)
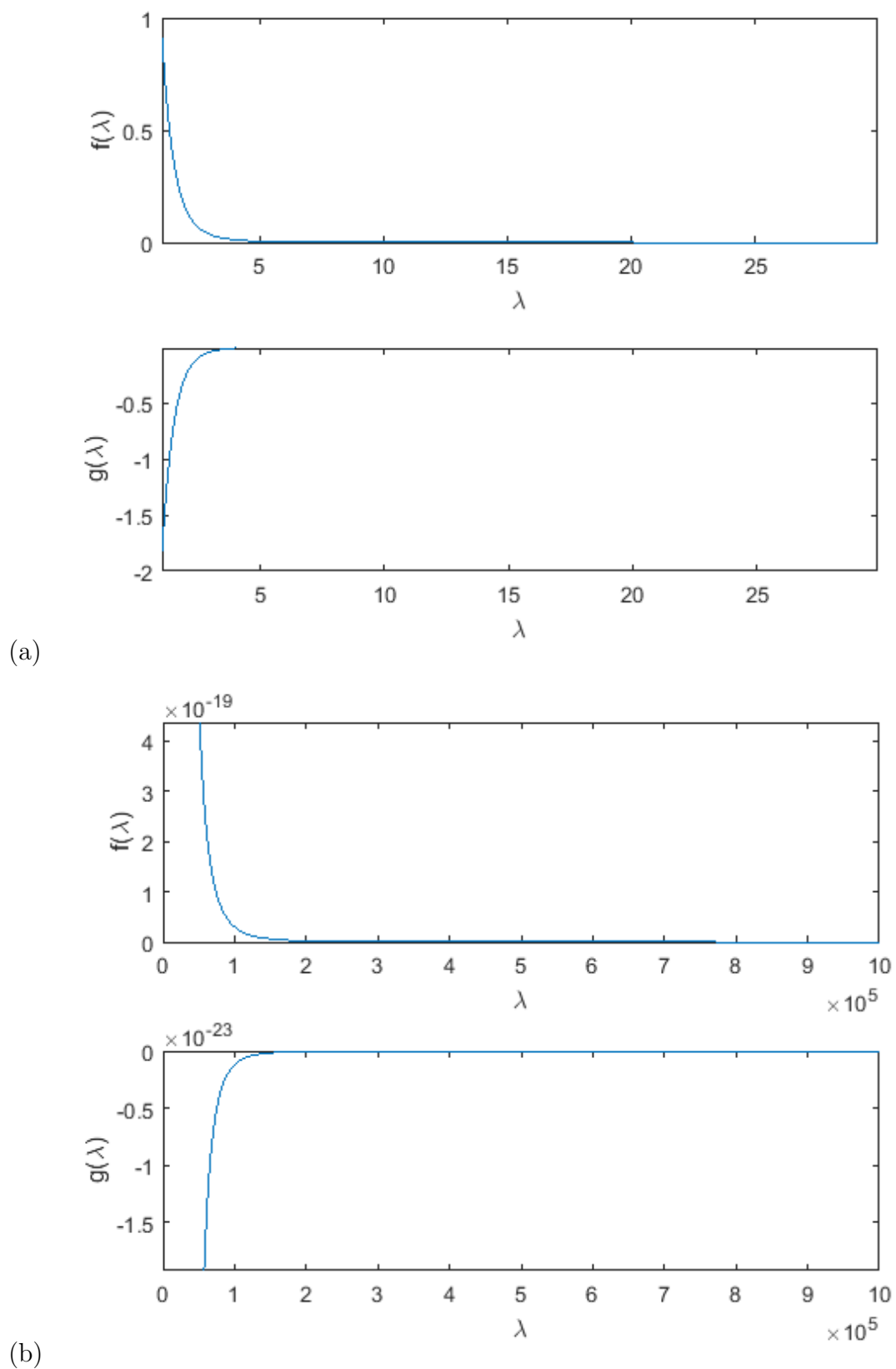
Figure 5.1: The behaviour of the functions $f(\lambda)$ (5.1.5) and $g(\lambda)$ (5.1.6), respectively: (a) at small values of λ, and (b) at large values of λ.
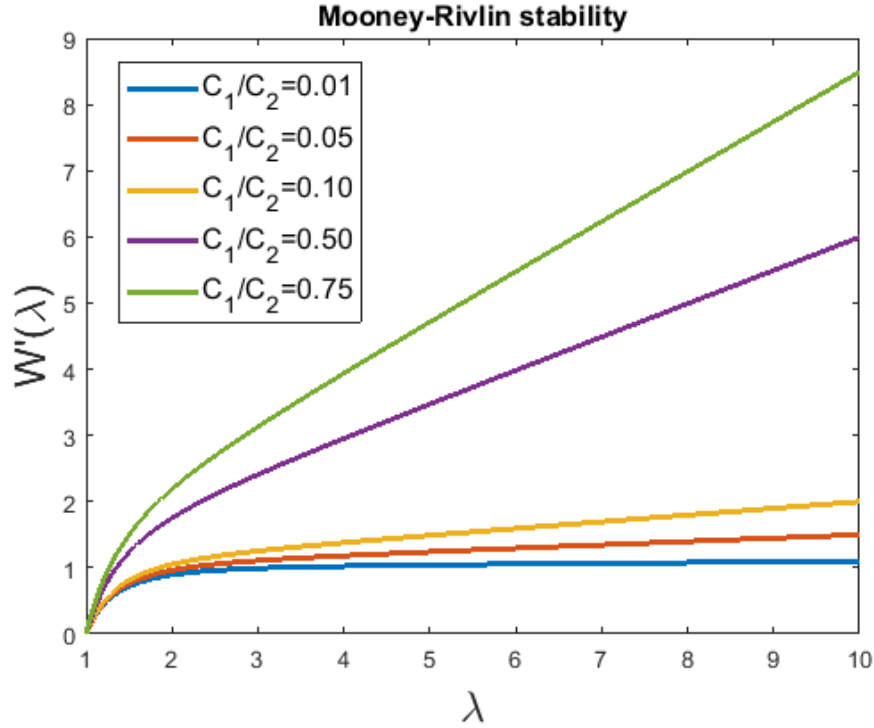
Figure 5.2: Plot demonstrating the stability of the Mooney-Rivlin model.

Setting (5.1.9) equal to 0, we have

$$C_1(1 + 2\lambda^{-3}) + \frac{C_2}{2}\left(2\lambda^{-3} - \frac{1}{2}\lambda^{-\frac{3}{2}}\right) = 0, \tag{5.1.10}$$

which can be rearranged to give

$$\frac{C_1}{C_2} = \frac{\frac{1}{4}\lambda^{-\frac{3}{2}} - \lambda^{-3}}{1 + 2\lambda^{-3}}. \tag{5.1.11}$$

It is then possible to deduce two conditions regarding the stability of the model using (5.1.11); when

$$\frac{C_1}{C_2} > \frac{\frac{1}{4}\lambda^{-\frac{3}{2}} - \lambda^{-3}}{1 + 2\lambda^{-3}}, \tag{5.1.12}$$

for any $\lambda > 1$, the model is stable, and when

$$\frac{C_1}{C_2} < \frac{\frac{1}{4}\lambda^{-\frac{3}{2}} - \lambda^{-3}}{1 + 2\lambda^{-3}}, \tag{5.1.13}$$

the model is unstable.

Let

$$f(\lambda) = \frac{\frac{1}{4}\lambda^{-\frac{3}{2}} - \lambda^{-3}}{1 + 2\lambda^{-3}}, \tag{5.1.14}$$

then, defining $g(\lambda) = f'(\lambda)$, we have

$$g(\lambda) = \frac{3\lambda^{-4} - \frac{3}{8}\lambda^{-\frac{5}{2}} + \frac{3}{4}\lambda^{-\frac{11}{2}}}{(1 + 2\lambda^{-3})^2}. \tag{5.1.15}$$

Expressions (5.1.14) and (5.1.15) are demonstrated in Figures 5.3(a) and (b), for small and large values of λ, respectively.

To find the maximum value of $f(\lambda)$, we set the expression for $g(\lambda)$ (5.1.15) equal to 0, solve this equation for λ, then substitute the obtained value of λ back into (5.1.14). Doing so, we obtain

$$\lambda = (34 + 24\sqrt{2})^{1/3}. \tag{5.1.16}$$

Substituting (5.1.16) back into (5.1.14), we obtain

$$\max_{\lambda} f(\lambda) \approx 0.0152. \tag{5.1.17}$$

Therefore, if $C_1/C_2 > \sup_{\lambda>1} f(\lambda) \approx 0.0152$, necking does not occur.

In (3.4.12), it was determined that $C_1/C_2 = R_1/(1 - R_1)$, so in this case, we have

$$\frac{R_1}{(1 - R_1)} > 0.0152, \tag{5.1.18}$$

from which it can then be deduced that $R_1 > 19/1269$. Therefore, for a necking instability to occur, we must have $R_1 < 19/1269$.

From a deterministic perspective, it would be possible to deduce whether or not a necking instability has occurred based on the values of the random variables C_1 and C_2. However, this approach only allows one particular piece of material to be dealt with. Adopting a stochastic approach enables us to deal with an infinite
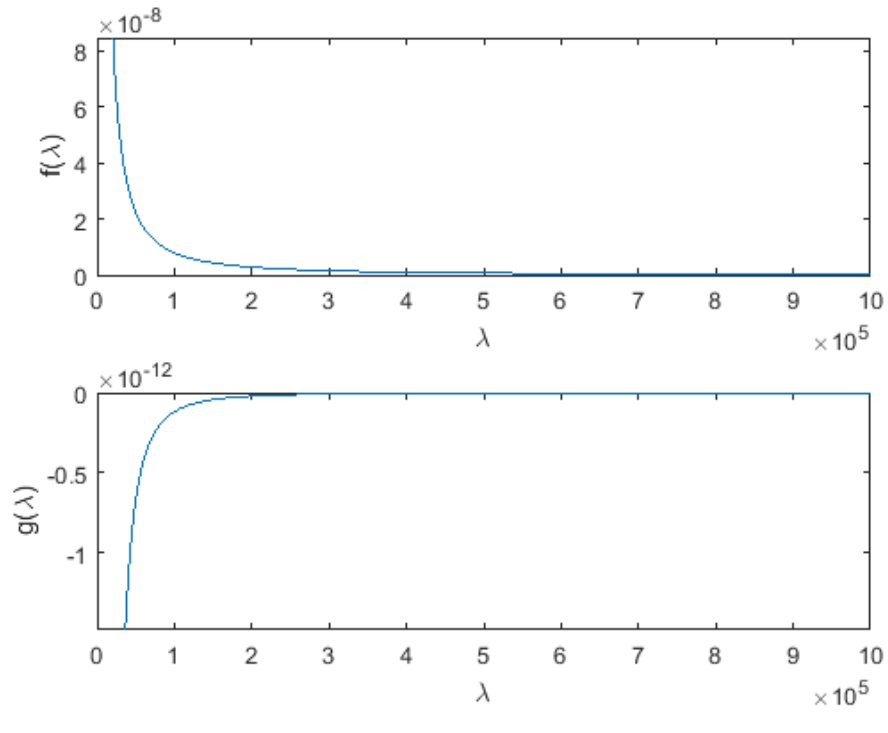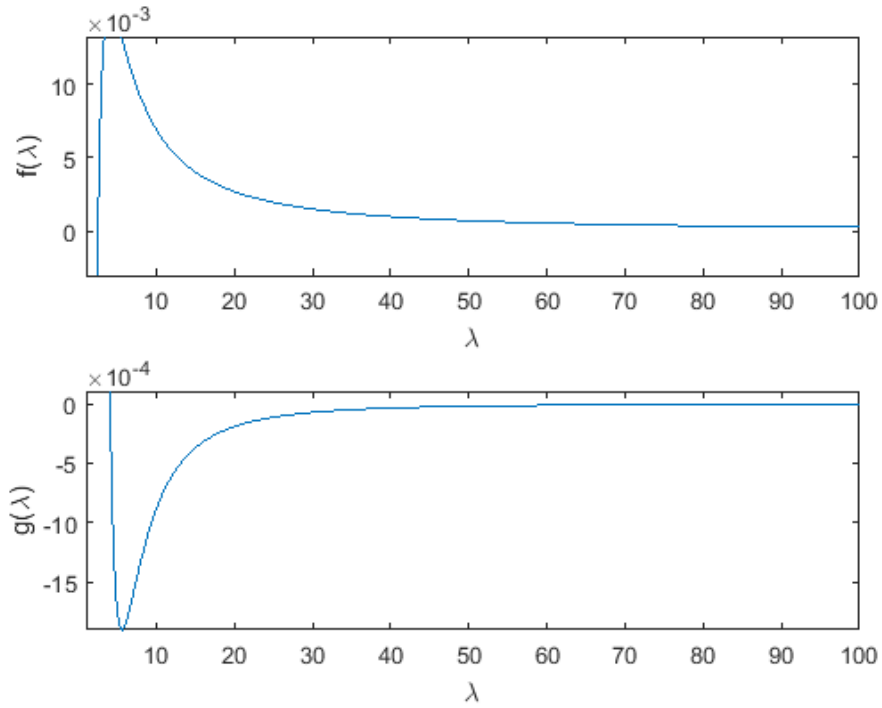
Figure 5.3: The behaviour of the functions $f(\lambda)$ (5.1.14) and $g(\lambda)$ (5.1.15), respectively: (a) at small values of λ, and (b) at large values of λ. Note that $f(\lambda)$ is the right-hand side of (5.1.12), and $g(\lambda)$ is the derivative of $f(\lambda)$.

set of materials, thus allowing the determination of the probability distribution that C_1 and C_2 follow. As a result, any uncertainties that may occur within the experimental data can be taken into account and, as such, we are able to give a more accurate suggestion as to whether or not necking is likely to occur for a given material, chosen at random from the set. Naturally, the question that now arises is; "what is the probability that the body chosen from the set is stable under necking tests?". In other words, "what is the probability that $R_1 > 19/1269$?".

It can be observed that R_1 follows a Beta distribution, given by the expression

$$\beta(x; \xi_1, \xi_2) = \frac{x^{\xi_1 - 1}(1 - x)^{\xi_2 - 1}}{B(\xi_1, \xi_2)}. \tag{5.1.19}$$

We then have

$$P\left(R_1 > \frac{19}{1269}\right) = 1 - \int_0^{\frac{19}{1269}} \beta(\lambda; \xi_1, \xi_2) \mathrm{d}\lambda, \tag{5.1.20}$$

which gives the probability that R_1 satisfies the inequality in question. Alternatively, since the random variables C_1 and C_2 follow a Gamma distribution, $\Gamma(\rho_1, \rho_2)$, it can be observed that

$$\frac{C_1}{C_2} > \sup_{\lambda > 1} f(\lambda) \implies C_1 > \bar{\mu}(1 - R_1)\alpha, \tag{5.1.21}$$

where $\sup_{\lambda > 1} f(\lambda) = \alpha$. Then we have

$$\bar{\mu} < C_1 \left(\frac{1 + \alpha}{\alpha}\right), \tag{5.1.22}$$

or equivalently,

$$\frac{C_1}{C_2} = \frac{C_1}{\bar{\mu} - C_1} > \alpha. \tag{5.1.23}$$

The mean nonlinear shear modulus is defined in (3.3.16), and we have $0 < \underline{C}_1 < \underline{\bar{\mu}}$. The probability that the inequality for $\bar{\mu}$ holds is then given by

$$P\left(\bar{\mu} < C_1 \frac{1 + \alpha}{\alpha}\right) = \int_0^{C_1 \frac{1+\alpha}{\alpha}} g(u; \rho_1, \rho_2) \mathrm{d}u, \tag{5.1.24}$$

where $g(u; \rho_1, \rho_2)$ denotes the Gamma distribution defined in (3.1.6). Where $\alpha \approx$ 0.0152, it can be determined that $\bar{\mu} < C_1(1269/19)$, and the integral (5.1.24) becomes

$$P\left(\bar{\mu} < C_1 \frac{1269}{19}\right) = \int_0^{C_1 \frac{1269}{19}} g(u; \rho_1, \rho_2)\mathrm{d}u. \tag{5.1.25}$$

In the deterministic case, with parameters $\rho_1 = 400$ and $\rho_2 = 0.0013$, the mean value of the nonlinear shear modulus is

$$\bar{\mu} = \rho_1 \rho_2 = 0.52. \tag{5.1.26}$$

For a necking instability to occur, the following inequality must be satisfied;

$$\frac{C_1}{C_2} = \frac{R_1}{1 - R_1} > \alpha, \tag{5.1.27}$$

or, equivalently,

$$R_1 > \frac{\alpha}{1 + \alpha}. \tag{5.1.28}$$

Since we have $C_1 = \bar{\mu} R_1$ (3.4.12), it can be observed that

$$C_1 > \bar{\mu} \frac{\alpha}{1 + \alpha}. \tag{5.1.29}$$

It has previously been deduced that $\sup_\lambda f(\lambda) \approx 0.0152$, and so $\alpha \approx 0.0152$, enabling the following expression to be determined;

$$C_1 = \underline{C_1} = \underline{\bar{\mu}} \frac{\alpha}{1 + \alpha} \approx 0.0078. \tag{5.1.30}$$

Therefore, the following conclusions can be made: If $C_1 < 0.0078$, a necking instability occurs, and if $C_1 > 0.0078$, necking does not occur.

This is a very black-and-white approach, and no account is taken of the fact that there is not necessarily a 100% guarantee of whether a necking instability will occur or not. The stochastic approach which follows takes this into account,

giving an enhanced understanding of the likelihood as to whether or not necking will occur [127, 133, 196].

Stochastically, if the value of C_1, calculated in the deterministic case, is given as $C_1 = 0.0078$, then in the immediate proximity of this value, there will be a 50% chance of a necking instability occurring, and, as such, a 50% chance that necking does not occur. Similarly, in the area surrounding C_1, denoted by $C_1 + \epsilon$, where $\epsilon > 0$ is a very small value, there will be a percentage chance of a necking instability occurring, denoted here by p, meaning that there will be a $(1 - p)\%$ chance that necking does not occur. Figure 5.4 demonstrates this concept; the black dashed line denoting the deterministic critical value, the red and blue lines denoting the probability of whether necking occurs or not, respectively, both in the analytical case (dark red/blue) and in the simulation (light red/blue), with each case in good agreement with each other.
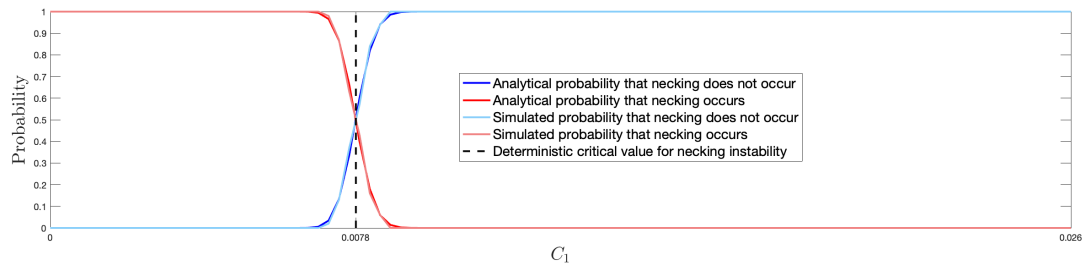
Figure 5.4: Probability distribution (5.1.24) of whether a necking instability occurs or not for a stochastic hyperelastic material described by (5.1.7) following a Gamma distribution (3.1.6) with parameters $\rho_1 = 400$ and $\rho_2 = 0.0013$, in both the simulated and analytical case around a deterministic critical point 0.0078.

A plot demonstrating the behaviour of the model given in (5.1.7) around the critical point 0.0078 is given in Figure 5.5.
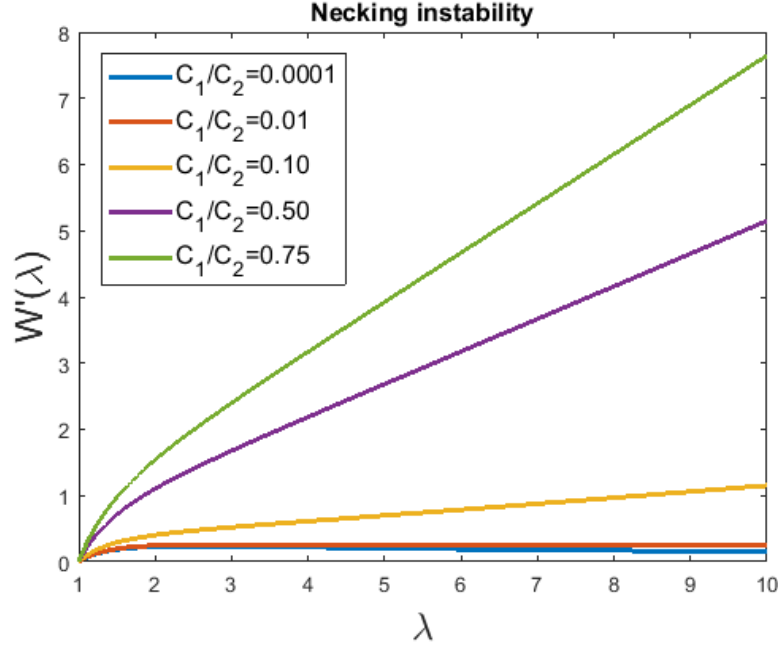
Figure 5.5: The occurence of a necking instability in the model given in (5.1.7) for different values around the critical point 0.0078.

5.1.2 Carroll model

The conditions under which a necking instability occurs for a material described by the Carroll model [38], characterised by the strain-energy function;

$$\mathcal{W}(\lambda_1, \lambda_2, \lambda_3) = \frac{C_1}{2}(\lambda_1^2 + \lambda_2^2 + \lambda_3^2 - 3) + \sqrt{3}C_2\left(\sqrt{\lambda_1^{-2} + \lambda_2^{-2} + \lambda_3^{-2}} - \sqrt{3}\right), \quad (5.1.31)$$

where C_1 and C_2 are constants, with $C_1, C_2 > 0$, are now discussed.

Assuming that this material is subject to the normal tension (5.1.2), the strain-energy function takes the equivalent form

$$W(\lambda) = \frac{C_1}{2}(\lambda^2 + 2\lambda^{-1} - 3) + \sqrt{3}C_2\left(\sqrt{\lambda^{-2} + 2\lambda} - \sqrt{3}\right), \quad (5.1.32)$$

with

$$W''(\lambda) = C_1(1 + 2\lambda^{-3}) + \sqrt{3}C_2\left[\frac{2\lambda^{-6} + 8\lambda^{-3} - 1}{(\lambda^{-2} + 2\lambda)^{\frac{3}{2}}}\right], \quad (5.1.33)$$

which, after setting the right-hand side equal to 0, gives

$$\frac{C_1}{C_2} - \frac{\sqrt{3}(1 - 8\lambda^{-3} - 2\lambda^{-6})}{(1 + 2\lambda^{-3})(\lambda^{-2} + 2\lambda)^{\frac{3}{2}}} = 0. \tag{5.1.34}$$

From this, the following two conditions regarding the stability of the model can be stated; when

$$\frac{C_1}{C_2} > \frac{\sqrt{3}(1 - 8\lambda^{-3} - 2\lambda^{-6})}{(1 + 2\lambda^{-3})(\lambda^{-2} + 2\lambda)^{\frac{3}{2}}}, \tag{5.1.35}$$

the model is stable, and when

$$\frac{C_1}{C_2} < \frac{\sqrt{3}(1 - 8\lambda^{-3} - 2\lambda^{-6})}{(1 + 2\lambda^{-3})(\lambda^{-2} + 2\lambda)^{\frac{3}{2}}}, \tag{5.1.36}$$

the model is unstable.

Let

$$f(\lambda) = \frac{\sqrt{3}(1 - 8\lambda^{-3} - 2\lambda^{-6})}{(1 + 2\lambda^{-3})(\lambda^{-2} + 2\lambda)^{\frac{3}{2}}}. \tag{5.1.37}$$

Then, for C_1/C_2 to be stable, we must have $C_1/C_2 > \sup_{\lambda > 1} f(\lambda)$. Define

$$g(\lambda) = f'(\lambda) = \frac{3\sqrt{3}(27\lambda^2 - \lambda^5 + 30\lambda^{-1} - 2\lambda^{-4} + 4\lambda^{-7})}{(2\lambda^3 + 1)^{\frac{5}{2}}(2\lambda^{-3} + 1)^2}. \tag{5.1.38}$$

Plots of both (5.1.37) and (5.1.38) are then presented in Figures 5.6(a) and (b), where it becomes clear that the function $f(\lambda)$ has a maximum.

To find the maximum value of $f(\lambda)$, we set (5.1.38) equal to 0 and solve the resulting equation for λ, which yields $\lambda = -1.0677$ and $\lambda = 3.0390$. Since $\lambda > 1$, we take $\lambda = 3.0390$ here. Substituting this value for λ back into (5.1.37), we obtain the following approximate maximum value of $f(\lambda)$;

$$\max_{\lambda} f(\lambda) \approx 0.0749. \tag{5.1.39}$$

Therefore, if $C_1/C_2 > \sup_{\lambda > 1} f(\lambda) \approx 0.0749$, necking does not occur.
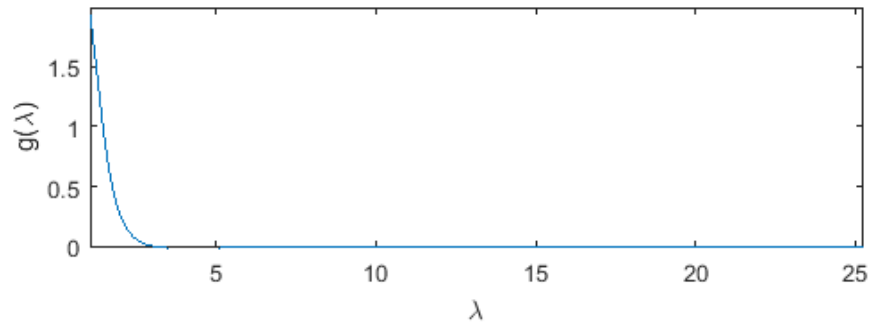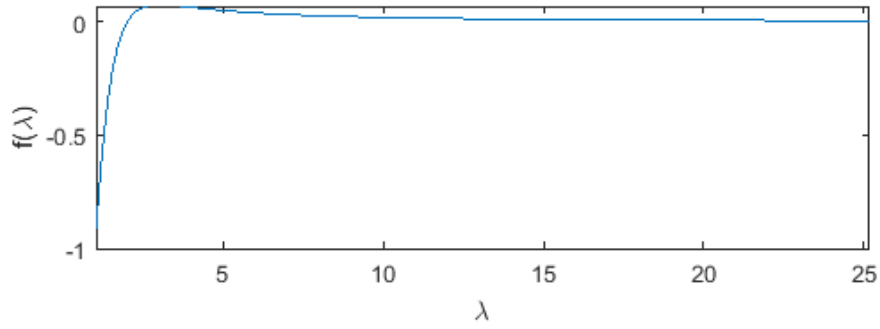
(a)
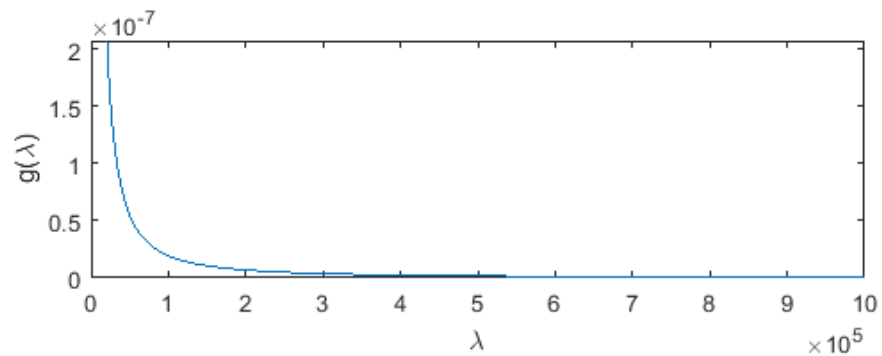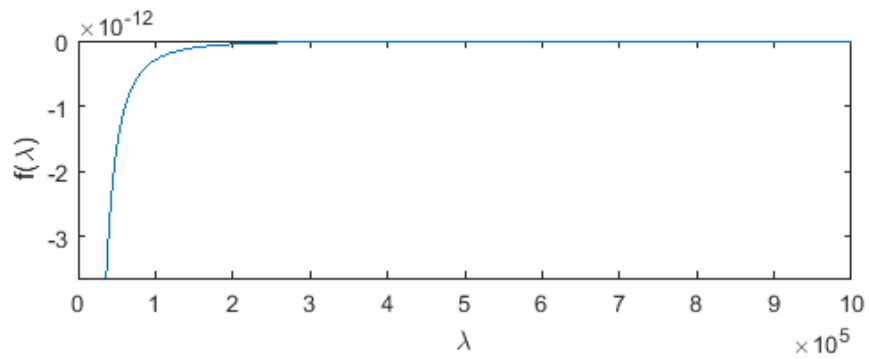
(b)

Figure 5.6: The behaviour of the functions $f(\lambda)$ (5.1.37) and $g(\lambda)$ (5.1.38), respectively: (a) at small values of λ, and (b) at large values of λ. Note that $f(\lambda)$ is the right-hand side of (5.1.35), and $g(\lambda)$ is the derivative of $f(\lambda)$.

From (3.4.12), for stability, we must have

$$\frac{R_1}{(1 - R_1)} > 0.0749. \tag{5.1.40}$$

It can then be deduced that $R_1 > 749/10749$. Hence, for a necking instability to occur, we must have $R_1 < 749/10749$. Approaching this from a stochastic perspective, the question of the probability that $R_1 > 749/10749$ will now be addressed.

As in Section 5.1.1, R_1 follows a Beta distribution given by (5.1.19). The probability that R_1 satisfies the given inequality is

$$P\left(R_1 > \frac{749}{10749}\right) = 1 - \int_0^{\frac{749}{10749}} \beta(\lambda; \xi_1, \xi_2) \mathrm{d}\lambda. \tag{5.1.41}$$

Since the random variables C_1 and C_2 follow a Gamma distribution, $\Gamma(\rho_1, \rho_2)$, we have the inequality (5.1.21) as before, where we let $\sup_{\lambda > 1} f(\lambda) = \alpha$. Some minor rearrangement then yields (5.1.22), and equivalently (5.1.23). Using (3.3.16) and $0 < C_1 < \bar{\mu}$, the probability that the inequality for $\bar{\mu}$ holds is given by (5.1.24). Where $\alpha \approx 0.0749$, it can be observed that $\bar{\mu} < C_1(10749/749)$, and the integral (5.1.24) becomes

$$P\left(\bar{\mu} < C_1 \frac{10749}{749}\right) = \int_0^{C_1 \frac{10749}{749}} g(u; \rho_1, \rho_2) \mathrm{d}u. \tag{5.1.42}$$

In the deterministic case, it can be established that (5.1.29) holds. Where $\alpha \approx 0.0749$, we have

$$C_1 = \underline{C_1} = 0.52 \frac{0.0749}{1 + 0.0749} \approx 0.0362. \tag{5.1.43}$$

Therefore, the following conclusion can be made: If $C_1 < 0.0362$, then a necking instability occurs, and if $C_1 > 0.0362$, necking does not occur.

Stochastically, if $C_1 = 0.0362$ as deduced in the deterministic case, then in

the immediate proximity of this value, there will be a 50% chance of necking occurring. In the area surrounding C_1, denoted by $C_1 + \epsilon$, where $\epsilon > 0$ is a very small value, there will be a $p\%$ chance of a necking instability occurring, and thus a $(1-p)\%$ chance that necking does not occur. This is demonstrated in Figure 5.7; the black dashed line denoting the deterministic critical value, the red and blue lines denoting the probability of whether necking occurs or not, respectively, both in the analytical case (dark red/blue), and in the simulation (light red/blue), each case in good agreement with each other. A plot demonstrating the behaviour of the Carroll Model around the critical point 0.0362 is given in Figure 5.8.
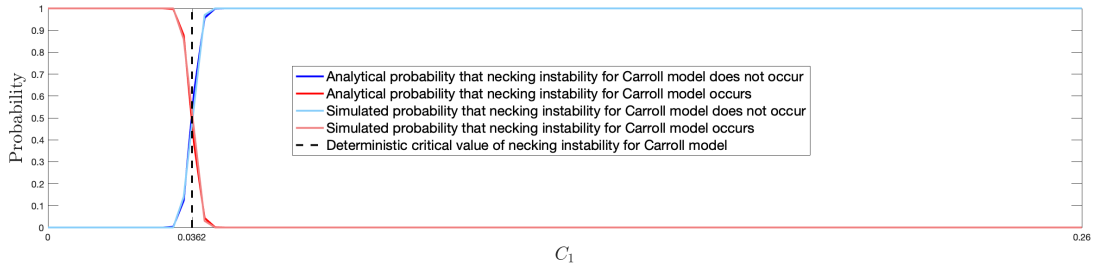
Figure 5.7: Probability distribution (5.1.24) of whether a necking instability occurs or not for a stochastic hyperelastic material described by the Carroll Model (5.1.31) following a Gamma distribution (3.1.6) with parameters $\rho_1 = 400$ and $\rho_2 = 0.0013$, in both the simulated and analytical case around a deterministic critical point 0.0362.

5.1.3 Gent-Thomas model

In this section, to model the particular material in question, we use the two-term Gent-Thomas model [64], characterised by the strain-energy function

$$\mathcal{W}(\lambda_1, \lambda_2, \lambda_3) = \frac{C_1}{2}(\lambda_1^2 + \lambda_2^2 + \lambda_3^2 - 3) + \frac{3C_2}{2}\ln\left(\frac{\lambda_1^{-2} + \lambda_2^{-2} + \lambda_3^{-2}}{3}\right), \quad (5.1.44)$$

where $C_1, C_2 > 0$ are constants.

Assuming that this material is subject to the normal tension (5.1.2), the strain-
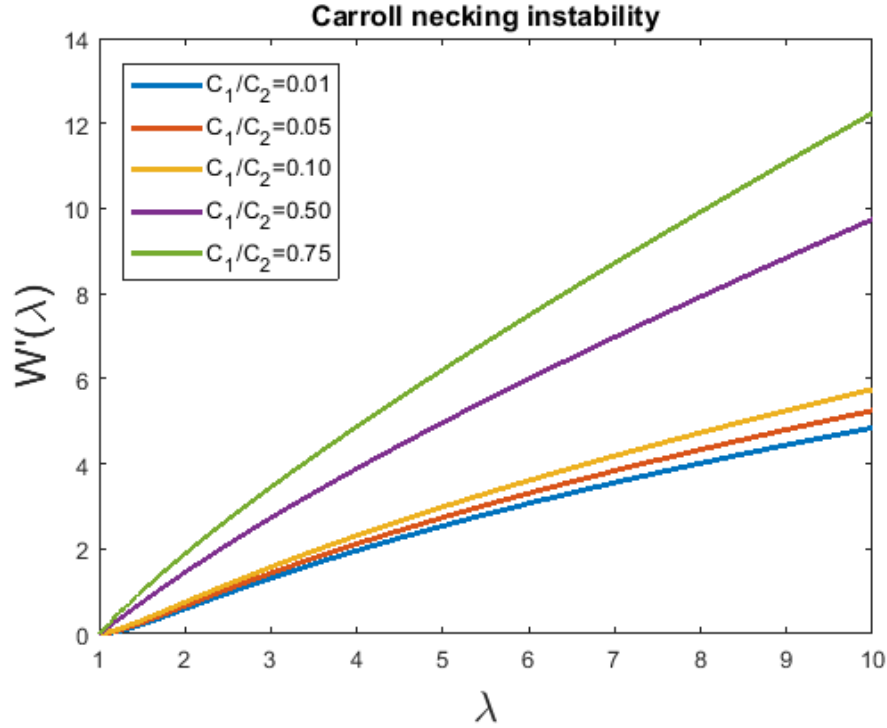
Figure 5.8: The occurence of a necking instability in the Carroll Model for different values around the critical point 0.0362.

energy function takes the equivalent form

$$W(\lambda) = \frac{C_1}{2}(\lambda^2 + 2\lambda^{-1} - 3) + \frac{3C_2}{2}\ln\left(\frac{\lambda^{-2} + 2\lambda}{3}\right), \qquad (5.1.45)$$

with

$$W''(\lambda) = C_1(1 + 2\lambda^{-3}) + 3C_2\left[\frac{-2\lambda^6 + 10\lambda^3 + 1}{(2\lambda^4 + \lambda)^2}\right]. \qquad (5.1.46)$$

Setting the right-hand side of (5.1.46) equal to 0, we then have

$$\frac{C_1}{C_2} = \frac{6\lambda^6 - 30\lambda^3 - 3}{4\lambda^8 + 12\lambda^5 + 9\lambda^2 + 2\lambda^{-1}} = 3\lambda\left(\frac{2\lambda^6 - 10\lambda^3 - 1}{4\lambda^9 + 12\lambda^6 + 9\lambda^3 + 2}\right). \qquad (5.1.47)$$

The model is stable when

$$\frac{C_1}{C_2} > 3\lambda\left(\frac{2\lambda^6 - 10\lambda^3 - 1}{4\lambda^9 + 12\lambda^6 + 9\lambda^3 + 2}\right), \qquad (5.1.48)$$

and a necking instability occurs when

$$\frac{C_1}{C_2} < 3\lambda\left(\frac{2\lambda^6 - 10\lambda^3 - 1}{4\lambda^9 + 12\lambda^6 + 9\lambda^3 + 2}\right). \tag{5.1.49}$$

Now, let

$$f(\lambda) = 3\lambda\left(\frac{2\lambda^6 - 10\lambda^3 - 1}{4\lambda^9 + 12\lambda^6 + 9\lambda^3 + 2}\right). \tag{5.1.50}$$

For reasons of comprehensibility, we now introduce the change of variable $x = \lambda^3$ into (5.1.50), and obtain

$$f(x) = 3x^{\frac{1}{3}}\left(\frac{2x^2 - 10x - 1}{4x^3 + 12x^2 + 9x + 2}\right). \tag{5.1.51}$$

Let $g(x) = f'(x)$. Then

$$g(x) = \frac{3x^{\frac{1}{3}}(4x - 10)}{4x^3 + 12x^2 + 9x + 2} - \frac{-2x^2 + 10x + 1}{x^{\frac{2}{3}}(4x^3 + 12x^2 + 9x + 2)} + \\ + \frac{3x^{\frac{1}{3}}(-2x^2 + 10x + 1)(12x^2 + 24x + 9)}{(4x^3 + 12x^2 + 9x + 2)^2}. \tag{5.1.52}$$

Plotting both (5.1.51) and (5.1.52) yields the graphs given in Figures 5.9(a) and (b). Figure 5.9(a) demonstrates the behaviour of these functions on a small scale, while Figure 5.9(b) serves to demonstrate their behaviour as the scale is greatly increased in both directions. From Figure 5.9(a), it can be seen that the function $f(x)$ has a maximum, occurring at the point $\max_x \ f(x) \approx 0.1355$. Analytically, this value can be found by setting $g(x) = 0$, solving for x, and then substituting the values obtained for x into $f(x)$.

In summary, it has been deduced that if $C_1/C_2 > \sup_{\lambda>1} \ f(\lambda) \approx 0.1355$, we have stability, and, as such, a necking instability does not occur. Applying the result in (3.4.12), we have $R_1/(1 - R_1) > 0.1355$, and so, after some minor rearrangement, it can be deduced that $R_1 > 271/2271$. Therefore, for necking to occur, we must have $R_1 < 271/2271$. The question regarding the probability that $R_1 > 271/2271$ will now be considered.
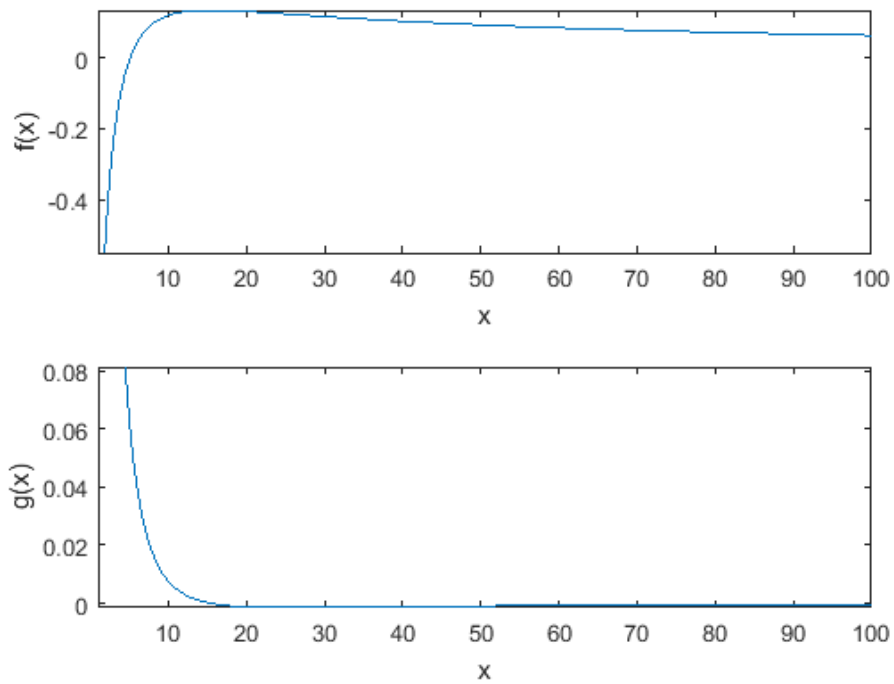
(a)
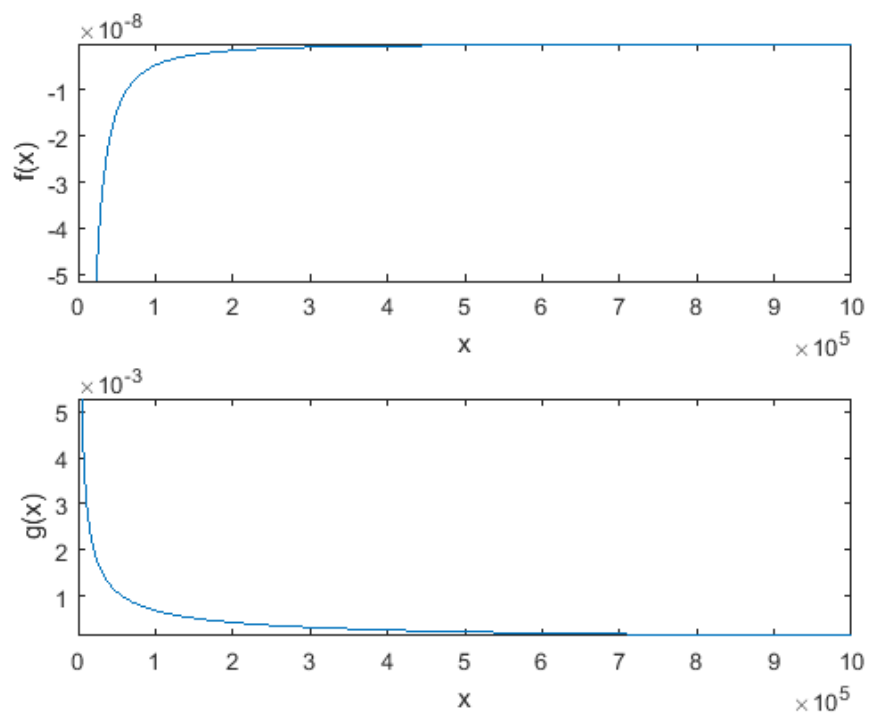
(b)

Figure 5.9: The behaviour of the functions $f(x)$ (5.1.51) and $g(x)$ (5.1.52), respectively: (a) at small values of x, and (b) at large values of x.

It has been determined that R_1 follows a Beta distribution given by (5.1.19). The probability that R_1 satisfies the above inequality is given by

$$P\left(R_1 > \frac{271}{2271}\right) = 1 - \int_0^{\frac{271}{2271}} \beta(x; \xi_1, \xi_2)\mathrm{d}x. \qquad (5.1.53)$$

Since the random variables C_1 and C_2 follow a Gamma distribution, $\Gamma(\rho_1, \rho_2)$, expression (5.1.21), where we let $\sup_{\lambda>1} f(\lambda) = \alpha$, holds. As a result, the inequalities (5.1.22) and (5.1.23) are also applicable here. Using (3.3.16) and $0 < C_1 < \underline{\mu}$, the probability that the inequality given for $\bar{\mu}$ holds is given by (5.1.24). Where $\alpha \approx 0.1355$, we have $\bar{\mu} < C_1(2271/271)$, and (5.1.24) becomes

$$P\left(\bar{\mu} < C_1 \frac{2271}{271}\right) = \int_0^{C_1 \frac{2271}{271}} g(u; \rho_1, \rho_2)\mathrm{d}u. \qquad (5.1.54)$$

As in Section 5.1.1, in the deterministic case, the inequality (5.1.29) holds. Where $\alpha \approx 0.1355$, we have

$$C_1 = \underline{C}_1 = 0.52\frac{0.1355}{1.1355} \approx 0.0621. \qquad (5.1.55)$$

Therefore, for a necking instability to occur, we must have $C_1 < 0.0621$, with the opposite being the case when $C_1 > 0.0621$.

Stochastically, if the value of C_1 is given as $C_1 = 0.0621$, then in the immediate proximity of this value, there will be a 50% chance of a necking instability occurring, and in the area surrounding C_1, there will be a $(1 - p)\%$ chance that necking does not occur. This is demonstrated in Figure 5.10, where the black dashed line denotes the deterministic critical value, the red and blue lines denote the respective probability that necking occurs or not, both in the analytical case (dark red/blue), and in the simulation (light red/blue), with each case in good agreement with each other.

The plot in Figure 5.11 demonstrates the behaviour of a material described by
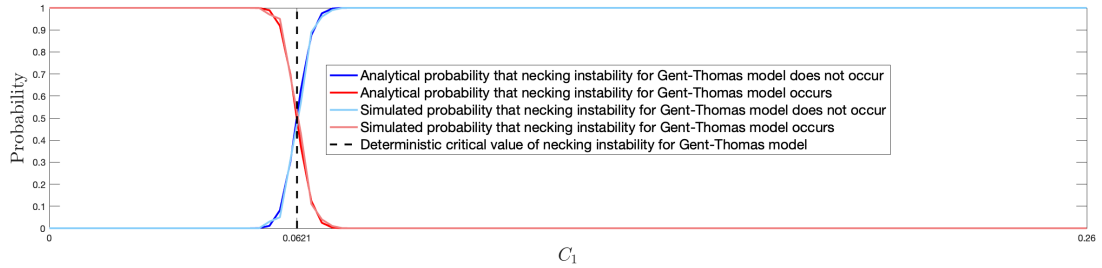
Figure 5.10: Probability distribution (5.1.53) of whether a necking instability occurs or not for a stochastic hyperelastic material described by the Gent-Thomas Model (5.1.44) following a Gamma distribution (3.1.6) with parameters $\rho_1 = 400$ and $\rho_2 = 0.0013$, in both the simulated and analytical case around a deterministic critical point 0.0621.

(5.1.44) for values around the critical value 0.0621.

The concepts presented here are now built upon and extended to develop a stochastic analysis of the inflation of spheres and circular cylinders in Section 5.2, and later of the cavitation of spheres in Section 5.3.
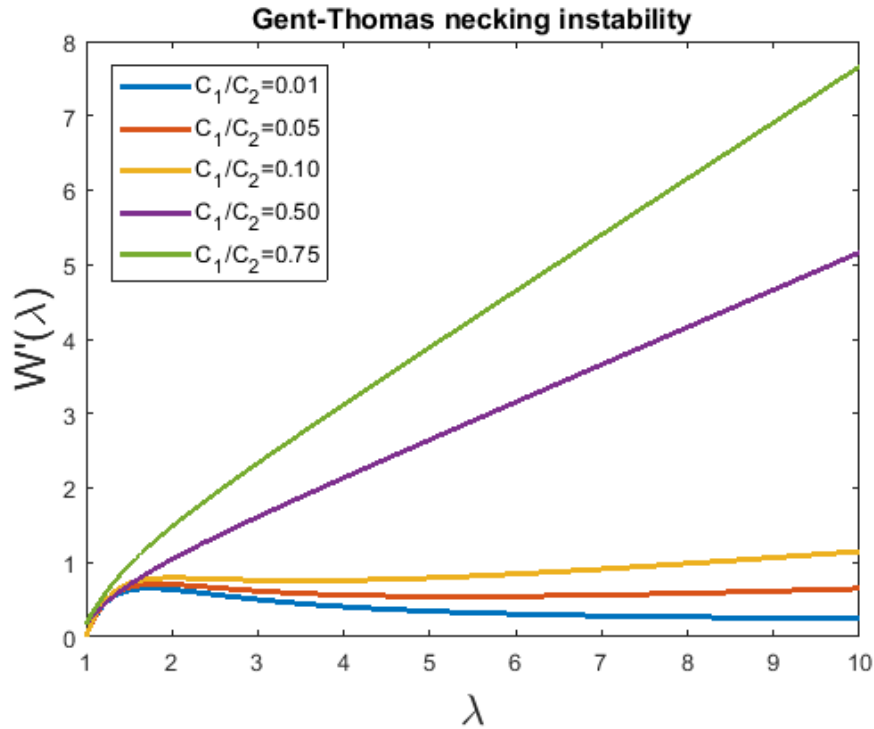
Figure 5.11: The occurence of a necking instability in the Gent-Thomas Model for different values around the critical point 0.0621.

5.2 Inflation of spheres and circular cylinders

Extending the theory presented in Section 5.1, the inflation of spheres and circular cylinders will now be investigated from a stochastic perspective. This is not a new concept in itself; the finite symmetric inflation and stretching of a cylindrical tube of homogeneous isotropic incompressible hyperelastic material was first investigated in [169], whilst the finite radially symmetric inflation of an elastic spherical shell was studied in [72]. However, the stochastic approach presented here will serve to enhance the previous studies relating to this subject. A general theory of possible qualitative behaviours of both elastic tubes and spherical shells was developed in [38], where it was demonstrated that, depending on the particular material and initial geometry, the internal pressure may increase monotonically (here, we will refer to materials which display this type of behaviour as type A, although materials of other types under specific conditions may also behave in this

way, as will be demonstrated in the upcoming sections), or it may increase and then decrease (materials of type B), or it may increase, decrease, and then increase again (materials of type C). This formed the basis for further studies where these deformations were examined for different material constitutive laws [69, 221], and opened the way to the modelling of more complex phenomena [79].

The behaviour of a structure depends on the inextricable relation between its material properties and its geometry. Hence, it is of the utmost importance to use suitable constitutive models for the materials in question, derived and validated through experience and experiments. Until now, the method has been to only consider average values to fit deterministic models. More recently, the use of the information about uncertainties and the variability in the acquired data in nonlinear elasticity has been proposed by the introduction of stochastic hyperelastic models.

A crucial part of assessing the elasticity of materials is to quantify the uncertainties in their mechanical responses under large deformations. As a result, in this section, the probability distributions of stable deformations for spherical shells and cylindrical tubes of stochastic isotropic hyperelastic material under radially symmetric inflation are determined. For the deterministic elastic problem involving isotropic incompressible materials, there is a critical parameter value that strictly separates the cases where inflation instability occurs or not, analogous to the theoretical investigation presented in Section 5.1 regarding the presence of a necking instability. However, for the stochastic problem, due to the probabilistic nature of the material law, there is always competition between the stable and unstable states. Hence, at a critical load, stable or unstable inflation occurs with a given probability, and there is also a probability that the inflation may occur under smaller or greater loads than the expected critical value. Therefore, it is no longer appropriate to refer to 'equilibria', but rather 'likely equilibria', obtained under a given internal pressure with a given probability.

The stochastic elastic setting outlined here provides a general mathematical framework applicable to a class of stochastic homogeneous hyperelastic materials for which similar results can be obtained. As a specific example, reference is made to the experimental data for vulcanised rubber of Rivlin and Saunders (1951) [170], from which the probability distribution of the random shear modulus is derived, and predictions of the inflation responses for a spherical shell and a cylindrical tube made of a material characterised by this parameter are made.

In Sections 5.2.1 and 5.2.2, the deterministic elastic case is investigated first, for stochastic spheres and circular cylinders, respectively. In both cases, an approach based on both the proposed methods outlined in [38] and [151] is developed, and the behaviour of the spheres and cylinders is analysed. Following this, a stochastic approach is presented, and an enhanced description of the criteria for instability is given.

5.2.1 Spheres
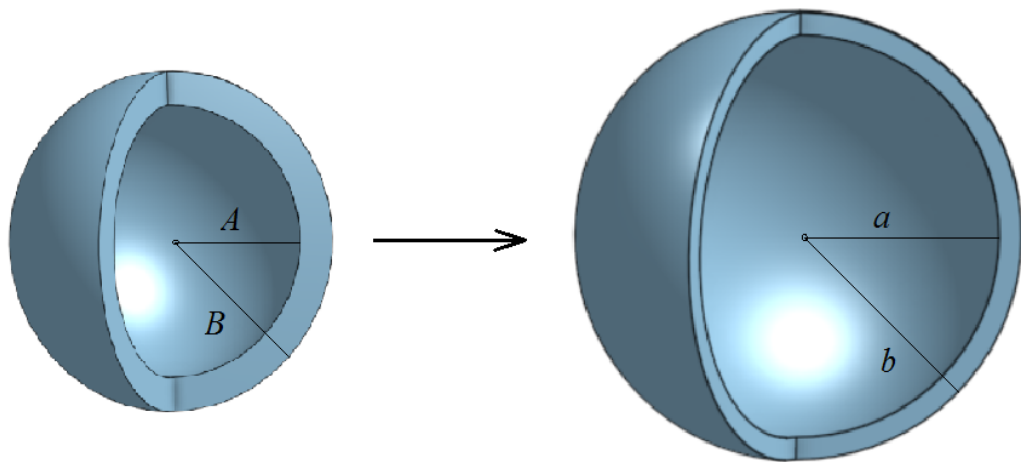
Figure 5.12: Schematic of inflation of a spherical shell, showing the reference state, with inner radius A and outer radius B (left), and the current (deformed) state, with inner radius a and outer radius b (right), respectively.

We begin with an investigation into the inflation of spheres made of a solid material. For a homogeneous isotropic incompressible hyperelastic material, the

strain energy function is defined as [38]

$$W = \mathcal{W}(I_1, I_2), \tag{5.2.1}$$

where the invariants I_1 and I_2 (2.1.6) are defined as

$$I_1 = \operatorname{tr} \mathbf{B} = \lambda_1^2 + \lambda_2^2 + \lambda_3^2 \qquad \text{and} \qquad I_2 = \operatorname{tr} \mathbf{B}^{-1} = \frac{1}{\lambda_1^2} + \frac{1}{\lambda_2^2} + \frac{1}{\lambda_3^2}, \tag{5.2.2}$$

where $\mathbf{B} = \mathrm{V}^2$ is the left Cauchy-Green tensor, V is the stretch tensor, and $\mathbf{F}$ is the deformation gradient (see Section 2.1 for further details). The incompressibility condition is given by

$$\det \mathbf{F} = \lambda_1 \lambda_2 \lambda_3 = 1, \tag{5.2.3}$$

where λ_i $(i = 1, 2, 3)$ are the principal stretches.

The Cauchy stress tensor, $\boldsymbol{\sigma}$, is given by

$$\boldsymbol{\sigma} = -p\mathrm{I} + 2\frac{\partial \mathcal{W}}{\partial I_1}\mathbf{B} - 2\frac{\partial \mathcal{W}}{\partial I_2}\mathbf{B}^{-1}, \tag{5.2.4}$$

where p denotes an unspecified scalar and I is the identity tensor. The principal directions of $\boldsymbol{\sigma}$ are the same as the principal directions of the stretch tensor V.

Next, functions $\widehat{W}$, $\widetilde{W}$ and $\overline{W}$ are introduced, defined by

$$\begin{aligned}
\widehat{W}(\lambda, \mu) &= W\left(\lambda^2 + \frac{1}{\lambda^2 \mu^2} + \mu^2, \frac{1}{\lambda^2} + \lambda^2 \mu^2 + \frac{1}{\mu^2}\right) \\
\widetilde{W}(\lambda) &= \widehat{W}\left(\lambda, \frac{1}{\sqrt{\lambda}}\right) \\
\overline{W}(\lambda) &= \widehat{W}(\lambda, 1).
\end{aligned} \tag{5.2.5}$$

Here, $\widehat{W}$ describes the general response in terms of two independent principal stretches, $\widetilde{W}$ describes the response in the axisymmetric deformation, and $\overline{W}$ describes the response in the plane deformation. For principal stretches defined

as

$$\lambda_1 = \lambda, \qquad \lambda_2 = \frac{1}{\lambda\mu}, \qquad \lambda_3 = \mu, \tag{5.2.6}$$

the principal stress differences are given by

$$\sigma_1 - \sigma_2 = \lambda\frac{\partial\widehat{W}}{\partial\lambda} \qquad \text{and} \qquad \sigma_3 - \sigma_2 = \mu\frac{\partial\widehat{W}}{\partial\mu}. \tag{5.2.7}$$

The main stress difference of interest here will be

$$T = \sigma_2 - \sigma_1, \tag{5.2.8}$$

where

$$T = \begin{cases} -\lambda\frac{\partial\widehat{W}}{\partial\lambda} = \widehat{T}(\lambda,\mu) \\[2mm] -\lambda\frac{\partial\widetilde{W}}{\partial\lambda} = \widetilde{T}(\lambda) \\[2mm] -\lambda\frac{\partial\overline{W}}{\partial\lambda} = \overline{T}(\lambda), \end{cases} \tag{5.2.9}$$

for general, axisymmetric and plane deformations, respectively. The function $\widetilde{T}(\lambda)$, which relates the compressive stress to the axial stretch in a uniaxial compressive stress test, is the tensile stress corresponding to an in-plane stretch $1/\sqrt{\lambda}$ in axisymmetric plane stress.

Now, a radially symmetric isochoric deformation of a hollow sphere is described by

$$r^3 - r_0^3 = a^3 - a_0^3, \qquad \theta = \theta_0, \qquad \phi = \phi_0, \tag{5.2.10}$$

where (r, θ, ϕ) are the spherical polar coordinates of a particle, a is the radius of the inner boundary, and the subscript 0 denotes the initial value. The deformation (5.2.10) can also be described using a nondimensional parameter α, with the initial value denoted as α_0, defined by

$$\alpha = \frac{b^3}{b^3 - a^3} \qquad \text{and} \qquad \alpha_0 = \frac{b_0^3}{b_0^3 - a_0^3}, \tag{5.2.11}$$

respectively, where b is the outer radius. The nondimensional parameter α is a measure of the porosity of the sphere. For a shell with arbitrary wall thickness, as the sphere inflates, the porosity α increases, which leads to the local deformation then being interpreted as a radial contraction. Since $\lambda = \mathrm{d}r/\mathrm{d}r_0$ with $r^3 = a^3 - a_0^3 + r_0^3$, the stretch is given by

$$\lambda = \frac{\mathrm{d}r}{\mathrm{d}r_0} = \frac{r_0^2}{r^2} = \left(1 - \frac{a^3 - a_0^3}{r^3}\right)^{\frac{2}{3}}, \tag{5.2.12}$$

with tangential and azimuthal stretches given by $1/\sqrt{\lambda}$. Since

$$\frac{b^3 a_0^3}{b_0^3 a^3} = \frac{\alpha(\alpha_0 - 1)}{\alpha_0(\alpha - 1)}, \tag{5.2.13}$$

equations (5.2.10)-(5.2.12) imply that

$$\frac{a^3}{a_0^3} = \frac{\alpha - 1}{\alpha_0 - 1}, \qquad \frac{b^3}{b_0^3} = \frac{\alpha}{\alpha_0} \qquad \text{and} \qquad \lambda^{\frac{3}{2}} = 1 - \frac{a_0^3(\alpha - \alpha_0)}{r^3(\alpha_0 - 1)}. \tag{5.2.14}$$

The radial equation of equilibrium is given by the expression

$$\frac{\mathrm{d}\sigma_{rr}}{\mathrm{d}r} + \frac{2}{r}(\sigma_{rr} - \sigma_{\theta\theta}) = 0. \tag{5.2.15}$$

For the case of internal pressurisation, the boundary conditions are

$$\sigma_{rr} = -P \quad \text{at} \quad r = a \qquad \text{and} \qquad \sigma_{rr} = 0 \quad \text{at} \quad r = b. \tag{5.2.16}$$

Since $\mu = 1/\sqrt{\lambda}$, we have $\widehat{W} = \widehat{W}(\lambda, 1/\sqrt{\lambda}) = \widetilde{W}(\lambda)$, and so (5.2.8) and (5.2.9) give the principle stress difference $\sigma_{\theta\theta} - \sigma_{rr}$ as

$$\sigma_{\theta\theta} - \sigma_{rr} = -\lambda \frac{\partial \widetilde{W}}{\partial \lambda} = \widetilde{T}(\lambda), \tag{5.2.17}$$

with the stretch λ given in (5.2.14). Substitution of (5.2.17) into (5.2.15), and

some minor rearrangement, allows us to determine that

$$\frac{\partial \sigma_{rr}}{\partial r} = \frac{2}{r}\widetilde{T}(\lambda),\tag{5.2.18}$$

which, after integration with respect to r between $r = a$ and $r = b$, and making use of the boundary conditions (5.2.16), yields the expression

$$P = 2\int_a^b \widetilde{T}(\lambda)\frac{\mathrm{d}r}{r}.\tag{5.2.19}$$

Making the change of variable $r = 1 - x$ in the integral (5.2.19), the expression for P can be rewritten as

$$P = \frac{2}{3}\int_{x_a}^{x_b} \widetilde{T}\big(x^{\frac{2}{3}}\big)\frac{\mathrm{d}x}{1-x},\tag{5.2.20}$$

where we are integrating between the larger value x_a and the smaller value x_b, with x, x_a and x_b defined as

$$x = \lambda^{\frac{3}{2}} = 1 - \frac{a^3 - a_0^3}{r^3} = 1 - \frac{a_0^3(\alpha - \alpha_0)}{r^3(\alpha_0 - 1)},\tag{5.2.21}$$

$$x_a = \frac{a_0^3}{a^3} = \frac{\alpha_0 - 1}{\alpha - 1}, \qquad \text{and} \qquad x_b = \frac{b_0^3}{b^3} = \frac{\alpha_0}{\alpha}.\tag{5.2.22}$$

A condition for the stationary values of the applied pressure P will now be developed. Using Leibniz' Rule, the expression given for P in (5.2.20) can be

differentiated as follows:

$$
\begin{aligned}
\frac{\mathrm{d}P}{\mathrm{d}\alpha} &= \frac{2}{3}\frac{\mathrm{d}}{\mathrm{d}\alpha}\int_{x_a}^{x_b}\widetilde{T}(x^{\frac{2}{3}})\frac{1}{1-x}\mathrm{d}x \\
&= \frac{2}{3}\int_{x_a}^{x_b}\frac{\partial}{\partial\alpha}\widetilde{T}(x^{\frac{2}{3}})\frac{1}{1-x}\mathrm{d}x + \frac{2}{3}\widetilde{T}\left(\left(\frac{\alpha_0}{\alpha}\right)^{\frac{2}{3}}\right)\frac{1}{1-\frac{\alpha_0}{\alpha}}\frac{\partial\left(\frac{\alpha_0}{\alpha}\right)}{\partial\alpha} - \\
&\quad - \frac{2}{3}\widetilde{T}\left(\left(\frac{\alpha_0-1}{\alpha-1}\right)^{\frac{2}{3}}\right)\frac{1}{1-\frac{\alpha_0-1}{\alpha-1}}\frac{\partial\left(\frac{\alpha_0-1}{\alpha-1}\right)}{\partial\alpha} \\
&= \frac{2}{3}\frac{1}{\alpha-\alpha_0}\left[\widetilde{T}\left(\left(\frac{\alpha_0-1}{\alpha-1}\right)^{\frac{2}{3}}\right)\left(\frac{\alpha_0-1}{\alpha-1}\right) - \widetilde{T}\left(\left(\frac{\alpha_0}{\alpha}\right)^{\frac{2}{3}}\right)\frac{\alpha_0}{\alpha}\right],
\end{aligned}
\tag{5.2.23}
$$

and so

$$
\frac{\mathrm{d}P}{\mathrm{d}\alpha} = \frac{2}{3(\alpha-\alpha_0)}\left[\frac{\alpha_0-1}{\alpha-1}\widetilde{T}\left(\left(\frac{\alpha_0-1}{\alpha-1}\right)^{\frac{2}{3}}\right) - \frac{\alpha_0}{\alpha}\widetilde{T}\left(\left(\frac{\alpha_0}{\alpha}\right)^{\frac{2}{3}}\right)\right].
\tag{5.2.24}
$$

For reasons of simplicity, we introduce a response function

$$
\tilde{g}(x) = x\widetilde{T}(x^{\frac{2}{3}})
\tag{5.2.25}
$$

into (5.2.24), and so

$$
\frac{\mathrm{d}P}{\mathrm{d}\alpha} = \frac{2}{3(\alpha-\alpha_0)}\left[\tilde{g}\left(\frac{\alpha_0-1}{\alpha-1}\right) - \tilde{g}\left(\frac{\alpha_0}{\alpha}\right)\right].
\tag{5.2.26}
$$

The condition for a stationary value of the pressure P is given by

$$
\tilde{g}\left(\frac{\alpha_0-1}{\alpha-1}\right) = \tilde{g}\left(\frac{\alpha_0}{\alpha}\right).
\tag{5.2.27}
$$

Using the expression $x = \lambda^{3/2}$, it can be deduced that

$$
x_a = \lambda_a^{\frac{3}{2}} \qquad \text{and} \qquad x_b = \lambda_b^{\frac{3}{2}},
\tag{5.2.28}
$$

with

$$
T_a \to \widetilde{T}_a(x_a) \qquad \text{and} \qquad T_b \to \widetilde{T}_b(x_b),
\tag{5.2.29}
$$

which then implies

$$g(x_a) = \lambda_a^{\frac{3}{2}} T_a \qquad \text{and} \qquad g(x_b) = \lambda_b^{\frac{3}{2}} T_b. \qquad (5.2.30)$$

Equation (5.2.27) can then be rewritten as

$$\lambda_a^{\frac{3}{2}} T_a = \lambda_b^{\frac{3}{2}} T_b, \qquad (5.2.31)$$

where the terms λ_a, λ_b, T_a and T_b denote the values of the radial stretch λ and the compressive radial stress $T = \sigma_{\theta\theta} - \sigma_{rr}$ at $r = a$ and $r = b$, respectively. An expression for $\mathrm{d}^2 P / \mathrm{d}\alpha^2$ at a stationary point can be deduced by differentiating (5.2.26), then using the condition stated in (5.2.27), so

$$\frac{\mathrm{d}^2 P}{\mathrm{d}\alpha^2} = \frac{2}{3(\alpha - \alpha_0)} \left[-\frac{\alpha_0 - 1}{(\alpha - 1)^2} \tilde{g}' \left(\frac{\alpha_0 - 1}{\alpha - 1} \right) + \frac{\alpha_0}{\alpha^2} \tilde{g}' \left(\frac{\alpha_0}{\alpha} \right) \right]. \qquad (5.2.32)$$

Expressions (5.2.27) and (5.2.32) establish that the qualitative behaviour of the pressure P in spherical inflation is determined by the form of the function $\tilde{g}$ on the interval $(0, 1)$.

A description of the qualitative behaviour of the pressure during finite inflation of a hollow sphere in terms of the uniaxial compressive stress response of the material can now be outlined. For convenience, the response will be detailed in terms of the compressive logarithmic strain ϵ, and so

$$T = T(\epsilon) = \widetilde{T}(e^\epsilon), \qquad \epsilon = -\ln \lambda. \qquad (5.2.33)$$

Using $x = \lambda^{3/2}$, $\tilde{g}(x) = x\widetilde{T}(x^{2/3})$ and (5.2.33), it can be deduced that

$$\tilde{g}(\lambda^{\frac{3}{2}}) = g(\epsilon) = e^{-\frac{3\epsilon}{2}} T(\epsilon). \qquad (5.2.34)$$

The condition for a stationary value of the pressure P, given in (5.2.27), deter-

mines that the function g must take the same value at both the inner boundary and the outer boundary of the hollow sphere in question. Hence, the monotonicity, or loss thereof, of the function g on $(0, \infty)$ is the relevant material property in this case. Rearranging (5.2.34), we obtain

$$T(\epsilon) = e^{\frac{3\epsilon}{2}} g(\epsilon). \tag{5.2.35}$$

Differentiation of this expression with respect to ϵ then yields

$$\frac{\mathrm{d}T(\epsilon)}{\mathrm{d}\epsilon} = \frac{3}{2} g(\epsilon) e^{\frac{3\epsilon}{2}} = \frac{3}{2} [e^{-\frac{3\epsilon}{2}} T(\epsilon)] e^{\frac{3\epsilon}{2}} = \frac{3}{2} T(\epsilon). \tag{5.2.36}$$

Due to this, it can then be observed that the function g is monotonic if

$$\frac{\mathrm{d}T}{\mathrm{d}\epsilon} \geq \frac{3}{2} T. \tag{5.2.37}$$

For a material of type A, the condition (5.2.37) is met over the entire range of the compressive axial strain ϵ; $0 \leq \epsilon < \infty$. It follows that $\tilde{g}(x)$ is monotonic for $0 < x \leq 1$, and so (5.2.27) does not have a real root α^* with $\alpha_0 < \alpha^* < \infty$. Hence, since P has no stationary values, the pressure increases monotonically.

For a material of type B, the condition (5.2.37) is met for $0 \leq \epsilon \leq \epsilon_1$, and is not met for $\epsilon_1 < \epsilon < \infty$. It follows that $\tilde{g}(x)$ has its maximum value in $(0, 1)$ at $x_1 = e^{-3\epsilon_1/2}$, so (5.2.27) has one real root, given by α^*, satisfying $\alpha_0 < \alpha^* < \infty$. Since $\alpha^* > \alpha_0$, it is clear that the following inequalities hold;

$$\tilde{g}'\left(\frac{\alpha_0 - 1}{\alpha^* - 1}\right) > 0 \qquad \text{and} \qquad \tilde{g}\left(\frac{\alpha_0}{\alpha^*}\right) < 0. \tag{5.2.38}$$

The pressure P increases monotonically to a maximum value, given here by P^*, at porosity α^*, and decreases monotonically thereafter. For the case where $\tilde{g}(x) = $ *constant* for $x \leq x_1$, the pressure reaches its maximum value at $\alpha^* = \alpha_0/x_1$ and remains constant thereafter.

For a material of type C, the condition (5.2.37) is met except on the finite interval $\epsilon_1 < \epsilon < \epsilon_2$. On the interval $(0, 1)$, the function $\tilde{g}$ has a local maximum at $x_1 = e^{-3\epsilon_1/2}$ and a local minimum at $x_2 = e^{-3\epsilon_2/2}$. From (5.2.22), it can be observed that

$$x_b = \frac{\alpha_0}{\alpha} \implies \alpha = \frac{\alpha_0}{x_b} \implies \alpha = \frac{1}{\beta_0 x_b}, \tag{5.2.39}$$

and so,

$$\beta_0 = \frac{1}{\alpha_0} \implies \alpha_0 = \frac{1}{\beta_0}. \tag{5.2.40}$$

Then

$$x_a = \frac{1 - \frac{1}{\alpha_0}}{\frac{1}{\alpha_0}(\alpha - 1)} = \frac{\frac{1}{\alpha}(1 - \frac{1}{\alpha_0})}{\frac{1}{\alpha_0}(1 - \frac{1}{\alpha})} = \frac{\beta_0 x_b(1 - \beta_0)}{\beta_0(1 - \beta_0 x_b)} = \frac{(1 - \beta_0)x_b}{(1 - \beta_0 x_b)}, \tag{5.2.41}$$

and hence

$$x_a = \frac{(1 - \beta_0)x_b}{(1 - \beta_0 x_b)} \quad \text{and} \quad \beta_0 = \frac{1}{\alpha_0}, \tag{5.2.42}$$

so that the values x_a and x_b are close for a thin-walled sphere and significantly different for a thick-walled sphere, where the values of α_0 are larger and smaller in the respective cases. Thus, for sufficiently thin-walled spheres, (5.2.27) has two admissible roots α^* and α^{**}. The pressure P increases monotonically to a local maximum P^* at α^*, decreases to a local minimum P^{**} at α^{**}, and then increases monotonically. For sufficiently thick-walled spheres, (5.2.27) does not have an admissible root, so the pressure P increases monotonically. In the case where (5.2.27) has one admissible repeated root, where there is a critical value of α_0, the pressure P is monotonic but has an inflection point.

Although three types of behaviour have been described in detail, these types do not exhaust the list of possibilities of different behaviours. The compressive uniaxial stress response of most materials, however, is typically of type A, B or C. Therefore, for a material of type A, and also a thick-walled sphere of material of type C, it is expected that the pressure in spherical inflation will increase

monotonically; for a material of type B, the pressure is expected to increase to a maximum value, then decrease; and for thin-walled spheres of material of type C, the pressure should increase, decrease, then increase again.

The pressure response for a pressurised spherical cavity of internal radius a_0 in a medium of infinite extent is given by the expression

$$P = \frac{2}{3} \int_{\frac{a_0^3}{a^3}}^{1} \widetilde{T}(x^{\frac{2}{3}}) \frac{\mathrm{d}x}{1 - x}. \tag{5.2.43}$$

Differentiating (5.2.43), we have

$$\frac{\mathrm{d}P}{\mathrm{d}a} = \frac{2}{3} \left[\int_{\frac{a_0^3}{a^3}}^{1} \frac{\partial}{\partial a} \left(\widetilde{T}(x^{\frac{2}{3}}) \frac{1}{1-x} \right) \mathrm{d}x + \widetilde{T}(1^{\frac{2}{3}}) \frac{\partial (1)}{\partial a} - \widetilde{T}\left(\left(\frac{a_0^3}{a^3} \right)^{\frac{2}{3}} \right) \frac{1}{1 - \frac{a_0^3}{a^3}} \frac{\partial \left(\frac{a_0^3}{a^3} \right)}{\partial a} \right], \tag{5.2.44}$$

which reduces to

$$\frac{\mathrm{d}P}{\mathrm{d}a} = \frac{2}{3} \left[-\widetilde{T}\left(\left(\frac{a_0^3}{a^3} \right)^{\frac{2}{3}} \right) \frac{1}{1 - \frac{a_0^3}{a^3}} \frac{\partial \left(\frac{a_0^3}{a^3} \right)}{\partial a} \right] = -\frac{2}{3} \widetilde{T}\left(\frac{a_0^2}{a^2} \right) \frac{a^3}{a^3 - a_0^3} \left(-\frac{3a_0^3}{a^4} \right). \tag{5.2.45}$$

Hence,

$$\frac{\mathrm{d}P}{\mathrm{d}a} = \frac{2a_0^3}{a(a^3 - a_0^3)} \widetilde{T}\left(\frac{a_0^2}{a^2} \right), \tag{5.2.46}$$

meaning that the pressure increases monotonically.

The three types of behaviour determined by Carroll (1987) [38] and outlined above can be illustrated by considering the well-known Mooney-Rivlin strain energy function

$$\mathcal{W} = D_1(I_1 - 3) + D_2(I_2 - 3), \tag{5.2.47}$$

where $D_1 = C_1/2$ and $D_2 = C_2/2$. The function $\tilde{g}$ can be determined using (5.2.5), (5.2.9), (5.2.25) and (5.2.47); from (5.1.1), and using (5.2.5), with (5.1.2), we have (5.1.3), which, in keeping with the notation adopted in this section, we call $\widetilde{W}(\lambda)$

here. Applying (5.2.9) allows us to determine that

$$\widetilde{T}(\lambda) = 2D_1\left(\frac{1}{\lambda} - \lambda^2\right) + 2D_2\left(\frac{1}{\lambda^2} - \lambda\right), \tag{5.2.48}$$

and (5.2.25) then yields

$$\tilde{g}(x) = x\widetilde{T}(x^{\frac{2}{3}}) = 2D_1\left[\left(x^{\frac{1}{3}} - x^{\frac{7}{3}}\right) + \frac{D_2}{D_1}\left(x^{-\frac{1}{3}} - x^{\frac{5}{3}}\right)\right]. \tag{5.2.49}$$

Letting $\kappa = D_2/D_1$, we then have

$$\tilde{g}(x) = 2D_1\left[\left(x^{\frac{1}{3}} - x^{\frac{7}{3}}\right) + \kappa\left(x^{-\frac{1}{3}} - x^{\frac{5}{3}}\right)\right]. \tag{5.2.50}$$

Differentiation of (5.2.50) with respect to x gives,

$$\tilde{g}'(x) = \frac{2}{3}D_1 x^{-\frac{4}{3}}\left[x^{\frac{2}{3}}(1 - 7x^2) - \kappa(1 + 5x^2)\right]. \tag{5.2.51}$$

For $\kappa = 0$, it can be determined that $\tilde{g}'$ has one zero in $(0,1)$, at the point $x_1 = 1/\sqrt{7}$. By considering the function

$$\hat{\kappa}(x) = \frac{x^{\frac{2}{3}}(1 - 7x^2)}{(1 + 5x^2)}, \tag{5.2.52}$$

it can be seen that there is a critical value $\kappa_{cr} \approx 0.2145$, such that the function $\tilde{g}$ has a local maximum and minimum in $(0,1)$ for $0 < \kappa < \kappa_{cr}$, and is monotonic in $(0,1)$ for $\kappa > \kappa_{cr}$. Hence, the Mooney-Rivlin strain-energy function defined in (5.2.47) allows all three types of behaviour in spherical inflation; the material is of type A for $\kappa \geq \kappa_{cr}$, of type B for $\kappa = 0$, and of type C for $0 < \kappa \leq \kappa_{cr}$. Type B behaviour in this case corresponds to a neo-Hookean material. In the case of behaviour of type C, the pressure maximum and minimum, denoted P^* and P^{**}

respectively, for a sufficiently thin-walled sphere, occur at the roots α^* and α^{**} of

$$
\begin{aligned}
\left[\left(\frac{\alpha_0 - 1}{\alpha - 1}\right)^{\frac{1}{3}} + \kappa\left(\frac{\alpha - 1}{\alpha_0 - 1}\right)^{\frac{1}{3}}\right]\left[1 - \left(\frac{\alpha_0 - 1}{\alpha - 1}\right)^2\right] = \\
= \left[\left(\frac{\alpha_0}{\alpha}\right)^{\frac{1}{3}} + \kappa\left(\frac{\alpha}{\alpha_0}\right)^{\frac{1}{3}}\right]\left[1 - \left(\frac{\alpha_0}{\alpha}\right)^2\right].
\end{aligned}
\tag{5.2.53}
$$

This result is included for theoretical significance purposes. We do not take this further.

Stochastic incompressible spherical shell

We consider now a spherical shell of stochastic hyperelastic material described by (3.1.2), subject to the radially symmetric deformation (see Figure 5.12)

$$
r = f(R)R, \qquad \theta = \Theta, \qquad \phi = \Phi,
\tag{5.2.54}
$$

where (R, Θ, Φ) and (r, θ, ϕ) are the spherical polar coordinates in the reference and current configurations, respectively, such that $A \leq R \leq B$ [151, pp. 283-288].

The deformation gradient is $\mathbf{F} = \mathrm{diag}\,(\lambda_1, \lambda_2, \lambda_3)$, where

$$
\lambda_1 = f(R) + R\frac{\mathrm{d}f}{\mathrm{d}R} = \lambda^{-2}, \qquad \lambda_2 = \lambda_3 = f(R) = \lambda,
\tag{5.2.55}
$$

and λ_1, λ_2 and λ_3 represent the radial, tangential and azimuthal stretch, respectively.

The radial equation of equilibrium (5.2.15) is equivalent to [38]

$$
\frac{\mathrm{d}P_{11}}{\mathrm{d}R} + \frac{2}{R}(P_{11} - P_{22}) = 0,
\tag{5.2.56}
$$

where $\mathbf{P} = (P_{ij})_{i,j=1,2,3}$ denotes the first Piola-Kirchhoff stress tensor. From

(5.2.56), it can be observed that

$$\frac{\mathrm{d}P_{11}}{\mathrm{d}\lambda}\frac{\mathrm{d}\lambda}{\mathrm{d}R} + \frac{2}{R}(P_{11} - P_{22}) = 0, \tag{5.2.57}$$

which, using equation (5.2.55), can be rewritten as

$$\frac{\mathrm{d}P_{11}}{\mathrm{d}\lambda}\frac{\lambda^{-2} - f(R)}{R} + \frac{2}{R}(P_{11} - P_{22}) = 0. \tag{5.2.58}$$

After some rearrangement and simplification, it is then determined that (5.2.56) can be equivalently expressed as

$$\frac{\mathrm{d}P_{11}}{\mathrm{d}\lambda}\lambda^{-2} + 2\frac{P_{11} - P_{22}}{1 - \lambda^3} = 0. \tag{5.2.59}$$

For an incompressible material,

$$P_{11} = \frac{\partial \mathcal{W}}{\partial \lambda_1} - \frac{p}{\lambda_1}, \qquad P_{22} = \frac{\partial \mathcal{W}}{\partial \lambda_2} - \frac{p}{\lambda_2}, \tag{5.2.60}$$

where p is the Lagrange multiplier for the incompressibility constraint ($\det \mathbf{F} = 1$).

The limit-point instability criterion for this type of material configuration will now be discussed.

Limit-point instability criterion for spherical shells

Denoting

$$W(\lambda) = \mathcal{W}(\lambda^{-2}, \lambda, \lambda), \tag{5.2.61}$$

where $\lambda = r/R > 1$, and using

$$\frac{\partial W}{\partial \lambda} = \frac{2\mu_1}{m}(\lambda^{2m-1} - \lambda^{-4m-1}) + \frac{2\mu_2}{n}(\lambda^{2n-1} - \lambda^{-4n-1}), \tag{5.2.62}$$

$$\frac{\partial \mathcal{W}}{\partial \lambda_1} = \frac{\mu_1}{m}\lambda_1^{2m-1} + \frac{\mu_2}{n}\lambda_1^{2n-1}, \tag{5.2.63}$$

and

$$\frac{\partial \mathcal{W}}{\partial \lambda_2} = \frac{\mu_1}{m}\lambda_2^{2m-1} + \frac{\mu_2}{n}\lambda_2^{2n-1},$$ (5.2.64)

we can deduce that,

$$\begin{aligned}
\frac{\mathrm{d}W}{\mathrm{d}\lambda} &= -\frac{2}{\lambda^3}\left[\frac{\partial \mathcal{W}}{\partial \lambda_1} - \frac{p}{\lambda_1}\right] + 2\left[\frac{\partial \mathcal{W}}{\partial \lambda_2} - \frac{p}{\lambda_2}\right] \\
&= -\frac{2}{\lambda^3}\frac{\partial \mathcal{W}}{\partial \lambda_1} + \frac{2p}{\lambda^3\lambda^{-2}} + 2\frac{\partial \mathcal{W}}{\partial \lambda_2} - \frac{2p}{\lambda} \\
&= -\frac{2}{\lambda^3}\frac{\partial \mathcal{W}}{\partial \lambda_1} + 2\frac{\partial \mathcal{W}}{\partial \lambda_2}.
\end{aligned}$$ (5.2.65)

Equivalently, we have

$$\frac{\mathrm{d}W}{\mathrm{d}\lambda} = -\frac{2}{\lambda^3}P_{11} + 2P_{22}.$$ (5.2.66)

Next, setting the external pressure (at $R = B$) equal to zero, by (5.2.59) and (5.2.66), the internal pressure (at $R = A$) is equal to

$$\begin{aligned}
T &= -\frac{P_{11}}{\lambda^2}\Big|_{\lambda=\lambda_a} \\
&= -2\int_{\lambda_a}^{\lambda_b}\frac{P_{11}}{\lambda^3}\mathrm{d}\lambda + \int_{\lambda_a}^{\lambda_b}\frac{\mathrm{d}P_{11}}{\mathrm{d}\lambda}\lambda^{-2}\mathrm{d}\lambda \\
&= -2\int_{\lambda_a}^{\lambda_b}\frac{P_{11}}{\lambda^3}\mathrm{d}\lambda - 2\int_{\lambda_a}^{\lambda_b}\frac{P_{11} - P_{22}}{1 - \lambda^3}\mathrm{d}\lambda \\
&= \int_{\lambda_a}^{\lambda_b}\frac{\mathrm{d}W}{\mathrm{d}\lambda}\frac{\mathrm{d}\lambda}{1 - \lambda^3},
\end{aligned}$$ (5.2.67)

where $\lambda_a = a/A$ and $\lambda_b = b/B$ are the stretches for the inner and outer radii, respectively. It is worth recalling here that a volume element $\mathrm{d}V$ from the reference configuation is transformed, after the deformation, into a volume element $\mathrm{d}v = (\det \mathbf{F})\mathrm{d}V$ in the current configuration [209, p. 240], [151, p. 87], [70, p. 274]. Then, by the material incompressibility condition, $\det \mathbf{F} = 1$, the material volume in the spherical shell is conserved, i.e. $4\pi(b^3 - a^3) = 4\pi(B^3 - A^3)$, or equivalently, as $a = A\lambda_a$ and $b = B\lambda_b$,

$$\lambda_b^3 = (\lambda_a^3 - 1)\left(\frac{A}{B}\right)^3 + 1.$$ (5.2.68)

Hence, the internal pressure T (5.2.67) can be expressed as a function of the inner stretch ratio, λ_a, only.

As in the case of a deterministic elastic shell, for a stochastic spherical shell, a *limit-point instability* occurs if there is a change in the monotonicity of T, defined by (5.2.67), as a function of λ_a. When the spherical shell is thin, $0 < \epsilon = (B - A)/A \ll 1$, the internal pressure can be approximated as follows [70, p. 443];

$$T(\lambda) = \frac{\epsilon}{\lambda^2} \frac{\mathrm{d}W}{\mathrm{d}\lambda}, \tag{5.2.69}$$

and the critical value of λ where a limit-point instability occurs can be found by solving

$$\frac{\mathrm{d}T}{\mathrm{d}\lambda} = 0 \tag{5.2.70}$$

for $\lambda > 1$, where T is described by (5.2.67).

A brief discussion of deterministic elastic spherical shells will now be presented, before extending the theory to the stochastic case.

Deterministic elastic shell

In the deterministic case, following the approach set out in [151], for a spherical shell of hyperelastic material defined by the strain-energy function (3.1.2), where μ_1 and μ_2 are fixed positive constants, and $\mu = \mu_1 + \mu_2 > 0$ is the corresponding shear modulus, (5.2.61) is equal to

$$W(\lambda) = \frac{\mu_1}{2m^2} \left(\lambda^{-4m} + 2\lambda^{2m} - 3 \right) + \frac{\mu_2}{2n^2} \left(\lambda^{-4n} + 2\lambda^{2n} - 3 \right). \tag{5.2.71}$$

The internal pressure, given by (5.2.69), then takes the form

$$T(\lambda) = 2\varepsilon \left[\frac{\mu_1}{m} \left(\lambda^{2m-3} - \lambda^{-4m-3} \right) + \frac{\mu_2}{n} \left(\lambda^{2n-3} - \lambda^{-4n-3} \right) \right], \tag{5.2.72}$$

and (5.2.70) is equivalent to

$$\frac{\mu_1}{m}\left[(2m-3)\lambda^{2m-4}+(4m+3)\lambda^{-4m-4}\right]+\frac{\mu_2}{n}\left[(2n-3)\lambda^{2n-4}+(4n+3)\lambda^{-4n-4}\right]=0.$$
(5.2.73)

Specifically, if $\mu_2=0$, then, when $-3/4<m<3/2$, the internal pressure increases to a maximum value then decreases, otherwise the internal pressure increases monotonically. If $\mu_2>0$, then (5.2.73) is equivalent to

$$\frac{\mu_1}{\mu}=\frac{m\left[(2n-3)\lambda^{2n-4}+(4n+3)\lambda^{-4n-4}\right]}{m\left[(2n-3)\lambda^{2n-4}+(4n+3)\lambda^{-4n-4}\right]-n\left[(2m-3)\lambda^{2m-4}+(4m+3)\lambda^{-4m-4}\right]},$$
(5.2.74)

where $0<\mu_1/\mu<1$.

In particular, for a spherical shell of Mooney-Rivlin material, with $m=1$ and $n=-1$, the minimum value of μ_1/μ such that an inflation instability occurs is the minimum value of

$$\eta(\lambda)=\frac{\lambda^8+5\lambda^2}{\lambda^8+5\lambda^2+\lambda^6-7},\qquad \lambda\geq 7^{1/6},$$
(5.2.75)

i.e.

$$\eta_{min}\approx 0.8234.$$
(5.2.76)

In this case:

(i) When $\eta_{min}\leq\mu_1/\mu<1$, the internal pressure increases to a maximum, then decreases to a minimum, then increases again;

(ii) When $0<\mu_1/\mu<\eta_{min}$, the internal pressure is always increasing.

For spherical shells of Mooney-Rivlin material, with $m=1$ and $n=-1$, the internal pressure $T(\lambda)$ (5.2.72), normalised by $2\epsilon\mu$, is plotted in Figure 5.13 (see also [38, 69, 221], [151, pp.283-288], [70, pp.442-447], and the references therein).

Stochastic elastic shell

For a spherical shell of stochastic Mooney-Rivlin material, characterised by the strain-energy function (3.1.2), with $m = 1$ and $n = -1$, the probability distribution of stable inflation, such that internal pressure monotonically increases as the radial stretch increases, is

$$P_1\left(\mu > \frac{\mu_1}{\eta_{min}}\right) = 1 - \int_0^{\mu_1/\eta_{min}} p_1(u)\mathrm{d}u, \qquad (5.2.77)$$

where η_{min} is given in (5.2.76), $p_1(u) = g(u; \rho_1, \rho_2)$ if the random shear modulus, μ, follows the Gamma distribution (3.1.6), with $\rho_1 = 405$ and $\rho_2 = 0.01$, and $p_1(u) = h(u; \underline{\mu}, \|\mu\|)$ if μ follows a normal distribution (3.4.44), with $\underline{\mu} = 4.09$ and $\|\mu\| = 0.23$ (see Table 3.2).

The probability distribution of inflation instability occurring, such that the internal pressure begins to decrease, is

$$P_2\left(\mu < \frac{\mu_1}{\eta_{min}}\right) = 1 - P_1\left(\mu > \frac{\mu_1}{\eta_{min}}\right) = \int_0^{\mu_1/\eta_{min}} p_1(u)\mathrm{d}u. \qquad (5.2.78)$$

The probability distributions given by equations (5.2.77)-(5.2.78) are illustrated numerically in Figure 5.14 (blue lines for P_1 and red lines for P_2). Specifically, $\mu_1 \in (0, \underline{\mu})$ was divided into 100 steps, then for each value of μ_1, 100 random values of μ were numerically generated from a specified Gamma (or normal) distribution and compared with the inequalities defining the two intervals for values of μ_1. For the deterministic elastic shell, which is based on the mean value of the shear modulus, $\underline{\mu} = \rho_1\rho_2 = 4.09$, the critical value of $\mu_1 = \eta_{min} \cdot \mu = 3.3683$ strictly separates the cases where inflation instability can occur or not. For the stochastic problem, for the same critical value, there is, by definition, exactly 50% chance of a randomly chosen shell for which inflation is stable (blue solid or dashed line if the shear modulus is Gamma or normal distributed, respectively), and 50% chance of a randomly chosen shell, such that a limit-point instability occurs (red solid or

dashed line). To increase the probability of stable inflation ($P_1 \approx 1$), sufficiently small values of μ_1, below the expected critical value, must be considered, whereas a limit-point instability is certain to occur ($P_2 \approx 1$) only if the model reduces to the neo-Hookean case. However, due to the natural variability in the probabilistic system, there will also exist events where there is competition between the two cases.

To illustrate this, in Figure 5.15, the probability distribution of the normalised internal pressure $T(\lambda)$, defined by (5.2.69), as a function of the inner stretch λ, when μ follows a Gamma distribution with $\rho_1 = 405$ and $\rho_2 = 0.01$, and $R_1 = \mu_1/\mu$ follows a Beta distribution with $\xi_1 = 287$ and $\xi_2 = 36$ (see Table 3.3) is demonstrated. In this case, $\underline{\mu}_1 = 3.63 = 0.89 \cdot \underline{\mu} > \eta_{min} \cdot \underline{\mu}$, and instability is expected to occur. Nevertheless, the probability distribution suggests that there is also around 10% chance that the inflation is stable.
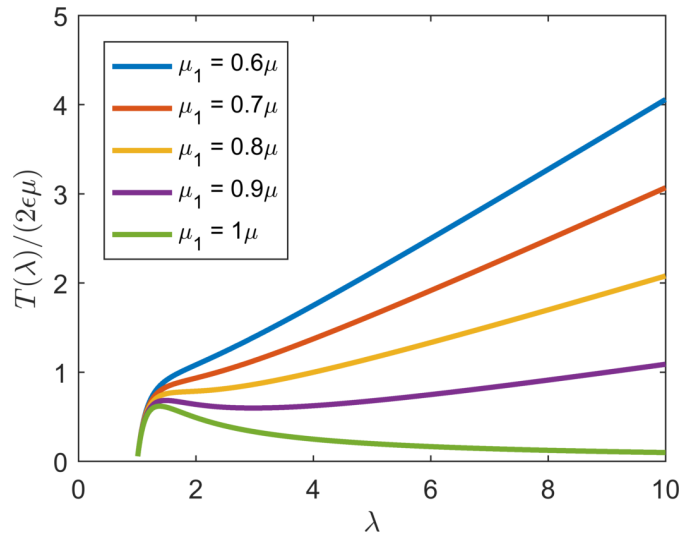
Figure 5.13: The normalised internal pressure $T(\lambda)$ defined by (5.2.72), for the inflation of spherical shells of Mooney-Rivlin material, defined by the strain-energy function (3.1.2) with $m = 1$ and $n = -1$. In this deterministic case, inflation instability occurs if $\mu_1/\mu > \eta_{min}$.
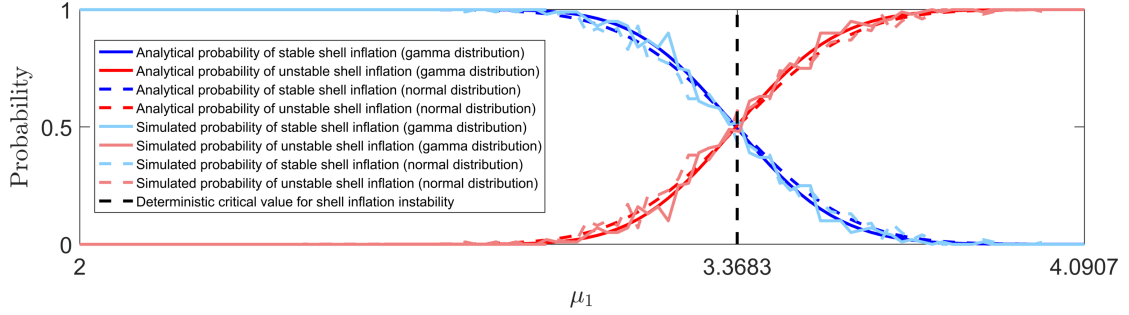
Figure 5.14: Probability distributions (5.2.77)-(5.2.78) of whether instability can occur or not for a spherical shell of stochastic Mooney-Rivlin material, described by (3.1.2) with $m = 1$ and $n = -1$, and the shear modulus, μ, following either a Gamma distribution (3.1.6) with $\rho_1 = 405$, $\rho_2 = 0.01$ (continuous lines), or a normal distribution (3.4.44) with $\underline{\mu} = 4.09$, $\|\mu\| = 0.23$ (dashed lines). Darker colours represent analytically derived solutions, given by equations (5.2.77)-(5.2.78), whereas lighter colours represent stochastically generated data. The vertical line at the critical value, $\mu_1 = 3.3683$, separates the expected regions based only on the mean value of the shear modulus.
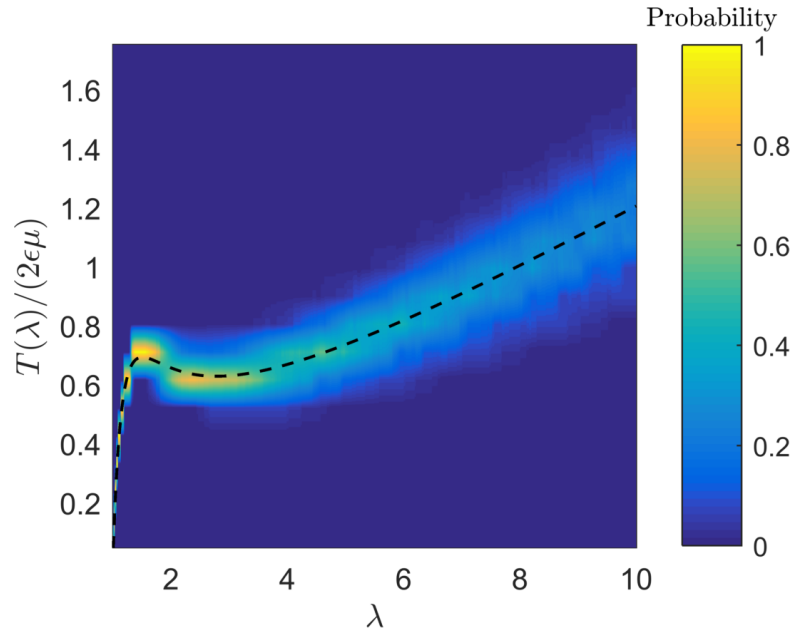
Figure 5.15: Computed probability distribution of the normalised internal pressure, $T(\lambda)$ (5.2.69), for the inflation of a spherical shell of stochastic Mooney-Rivlin material, given by (3.1.2) with $m = 1$ and $n = -1$, when μ follows a Gamma distribution (3.1.6) with $\rho_1 = 405$, $\rho_2 = 0.01$, and $R_1 = \mu_1/\mu$ follows a Beta distribution (3.1.12) with $\xi_1 = 287$, $\xi_2 = 36$. As $\underline{\mu}_1 = 3.63 = 0.89 \cdot \underline{\mu} > \eta_{min} \cdot \underline{\mu}$, instability is expected to occur, but there is also around 10% chance that the inflation is stable. The dashed black lines correspond to the expected pressure based only on mean parameter values.

5.2.2 Circular cylinders

In this section, analysis analogous to that in Section 5.2.1 will be presented with regard to the inflation of circular cylindrical tubes.
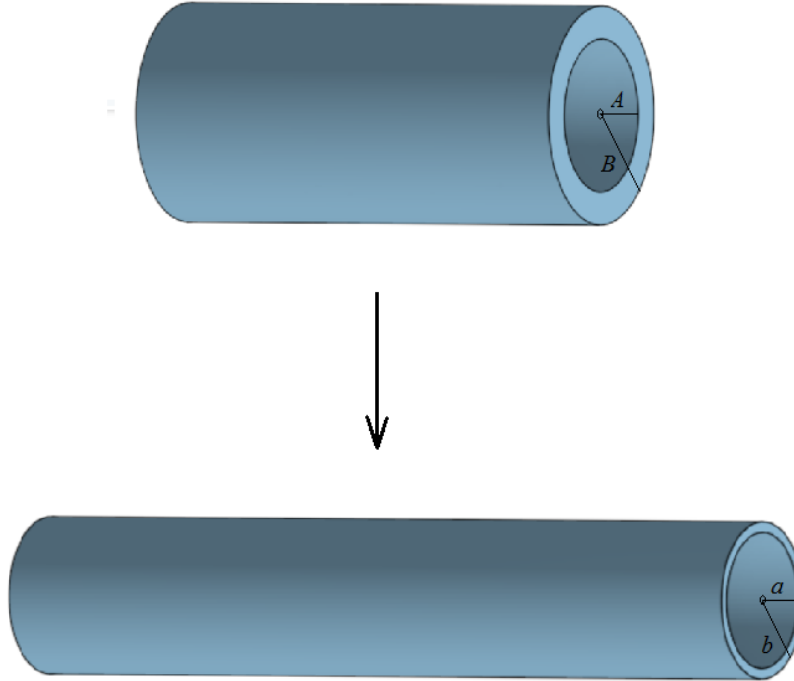
Figure 5.16: Schematic of inflation and stretching of a cylindrical tube, showing the reference state, with inner radius A and outer radius B (top), and the current (deformed) state, with inner radius a and outer radius b (bottom), respectively.

For a homogeneous isotropic incompressible elastic material, the strain energy function, invariants I_1 and I_2, and the Cauchy stress tensor $\boldsymbol{\sigma}$ are defined as in (5.2.1), (5.2.2), and (5.2.4), respectively.

The functions $\widehat{W}$, $\widetilde{W}$ and $\overline{W}$ are now introduced, defined as in (5.2.5). As before, $\widehat{W}$ describes the general response in terms of two independent principal stretches, $\widetilde{W}$ describes the response in the axisymmetric deformation, and $\overline{W}$ describes the response in the plane deformation. For principal stretches defined as

$$\lambda_i = \left(\lambda, \frac{1}{\lambda\mu}, \mu\right), \quad i = 1, 2, 3, \tag{5.2.79}$$

the principal stress differences are given by (5.2.7). The main stress difference of interest is once again given by (5.2.8), and explicitly defined in (5.2.9).

In the case of a hollow cylinder, the deformation is described by

$$r^2 - \frac{r_0^2}{\mu} = a^2 - \frac{a_0^2}{\mu}, \qquad \theta = \theta_0, \qquad z = \mu z_0, \qquad (5.2.80)$$

where (r, θ, z) are cylindrical coordinates and μ is a positive constant. Here, the deformation in question describes the radial inflation and uniform axial stretching of a circular cylindrical tube of initial inner radius a_0. For convenience, we once again introduce a measure of the porosity, denoted by α, with

$$\alpha = \frac{b^2}{b^2 - a^2}, \qquad \text{and} \qquad \alpha_0 = \frac{b_0^2}{b_0^2 - a_0^2}, \qquad (5.2.81)$$

where b_0 denotes the initial outer radius. After an initial axial stretching described by

$$r^2 = \frac{r_0^2}{\mu}, \qquad \theta = \theta_0, \qquad z = \mu z_0, \qquad (5.2.82)$$

the porosity does not change, and so the subsequent radial inflation, for fixed values of μ, will be decribed by the variable α.

In this current case, the principal stretches in the coordinate directions are defined as

$$\lambda_i = \left(\frac{\mathrm{d}r}{\mathrm{d}r_0}, \frac{r}{r_0}, \frac{\mathrm{d}z}{\mathrm{d}z_0} \right) = \left(\lambda, \frac{1}{\lambda\mu}, \mu \right), \quad i = 1, 2, 3, \qquad (5.2.83)$$

with the radial stretch, λ, given by $\lambda = \mathrm{d}r/\mathrm{d}r_0$ with $r^2 = a^2 - a_0^2/\mu + r_0^2/\mu$, determined to give

$$\lambda^2 = \frac{1}{\mu} \left[1 - \frac{\mu a^2 - a_0^2}{\mu r^2} \right]. \qquad (5.2.84)$$

Using (5.2.80), (5.2.81) and (5.2.84), it can then be deduced that

$$\frac{\mu a^2}{a_0^2} = \frac{\alpha - 1}{\alpha_0 - 1}, \qquad \frac{\mu b^2}{b_0^2} = \frac{\alpha}{\alpha_0}, \qquad \text{and} \qquad \lambda^2 = \frac{1}{\mu} \left[1 - \frac{a_0^2(\alpha - \alpha_0)}{\mu r^2(\alpha_0 - 1)} \right]. \qquad (5.2.85)$$

The radial equation of equilibrium is defined as

$$\frac{\mathrm{d}\sigma_{rr}}{\mathrm{d}r} + \frac{1}{r}(\sigma_{rr} - \sigma_{\theta\theta}) = 0, \tag{5.2.86}$$

and the boundary conditions for the internal pressurisation of the tube are

$$\sigma_{rr} = -P \quad \text{at} \quad r = a \qquad \text{and} \qquad \sigma_{rr} = 0 \quad \text{at} \quad r = b. \tag{5.2.87}$$

From (5.2.83), it can be deduced that

$$\widehat{W}(\lambda, \mu) = W\left(\lambda, \frac{1}{\lambda\mu}, \mu\right), \tag{5.2.88}$$

and so, using (5.2.8), we see that

$$T = \sigma_2 - \sigma_1 = -\lambda\frac{\partial\widehat{W}}{\partial\lambda} = \hat{T}(\lambda, \mu), \tag{5.2.89}$$

leading to the condition

$$\sigma_{\theta\theta} - \sigma_{rr} = \widehat{T}(\lambda, \mu), \tag{5.2.90}$$

with the function $\widehat{T}$ defined by (5.2.5) and (5.2.9). Expressions (5.2.86)-(5.2.90) give

$$\int_a^b \frac{\mathrm{d}\sigma_{rr}}{\mathrm{d}r}\mathrm{d}r = \int_a^b \frac{1}{r}\widehat{T}(\lambda, \mu)\mathrm{d}r \tag{5.2.91}$$

which, using the boundary conditions stated in (5.2.87), yields

$$P = \int_a^b \widehat{T}(\lambda, \mu)\frac{\mathrm{d}r}{r}. \tag{5.2.92}$$

Introducing the change of variables $r = 1 - x$ into (5.2.92) then gives

$$P = \frac{1}{2}\int_{x_a}^{x_b} \widetilde{T}\left(\left(\frac{x}{\mu}\right)^{\frac{1}{2}}, \mu\right)\frac{\mathrm{d}x}{1-x}, \tag{5.2.93}$$

where we are integrating between the larger value x_a and the smaller value x_b,

with

$$x = \mu\lambda^2, \qquad x_a = \frac{a_0^2}{\mu a^2} = \frac{\alpha_0 - 1}{\alpha - 1}, \qquad x_b = \frac{b_0^2}{\mu b^2} = \frac{\alpha_0}{\alpha}. \tag{5.2.94}$$

The expression (5.2.93) gives the pressure as a function of the kinematical variable α for the inflation of a hollow circular cylinder with axial prestretch. For the case where inflation occurs with no prestretching, in other words, when $\mu = 1$, (5.2.93) may be written as

$$P = \frac{1}{2} \int_{x_a}^{x_b} \overline{T}(x^{\frac{1}{2}}) \frac{\mathrm{d}x}{1 - x}, \tag{5.2.95}$$

since $\widehat{T}[(x/1)^{1/2}, 1] = \widehat{T}(x^{1/2}, 1) = \overline{T}(x^{1/2})$ with $\widehat{W}(\lambda, 1) = \overline{W}(\lambda)$, where $\overline{T}$ is the plane strain response function defined in (5.2.9).

A condition for the stationary values of the pressure P will now be developed. Differentiation of (5.2.95) yields

$$\begin{aligned}
\frac{\mathrm{d}P}{\mathrm{d}\alpha} &= \frac{1}{2} \frac{\mathrm{d}}{\mathrm{d}\alpha} \int_{x_a}^{x_b} \widehat{T}\left(\left(\frac{x}{\mu}\right)^{\frac{1}{2}}, \mu\right) \frac{\mathrm{d}x}{1 - x} \\
&= \frac{1}{2}\left[\int_{x_a}^{x_b} \frac{\partial}{\partial\alpha} \frac{\widehat{T}\left(\left(\frac{x}{\mu}\right)^{\frac{1}{2}}, \mu\right)}{1 - x} \mathrm{d}x + \frac{\widehat{T}\left(\left(\frac{x_b}{\mu}\right)^{\frac{1}{2}}, \mu\right)}{1 - x_b} \frac{\partial x_b}{\partial\alpha} - \frac{\widehat{T}\left(\left(\frac{x_a}{\mu}\right)^{\frac{1}{2}}, \mu\right)}{1 - x_a} \frac{\partial x_a}{\partial\alpha} \right].
\end{aligned} \tag{5.2.96}$$

Using $x_a = \alpha_0 - 1/\alpha - 1$ and $x_b = \alpha_0/\alpha$ then gives

$$\frac{\mathrm{d}P}{\mathrm{d}\alpha} = \frac{1}{2(\alpha - \alpha_0)} \left[\frac{\alpha_0 - 1}{\alpha - 1} \widehat{T}\left(\left(\frac{\alpha_0 - 1}{\mu(\alpha - 1)}\right)^{\frac{1}{2}}, \mu\right) - \frac{\alpha_0}{\alpha} \widehat{T}\left(\left(\frac{\alpha_0}{\mu\alpha}\right)^{\frac{1}{2}}, \mu\right) \right]. \tag{5.2.97}$$

Introducing a response function h, defined as

$$h(\lambda^2, \mu) = \lambda^2 \widehat{T}(\lambda, \mu), \tag{5.2.98}$$

gives the condition for stationary values of the applied pressure P in the form

$$h\left(\frac{\alpha_0 - 1}{\mu(\alpha - 1)}, \mu\right) = h\left(\frac{\alpha_0}{\mu\alpha}, \mu\right), \tag{5.2.99}$$

since $\lambda = [\alpha_0 - 1/\mu(\alpha - 1)]^{1/2}$. Where

$$x = \lambda^2 \implies x_a = \lambda_a^2, \quad x_b = \lambda_b^2, \tag{5.2.100}$$

and

$$T_a \to \widetilde{T}_a(x_a) \quad \text{and} \quad T_b \to \widetilde{T}_b(x_b), \tag{5.2.101}$$

we have

$$h(x_a) = \lambda_a^2 T_a \quad \text{and} \quad h(x_b) = \lambda_b^2 T_b, \tag{5.2.102}$$

and so

$$\lambda_a^2 T_a = \lambda_b^2 T_b, \tag{5.2.103}$$

where λ_a and λ_b denote radial stretches, and T_a and T_b denote principal stress differences $T = \sigma_{\theta\theta} - \sigma_{rr}$, evaluated at the inner and outer boundaries, given by $r = a$ and $r = b$, respectively.

The condition (5.2.103) is analogous to the condition (5.2.27) in the case of spherical inflation. Performing a similar analysis to that detailed in Section 5.2.1, it can be observed that the qualitative behaviour in cylindrical inflation depends on the monotonicity of the function $h(\lambda^2, \mu)$ on the interval $0 < \lambda < 1/\sqrt{\mu}$. This function could be monotonic, have a local maximum or have a local maximum and minimum. Corresponding to these cases, the pressure in cylindrical inflation may increase monotonically in the case of type A behaviour, or type C for thick-walled cylinders, it may increase to a maximum value P^*, then decrease, which is the case for type B, or it may increase to a maximum value P^*, decrease to a minimum P^{**}, then increase again, as is the case for type C behaviour for thin-walled cylinders. The axial prestretch, μ, expands or contracts the range of relevant values of the radial stretch, λ, $\left(0 < \lambda \leq 1/\sqrt{\mu}\right)$, depending on whether the prestretch is compressive ($\mu < 1$) or tensile ($\mu > 1$).

For a material described by the strain energy function

$$\mathcal{W} = C(\lambda_1^m + \lambda_2^m + \lambda_3^m - 3) \tag{5.2.104}$$

with $\lambda_i = \left(\lambda, 1/\lambda\mu, \mu\right)$, equation (5.2.9) gives

$$\widehat{T} = -\lambda\frac{\partial\widehat{W}}{\partial\lambda} = mC\left(\frac{1}{\lambda^m\mu^m} - \lambda^m\right), \tag{5.2.105}$$

since, using (5.2.5), $\widehat{W}(\lambda, \mu) = \mathcal{W}$. Hence

$$\widehat{T}(\lambda, \mu) = mC\left(\frac{1}{\lambda^m\mu^m} - \lambda^m\right). \tag{5.2.106}$$

Expressions (5.2.98) and (5.2.106) give

$$h(\lambda^2, \mu) = \lambda^2\widehat{T}(\lambda, \mu) = \lambda^2 mC\left(\frac{1}{\lambda^m\mu^m} - \lambda^m\right), \tag{5.2.107}$$

so

$$h(\lambda^2, \mu) = mC(\mu^{-m}\lambda^{2-m} - \lambda^{m+2}). \tag{5.2.108}$$

The behaviour of such a material in cylindrical inflation is of type B for

$$-2 < m < 2, \tag{5.2.109}$$

and is of type A otherwise. In particular, neo-Hookean and Mooney-Rivlin materials do not have a pressure maximum instability for cylindrical inflation. For $|m| < 2$, the porosity α^*, at which the pressure reaches a maximum, is a root of

$$\left[\frac{\alpha_0 - 1}{\mu(\alpha - 1)}\right]^{1+\frac{m}{2}} - \left[\frac{\alpha_0 - 1}{\mu(\alpha - 1)}\right]^{1-\frac{m}{2}} = \left(\frac{\alpha_0}{\mu\alpha}\right)^{1+\frac{m}{2}} - \left(\frac{\alpha_0}{\mu\alpha}\right)^{1-\frac{m}{2}}, \tag{5.2.110}$$

which gives the same value for m and $-m$.

For a material with strain energy function

$$\mathcal{W} = M(\lambda_1^m + \lambda_2^m + \lambda_3^m - 3) + N(\lambda_1^n + \lambda_2^n + \lambda_3^n - 3), \qquad (5.2.111)$$

where m, n, M and N are constants, with $|m| < 2$ and $|n| > 2$, expression (5.2.108), along with (5.2.9), leads to

$$h(\lambda^2, \mu) = mM(\mu^{-m}\lambda^{2-m} - \lambda^{2+m}) + nN(\mu^{-n}\lambda^{2-n} - \lambda^{2+n}). \qquad (5.2.112)$$

Analysis akin to that in Section 5.2.1 for spherical inflation demonstrates that this material displays behaviour of type C in cylindrical inflation for sufficiently small values of the ratio N/M.

For pressurisation of a cylindrical cavity of radius a_0 in a medium of infinite extent, with axial stretch μ, the pressure is given by the expression

$$P = \frac{1}{2} \int_{\frac{a_0^2}{\mu a^2}}^{1} \widehat{T}\left(\left(\frac{x}{\mu}\right)^{\frac{1}{2}}, \mu\right) \frac{\mathrm{d}x}{1-x}. \qquad (5.2.113)$$

Differentiation of (5.2.113) yields

$$\frac{\mathrm{d}P}{\mathrm{d}\alpha} = \frac{a_0^2}{a(\mu a^2 - a_0^2)} \widehat{T}\left(\frac{a_0}{\mu a}, 1\right), \qquad (5.2.114)$$

and so it can be observed that the pressure P increases monotonically.

Stochastic incompressible cylindrical tube

Next, a cylindrical tube of stochastic hyperelastic material, characterised by the strain energy function (3.1.2), is deformed through the combined effects of radially symmetric inflation and axial extension [169] as follows (see Figure 5.16);

$$r = f(R)R, \qquad \theta = \Theta, \qquad z = \alpha Z, \qquad (5.2.115)$$

where (R, Θ, Z) and (r, θ, z) are the cylindrical polar coordinates in the reference and current configurations, respectively, such that $A \le R \le B$, $\alpha > 0$ is a given deterministic constant, and $f(R) \ge 0$ is to be determined. When $\alpha < 0$, the tube is everted so that the inner surface becomes the outer surface, and vice-versa.

The deformation gradient in this case is $\mathbf{F} = \operatorname{diag}(\lambda_1, \lambda_2, \lambda_3)$, where

$$\lambda_1 = f(R) + R\frac{\mathrm{d}f}{\mathrm{d}R} = \lambda^{-1}\alpha^{-1}, \qquad \lambda_2 = f(R) = \lambda, \qquad \lambda_3 = \alpha, \qquad (5.2.116)$$

and λ_1, λ_2 and λ_3 represent the radial, tangential and longitudinal stretch, respectively.

For a cylindrical tube, the radial equation is given by (5.2.86), and is equivalent to

$$\frac{\mathrm{d}P_{11}}{\mathrm{d}\lambda}\lambda^{-1}\alpha^{-1} + \frac{P_{11} - P_{22}}{1 - \lambda^2\alpha} = 0. \qquad (5.2.117)$$

Comparable to the analysis of spherical shells, the limit-point instability criterion for cylindrical tubes will now be discussed.

Limit-point instability criterion for cylindrical tubes

For a cylindrical tube of hyperelastic material described by the strain energy function (3.1.2), the limit-point instability criterion can be deduced in a way that is analogous to that presented for spherical shells in Section 5.2.1.

Denoting

$$W(\lambda) = \mathcal{W}(\lambda^{-1}\alpha^{-1}, \lambda, \alpha), \qquad (5.2.118)$$

where $\lambda = r/R$ and $\alpha = z/Z$, and using

$$\frac{\partial\mathcal{W}}{\partial\lambda_1} = \frac{\mu_1}{m}\lambda^{-2m+1}\alpha^{-2m+1} + \frac{\mu_2}{n}\lambda^{-2n+1}\alpha^{-2n+1}, \qquad (5.2.119)$$

$$\frac{\partial\mathcal{W}}{\partial\lambda_2} = \frac{\mu_1}{m}\lambda^{2m-1} + \frac{\mu_2}{n}\lambda^{2n-1}, \qquad (5.2.120)$$

and (5.2.60), it can be observed that

$$
\begin{aligned}
\frac{\partial W}{\partial \lambda} &= -\frac{1}{\lambda^2 \alpha}\left[\frac{\partial W}{\partial \lambda_1} - \frac{p}{\lambda_1}\right] + \left[\frac{\partial W}{\partial \lambda_2} - \frac{p}{\lambda_2}\right] \\
&= -\frac{1}{\lambda^2 \alpha}\frac{\partial W}{\partial \lambda_1} + \frac{p}{\lambda^2 \alpha \lambda^{-1}\alpha^{-1}} + \frac{\partial W}{\partial \lambda_2} - \frac{p}{\lambda} \\
&= -\frac{1}{\lambda^2 \alpha}\frac{\partial W}{\partial \lambda_1} + \frac{\partial W}{\partial \lambda_2},
\end{aligned}
\tag{5.2.121}
$$

which then gives

$$
\frac{\mathrm{d}W}{\mathrm{d}\lambda} = -\frac{P_{11}}{\lambda^2 \alpha} + P_{22},
\tag{5.2.122}
$$

where $P_{11} = \partial W/\partial \lambda_1$ and $P_{22} = \partial W/\partial \lambda_2$. Setting the external pressure (at $R = B$) equal to zero, by (5.2.117) and (5.2.122), the internal pressure (at $R = A$) is equal to

$$
\begin{aligned}
T &= -\int_{\lambda_a}^{\lambda_b} \frac{P_{11}}{\lambda^2 \alpha}\mathrm{d}\lambda + \int_{\lambda_a}^{\lambda_b} \frac{\mathrm{d}P_{11}}{\mathrm{d}\lambda}\lambda^{-1}\alpha^{-1}\mathrm{d}\lambda \\
&= -\int_{\lambda_a}^{\lambda_b} \frac{P_{11}}{\lambda^2 \alpha}\mathrm{d}\lambda - \int_{\lambda_a}^{\lambda_b} \frac{P_{11} - P_{22}}{1 - \lambda^2 \alpha}\mathrm{d}\lambda \\
&= \int_{\lambda_a}^{\lambda_b} \frac{\mathrm{d}W}{\mathrm{d}\lambda}\frac{\mathrm{d}\lambda}{1 - \lambda^2 \alpha},
\end{aligned}
\tag{5.2.123}
$$

where $\lambda_a = a/A$ and $\lambda_b = b/B$ are the stretches for the inner and outer radii, respectively. Due to the material incompressibility, the material volume in the cylindrical tube is conserved, i.e. $\pi\alpha(b^2 - a^2) = \pi(B^2 - A^2)$, or equivalently, as $a = A\lambda_a$ and $b = B\lambda_b$,

$$
b^2 = a^2 - \frac{A^2}{\alpha} + \frac{B^2}{\alpha},
\tag{5.2.124}
$$

and so,

$$
\frac{b^2}{B^2} = \frac{a^2}{B^2} - \frac{A^2}{\alpha B^2} + \frac{B^2}{\alpha B^2} \quad \Longrightarrow \quad \lambda_b^2 = \frac{a^2}{A^2}\frac{A^2}{B^2} - \frac{A^2}{\alpha B^2} + \frac{1}{\alpha},
\tag{5.2.125}
$$

which then gives

$$
\lambda_b^2 = \left(\lambda_a^2 - \frac{1}{\alpha}\right)\left(\frac{A}{B}\right)^2 + \frac{1}{\alpha}.
\tag{5.2.126}
$$

Hence, the internal pressure T is a function of the inner stretch ratio, λ_a, only.

For the cylindrical tube, a limit-point instability occurs if there is a change in the monotonicity of T, given by (5.2.123), as a function of λ_a. Assuming that the tube is thin, where $0 < \epsilon = (B - A)/A \ll 1$, we approximate the internal pressure as [151, p.290]

$$T(\lambda) = \frac{\epsilon}{\lambda \alpha} \frac{\mathrm{d}W}{\mathrm{d}\lambda}, \qquad (5.2.127)$$

and find the point instability by solving the equation (5.2.70) for $\lambda > 1$, with T given by (5.2.127).

Deterministic elastic tube

In the deterministic case, once again following the approach set out in [151, pp. 288-291], for a cylindrical tube of hyperelastic material described by the strain-energy function (3.1.2), with μ_1 and μ_2 given positive constants, the function (5.2.118) takes the form

$$W(\lambda) = \frac{\mu_1}{2m^2} \left(\lambda^{-2m} \alpha^{-2m} + \lambda^{2m} + \alpha^{2m} - 3 \right) + \frac{\mu_2}{2n^2} \left(\lambda^{-2n} \alpha^{-2n} + \lambda^{2n} + \alpha^{2n} - 3 \right).$$
$$(5.2.128)$$

The internal pressure (5.2.127) is then equal to

$$T(\lambda) = \frac{\varepsilon}{\alpha} \left[\frac{\mu_1}{m} \left(\lambda^{2m-2} - \lambda^{-2m-2} \alpha^{-2m} \right) + \frac{\mu_2}{n} \left(\lambda^{2n-2} - \lambda^{-2n-2} \alpha^{-2n} \right) \right], \quad (5.2.129)$$

and (5.2.70) becomes

$$\frac{\mu_1}{m} \left[(m-1)\lambda^{2m-3} + (m+1)\lambda^{-2m-3} \alpha^{-2m} \right] +$$
$$+ \frac{\mu_2}{n} \left[(n-1)\lambda^{2n-3} + (n+1)\lambda^{-2n-3} \alpha^{-2n} \right] = 0. \qquad (5.2.130)$$

In this case, if $\mu_2 = 0$, then, when $-1 < m < 1$, the internal pressure increases to a maximum value then decreases, otherwise the internal pressure is always

increasing. If $\mu_2 > 0$, then (5.2.130) is equivalent to

$$\frac{\mu_1}{\mu} = \frac{m\left[(n-1)\lambda^{2n-3} + (n+1)\lambda^{-2n-3}\alpha^{-2n}\right]}{m\left[(n-1)\lambda^{2n-3} + (n+1)\lambda^{-2n-3}\alpha^{-2n}\right] - n\left[(m-1)\lambda^{2m-3} + (m+1)\lambda^{-2m-3}\alpha^{-2m}\right]},$$
(5.2.131)

where $0 < \mu_1/\mu < 1$.

We now specialise to the case where $m = 1/2$, $n = -3/2$, and $\alpha = 1$. In this case, (5.2.131) takes the form

$$\frac{\mu_1}{\mu} = \frac{1 + 5\lambda^{-6}}{1 + 5\lambda^{-6} + 3\lambda^{-2} - 9\lambda^{-4}}.$$
(5.2.132)

The minimum value of μ_1/μ for which inflation instability occurs is then the minimum of the function

$$\eta(\lambda) = \frac{\lambda^6 + 5}{\lambda^6 + 5 + 3\lambda^4 - 9\lambda^2}, \qquad \lambda > 1,$$
(5.2.133)

i.e.

$$\eta_{min} \approx 0.8035.$$
(5.2.134)

For cylindrical tubes of hyperelastic material given by the strain-energy function (3.1.2), with $m = 1/2$ and $n = -3/2$, under the deformation (5.2.115), with $\alpha = 1$, the internal pressure, $T(\lambda)$, defined by (5.2.129) and normalised by $2\varepsilon\mu$, is plotted in Figure 5.17 (see also [38], [151, pp. 288-291]).

Stochastic elastic tube

For a cylindrical tube of stochastic hyperelastic material described by the strain-energy function (3.1.2), with $m = 1/2$ and $n = -3/2$, following the approach in [151], the probability distribution of stable inflation, such that the internal pressure always increases as the radial stretch increases, is

$$P_1\left(\mu > \frac{\mu_1}{\eta_{min}}\right) = 1 - \int_0^{\mu_1/\eta_{min}} p_1(u)\mathrm{d}u,$$
(5.2.135)
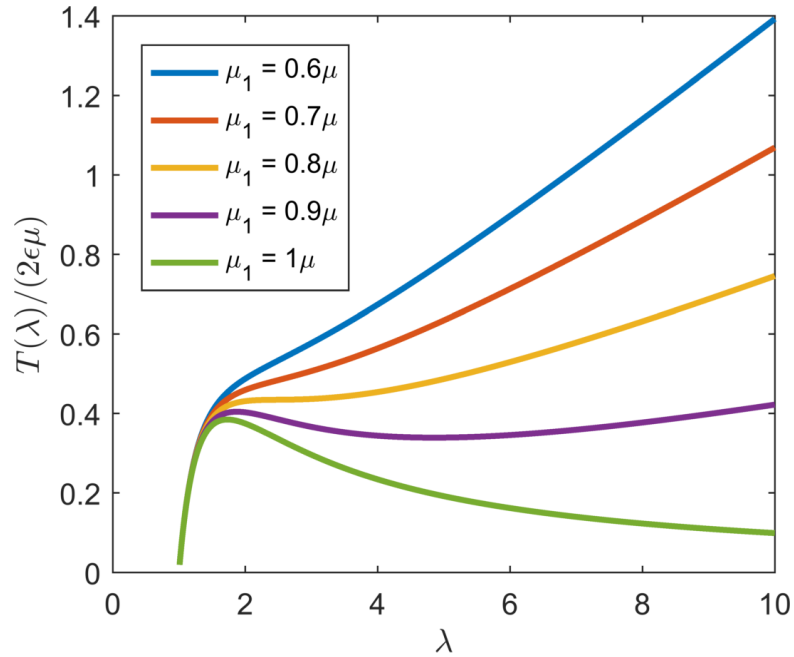
Figure 5.17: The normalised internal pressure, $T(\lambda)$ (5.2.129), for the inflation of cylindrical tubes of hyperelastic materials, described by (3.1.2) with $m = 1/2$ and $n = -3/2$. In this deterministic case, inflation instability occurs if $\mu_1/\mu > \eta_{min}$.
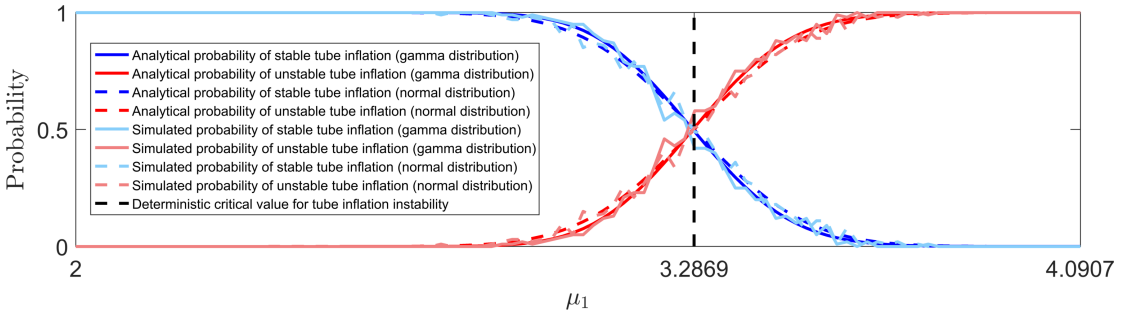
Figure 5.18: Probability distributions (5.2.135)-(5.2.136) of whether instability can occur or not for a cylindrical tube of stochastic hyperelastic material, described by (3.1.2) with $m = 1/2$ and $n = -3/2$, and the shear modulus, μ, following either a Gamma distribution (3.1.6) with $\rho_1 = 405$, $\rho_2 = 0.01$ (continuous lines), or a normal distribution (3.4.44) with $\underline{\mu} = 4.09$, $\|\mu\| = 0.23$ (dashed lines). Darker colours represent analytically derived solutions, given by equations (5.2.135)-(5.2.136), whereas lighter colours represent stochastically generated data. The vertical line at the critical value, $\mu_1 = 3.2869$, separates the expected regions based only on the mean value of the shear modulus.
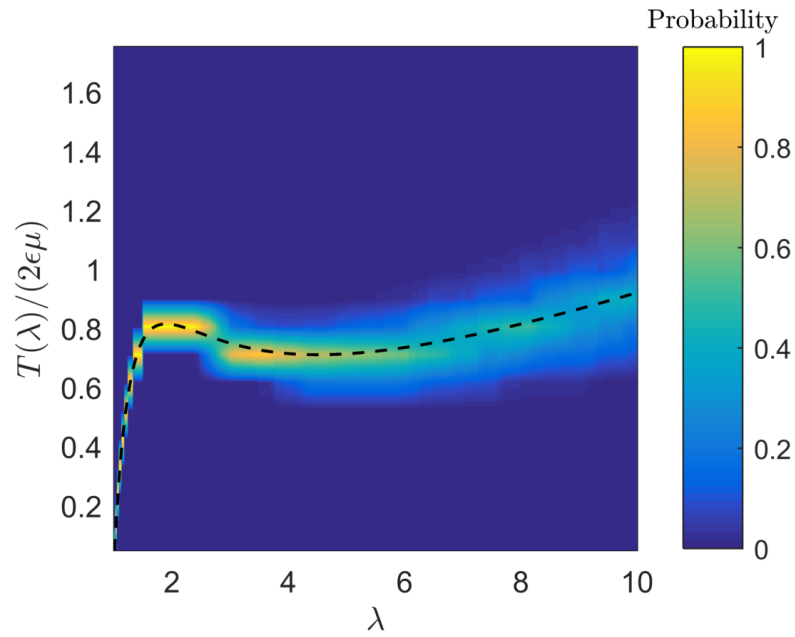
Figure 5.19: Probability distribution of the normalised internal pressure, $T(\lambda)$ (5.2.127), for the inflation of a cylindrical tube of stochastic hyperelastic material, described by (3.1.2) with $m = 1/2$ and $n = -3/2$, when μ follows a Gamma distribution (3.1.6) with $\rho_1 = 405$, $\rho_2 = 0.01$, and $R_1 = \mu_1/\mu$ follows a Beta distribution (3.1.12) with $\xi_1 = 287$, $\xi_2 = 36$. As $\underline{\mu}_1 = 3.63 = 0.89 \cdot \underline{\mu} > \eta_{min} \cdot \underline{\mu}$, instability is expected to occur, but there is also around 5% chance that the inflation is stable. The dashed black lines correspond to the expected pressure based only on mean parameter values.

where η_{min} is given in (5.2.134), $p_1(u) = g(u; \rho_1, \rho_2)$ if the random shear modulus, μ, follows the Gamma distribution (3.1.6), with $\rho_1 = 405$ and $\rho_2 = 0.01$, or $p_1(u) = h(u; \underline{\mu}, \|\mu\|)$ if μ follows the normal distribution (3.4.44), with $\underline{\mu} = 4.09$ and $\|\mu\| = 0.23$ (see Table 3.2).

The probability distribution of an inflation instability occurring is

$$P_2\left(\mu < \frac{\mu_1}{\eta_{min}}\right) = 1 - P_1\left(\mu > \frac{\mu_1}{\eta_{min}}\right) = \int_0^{\mu_1/\eta_{min}} p_1(u)\mathrm{d}u. \tag{5.2.136}$$

The probability distributions given by (5.2.135)-(5.2.136) are shown in Figure 5.18 (blue lines for P_1 and red lines for P_2). For the deterministic elastic tube, the critical value, $\mu_1 = \eta_{min} \cdot \mu = 3.2869$, strictly divides the cases of inflation instability occurring or not. However, in the stochastic case, to increase the chance that inflation is always stable ($P_1 \approx 1$), sufficiently small values of the parameter μ_1, below the expected critical point, must be taken, while instability is guaranteed ($P_2 \approx 1$) only for the stochastic neo-Hookean tube.

As an example, in Figure 5.19, the probability distribution of the normalised internal pressure $T(\lambda)$ (5.2.127) as a function of the inner stretch λ, when μ follows a Gamma distribution with $\rho_1 = 405$ and $\rho_2 = 0.01$, and $R_1 = \mu_1/\mu$ follows a Beta distribution with $\xi_1 = 287$ and $\xi_2 = 36$ (see Table 3.3) is demonstrated. Hence, $\underline{\mu}_1 = 3.63 = 0.89 \cdot \underline{\mu} > \eta_{min} \cdot \underline{\mu}$, and so an instability is expected to occur. However, the probability distribution suggests that there is also around a 5% chance that the inflation is stable.

By approaching the problem from this stochastic perspective, for both the spherical shells in Section 5.2.1 and the cylindrical tubes discussed here, opportunities arise to gain more insight into the onset of instabilities within these configurations. This view point can now be employed with the same aim to a range of other potential deformations within the field of solid mechanics, as will now be demonstrated with an in-depth analysis of the cavitation of stochastic isotropic hyperelastic spheres.

5.3 Cavitation of spheres

Building on the approach presented in Section 5.2 for the inflation of spherical shells and cylindrical tubes, the phenomenon of cavitation, contained within the theoretical context of finite elastostatics, will be the topic of focus within this section. Finite elasticity theory covers the simplest case where internal forces only depend on the current deformation of the material, and not on its history, and is based on average data values. Here, within the context of stochastic elasticity, the explicit solution to the cavitation problems of incompressible spheres of stochastic isotropic hyperelastic material, described by a two-term Ogden-type model [129,194,196], under radial tensile dead loads will be investigated. The word "cavitation" was used to describe this void-formation within a solid by analogy to the similar phenomenon observed in an elastic fluid [19,64].

For all homogeneous isotropic hyperelastic models considered so far in the literature, cavitation appears as a supercritical bifurcation, where typically, following the bifurcation, the cavity radius increases monotonically as the applied load increases [41]. It will be demonstrated here, however, that the restriction that a material satisfies the Baker-Ericksen inequalities (3.1.1) is not sufficient to exclude the possibility of a subcritical bifurcation, which in this case would be expected to be a snap cavitation. This occurs when there is a jump in the radius of the cavitation immediately after bifurcation. The general conditions under which a cavitation can appear through a supercritical or subcritical bifurcation will be determined here, and further we will construct explicit examples of isotropic hyperelastic models that exhibit snap cavitation. We will combine finite elasticity and information theory, and rely on the general hypotheses outlined in Section 3.1 [129,130,133]. Analogous to the case in Section 5.2, for the deterministic elastic problem involving isotropic incompressible materials, there is a critical tensile traction that strictly separates the cases where cavitation occurs or not. The stochastic approach is then explored, where, due to the probabilistic nature of

the model parameters, supercritical or subcritical bifurcation occurs with a given probability, and there is also a probability that the cavity may form under smaller or greater loads than the expected critical value. These phenomena are referred to here as "likely cavitation".

5.3.1 Stochastic isotropic hyperelastic models

Attention is now focused on stochastic homogeneous incompressible hyperelastic materials characterised by the strain-energy function (3.1.2) [129, 194, 196], where m and n are deterministic constants, and μ_1 and μ_2 are random variables following given probability distributions. In the deterministic elastic case, μ_1, μ_2, m and n are constants, and the model contains, as special cases, the neo-Hookean model, the Mooney-Rivlin model, and the one- and two-term Ogden models. In both the deterministic elastic and stochastic cases, the shear modulus for infinitesimal deformations of these models is defined as $\mu = \mu_1 + \mu_2$ [128, 129]. Further, this description could be easily extended to include m and n as stochastic variables as well.

As it is well known, the deformation of a homogenous isotropic hyperelastic material under uniaxial tension is a simple extension in the direction of the tensile force if and only if the BE inequalities (3.1.1) hold [120]. In this case, the BE inequalities are equivalent to (3.1.3). Under these conditions, the shear modulus is positive, but the individual coefficients may be either positive or negative, allowing for some interesting nonlinear elastic effects to be captured (see [124, 125, 127, 133] and the references therein). In particular, here, the initiation of either stable or unstable snap cavitation in a homogeneous isotropic sphere will be investigated.

For the stochastic materials described by (3.1.2), condition (A4) in Section 3.1 is guaranteed by the constraints on the expected values stated in (3.1.4). Specifically, under these constraints, the random shear modulus μ, with mean value $\underline{\mu}$ and standard deviation $\|\mu\| = \sqrt{\text{Var}\,[\mu]}$, follows a Gamma probability

distribution [187, 188], with hyperparameters $\rho_1 > 0$ and $\rho_2 > 0$ satisfying (3.1.5). The corresponding probability density function takes the form (3.1.6), where $\Gamma : \mathbb{R}_+^* \to \mathbb{R}$ is the complete Gamma function defined in (3.1.7).

As in Section 3.1, the auxiliary random variable is defined in (3.1.8) [129]. The random model parameters are then expressed as in (3.1.9). Making the assumption that (3.1.10) holds, the random variable R_1 can be seen to follow a standard Beta distribution [1, 100], with hyperparameters $\xi_1 > 0$ and $\xi_2 > 0$ satisfying (3.1.11). The associated probability density function is given in (3.1.12), where $B : \mathbb{R}_+^* \times \mathbb{R}_+^* \to \mathbb{R}$ is the Beta function (3.1.13). For the random coefficients given in (3.1.9), the corresponding mean values take the form (3.1.14), and the variances and covariance, respectively, are given in (3.1.15), (3.1.16), and (3.1.17). It should be noted that the random variables μ and R_1 are independent, depending on parameters (ρ_1, ρ_2) and (ξ_1, ξ_2), respectively, which are derived by fitting distributions to given data. However, μ_1 and μ_2 are dependent variables as they both require (μ, R_1) to be defined. Explicit derivations of the probability distributions for the random parameters when stochastic isotropic hyperelastic models are calibrated to experimental data are presented in [129, 196].

The overall aim in this section is to analyse the radially symmetric finite deformations of a sphere of stochastic hyperelastic material defined by (3.1.2), under tension, when subject to prescribed surface dead loads applied uniformly in the radial direction. The stochastic sphere can be regarded as an ensemble, or population, of spheres, where each sphere has the same initial radius and is made from a homogeneous isotropic incompressible hyperelastic material, with the elastic parameters not known with certainty, but drawn from known probability distributions. The finite elasticity theory then applies for every hyperelastic sphere. For the stochastic hyperelastic body, the question is: *what is the probability distribution of stable radially symmetric deformation under a given surface dead load?*

5.3.2 Incompressible spheres

We begin by exploring the problem of a sphere of stochastic hyperelastic material, described by the strain energy function (3.1.2), subject to a radially symmetric deformation, caused by the sole action of a given radial tensile dead load. As in [19], conditions on the constitutive law, such that, setting the internal pressure equal to zero, where the radius tends to zero, the required external dead load is finite, and therefore cavitation occurs, are obtained. Further, the stability of the cavitated solution is analysed, and thus we distinguish between supercritical cavitation, where the cavity radius monotonically increases as the dead load increases, and subcritical (snap) cavitation, with a sudden jump to a finite internal radius immediately after initiation. Up to now, in the deterministic elastic case, the onset of snap cavitation in a homogenous isotropic sphere has not been discussed.

For the stochastic sphere, the radially symmetric deformation takes the form

$$r = g(R), \qquad \theta = \Theta, \qquad \phi = \Phi, \tag{5.3.1}$$

where (R, Θ, Φ) and (r, θ, ϕ) are the spherical polar coordinates in the reference and current configurations, respectively, such that $0 \leq R \leq B$, and $g(R) \geq 0$ is to be determined. A demonstration of the effect of cavitation on a spherical shell is given in Figure 5.20.

The corresponding deformation gradient is $\mathbf{F} = \text{diag} \, (\lambda_1, \lambda_2, \lambda_3)$, with

$$\lambda_1 = \frac{\mathrm{d}g(R)}{\mathrm{d}R} = \lambda^{-2}, \qquad \lambda_2 = \lambda_3 = \frac{g(R)}{R} = \lambda, \tag{5.3.2}$$

where λ_1 and $\lambda_2 = \lambda_3$ are the radial and hoop stretches, respectively, and dg/dR denotes the derivative of g with respect to R. By (5.3.2),

$$g^2 \frac{\mathrm{d}g}{\mathrm{d}R} = R^2. \tag{5.3.3}$$
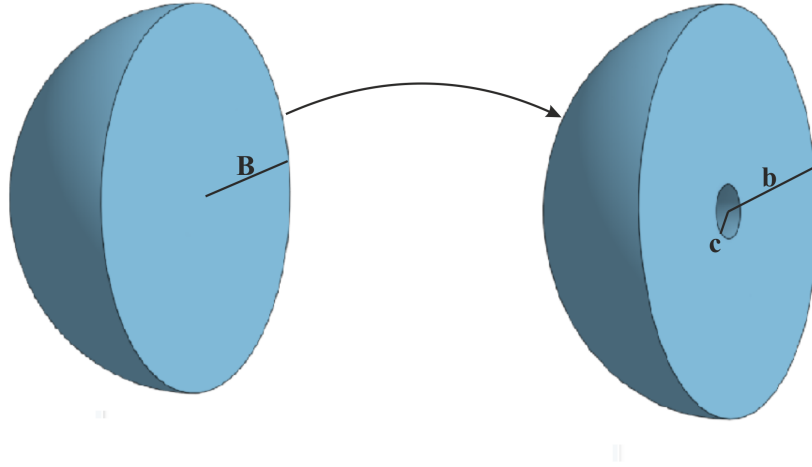
Figure 5.20: Schematic of cross-section of a sphere, showing the reference state, with outer radius B (left), and the deformed state, with cavity radius c and outer radius b (right), respectively.

Rewriting (5.3.3) yields

$$\frac{1}{3}(g^3)' = R^2, \tag{5.3.4}$$

which can then be rearranged and integrated to give

$$g(R) = (R^3 + c^3)^{\frac{1}{3}}, \tag{5.3.5}$$

where $c \geq 0$ is some constant to be determined. If $c > 0$, then $g(R) \to c > 0$ as $R \to 0_+$, and a spherical cavity of radius c forms at the centre of the sphere, from zero initial radius (see Figure 5.20). Otherwise, the sphere remains undeformed.

Assuming that the deformation (5.3.1) is due to a prescribed uniform radial tensile dead-load applied uniformly on the surface of the sphere, in the reference configuration, in the absence of body forces, the radial equation of equilibrium is given by

$$\frac{dP_{11}}{dR} + \frac{2}{R}(P_{11} - P_{22}) = 0, \tag{5.3.6}$$

or equivalently, by the chain rule, and using (5.3.2)

$$\frac{\mathrm{d}P_{11}}{\mathrm{d}\lambda}\frac{\lambda}{\mathrm{d}R} + 2\frac{P_{11} - P_{22}}{R} = \frac{\mathrm{d}P_{11}}{\mathrm{d}\lambda}\left(\frac{\mathrm{d}g(R)}{\mathrm{d}R} - \frac{g(R)}{R}\right) + 2(P_{11} - P_{22})$$

$$= \frac{\mathrm{d}P_{11}}{\mathrm{d}\lambda}(\lambda^{-2} - \lambda) + 2(P_{11} - P_{22})$$

$$= 0$$

i.e.

$$\frac{\mathrm{d}P_{11}}{\mathrm{d}\lambda}\lambda^{-2} + 2\frac{P_{11} - P_{22}}{1 - \lambda^3} = 0, \tag{5.3.7}$$

where $\mathbf{P} = (P_{ij})_{i,j=1,2,3}$ is the first Piola-Kirchhoff stress tensor. By (5.2.61), with $\lambda = r/R = g(R)/R = (1 + c^3/R^3)^{1/3} > 1$, we have

$$W(\lambda) = \frac{\mu_1}{2m^2}(\lambda^{-4m} + 2\lambda^{2m} - 3) + \frac{\mu_2}{2n^2}(\lambda^{-4n} + 2\lambda^{2n} - 3), \tag{5.3.8}$$

and so

$$\frac{\mathrm{d}W}{\mathrm{d}\lambda} = 2\left(\frac{\mu_1}{m}\lambda^{2m-1} + \frac{\mu_2}{n}\lambda^{2n-1}\right) - 2\left(\frac{\mu_1}{m}\lambda^{-(4m+1)} + \frac{\mu_2}{n}\lambda^{-(4n+1)}\right). \tag{5.3.9}$$

For an incompressible material,

$$P_{11} = \frac{\partial \mathcal{W}}{\partial \lambda_1} - \frac{p}{\lambda_1}, \qquad P_{22} = \frac{\partial \mathcal{W}}{\partial \lambda_2} - \frac{p}{\lambda_2}, \tag{5.3.10}$$

and so

$$\frac{\mathrm{d}W}{\mathrm{d}\lambda} = -\frac{2}{\lambda^3}\left[\frac{\partial \mathcal{W}}{\partial \lambda_1} - \frac{p}{\lambda_1}\right] + 2\left[\frac{\partial \mathcal{W}}{\partial \lambda_2} - \frac{p}{\lambda_2}\right]$$

$$= -\frac{2}{\lambda^3}\frac{\partial \mathcal{W}}{\partial \lambda_1} + \frac{2p}{\lambda^3\lambda^{-2}} + 2\frac{\partial \mathcal{W}}{\partial \lambda_2} - \frac{2p}{\lambda} \tag{5.3.11}$$

$$= -\frac{2}{\lambda^3}\frac{\partial \mathcal{W}}{\partial \lambda_1} + 2\frac{\partial \mathcal{W}}{\partial \lambda_2}.$$

Hence

$$\frac{\mathrm{d}W}{\mathrm{d}\lambda} = -\frac{2P_{11}}{\lambda^3} + 2P_{22}, \tag{5.3.12}$$

where $P_{11} = \partial \mathcal{W}/\partial \lambda_1$ and $P_{22} = \partial \mathcal{W}/\partial \lambda_2$. Next, setting the internal pressure (at

$R \to 0_+$) equal to zero, by (5.3.7) and (5.3.12), the external tension (at $R = B$) is equal to

$$T = \frac{P_{11}}{\lambda^2}\Big|_{\lambda=\lambda_b} = \int_{\lambda_b}^{\lambda_c} \frac{\mathrm{d}W}{\mathrm{d}\lambda} \frac{\mathrm{d}\lambda}{\lambda^3 - 1}, \tag{5.3.13}$$

and the applied dead load, in the reference configuration, is

$$P = T\lambda_b^2 = \lambda_b^2 \int_{\lambda_b}^{\lambda_c} \frac{\mathrm{d}W}{\mathrm{d}\lambda} \frac{\mathrm{d}\lambda}{\lambda^3 - 1}, \tag{5.3.14}$$

where λ_c and λ_b represent the stretches at the centre and outer surface, respectively. The value of the required dead load, P_0, for the onset of cavitation, or in other words, for a bifurcation from the reference state, is obtained by taking $\lambda_c \to \infty$ and $\lambda_b = (1 + c^3/B^3)^{1/3} \to 1$ as $c \to 0_+$, so

$$P_0 = \int_1^\infty \frac{\mathrm{d}W}{\mathrm{d}\lambda} \frac{\mathrm{d}\lambda}{\lambda^3 - 1}. \tag{5.3.15}$$

The BE inequalities (3.1.3) imply

$$\frac{\mathrm{d}W}{\mathrm{d}\lambda} \frac{1}{\lambda^3 - 1} > 0, \tag{5.3.16}$$

and hence $P_0 > 0$. If the critical dead load, given by (5.3.15), is finite, then cavitation takes place, else, the sphere remains undeformed.

We now revisit briefly the deterministic elastic case, before extending to consider the same problem in a stochastic setting.

5.3.3 Deterministic elastic spheres

In the deterministic elastic case, for a spherical shell of hyperelastic material described by the strain-energy function (3.1.2), the function (5.2.61) takes the form

$$W(\lambda) = \frac{\mu_1}{2m^2}(\lambda^{-4m} + 2\lambda^{2m} - 3) + \frac{\mu_2}{2n^2}(\lambda^{-4n} + 2\lambda^{2n} - 3), \tag{5.3.17}$$

which then yields

$$\frac{\mathrm{d}W}{\mathrm{d}\lambda} = \frac{2\mu_1}{m}(\lambda^{2m-1} - \lambda^{-4m-1}) + \frac{2\mu_2}{n}(\lambda^{2n-1} - \lambda^{-4n-1}), \tag{5.3.18}$$

after differentiation with respect to λ. For the onset of cavitation, the critical dead load defined by (5.3.13) is equal to

$$P_0 = \frac{2\mu_1}{m}\int_{\lambda_b}^{\lambda_c} \frac{\lambda^{2m-1} - \lambda^{-4m-1}}{\lambda^3 - 1}\mathrm{d}\lambda + \frac{2\mu_2}{n}\int_{\lambda_b}^{\lambda_c} \frac{\lambda^{2n-1} - \lambda^{-4n-1}}{\lambda^3 - 1}\mathrm{d}\lambda. \tag{5.3.19}$$

Introducing the change of variables $x = \lambda^3 - 1$, (5.3.19) becomes

$$\begin{aligned}
P_0 ={}& \frac{2\mu_1}{m}\int_{(x_b+1)^{1/3}}^{(x_c+1)^{1/3}} \frac{(x+1)^{\frac{2m-1}{3}} - (x+1)^{-\frac{(4m+1)}{3}}}{x}\frac{1}{3}(x+1)^{-\frac{2}{3}}\mathrm{d}x + \\
&+ \frac{2\mu_2}{n}\int_{(x_b+1)^{1/3}}^{(x_c+1)^{1/3}} \frac{(x+1)^{\frac{2n-1}{3}} - (x+1)^{-\frac{(4n+1)}{3}}}{x}\frac{1}{3}(x+1)^{-\frac{2}{3}}\mathrm{d}x,
\end{aligned} \tag{5.3.20}$$

which, after simplification, yields the expression

$$\begin{aligned}
P_0 ={}& \frac{2\mu_1}{3m}\int_0^\infty \frac{(x+1)^{\frac{2m-3}{3}} - (x+1)^{-\frac{(4m+3)}{3}}}{x}\mathrm{d}x + \\
&+ \frac{2\mu_2}{3n}\int_0^\infty \frac{(x+1)^{\frac{2n-3}{3}} - (x+1)^{-\frac{(4n+3)}{3}}}{x}\mathrm{d}x,
\end{aligned} \tag{5.3.21}$$

where $x_c = \lambda_c^3 - 1 \to \infty$ and $x_b = \lambda_b^3 - 1 \to 0$. By (5.3.21), P_0 is finite, and hence a spherical cavity forms if and only if the following conditions are simultaneously satisfied:

$$2m - 3 < 0, \qquad -4m - 3 < 0, \qquad 2n - 3 < 0, \qquad -4n - 3 < 0, \tag{5.3.22}$$

or equivalently [41, 88] (see also Example 5.1 of [19]), if and only if

$$-3/4 < m, n < 3/2. \tag{5.3.23}$$

In particular, cavitation is found in a neo-Hookean sphere (with $m = 1$ and $n = 0$), but not in a Mooney-Rivlin sphere (with $m = 1$ and $n = -1$). The special cases where $m \in \{-1/2, 1\}$ and $n = 0$ are given as examples in [19], and when $m \in \{1/2, 3/4, 1, 5/4\}$ and $n = 0$, the explicit critical loads are presented in [41]. When these bounds and the BE inequalities (3.1.1) are satisfied, the critical pressure P_0 is finite and the problem is to find the behaviour of the cavity in a neighbourhood of this critical value. In each of those previously studied cases (see, for example, Figure 2 of [41]), cavitation forms from zero radius and then presents itself as a supercritical bifurcation with stable cavitation. In other words, the new bifurcated solution exists locally for values of $P > P_0$, and the radius of the cavity monotonically increase with the applied load post-bifurcation.

Another theoretical possibility is that the bifurcation could be subcritical, so the cavitated solution exists locally for values less than P_0 and is unstable. A snap cavitation, with a sudden jump to a cavitated solution with a finite radius, would then be expected to occur. Here, it will be shown that, depending on the model parameters, the family of materials (5.3.2) can exhibit both behaviours.

As an example, the variety of behaviours with the case $m = 1$ and $n = -1/2$, for which (5.3.17) takes the form

$$W(\lambda) = \frac{\mu_1}{2} \left(\lambda^{-4} + 2\lambda^2 - 3 \right) + 2\mu_2 \left(\lambda^2 + 2\lambda^{-1} - 3 \right), \qquad (5.3.24)$$

will be illustrated. In this case, under the deformation (5.3.1), the BE inequalities (3.1.3) are reduced to

$$\mu_1 + 2\mu_2 \frac{\lambda^3}{1 + \lambda^3} > 0. \qquad (5.3.25)$$

In particular, when $\lambda \to 1$, (5.3.25) implies that the random shear modulus is positive, i.e. $\mu = \mu_1 + \mu_2 > 0$, while if $\lambda \to \infty$, then $\mu_1 + 2\mu_2 > 0$. The function of λ on the left-hand side of (5.3.25) is monotonically increasing when μ_2 is positive, and decreasing if μ_2 is negative. Taking $\mu_1 > 0$, the two limits imply that the BE

inequalities are satisfied for all values λ if

$$0 < \frac{\mu_1}{\mu} < 2. \tag{5.3.26}$$

For sufficiently small c/B, the corresponding dead-load traction, defined by (5.3.14), is equal to

$$
\begin{aligned}
P &= \left(1 + \frac{c^3}{B^3}\right)^{2/3} \int_{(1+c^3/B^3)^{1/3}}^{\infty} \frac{\mathrm{d}W}{\mathrm{d}\lambda} \frac{\mathrm{d}\lambda}{\lambda^3 - 1} \\
&= 2\mu_1 \left[\left(1 + \frac{c^3}{B^3}\right)^{1/3} + \frac{1}{4}\left(1 + \frac{c^3}{B^3}\right)^{-2/3}\right] + 4\mu_2\left(1 + \frac{c^3}{B^3}\right)^{1/3} \\
&= 4\mu\left(1 + \frac{c^3}{B^3}\right)^{1/3} - 2\mu_1\left[\left(1 + \frac{c^3}{B^3}\right)^{1/3} - \frac{1}{4}\left(1 + \frac{c^3}{B^3}\right)^{-2/3}\right],
\end{aligned}
\tag{5.3.27}
$$

where the last expression was obtained by taking into account relation (3.1.8). Letting $c \to 0_+$ in (5.3.27), the critical tensile dead load (5.3.15) takes the form

$$P_0 = 4\mu - \frac{3\mu_1}{2}. \tag{5.3.28}$$

As P_0 is positive in (5.3.28), we have

$$0 < \frac{\mu_1}{\mu} < \frac{8}{3}, \tag{5.3.29}$$

which is guaranteed by (5.3.26).

The problem to be addressed now is to find the possible behaviour of the cavity opening c as a function of P in a neighbourhood of P_0. On differentiating (5.3.27) with respect to c/B, we obtain

$$\frac{\mathrm{d}P}{\mathrm{d}(c/B)} = 2\frac{c^2}{B^2}\left\{2\mu\left(1 + \frac{c^3}{B^3}\right)^{-2/3} - \mu_1\left[\left(1 + \frac{c^3}{B^3}\right)^{-2/3} + \frac{1}{2}\left(1 + \frac{c^3}{B^3}\right)^{-5/3}\right]\right\}. \tag{5.3.30}$$
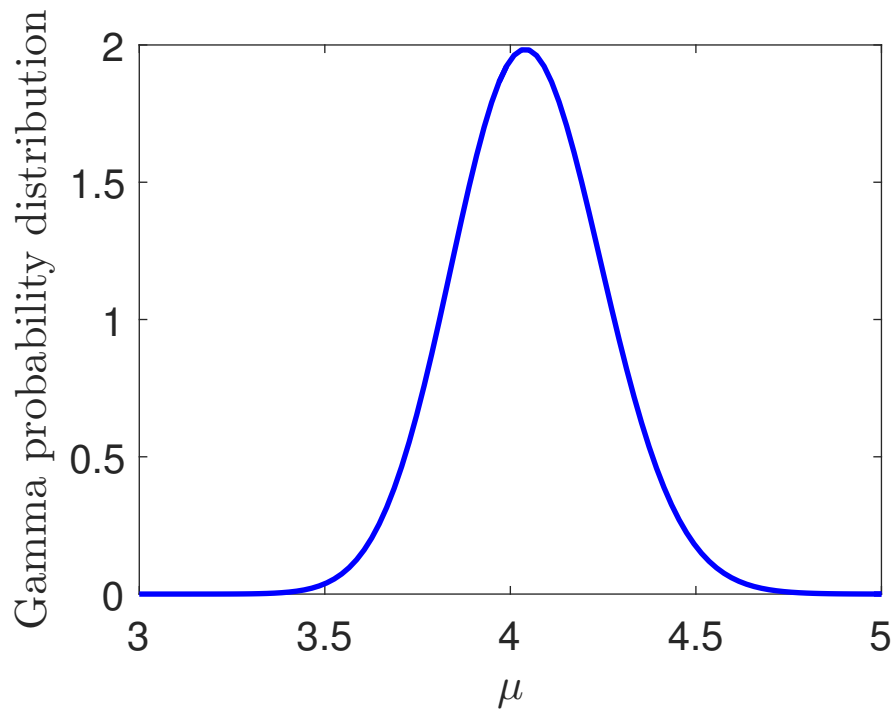
Figure 5.21: Gamma distribution (3.1.6), with $\rho_1 = 405$, $\rho_2 = 0.01$, for the random shear modulus, $\mu > 0$.
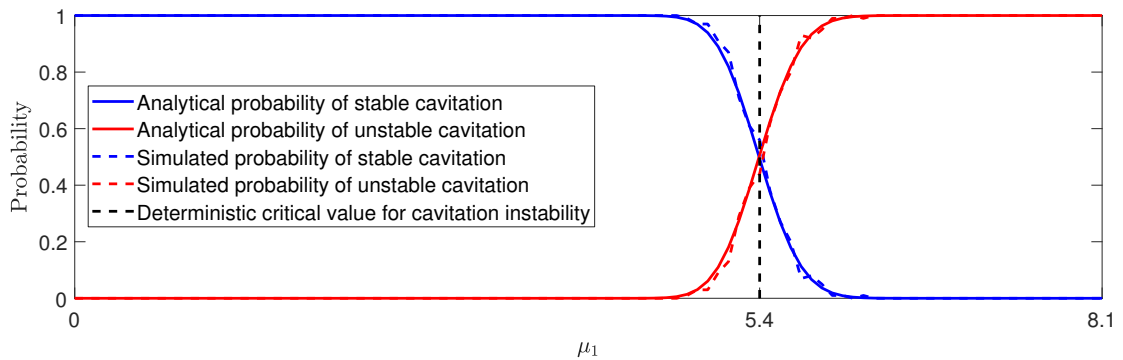
Figure 5.22: Probability distributions of whether cavitation can occur or not in a sphere of stochastic material, described by (3.1.2) with $m = 1$ and $n = -1/2$, and the shear modulus, μ, following a Gamma distribution (3.1.6) with $\rho_1 = 405$, $\rho_2 = 0.01$. Continuous coloured lines represent analytically derived solutions, given by equations (5.3.34) and (5.3.35), and the dashed versions represent stochastically generated data. The vertical line at the critical value, $5.4 = 4\underline{\mu}/3$, separates the expected regions based only on the mean value of the shear modulus, $\underline{\mu} = \rho_1 \rho_2 = 4.05$.

Hence, by Proposition E.0.1 given in Appendix E (with $n = 3$), when

$$\frac{\mu_1}{\mu} < \frac{4}{3} = \inf_{0 < c/B < 1} \left[2 \left(1 + \frac{c^3}{B^3} \right) \left(\frac{3}{2} + \frac{c^3}{B^3} \right)^{-1} \right], \qquad (5.3.31)$$

where "inf" denotes infimum, the bifurcation is supercritical and the radius of the cavity monotonically increases as the tensile dead load increases. However, if there exists $c_0 > 0$, such that

$$2 \left(1 + \frac{c_0^3}{B^3} \right) \left(\frac{3}{2} + \frac{c_0^3}{B^3} \right)^{-1} < \frac{\mu_1}{\mu} < 2, \qquad (5.3.32)$$

then the bifurcation is subcritical, and the required applied load starts to decrease at $c = c_0$, where there is a sudden jump in the opening of the cavity. In particular, if (5.3.32) holds for $c_0 = 0$, so

$$\frac{4}{3} < \frac{\mu_1}{\mu} < 2, \qquad (5.3.33)$$

then (5.3.29) is valid and the cavitation becomes unstable.

Thus, $\mathrm{d}P/\mathrm{d}(c/B) \to 0$ as $c \to 0_+$, and, as in [131], the bifurcation at the critical load P_0 is supercritical (respectively, subcritical) if $\mathrm{d}P/\mathrm{d}(c/B) > 0$ (respectively, $\mathrm{d}P/\mathrm{d}(c/B) < 0$) for arbitrary small c/B. Examples of both of these behaviours are illustrated in Figures 5.23 and 5.24.
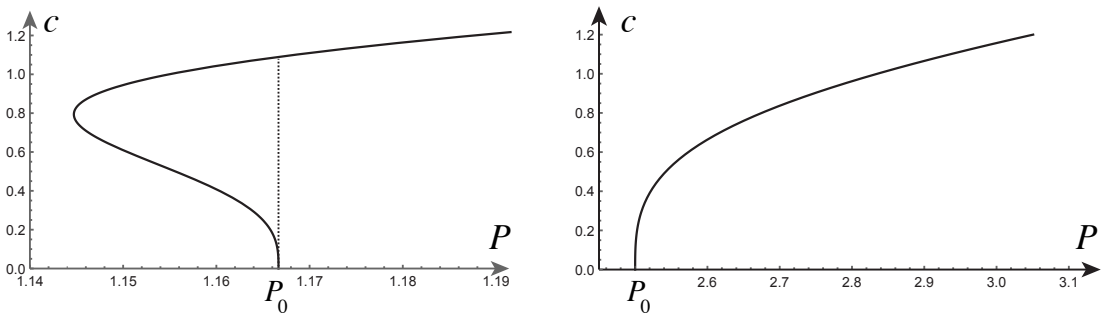
Figure 5.23: Subcritical (left) and supercritical (right) cavitation found in a unit sphere (with $B = 1$) of material model (5.3.17) with $\mu_1 = 1$ and either $\mu = 2/3$ (left) or $\mu = 1$ (right). The dashed line indicates the snap cavitation expected at the bifurcation, leading to a sudden increase of the cavity size in the subcritical case.
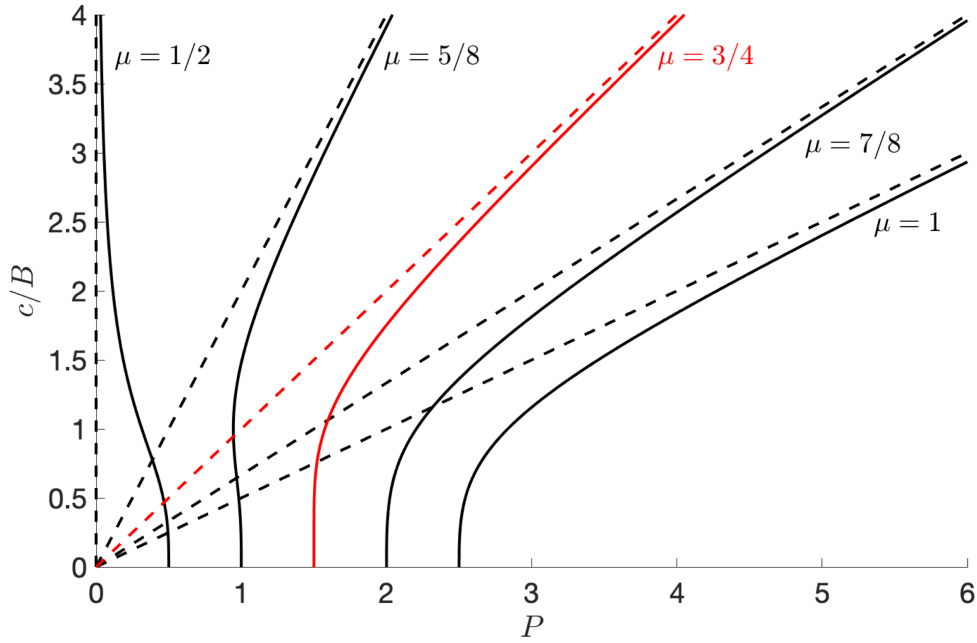
Figure 5.24: Change of behaviour under various parameter values found in a unit sphere (with $B = 1$) of material model (5.3.17) with $\mu_1 = 1$. Note the critical case at $\mu = 3/4$. The dashed line indicates the asymptotic behaviour for large values of P and is given by $P = (4\mu - 2\mu_1)c/B$.

5.3.4 Stochastic elastic spheres

Our attention now is turned to the stochastic case, with the stochastic model described by (3.1.2), with $m = 1$ and $n = -1/2$, and the other model parameters drawn from probability distributions. In this case, recalling that μ follows a Gamma distribution, $g(u; \rho_1, \rho_2)$, defined by (3.1.6), the probability distribution of stable cavitation is equal to

$$P_1\left(\mu > \frac{3\mu_1}{4}\right) = 1 - \int_0^{3\mu_1/4} g(u; \rho_1, \rho_2)\mathrm{d}u, \qquad (5.3.34)$$

and that of unstable cavitation is

$$P_2\left(\mu < \frac{3\mu_1}{4}\right) = \int_0^{3\mu_1/4} g(u; \rho_1, \rho_2)\mathrm{d}u. \qquad (5.3.35)$$

For condition (5.3.33) to be satisfied in mean value, we choose

$$\frac{4}{3} < \underline{R}_1 < 2, \tag{5.3.36}$$

where $R_1 = \mu_1/\mu$.

Taking, for example, $\rho_1 = 405$ and $\rho_2 = 0.01$ (see Figure 5.21), the mean value of the shear modulus is $\underline{\mu} = \rho_1\rho_2 = 4.05$, and the probability distributions given by (5.3.34) and (5.3.35) are illustrated numerically in Figure 5.22 (blue lines for P_1 and red lines for P_2). In this case, if $\underline{\mu}_1 = 5 < 5.4 = 4\underline{\mu}/3$, then stable cavitation is expected, but there is also about a 10% chance that unstable snap cavitation occurs. Similarly, when $4\underline{\mu}/3 = 5.4 < \underline{\mu}_1 = 5.8 < 8.1 = 2\underline{\mu}$, unstable cavitation is expected, but there is also about a 10% chance that the cavitation is stable. Stable and unstable cavitation of a stochastic sphere are illustrated numerically in Figure 5.25. Specifically:

a) In Figure 5.25A, $b = 0$ in (3.1.8), and the random variable $R_1 = \mu_1/\mu$ is drawn from a Beta distribution with $\xi_1 = 287$ and $\xi_2 = 36$. In this case, $\underline{\mu}_1 = 3.6 < 5.4 = 4\underline{\mu}/3$, and stable cavitation, with supercritical bifurcation after the spherical cavity opens, is expected.

b) In Figure 5.25B, $b = -3$ in (3.1.8), and the random variable $R_1 = (\mu_1 + 3)/(\mu + 6)$ draws its values from a Beta distribution with $\xi_1 = 325$ and $\xi_2 = 10$. Thus, $\underline{\mu}_1 = 6.75 > 5.4 = 4\underline{\mu}/3$, and unstable cavitation, with subcritical bifurcation after the spherical cavity forms, is expected.

For the numerical examples shown in Figure 5.25, the critical dead load is $P_0 = 4\mu - 3\mu_1/2$, as given by (5.3.28), with μ and μ_1 following probability distributions. In each case, the expectation is that the onset of cavitation occurs at the mean value $\underline{P}_0 = 4\underline{\mu} - 3\underline{\mu}_1/2$, found at the intersection of the dashed black line with the horizontal axis. However, there is a chance that a cavity can form under smaller or greater critical loads than the expected load value, as shown by the coloured

interval about the mean value along the horizontal axis.

To briefly reiterate, in this section, for a stochastic elastic sphere under uniform tensile dead load, the probabilities of stable or unstable cavitation are obtained, given that the material parameters are generated from known probability density functions. In the deterministic elastic case, there is a critical parameter value that strictly separates the cases where either stable or unstable cavitation occurs. By contrast, in the stochastic case, there is a probabilistic interval, containing the deterministic critical value, where there is always a competition between the stable and unstable states in the sense that both have a quantifiable chance to be found. For the onset of cavitation, there is also a probabilistic interval where a cavity may form, with a given probability, under smaller or greater loads than the expected critical value.

5.4   Summary

In this chapter, the likely deformations and instabilities of stochastic hyperelastic bodies were discussed. Firstly, in Section 5.1, an in-depth analysis into the occurrence of a necking instability in materials modelled by four different strain-energy functions was presented. The conditions under which necking occurs for a particular material were outlined, followed by a deterministic analysis, which allows a critical point to be established. A stochastic analysis is then imparted, in which the stability of points within an interval surrounding the deterministic critical value is analysed, allowing the determination of the probability of necking occurring at points within this interval, leading to an enhanced representation of the occurrence of a necking instability for each respective material model.

For hyperelastic spheres and circular cylinders under symmetric finite inflation, it has been demonstrated in Section 5.2 that, when material parameters are random variables, there is always competition between monotonic expansion and limit-point instability. Specifically, in contrast to the deterministic elastic prob-

A

B
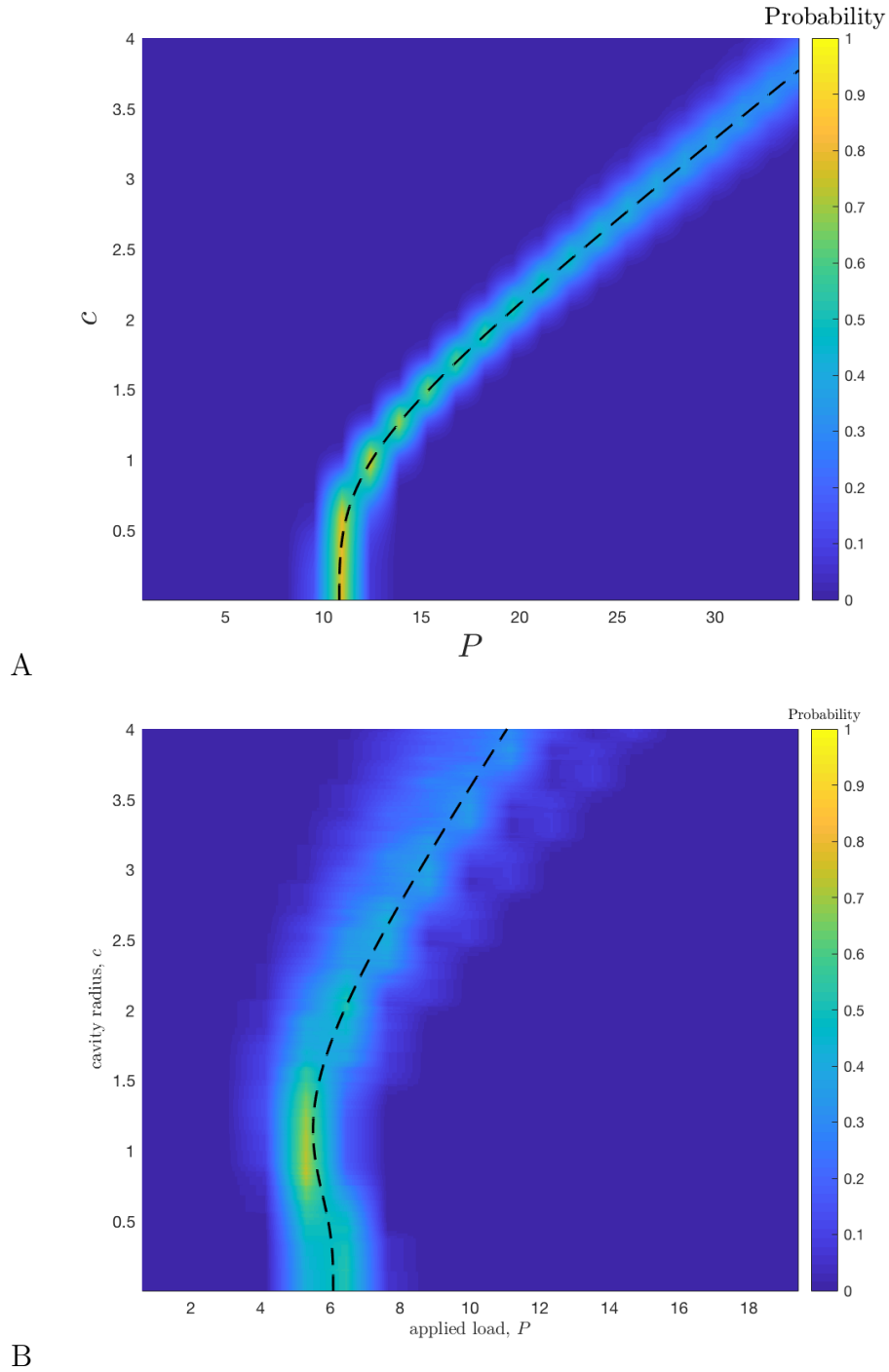
Figure 5.25: Probability distribution of the applied load, P, producing cavitation of radius c in a unit sphere ($B = 1$) of stochastic material, described by (3.1.2) with $m = 1$ and $n = -1/2$, when μ follows a Gamma distribution (3.1.6) with $\rho_1 = 405$, $\rho_2 = 0.01$, and: (A) $R_1 = \mu_1/\mu$ follows a Beta distribution (3.1.12) with $\xi_1 = 287$, $\xi_2 = 36$. As $\underline{\mu}_1 = 3.6 < 5.4 = 4\mu/3$, stable cavitation is expected; (B) $R_1 = (\mu_1 + 3)/(\mu + 6)$ follows a Beta distribution (3.1.12) with $\xi_1 = 325$, $\xi_2 = 10$. As $\underline{\mu}_1 = 6.75 > 5.4 = 4\mu/3$, instability is expected during cavitation. The dashed black lines correspond to the expected bifurcation based only on mean parameter values.

lem where there is a critical value that strictly separates the cases where either the radially symmetric inflation is stable or a limit-point instability occurs, for the stochastic problem, there are probabilistic intervals for the model parameters, where there is a quantifiable chance for both the stable and unstable states to be found. This approach was then applied in the context of the cavitation of spheres in Section 5.3.

For homogeneous isotropic incompressible spheres of stochastic hyperelastic material, subject to radially symmetric surface dead loads, the possible homogeneous deformations were examined in Section 5.3. It was then determined which of these deformations are stable. Here, it was demonstrated that a sudden jump in the cavity opening, causing unstable snap cavitation, at the critical dead load, can also occur in a homogeneous isotropic incompressible sphere, provided that the material satisfies the Baker-Ericksen inequalities. If such a material could be found, a sphere made of this material would suddenly increase its volume at a critical load and show some form of hysteresis as the load is removed. In the stochastic case, the probabilistic nature of the solution reflects the probability in the constitutive law, and bifurcation and stability can be quantified in terms of probabilities. In contrast to the deterministic elastic problem, where critical parameter values strictly separate the cases where either stable or unstable cavitation occurs, for the stochastic problem, probabilistic intervals where both states have a quantifiable chance to exist were obtained, analogous to the results obtained in Section 5.2 for the inflation of spherical shells and cylindrical tubes. For the onset of cavitation, there is a probabilistic interval where the cavity may form, with a given probability, under smaller or greater loads than the expected critical value.

The stochastic approach that has been considered and applied to various deformations and instabilities in this chapter can be applied to a class of stochastic hyperelastic models, enhancing further the understanding of the likelihood that the deformations and instabilities in question take place, and the conditions under

which they occur. The approach used in Section 5.2 in the analysis of the inflation of spheres and cylinders has many practical applications. With the stochastic approach outlined here, a greater appreciation of the likelihood of deformations and instabilities occuring is gained, thus improving knowledge of biological structures and commercial vehicles, which could be mathematically modelled in this way. This, in turn, could lead to an increase in the safety and performance of the vehicles in question, or an enhancement in medical research in terms of treating disease.

Chapter 6

Likely quasi-equilibrated motion of stochastic hyperelastic solids

Motivated by numerous long-standing and modern engineering problems, oscillatory motions of cylindrical and spherical shells made of linear elastic material have generated a wide range of experimental, theoretical, and computational studies [6–8,31,50], whereas time-dependent finite oscillations of cylindrical tubes and spherical shells of nonlinear hyperelastic material, relevant to the modelling of physical responses in many biological and synthetic systems [3,10,47,79,81,83,110], have been less investigated.

In this section, the stochastic framework developed in Chapter 5, and also in [130, 132–134], is extended to study the dynamic problems of shear motions of stochastic hyperelastic cuboids, and the radial oscillations of cylindrical and spherical shells of stochastic incompressible isotropic hyperelastic material formulated as quasi-equilibrated motions, building directly on the stochastic theory presented in Sections 5.2 and 5.3. For these motions, the system is in equilibrium at every time instant. Finite shear motions of a stochastic hyperelastic cuboid, which are not quasi-equilibrated, under dynamic generalised shear are considered in Section 6.1, to bridge the gap between the investigation of static deformations in Chapter 5 and the dynamic problems considered here. It is found that, for hyperelastic bodies

of stochastic neo-Hookean material, the amplitude and period of the oscillations follow probability distributions that can be fully characterised. This is followed, in Sections 6.2 and 6.3, by an investigation into the radial oscillatory motions of stochastic cylindrical tubes and spherical shells with bounded wall thickness, respectively. The dynamic evolution of these elastic systems, which exhibit inherent uncertainties due to the material properties, is referred to here as "likely oscillatory motions". A summary of the quasi-equilibrated motion prerequisites which will be relied upon for the following analysis is presented in Section 2.2.

The limiting cases of thin- and infinitely thick-walled structures are also discussed. Some less straight-forward calculations essential for these problems are deferred to Appendix F. Ultimately, it is determined that the amplitude and period of the oscillation of these stochastic bodies are characterised by probability distributions. Specifically, for the cylindrical and spherical shells, when an impulse surface traction was applied, a parameter interval where both the oscillatory and non-oscillatory motions can occur with a given probability was observed, in a complete contrast to the deterministic case, in which a single critical parameter value separates the cases in which oscillations can or cannot occur. Concluding remarks are then drawn in Section 6.4.

6.1 Generalised shear motion of a stochastic hyperelastic cuboid

We begin by considering a stochastic hyperelastic cuboid subject to dynamic generalised shear, before the specific case of a cuboid made of a stochastic neo-Hookean material is investigated.

6.1.1 Dynamic generalised shear

The generalised shear motion of an elastic body is described by [47]

$$x = \frac{X}{\sqrt{\alpha}}, \qquad y = \frac{Y}{\sqrt{\alpha}}, \qquad z = \alpha Z + u\left(X, Y, t\right), \qquad (6.1.1)$$

where (X, Y, Z) and (x, y, z) are the Cartesian coordinates for the reference and current configuration, respectively, $\alpha > 0$ is a given constant, and $u = z - \alpha Z$, representing the displacement in the third direction, is a time-dependent function to be determined. It is assumed here that the edges of the cuboid are aligned with the directions of the Cartesian axes in the undeformed state (see Figure 6.1).
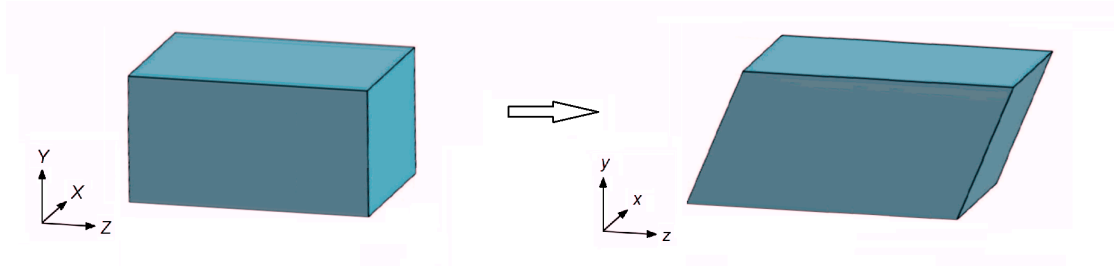
Figure 6.1: Schematic of generalised shear of a cuboid, showing the reference state (left) and the deformed state (right), respectively.

By the governing equations (6.1.1), the condition (2.2.4) is valid for $\boldsymbol{x} = (x, y, z)^T$ if and only if

$$\mathbf{0} = \operatorname{curl} \ddot{\boldsymbol{x}} = \begin{bmatrix} \partial\ddot{z}/\partial y - \partial\ddot{y}/\partial z \\ \partial\ddot{x}/\partial z - \partial\ddot{z}/\partial x \\ \partial\ddot{y}/\partial x - \partial\ddot{x}/\partial y \end{bmatrix} = \begin{bmatrix} \partial\ddot{u}/\partial Y \\ -\partial\ddot{u}/\partial X \\ 0 \end{bmatrix}. \qquad (6.1.2)$$

This condition imposes very strict constraints on the motion. However, even though the generalised shear motion (6.1.1) is not quasi-equilibrated, exact solutions are still available, although these solutions are not universal [143, 214].

For the deformation (6.1.1), the gradient tensor (2.1.1) is equal to

$$\mathbf{F} = \begin{bmatrix} 1/\sqrt{\alpha} & 0 & 0 \\ 0 & 1/\sqrt{\alpha} & 0 \\ u_X & u_Y & \alpha \end{bmatrix}, \tag{6.1.3}$$

where u_X and u_Y denote the partial first derivatives of u with respect to X and Y, respectively. The corresponding left Cauchy-Green tensor is

$$\mathbf{B} = \begin{bmatrix} 1/\alpha & 0 & u_X/\sqrt{\alpha} \\ 0 & 1/\alpha & u_Y/\sqrt{\alpha} \\ u_X/\sqrt{\alpha} & u_Y/\sqrt{\alpha} & u_X^2 + u_Y^2 + \alpha^2 \end{bmatrix}, \tag{6.1.4}$$

and, in this case, the principal invariants (2.1.6) are

$$I_1 = u_X^2 + u_Y^2 + \frac{2}{\alpha} + \alpha^2,$$
$$I_2 = \frac{u_X^2}{\alpha} + \frac{u_Y^2}{\alpha} + \frac{1}{\alpha^2} + 2\alpha, \tag{6.1.5}$$
$$I_3 = 1.$$

The associated Cauchy stress tensor takes the form (2.1.8) [73, pp. 87-91], where p is the Lagrange multiplier for the incompressibility constraint ($I_3 = 1$), and

$$\beta_1 = 2\frac{\partial W}{\partial I_1}, \qquad \beta_{-1} = -2\frac{\partial W}{\partial I_2} \tag{6.1.6}$$

are the nonlinear material parameters, with I_1, I_2 given in (6.1.5).

6.1.2 Shear oscillations of a cuboid of stochastic neo-Hookean material

The case of a cuboid of stochastic neo-Hookean material is now presented, with $\mu_1 = \mu > 0$ and $\mu_2 = 0$ in (3.1.2) (where $m = 1$ and $n = 1$), where the non-zero

components of the Cauchy stress tensor (2.1.8) are as follows;

$$\sigma_{xx} = \sigma_{yy} = -p + \frac{\mu}{\alpha},$$

$$\sigma_{zz} = -p + \mu \left(u_X^2 + u_Y^2 + \alpha^2 \right),$$

$$\sigma_{xz} = \frac{\mu}{\sqrt{\alpha}} u_X,$$

$$\sigma_{yz} = \frac{\mu}{\sqrt{\alpha}} u_Y.$$

(6.1.7)

The neo-Hookean model was chosen for use here because the results can be demonstrated explicitly. Then, by the equation of motion (2.2.1),

$$\frac{\partial p}{\partial x} = 0,$$

$$\frac{\partial p}{\partial y} = 0,$$

$$\frac{\partial p}{\partial z} = -\rho \ddot{u} + \mu \left(u_{XX} + u_{YY} \right),$$

(6.1.8)

where u_{XX} and u_{YY} represent the second derivatives of u with respect to X and Y, respectively. Hence, p is independent of x and y.

The undeformed cuboid is now considered to be long in the Z-direction, and an initial displacement $u_0(X, Y) = u(X, Y, 0)$ and velocity $\dot{u}_0(X, Y) = \dot{u}(X, Y, 0)$ are imposed. For the boundary condition, the following two cases are distinguished:

(i) If null normal Cauchy stresses, $\sigma_{xx} = \sigma_{yy} = 0$, are imposed on the faces perpendicular to the X- and Y-directions, at all time, then $p = \mu/\alpha$ is constant and $\sigma_{zz} = \mu \left(u_X^2 + u_Y^2 + \alpha^2 - 1/\alpha \right)$.

(ii) If $\sigma_{xx} = \sigma_{yy} \neq 0$, as σ_{zz} cannot be made point-wise zero, the normal force acting on the cross-sections of area A in the z-direction at time t is denoted by

$$N_z(t) = \int_A \sigma_{zz} \mathrm{d}A.$$

(6.1.9)

This force is considered to be zero, so $N_z(t) = 0$, at all times. Hence, p is independent of z, and, by (6.1.8), the conclusion that $p = p(t)$ can be made.

In both the above cases, (i) and (ii), respectively, by (6.1.8),

$$\ddot{u} = \frac{\mu}{\rho} \left(u_{XX} + u_{YY} \right). \tag{6.1.10}$$

The linear wave equation (6.1.10), describing the propagation of waves, will now be solved by standard procedures, subject to the given initial and boundary conditions. To solve this equation, the shear stresses σ_{xz} and σ_{yz} defined by (6.1.7) are allowed to vanish at the sides, i.e.

$$\sigma_{xz}(0, Y, Z, t) = \sigma_{xz}(1, Y, Z, t) = 0 \qquad \Longleftrightarrow \qquad u_X(0, Y, t) = u_X(1, Y, t) = 0,$$

$$\sigma_{yz}(X, 0, Z, t) = \sigma_{yz}(X, 1, Z, t) = 0 \qquad \Longleftrightarrow \qquad u_Y(X, 0, t) = u_Y(X, 1, t) = 0. \tag{6.1.11}$$

In this case, the general solution takes the form

$$u(X, Y, t) = \sum_{m=1}^{\infty} \sum_{n=1}^{\infty} \left[A_{mn} \cos \left(\omega_{mn} t \right) + B_{mn} \sin \left(\omega_{mn} t \right) \right] \cos \left(\pi m X \right) \cos \left(\pi n Y \right), \tag{6.1.12}$$

where

$$\omega_{mn} = \pi \sqrt{(m^2 + n^2) \frac{\mu}{\rho}}, \tag{6.1.13}$$

and

$$A_{mn} = 4 \int_0^1 \left[\int_0^1 u_0(X, Y) \cos \left(\pi m X \right) \mathrm{d}X \right] \cos \left(\pi n Y \right) \mathrm{d}Y, \tag{6.1.14}$$

$$B_{mn} = \frac{4}{\omega_{mn}} \int_0^1 \left[\int_0^1 \dot{u}_0(X, Y) \cos \left(\pi m X \right) \mathrm{d}X \right] \cos \left(\pi n Y \right) \mathrm{d}Y. \tag{6.1.15}$$

These oscillations under the generalised shear motion (6.1.1) cannot be completely 'free', due to the non-zero tractions corresponding to the cases (i) and (ii), respectively. The condition (6.1.2) is not satisfied here.

As μ is a random variable, it follows that the speed of wave propagation, $\sqrt{\mu/\rho}$, is stochastic. Hence, both the period and the amplitude of the oscillations are stochastic. As an example, the initial data $u_0(X, Y) = \cos(\pi X)\cos(\pi Y)$ and $\dot{u}_0(X, Y) = 0$, leading to $A_{11} = 1$ and $B_{11} = 0$, are considered. In Figure 6.2, the stochastic dynamic displacement on the edges $(X, Y, Z) \in \{(0, 0, Z), (1, 1, Z)\}$ is illustrated in the case when $m = n = 1$, $A_{11} = 1$, $B_{11} = 0$, $\rho = 1$, and μ is drawn from the Gamma distribution (3.1.6) with hyperparameters $\rho_1 = 405$ and $\rho_2 = 0.01$, as represented in Figure 5.21. The top plot of Figure 6.2 represents two single simulations, with two different values of μ drawn from the distribution, illustrating the variety of outcomes that can be obtained. The middle plot of Figure 6.2 then represents histograms of the ensemble data. Namely, since not all material parameters are equally likely, not all outcomes are equally likely. Specifically, the values of $u(0, 0, t)$ are most likely going to be near the mean value (dashed line) with the probability of observing alternative values of u decreasing as we tend away from the mean. From Figure 6.2, it can be noted that extremal probabilities always occur at the extreme displacement of the oscillations, or in other words, when the cuboid is slowest. This is to be expected. However, in between these probability maxima, the variance grows over time. Thus, although the displacements are initially close (seen explicitly in the top of Figure 6.2 and by the tight distribution around the mean in the bottom left of Figure 6.2), eventually, the phase difference dominates, causing the displacements to diverge (top of Figure 6.2), and an increase in the variance of the distribution (bottom right of Figure 6.2).
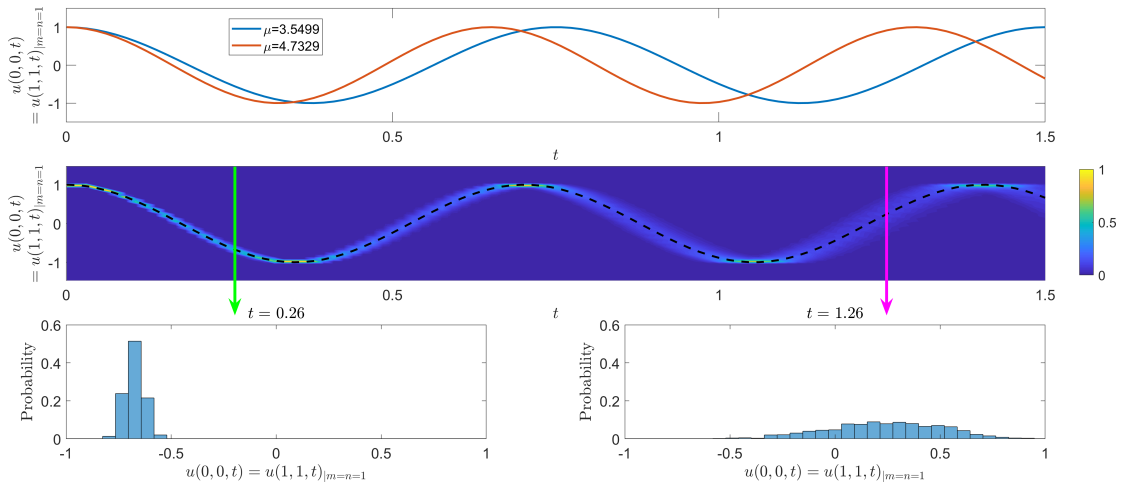
Figure 6.2: Stochastic displacement $u(X, Y, t)$ of the edges $(X, Y, Z) \in \{(0, 0, Z), (1, 1, Z)\}$ of the cuboid in dynamic generalised shear, when $m = n = 1$, $A_{11} = 1$, $B_{11} = 0$, $\rho = 1$, and μ is drawn from the Gamma distribution (3.1.6) with $\rho_1 = 405$ and $\rho_2 = 0.01$. The top figure illustrates the displacement over time of two cuboids, with randomly chosen values of μ, derived from the specified Gamma distribution. The middle figure illustrates a probability histogram at each time instant. Specifically, the integral of the probabilities over the displacements at any given time instant is equal to 1. The histogram comprises of 1000 stochastic simulations and the colour bar defines the probability of finding a given displacement at a given time. The dashed black line corresponds to the expected values based only on mean value, $\underline{\mu} = \rho_1\rho_2 = 4.05$. The bottom two figures illustrate specific histogram distributions at two given times (noted above each figure). These are the distributions that would be seen if the middle figure was cut along the green and magenta arrows, respectively.

6.2 Quasi-equilibrated radial-axial motion of a stochastic hyperelastic cylindrical tube

In this section, the stability and finite amplitude oscillations of a stochastic hyperelastic cylindrical tube, subject to the combined radial and axial quasi-equilibrated dynamic deformation, are analysed.

6.2.1 Dynamic radial-axial deformation of a cylindrical tube

For a circular cylindrical tube, the combined radial and axial motion is described by (see Figure 6.3)

$$r^2 = a^2 + \frac{R^2 - A^2}{\alpha}, \qquad \theta = \Theta, \qquad z = \alpha Z, \qquad (6.2.1)$$

where (R, Θ, Z) and (r, θ, z) are the cylindrical polar coordinates in the reference and current configuration, respectively, such that $A \leq R \leq B$, A and B are the inner and outer radii in the undeformed state, respectively, $a = a(t)$ and $b = b(t) = \sqrt{a^2 + (B^2 - A^2)/\alpha}$ are the inner and outer radius at time t, respectively, and $\alpha > 0$ is a given constant (when $\alpha < 0$, the tube is everted, so that the inner surface becomes the outer surface). When $\alpha = 1$, the time-dependent deformation (6.2.1) simplifies to that studied in [23, 106, 107]. The case when α is time-dependent was considered in [176].

The radial-axial motion (6.2.1) of the cylindrical tube is fully determined by the inner radius a at time t, which in turn is obtained from the initial conditions. Thus, the acceleration $\ddot{r}$ can be computed in terms of the acceleration $\ddot{a}$ on the inner surface. By the governing equations (6.2.1), the condition (2.2.4) is valid for the vector field $\boldsymbol{x} = r\boldsymbol{e}_r$, since

$$\ddot{\boldsymbol{x}} = (\ddot{r} - r\dot{\theta}^2)\boldsymbol{e}_r + (r\ddot{\theta} + 2\dot{r}\dot{\theta})\boldsymbol{e}_\theta + \ddot{z}\boldsymbol{e}_z, \qquad (6.2.2)$$
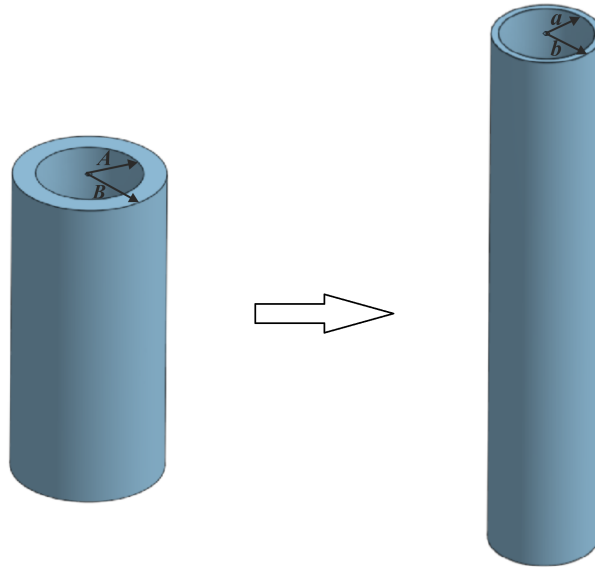
Figure 6.3: Schematic of inflation of a cylindrical tube, showing the reference state, with inner radius A and outer radius B (left), and the deformed state, with inner radius a and outer radius b (right), respectively.

and

$$\mathbf{0} = \operatorname{curl} \ddot{\boldsymbol{x}} = \left(\frac{1}{r} \frac{\partial \ddot{x}_z}{\partial \theta} - \frac{\partial \ddot{x}_\theta}{\partial z} \right) \boldsymbol{e}_r + \left(\frac{\partial \ddot{x}_r}{\partial z} - \frac{\partial \ddot{x}_z}{\partial r} \right) \boldsymbol{e}_\theta + \frac{1}{r} \left(\frac{\partial (r \ddot{x}_\theta)}{\partial r} - \frac{\partial \ddot{x}_r}{\partial \theta} \right) \boldsymbol{e}_z,$$

$$(6.2.3)$$

where $\ddot{x}_r$, $\ddot{x}_\theta$ and $\ddot{x}_z$ are the components of (6.2.2), $\boldsymbol{e}_r$, $\boldsymbol{e}_\theta$, and $\boldsymbol{e}_z$ are the associated basis vectors in cylindrical coordinates, and the acceleration potential, ξ, satisfies (2.2.3). Hence, this is a quasi-equilibrated motion, such that

$$-\frac{\partial \xi}{\partial r} = \ddot{r} = \frac{\dot{a}^2}{r} + \frac{a \ddot{a}}{r} - \frac{a^2 \dot{a}^2}{r^3}, \qquad (6.2.4)$$

and, by integrating (6.2.4), the acceleration potential, ξ, is given by [209, p. 215]

$$-\xi = \dot{a}^2 \log r + a \ddot{a} \log r + \frac{a^2 \dot{a}^2}{2r^2} = \dot{r}^2 \log r + r \ddot{r} \log r + \frac{1}{2} \dot{r}^2. \qquad (6.2.5)$$

The deformation gradient of (6.2.1), with respect to the polar coordinates (R, Θ, Z),

is equal to

$$\mathbf{F} = \text{diag}\left(\frac{R}{\alpha r}, \frac{r}{R}, \alpha\right), \tag{6.2.6}$$

the Cauchy-Green deformation tensor is

$$\mathbf{B} = \text{diag}\left(\frac{R^2}{\alpha^2 r^2}, \frac{r^2}{R^2}, \alpha^2\right), \tag{6.2.7}$$

and the principal invariants (2.1.6) take the form

$$\begin{aligned}
I_1 &= \frac{R^2}{\alpha^2 r^2} + \frac{r^2}{R^2} + \alpha^2, \\
I_2 &= \frac{\alpha^2 r^2}{R^2} + \frac{R^2}{r^2} + \frac{1}{\alpha^2}, \\
I_3 &= 1.
\end{aligned} \tag{6.2.8}$$

Thus, the principal components of the equilibrium Cauchy stress tensor at time t

are

$$\begin{aligned}
\sigma_{rr}^{(0)} &= -p^{(0)} + \beta_1 \frac{R^2}{\alpha^2 r^2} + \beta_{-1} \frac{\alpha^2 r^2}{R^2}, \\
\sigma_{\theta\theta}^{(0)} &= \sigma_{rr}^{(0)} + \left(\beta_1 - \beta_{-1}\alpha^2\right)\left(\frac{r^2}{R^2} - \frac{R^2}{\alpha^2 r^2}\right), \\
\sigma_{zz}^{(0)} &= \sigma_{rr}^{(0)} + \left(\beta_1 - \beta_{-1}\frac{r^2}{R^2}\right)\left(\alpha^2 - \frac{R^2}{\alpha^2 r^2}\right),
\end{aligned} \tag{6.2.9}$$

where $p^{(0)}$ is the Lagrangian multiplier for the incompressibility constraint ($I_3 = 1$), and the nonlinear material parameters are given by (6.1.6), with I_1 and I_2 given in (6.2.8).

As the stress components depend only on the radius r, the system of equilibrium equations reduces to

$$\frac{\partial \sigma_{rr}^{(0)}}{\partial r} = \frac{\sigma_{\theta\theta}^{(0)} - \sigma_{rr}^{(0)}}{r}. \tag{6.2.10}$$

Hence, by (6.2.9) and (6.2.10), the radial Cauchy stress for the equilibrium state

at time t is equal to

$$\sigma_{rr}^{(0)}(r,t) = \int \left(\beta_1 - \beta_{-1}\alpha^2\right) \left(\frac{r^2}{R^2} - \frac{R^2}{\alpha^2 r^2}\right) \frac{\mathrm{d}r}{r} + \psi(t), \qquad (6.2.11)$$

where $\psi = \psi(t)$ is an arbitrary function of time. Substitution of (6.2.5) and (6.2.11) into (2.2.5) then gives the principal Cauchy stress components at time t as follows;

$$\sigma_{rr}(r,t) = \rho \left(a\ddot{a}\log r + \dot{a}^2 \log r + \frac{a^2\dot{a}^2}{2r^2}\right) + \int \left(\beta_1 - \beta_{-1}\alpha^2\right) \left(\frac{r^2}{R^2} - \frac{R^2}{\alpha^2 r^2}\right) \frac{\mathrm{d}r}{r} +$$

$$+ \psi(t),$$

$$\sigma_{\theta\theta}(r,t) = \sigma_{rr}(r,t) + \left(\beta_1 - \beta_{-1}\alpha^2\right) \left(\frac{r^2}{R^2} - \frac{R^2}{\alpha^2 r^2}\right),$$

$$\sigma_{zz}(r,t) = \sigma_{rr}(r,t) + \left(\beta_1 - \beta_{-1}\frac{r^2}{R^2}\right) \left(\alpha^2 - \frac{R^2}{\alpha^2 r^2}\right).$$

$$(6.2.12)$$

In (6.2.12), the function $\beta_1 - \alpha^2\beta_{-1}$ can be interpreted as the following nonlinear shear modulus [127];

$$\widetilde{\mu} = \beta_1 - \beta_{-1}\alpha^2, \qquad (6.2.13)$$

corresponding to the combined deformation of simple shear superposed on axial stretch, with shear parameter $k = \sqrt{\alpha^2 R^2/r^2 + \alpha^4 r^2/R^2 - \alpha^6 - 1}$ and stretch parameter α. As shown in [127], this modulus is positive if the BE inequalities (3.1.1) hold. In this case, the integrand is negative for $0 < r^2/R^2 < 1/\alpha$ and positive for $r^2/R^2 > 1/\alpha$. Using the first equation in (6.2.1), it is straightforward to show that $0 < r^2/R^2 < 1/\alpha$ (respectively, $r^2/R^2 > 1/\alpha$) is equivalent to $0 < a^2/A^2 < 1/\alpha$ (respectively, $a^2/A^2 > 1/\alpha$). When $\alpha = 1$, the modulus defined by (6.2.13) coincides with the generalised shear modulus defined in [209, p. 174], and also in [23].

In the limiting case when $\alpha \to 1$ and $k \to 0$, the nonlinear shear modulus (6.2.13) converges to the classical shear modulus from the infinitesimal theory [127]

(see (2.1.30)),

$$\mu = \lim_{\alpha \to 1} \lim_{k \to 0} \widetilde{\mu}. \tag{6.2.14}$$

In this case, as $R^2/r^2 \to 1$, the three stress components defined by (6.2.12) are equal.

Next, for the cylindrical tube deforming by (6.2.1), the inner and outer radial pressures acting on the curvilinear surfaces $r = a(t)$ and $r = b(t)$ at time t (measured per unit area in the present configuration), are set as $\sigma_1(t)$ and $\sigma_2(t)$, respectively [209, pp. 214-217]. Evaluating $\sigma_1(t) = -\sigma_{rr}(a,t)$ and $\sigma_2(t) = -\sigma_{rr}(b,t)$, using (6.2.12), with $r = a$ and $r = b$, respectively, then subtracting the results, gives

$$
\begin{aligned}
\sigma_1(t) - \sigma_2(t) &= \frac{\rho}{2}\left[(a\ddot{a} + \dot{a}^2)\log\frac{b^2}{a^2} + \dot{a}^2\left(\frac{a^2}{b^2} - 1\right)\right] + \int_a^b \widetilde{\mu}\left(\frac{r^2}{R^2} - \frac{R^2}{\alpha^2 r^2}\right)\frac{\mathrm{d}r}{r} \\
&= \frac{\rho A^2}{2}\left[\left(\frac{a}{A}\frac{\ddot{a}}{A} + \frac{\dot{a}^2}{A^2}\right)\log\frac{b^2}{a^2} + \frac{\dot{a}^2}{A^2}\left(\frac{a^2}{b^2} - 1\right)\right] + \\
&\quad + \int_a^b \widetilde{\mu}\left(\frac{r^2}{R^2} - \frac{R^2}{\alpha^2 r^2}\right)\frac{\mathrm{d}r}{r}.
\end{aligned}
\tag{6.2.15}
$$

Setting the notation

$$
u = \frac{r^2}{R^2} = \frac{r^2}{\alpha(r^2 - a^2) + A^2}, \qquad x = \frac{a}{A}, \qquad \gamma = \frac{B^2}{A^2} - 1, \tag{6.2.16}
$$

we can rewrite the terms in (6.2.15) as

$$
\begin{aligned}
\left(\frac{a}{A}\frac{\ddot{a}}{A} + \frac{\dot{a}^2}{A^2}\right)\log\frac{b^2}{a^2} + \frac{\dot{a}^2}{A^2}\left(\frac{a^2}{b^2} - 1\right) &= (\ddot{x}x + \dot{x}^2)\log\left(1 + \frac{\gamma}{\alpha x^2}\right) - \dot{x}^2\frac{\frac{\gamma}{\alpha x^2}}{1 + \frac{\gamma}{\alpha x^2}} \\
&= \frac{1}{2x}\frac{\mathrm{d}}{\mathrm{d}x}\left[\dot{x}^2 x^2 \log\left(1 + \frac{\gamma}{\alpha x^2}\right)\right]
\end{aligned}
\tag{6.2.17}
$$

and

$$\int_a^b \widetilde{\mu} \left(\frac{r^2}{R^2} - \frac{R^2}{\alpha^2 r^2} \right) \frac{\mathrm{d}r}{r} = \int_a^b \widetilde{\mu} \left[\frac{r^2}{\alpha \left(r^2 - a^2 \right) + A^2} - \frac{\alpha \left(r^2 - a^2 \right) + A^2}{\alpha^2 r^2} \right] \frac{\mathrm{d}r}{r}$$
$$= \frac{1}{2} \int_{\frac{x^2 + \gamma/\alpha}{1 + \gamma}}^{x^2} \widetilde{\mu} \frac{1 + \alpha u}{\alpha^2 u^2} \mathrm{d}u.$$

(6.2.18)

Hence, (6.2.15) can be expressed equivalently as follows,

$$2x \frac{\sigma_1(t) - \sigma_2(t)}{\rho A^2} = \frac{1}{2} \frac{\mathrm{d}}{\mathrm{d}x} \left[\dot{x}^2 x^2 \log \left(1 + \frac{\gamma}{\alpha x^2} \right) \right] + \frac{x}{\rho A^2} \int_{\frac{x^2 + \gamma/\alpha}{1 + \gamma}}^{x^2} \widetilde{\mu} \frac{1 + \alpha u}{\alpha^2 u^2} \mathrm{d}u. \quad (6.2.19)$$

Note here that when the BE inequalities (3.1.1) hold, $\widetilde{\mu} > 0$, and the integral in (6.2.15), or equivalently in (6.2.19), is negative if $0 < u < 1/\alpha$ (i.e. if $0 < x < 1/\sqrt{\alpha}$), and positive if $u > 1/\alpha$ (i.e. if $x > 1/\sqrt{\alpha}$).

In the static case where $\dot{a} = 0$ and $\ddot{a} = 0$, (6.2.15) becomes

$$\sigma_1(t) - \sigma_2(t) = \int_a^b \widetilde{\mu} \left(\frac{r^2}{R^2} - \frac{R^2}{\alpha^2 r^2} \right) \frac{\mathrm{d}r}{r}, \quad (6.2.20)$$

and (6.2.19) reduces to

$$2 \frac{\sigma_1(t) - \sigma_2(t)}{\rho A^2} = \frac{1}{\rho A^2} \int_{\frac{x^2 + \gamma/\alpha}{1 + \gamma}}^{x^2} \widetilde{\mu} \frac{1 + \alpha u}{\alpha^2 u^2} \mathrm{d}u. \quad (6.2.21)$$

For the cylindrical tube in finite dynamic deformation, we set

$$G(x, \gamma) = \frac{1}{\rho A^2} \int_{1/\sqrt{\alpha}}^x \left(\zeta \int_{\frac{\zeta^2 + \gamma/\alpha}{1 + \gamma}}^{\zeta^2} \widetilde{\mu} \frac{1 + \alpha u}{\alpha^2 u^2} \mathrm{d}u \right) \mathrm{d}\zeta, \quad (6.2.22)$$

and find that $G(x, \gamma)$ is monotonically decreasing when $0 < x < 1/\sqrt{\alpha}$, and increasing when $x > 1/\sqrt{\alpha}$. This function will be useful in establishing whether the radial motion is oscillatory or not, as will be shown below.

The pressure impulse, or, in other words, the suddenly applied pressure differ-

ence, is set as

$$2\alpha\frac{\sigma_1(t) - \sigma_2(t)}{\rho A^2} = \begin{cases} 0 & \text{if } t \leq 0, \\ \\ p_0 & \text{if } t > 0, \end{cases} \tag{6.2.23}$$

where p_0 is constant in time. Integrating (6.2.19) once then gives

$$\frac{1}{2}\dot{x}^2 x^2 \log\left(1 + \frac{\gamma}{\alpha x^2}\right) + G(x, \gamma) = \frac{p_0}{2\alpha}\left(x^2 - \frac{1}{\alpha}\right) + C, \tag{6.2.24}$$

with $G(x, \gamma)$ defined by (6.2.22), and

$$C = \frac{1}{2}\dot{x}_0^2 x_0^2 \log\left(1 + \frac{\gamma}{\alpha x_0^2}\right) + G(x_0, \gamma) - \frac{p_0}{2\alpha}\left(x_0^2 - \frac{1}{\alpha}\right), \tag{6.2.25}$$

where $x(0) = x_0$ and $\dot{x}(0) = \dot{x}_0$ are the initial conditions. By (6.2.24),

$$\dot{x} = \pm\sqrt{\frac{\frac{p_0}{\alpha}\left(x^2 - \frac{1}{\alpha}\right) + 2C - 2G(x, \gamma)}{x^2 \log\left(1 + \frac{\gamma}{\alpha x^2}\right)}}. \tag{6.2.26}$$

Physically, this system is analogous to the motion of a point mass with energy

$$E = \frac{1}{2}m(x)\dot{x}^2 + V(x). \tag{6.2.27}$$

The energy is $E = C$, the potential is given by $V(x) = G(x, \gamma) - \frac{p_0}{2\alpha}\left(x^2 - \frac{1}{\alpha}\right)$, and the position-dependent mass is $m(x) = x^2 \log\left(1 + \frac{\gamma}{\alpha x^2}\right)$. Due to the constraints on the function G, this system has simple dynamics. Depending on the constant μ, the system may have a static state or periodic motion. The radial motion is periodic if and only if the following equation,

$$G(x, \gamma) = \frac{p_0}{2\alpha}\left(x^2 - \frac{1}{\alpha}\right) + C, \tag{6.2.28}$$

has exactly two distinct solutions, representing the amplitudes of the oscillation, $x = x_1$ and $x = x_2$, such that $0 < x_1 < x_2 < \infty$. Physically, these solutions represent the points between which inflation and deflation occurs. By (6.2.16),

the minimum and maximum radii of the inner surface in the oscillation are then equal to $x_1 A$ and $x_2 A$, respectively, and by (6.2.26), the period of oscillation is

$$T = 2 \left| \int_{x_1}^{x_2} \frac{\mathrm{d}x}{\dot{x}} \right| = 2 \left| \int_{x_1}^{x_2} \sqrt{\frac{x^2 \log\left(1 + \frac{\gamma}{\alpha x^2}\right)}{\frac{p_0}{\alpha}\left(x^2 - \frac{1}{\alpha}\right) + 2C - 2G(x, \gamma)}} \, \mathrm{d}x \right|. \qquad (6.2.29)$$

Both the amplitudes and period of the oscillation are random variables described in terms of probability distributions.

The specific case of the radial oscillations of a cylindrical tube of stochastic Mooney-Rivlin material will now be presented.

6.2.2 Radial oscillations of a cylindrical tube of stochastic Mooney-Rivlin material

For cylindrical tubes of a stochastic Mooney-Rivlin material, defined by (3.1.2) with $m = n = 1$ and $\mu = \mu_1 + \mu_2 > 0$, evaluating the integral in (6.2.22) gives (see Appendix F for detailed calculations)

$$G(x, \gamma) = \frac{\widetilde{\mu}}{2\alpha\rho A^2} \left(x^2 - \frac{1}{\alpha}\right) \log \frac{1 + \gamma}{1 + \frac{\gamma}{\alpha x^2}}, \qquad (6.2.30)$$

where $\widetilde{\mu} = \mu_1 + \mu_2 \alpha^2$. In this case, assuming that the nonlinear shear modulus μ has a uniform lower bound, i.e.

$$\mu > \eta, \qquad (6.2.31)$$

for some constant $\eta > 0$, it follows that

$$\lim_{x \to 0} G(x, \gamma) = \lim_{x \to \infty} G(x, \gamma) = \infty. \qquad (6.2.32)$$

There is no connection between the existence, or indeed the non-existence, of an oscillatory solution and a limit point instability. As an example, oscillatory motions can be observed in tubes made of both neo-Hookean and Mooney-Rivlin

materials, but in the neo-Hookean case, we have stability.

(i) If $p_0 = 0$ and $C > 0$, then equation (6.2.28) has exactly two solutions, $x = x_1$ and $x = x_2$, satisfying $0 < x_1 < 1/\sqrt{\alpha} < x_2 < \infty$, for any positive constant C. It should be noted that, by (6.2.12), if $\sigma_{rr}(r,t) = 0$ at $r = a$ and $r = b$, so that $\sigma_1(t) = \sigma_2(t) = 0$, then $\sigma_{\theta\theta}(r,t) \neq 0$ and $\sigma_{zz}(r,t) \neq 0$ at $r = a$ and $r = b$, unless $\alpha \to 1$ and $r^2/R^2 \to 1$. That is, in general, these oscillations cannot be 'free', due to the nonzero tractions [176].
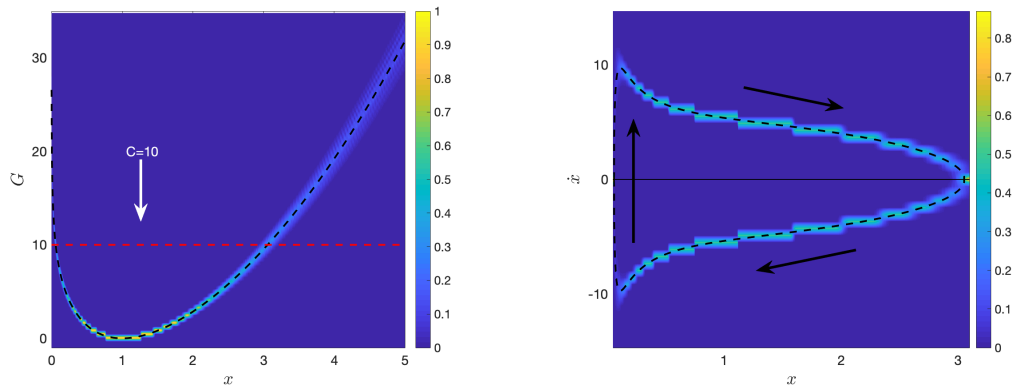
Figure 6.4: The function $G(x, \gamma)$, defined by (6.2.30), intersecting the (dashed red) line $C = 10$ when $p_0 = 0$ (left), and the associated velocity, given by (6.2.26) (right), for a cylindrical tube of stochastic Mooney-Rivlin material when $\alpha = 1$, $\rho = 1$, $A = 1$, $\gamma = 1$, and $\widetilde{\mu} = \mu = \mu_1 + \mu_2$ is drawn from the Gamma distribution (3.1.6) with $\rho_1 = 405$ and $\rho_2 = 0.01$. The dashed black lines correspond to the expected values based only on mean value, $\underline{\mu} = \rho_1\rho_2 = 4.05$. Each distribution was calculated from the average of 1000 stochastic simulations.

In Figure 6.4, for example, the stochastic function $G(x, \gamma)$ (6.2.30) is represented as intersecting the line $C = 10$ to solve equation (6.2.28) when $p_0 = 0$, and the associated velocity (6.2.26), assuming that $\alpha = 1$, $\rho = 1$, $A = 1$, $\gamma = 1$, and μ follows the Gamma distribution (3.1.6) with hyperparameters $\rho_1 = 405$ and $\rho_2 = 0.01$ (see Figure 5.21).

For a thin-walled tube [106, 175], where $\alpha = 1$ and $\gamma \to 0$, equation (6.2.24)

takes the form

$$\dot{x}^2 + \frac{\mu}{\rho A^2}\left(x^2 + \frac{1}{x^2}\right) = \dot{x}_0^2 + \frac{\mu}{\rho A^2}\left(x_0^2 + \frac{1}{x_0^2}\right), \tag{6.2.33}$$

and has the explicit solution [175]

$$x = \sqrt{\left[x_0 \cos\left(\frac{t}{A}\sqrt{\frac{\mu}{\rho}}\right) + \dot{x}_0 A\sqrt{\frac{\rho}{\mu}}\sin\left(\frac{t}{A}\sqrt{\frac{\mu}{\rho}}\right)\right]^2 + \frac{1}{x_0^2}\sin^2\left(\frac{t}{A}\sqrt{\frac{\mu}{\rho}}\right)}. \tag{6.2.34}$$

From this, it is clear that oscillatory motions depend on the initial conditions. In this case, assuming that the shear modulus, μ, has a uniform lower bound, equation (6.2.33) becomes [106]

$$x^2 + \frac{1}{x^2} = \frac{\rho A^2}{\mu}\dot{x}_0^2 + x_0^2 + \frac{1}{x_0^2}. \tag{6.2.35}$$

This equation can be solved directly to find the amplitudes;

$$x_{1,2} = \sqrt{\frac{\frac{\rho A^2}{\mu}\dot{x}_0^2 + x_0^2 + \frac{1}{x_0^2} \pm \sqrt{\left(\frac{\rho A^2}{\mu}\dot{x}_0^2 + x_0^2 + \frac{1}{x_0^2}\right)^2 - 4}}{2}}. \tag{6.2.36}$$

Noting that $x_2 = 1/x_1$, the period of the oscillations can be calculated as

$$T = 2\sqrt{\frac{\rho A^2}{\mu}}\left|\int_{x_1}^{1/x_1} \frac{\mathrm{d}x}{\sqrt{\frac{\rho A^2}{\mu}\dot{x}_0^2 + x_0^2 + \frac{1}{x_0^2} - x^2 - \frac{1}{x^2}}}\right| = \pi A\sqrt{\frac{\rho}{\mu}}. \tag{6.2.37}$$

In Figure 6.5, the stochastic solution given by (6.2.34) is illustrated, with the initial conditions $x_0 = 1$ and $\dot{x}_0 = 4.5$, assuming that $\rho = 1$, $A = 1$, and μ satisfies the Gamma distribution (3.1.6) with hyperparameters $\rho_1 = 405$ and $\rho_2 = 0.01$.

(ii) When $p_0 \neq 0$ and $C \geq 0$, substitution of (6.2.30) in (6.2.28) gives

$$p_0 = \frac{\widetilde{\mu}}{\rho A^2}\log\frac{1+\gamma}{1+\frac{\gamma}{\alpha x^2}} - \frac{2\alpha C}{x^2 - \frac{1}{\alpha}}. \tag{6.2.38}$$
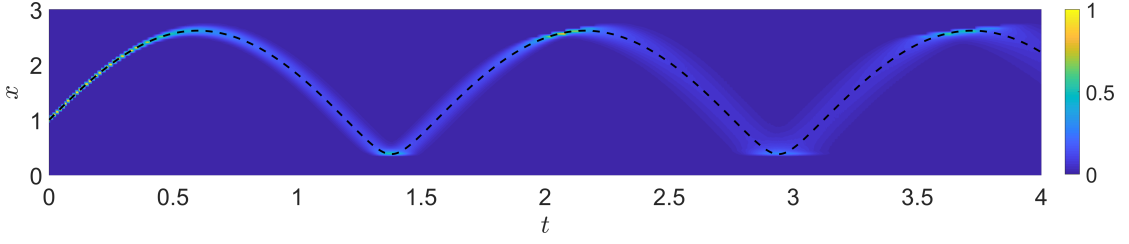
Figure 6.5: Stochastic solution given by (6.2.34), with the initial conditions $x_0 = 1$ and $\dot{x}_0 = 4.5$, for a thin-walled tube, where $\rho = 1$, $A = 1$, and μ is drawn from the Gamma distribution (3.1.6) with $\rho_1 = 405$ and $\rho_2 = 0.01$. The dashed black line corresponds to the expected values based only on mean value, $\underline{\mu} = \rho_1 \rho_2 = 4.05$. The distribution was calculated from the average of 1000 stochastic simulations.

As the right-hand side of the above equation is a monotonically increasing function of x, there exists a unique positive x satisfying (6.2.38) if and only if the following condition holds,

$$\lim_{x \to 0} \left(\frac{\widetilde{\mu}}{\rho A^2} \log \frac{1 + \gamma}{1 + \frac{\gamma}{\alpha x^2}} - \frac{2\alpha C}{x^2 - \frac{1}{\alpha}} \right) < p_0 < \lim_{x \to \infty} \left(\frac{\widetilde{\mu}}{\rho A^2} \log \frac{1 + \gamma}{1 + \frac{\gamma}{\alpha x^2}} - \frac{2\alpha C}{x^2 - \frac{1}{\alpha}} \right), \tag{6.2.39}$$

that is,

$$-\infty < p_0 < \frac{\widetilde{\mu}}{\rho A^2} \log (1 + \gamma). \tag{6.2.40}$$

By (6.2.16), (6.2.23), and (6.2.40), the necessary and sufficient condition that oscillatory motions occur is that the nonlinear shear modulus, $\widetilde{\mu}$, is uniformly bounded from below as follows,

$$\widetilde{\mu} > \frac{p_0 \rho A^2}{\log (1 + \gamma)} = \alpha \frac{\sigma_1(t) - \sigma_2(t)}{\log B - \log A}, \tag{6.2.41}$$

i.e. where p_0 is small enough. By (6.2.13),

$$\widetilde{\mu} = \mu_1 + \mu_2 \alpha^2 = \mu_1 + (\mu - \mu_1) \alpha^2 = \mu \alpha^2 + \mu_1 (1 - \alpha^2). \tag{6.2.42}$$

Hence, (6.2.41) is equivalent to

$$\mu > \frac{p_0 \rho A^2}{\alpha^2 \log(1+\gamma)} + \mu_1 \frac{1-\alpha^2}{\alpha^2}. \tag{6.2.43}$$

The probability distribution of oscillatory motions occurring is then

$$P_1\left(\mu > \frac{p_0 \rho A^2}{\alpha^2 \log(1+\gamma)} + \mu_1 \frac{1-\alpha^2}{\alpha^2}\right) = 1 - \int_0^{\frac{p_0 \rho A^2}{\alpha^2 \log(1+\gamma)} + \mu_1 \frac{1-\alpha^2}{\alpha^2}} g(u; \rho_1, \rho_2)\mathrm{d}u, \tag{6.2.44}$$

where $g(u; \rho_1, \rho_2)$ is the Gamma probability density function defined by (3.1.6), and that of non-oscillatory motions, or in other words, the probability distribution of a monotonic inflation, is

$$P_2\left(\mu < \frac{p_0 \rho A^2}{\alpha^2 \log(1+\gamma)} + \mu_1 \frac{1-\alpha^2}{\alpha^2}\right) = 1 - P_1\left(\mu > \frac{p_0 \rho A^2}{\alpha^2 \log(1+\gamma)} + \mu_1 \frac{1-\alpha^2}{\alpha^2}\right)$$
$$= \int_0^{\frac{p_0 \rho A^2}{\alpha^2 \log(1+\gamma)} + \mu_1 \frac{1-\alpha^2}{\alpha^2}} g(u; \rho_1, \rho_2)\mathrm{d}u. \tag{6.2.45}$$

For example, when $\alpha = 1$, $\rho = 1$, $A = 1$, $\gamma = 1$, and $\widetilde{\mu} = \mu = \mu_1 + \mu_2$ satisfies the Gamma distribution (3.1.6) with $\rho_1 = 405$ and $\rho_2 = 0.01$, the probability distributions given by (6.2.44)-(6.2.45) are shown in Figure 6.6 (blue lines for P_1 and red lines for P_2). Specifically, $(0, \underline{\mu})$, where $\underline{\mu} = \rho_1 \rho_2 = 4.05$ is the mean value of μ, was divided into 100 steps, then for each value of p_0, 100 random values of μ were numerically generated from the specified Gamma distribution and compared with the inequalities defining the two intervals for values of p_0. For the deterministic elastic tube, the critical value $p_0 = \underline{\mu}\log 2 \approx 2.8072$ strictly divides the cases of oscillations occurring or not. For the stochastic problem, for the same critical value, there is, by definition, exactly 50% chance that the motion is oscillatory, and 50% chance that it is not. To increase the probability of oscillatory motion ($P_1 \approx 1$), a sufficiently small impulse, p_0, must be applied below the expected critical point, whereas a non-oscillatory motion, or monotonic inflation, is certain to occur ($P_2 \approx 1$) if p_0 is sufficiently large. However, analogous to the
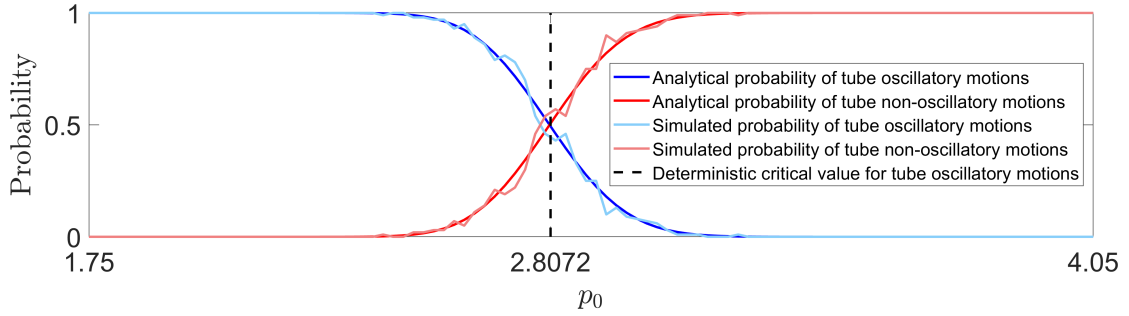
Figure 6.6: Probability distributions of whether oscillatory motions can occur or not for a cylindrical tube of stochastic Mooney-Rivin material, with $\alpha = 1$, $\rho = 1$, $A = 1$, $\gamma = 1$, and the shear modulus, μ, following the Gamma distribution (3.1.6) with $\rho_1 = 405$, $\rho_2 = 0.01$. Dark coloured lines represent analytically derived solutions, given by equations (6.2.44)-(6.2.45), whereas the lighter versions represent stochastically generated data. The vertical line at the critical value, $p_0 = 2.8072$, separates the expected regions based only on mean value, $\underline{\mu} = \rho_1\rho_2 = 4.05$. The probabilities were calculated from the average of 100 stochastic simulations.
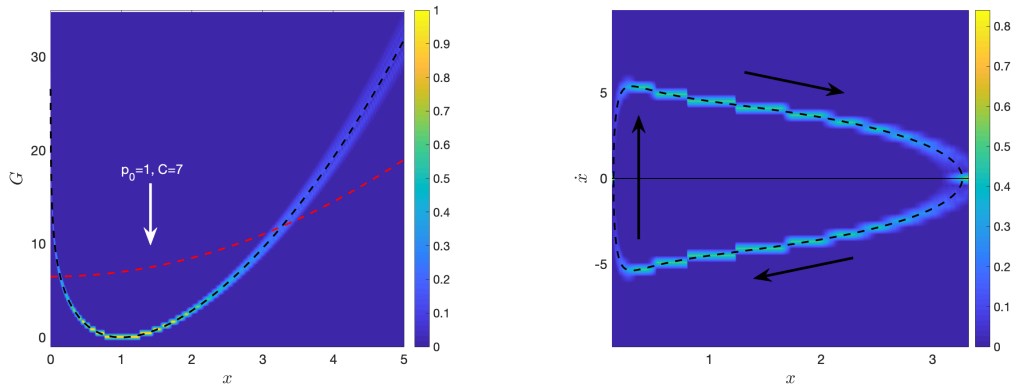
Figure 6.7: The function $G(x, \gamma)$ (6.2.30) intersecting the (dashed red) curve $p_0 \left(x^2 - 1/\alpha\right)/(2\alpha) + C$, with $p_0 = 1$ and $C = 7$, (left), and the associated velocity (6.2.26) (right) for a cylindrical tube of stochastic Mooney-Rivlin material when $\alpha = 1$, $\rho = 1$, $A = 1$, $\gamma = 1$, and $\widetilde{\mu} = \mu = \mu_1 + \mu_2$ is drawn from the Gamma distribution (3.1.6) with $\rho_1 = 405$ and $\rho_2 = 0.01$. The dashed black lines correspond to the expected values based only on mean value, $\underline{\mu} = \rho_1\rho_2 = 4.05$. Each distribution was calculated from the average of 1000 stochastic simulations.

cases presented in Sections 5.2 and 5.3, the inherent variability in the probabilistic system means that there will also exist events where there is competition between the two cases.

In Figure 6.7, the stochastic function $G(x, \gamma)$ (6.2.30) is illustrated as intersecting the curve $p_0 \left(x^2 - 1/\alpha\right)/(2\alpha) + C$, with $p_0 = 1$ and $C = 7$, to find the

solutions of equation (6.2.28), and the associated velocity (6.2.26), assuming that $\alpha = 1$, $\rho = 1$, $A = 1$, $\gamma = 1$, and μ satisfies the Gamma distribution (3.1.6) with $\rho_1 = 405$ and $\rho_2 = 0.01$ (see Figure 5.21).

When $C = 0$, equation (6.2.38) can be solved explicitly to find the amplitude

$$x_1 = \sqrt{\frac{\gamma/\alpha}{(1 + \gamma) \exp\left[-(p_0 \rho A^2)/(\widetilde{\mu})\right] - 1}} = \sqrt{\frac{(B^2 - A^2)/\alpha}{B^2 \exp\left[-2\alpha(P_1 - P_2)/\widetilde{\mu}\right] - A^2}}.$$ (6.2.46)

In the static case, by (6.2.21) and (6.2.23), at $x = x_1$, the required pressure takes the form

$$p_0^{(s)} = \frac{\widetilde{\mu}}{\alpha x^2 \rho A^2} \frac{\gamma - \frac{\gamma}{\alpha x^2}}{1 + \frac{\gamma}{\alpha x^2}} + \frac{\widetilde{\mu}}{\rho A^2} \log \frac{1 + \gamma}{1 + \frac{\gamma}{\alpha x^2}}.$$ (6.2.47)

Thus, the difference between the applied pressure in the static and dynamic case, given by (6.2.47) and (6.2.38), respectively, with $C = 0$, is

$$p_0^{(s)} - p_0 = \frac{\widetilde{\mu}}{\alpha x^2 \rho A^2} \frac{\gamma - \frac{\gamma}{\alpha x^2}}{1 + \frac{\gamma}{\alpha x^2}}.$$ (6.2.48)

Hence, $p_0^{(s)} < p_0$ if $0 < x_1 < \sqrt{\alpha}$, and $p_0^{(s)} > p_0$ if $x_1 > \sqrt{\alpha}$.

If the tube wall is thin [107, 175], then $0 < \gamma \ll 1$ and $\alpha = 1$, and (6.2.38) becomes

$$\frac{p_0}{\gamma} = \frac{\mu}{\rho A^2}\left(1 - \frac{1}{x^2}\right) - \frac{2\alpha C}{x^2 - \frac{1}{\alpha}}.$$ (6.2.49)

The necessary and sufficient condition that oscillatory motions occur is that

$$-\infty = \lim_{x \to 0}\left[\frac{\mu}{\rho A^2}\left(1 - \frac{1}{x^2}\right) - \frac{2\alpha C}{x^2 - \frac{1}{\alpha}}\right] < \frac{p_0}{\gamma} < \lim_{x \to \infty}\left[\frac{\mu}{\rho A^2}\left(1 - \frac{1}{x^2}\right) - \frac{2\alpha C}{x^2 - \frac{1}{\alpha}}\right]$$

$$= \frac{\mu}{\rho A^2}.$$ (6.2.50)

Thus, for the motion to be oscillatory, the shear modulus must be bounded from below as follows;

$$\mu > \frac{p_0}{\gamma} \rho A^2 = \frac{2}{\gamma}\left(\sigma_1(t) - \sigma_2(t)\right).$$ (6.2.51)

The probability distribution of oscillatory motions occurring is then

$$P_1\left(\mu > \frac{p_0}{\gamma}\rho A^2\right) = 1 - \int_0^{\frac{p_0}{\gamma}\rho A^2} g(u; \rho_1, \rho_2)\mathrm{d}u, \qquad (6.2.52)$$

and that of non-oscillatory motions is

$$P_2\left(\mu < \frac{p_0}{\gamma}\rho A^2\right) = 1 - P_1\left(\mu > \frac{p_0}{\gamma}\rho A^2\right) = \int_0^{\frac{p_0}{\gamma}\rho A^2} g(u; \rho_1, \rho_2)\mathrm{d}u. \qquad (6.2.53)$$
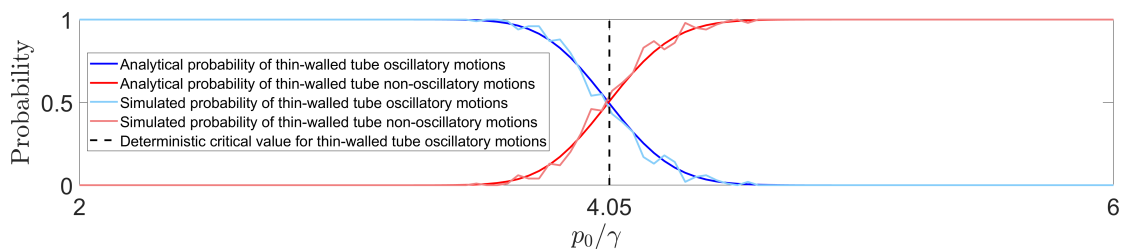
Figure 6.8: Probability distributions of whether oscillatory motions can occur or not for a thin-walled cylindrical tube of stochastic Mooney-Rivin material, with $\rho = 1$, $A = 1$, and the shear modulus, μ, following the Gamma distribution (3.1.6) with $\rho_1 = 405$, $\rho_2 = 0.01$. Dark coloured lines represent analytically derived solutions, given by equations (6.2.52)-(6.2.53), whereas the lighter versions represent stochastically generated data. The vertical line at the critical value, $p_0/\gamma = 4.05$, separates the expected regions based only on mean value, $\underline{\mu} = \rho_1\rho_2 = 4.05$. The probabilities were calculated from the average of 100 stochastic simulations.
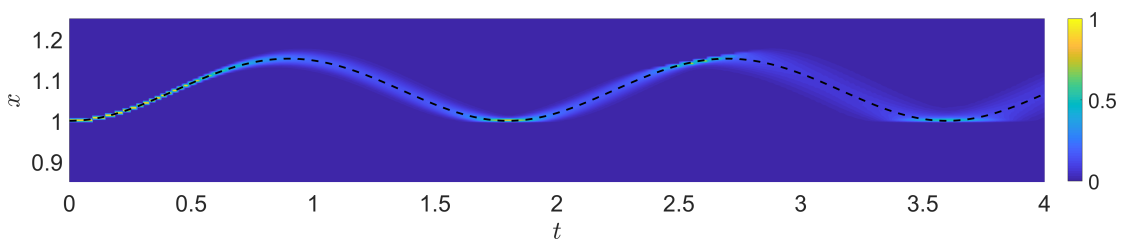
Figure 6.9: Stochastic solution given by (6.2.54), with $p_0/\gamma = 1$, for a thin-walled tube, where $\rho = 1$, $A = 1$, and μ is drawn from the Gamma distribution (3.1.6) with $\rho_1 = 405$ and $\rho_2 = 0.01$. The dashed black line corresponds to the expected values based only on mean value, $\underline{\mu} = \rho_1\rho_2 = 4.05$. The distribution was calculated from the average of 1000 stochastic simulations.

For $\rho = 1$, $A = 1$, and $\widetilde{\mu} = \mu = \mu_1 + \mu_2$ drawn from the Gamma distribution (3.1.6) with $\rho_1 = 405$ and $\rho_2 = 0.01$, the probability distributions given by (6.2.52)-(6.2.53) are shown in Figure 6.8 (blue lines for P_1 and red lines for P_2). For the

deterministic thin-walled tube, the critical value $p_0/\gamma = \underline{\mu} = 4.05$ strictly separates the cases of oscillations occurring or not. However, in the stochastic instance, the two cases compete.

If $C = 0$, then setting $x_0 = 1$ and $\dot{x}_0 = 0$, the equation of motion has the explicit solution [175]

$$x = \sqrt{\frac{\frac{\mu}{\rho A^2} - \frac{p_0}{2\gamma}}{\frac{\mu}{\rho A^2} - \frac{p_0}{\gamma}} - \frac{\frac{p_0}{2\gamma}}{\frac{\mu}{\rho A^2} - \frac{p_0}{\gamma}} \cos\left(2t\sqrt{\frac{\mu}{\rho A^2} - \frac{p_0}{\gamma}}\right)}. \qquad (6.2.54)$$

In Figure 6.9, the stochastic solution given by (6.2.54), with $p_0/\gamma = 1$, is illustrated, assuming that $\rho = 1$, $A = 1$, and μ satisfies the Gamma distribution (3.1.6) with hyperparameters $\rho_1 = 405$ and $\rho_2 = 0.01$.

If the tube wall is infinitely thick [176], then $\gamma \to \infty$, and assuming that the nonlinear shear modulus, $\widetilde{\mu}$, has a uniform lower bound, (6.2.40) becomes

$$-\infty = \lim_{x \to 0} \left[\frac{\widetilde{\mu}}{\rho A^2} \log\left(\alpha x^2\right) - \frac{2\alpha C}{x^2 - \frac{1}{\alpha}}\right] < p_0 < \lim_{x \to \infty} \left[\frac{\widetilde{\mu}}{\rho A^2} \log\left(\alpha x^2\right) - \frac{2\alpha C}{x^2 - \frac{1}{\alpha}}\right]$$

$$= \infty. \qquad (6.2.55)$$

Hence, the motion is always oscillatory for any value of the applied impulse.

6.3 Quasi-equilibrated radial motion of a stochastic hyperelastic spherical shell

In this section, comparable to the analysis presented in Section 6.2 for cylindrical tubes, the stability and finite amplitude oscillations of a stochastic hyperelastic spherical shell under quasi-equilibrated dynamic radial deformation is examined, beginning with the dynamic radial deformation of a spherical shell in Section 6.3.1, before extending to the specific case of the radial oscillations of a spherical shell made of a stochastic neo-Hookean material in Section 6.3.2.

6.3.1 Dynamic radial deformation of a spherical shell

For a spherical shell, the radial motion is described by [18, 25, 86, 108] (see Figure 6.10)

$$r^3 = a^3 + R^3 - A^3, \qquad \theta = \Theta, \qquad \phi = \Phi, \tag{6.3.1}$$

where (R, Θ, Φ) and (r, θ, ϕ) are the spherical polar coordinates in the reference and current configuration, respectively, such that $A \leq R \leq B$, A and B are the inner and outer radii in the undeformed state, and $a = a(t)$ and $b = b(t) = \sqrt[3]{a^3 + B^3 - A^3}$ are the inner and outer radii at time t, respectively.
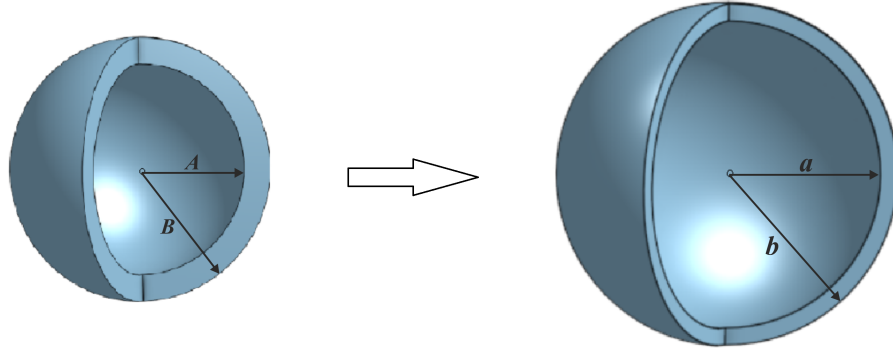
Figure 6.10: Schematic of inflation of a spherical shell, showing the reference state, with inner radius A and outer radius B (left), and the deformed state, with inner radius a and outer radius b (right), respectively.

As for the cylindrical tube, the radial motion (6.3.1) of the spherical shell is determined entirely by the inner radius a at time t. By the governing equations (6.3.1), the condition (2.2.4) is valid for the vector field $\boldsymbol{x} = r\boldsymbol{e}_r$, since

$$\begin{aligned}
\ddot{\boldsymbol{x}} = {} & (\ddot{r} - r\dot{\theta}^2 \sin^2 \phi - r\dot{\phi}^2)\boldsymbol{e}_r + \\
& + (r\ddot{\theta} \sin \phi + 2\dot{r}\dot{\theta} \sin \phi + 2r\dot{\theta}\dot{\phi} \cos \phi)\boldsymbol{e}_\theta + \\
& + (r\ddot{\phi} + 2\dot{r}\dot{\phi} - r\dot{\theta}^2 \sin \phi \cos \phi)\boldsymbol{e}_\phi,
\end{aligned} \tag{6.3.2}$$

and

$$
\mathbf{0} = \operatorname{curl} \ddot{\boldsymbol{x}} = \frac{1}{r \sin \theta} \left[\frac{\partial (\ddot{x}_\phi \sin \theta)}{\partial \theta} - \frac{\partial \ddot{x}_\theta}{\partial \phi} \right] \boldsymbol{e}_r + \frac{1}{r} \left[\frac{1}{\sin \theta} \frac{\partial \ddot{x}_r}{\partial \phi} - \frac{\partial (r \ddot{x}_\phi)}{\partial r} \right] \boldsymbol{e}_\theta +
$$
$$
+ \frac{1}{r} \left[\frac{\partial (r \ddot{x}_\theta)}{\partial r} - \frac{\partial \ddot{x}_r}{\partial \theta} \right] \boldsymbol{e}_\phi,
$$

(6.3.3)

where $\ddot{x}_r$, $\ddot{x}_\theta$, and $\ddot{x}_\phi$ are the components of (6.3.2), $\boldsymbol{e}_r$, $\boldsymbol{e}_\theta$ and $\boldsymbol{e}_\phi$ are the associated basis vectors in sperical coordinates, and the acceleration potential ξ satisfies (2.2.3). Hence, this is a quasi-equilibrated motion, such that

$$
-\frac{\partial \xi}{\partial r} = \ddot{r} = \frac{2a\dot{a}^2 + a^2 \ddot{a}}{r^2} - \frac{2a^4 \dot{a}^2}{r^5},
$$

(6.3.4)

and integrating (6.3.4) gives [209, p. 217]

$$
-\xi = -\frac{2a\dot{a}^2 + a^2 \ddot{a}}{r} + \frac{a^4 \dot{a}^2}{2r^4} = -r\ddot{r} - \frac{3}{2}\dot{r}^2.
$$

(6.3.5)

For the deformation (6.3.1), the gradient tensor with respect to the polar coordinates (R, Θ, Φ) takes the form

$$
\mathbf{F} = \operatorname{diag}\left(\frac{R^2}{r^2}, \frac{r}{R}, \frac{r}{R} \right),
$$

(6.3.6)

the Cauchy-Green tensor is equal to

$$
\mathbf{B} = \operatorname{diag}\left(\frac{R^4}{r^4}, \frac{r^2}{R^2}, \frac{r^2}{R^2} \right),
$$

(6.3.7)

and the corresponding principal invariants (2.1.6) are

$$
I_1 = \frac{R^4}{r^4} + 2\frac{r^2}{R^2},
$$
$$
I_2 = \frac{r^4}{R^4} + 2\frac{R^2}{r^2},
$$
$$
I_3 = 1.
$$

(6.3.8)

The principal components of the equilibrium Cauchy stress at time t are then

$$\sigma_{rr}^{(0)} = -p^{(0)} + \beta_1 \frac{R^4}{r^4} + \beta_{-1} \frac{r^4}{R^4},$$

$$\sigma_{\theta\theta}^{(0)} = \sigma_{rr}^{(0)} + \left(\beta_1 - \beta_{-1} \frac{r^2}{R^2}\right)\left(\frac{r^2}{R^2} - \frac{R^4}{r^4}\right), \tag{6.3.9}$$

$$\sigma_{\phi\phi}^{(0)} = \sigma_{\theta\theta}^{(0)},$$

where $p^{(0)}$ is the Lagrangian multiplier for the incompressibility constraint ($I_3 = 1$), and the nonlinear material parameters are given by (6.1.6), with I_1 and I_2 given in (6.3.8).

As the stress components depend only on the radius r, the system of equilibrium equations reduces to

$$\frac{\partial \sigma_{rr}^{(0)}}{\partial r} = 2 \frac{\sigma_{\theta\theta}^{(0)} - \sigma_{rr}^{(0)}}{r}. \tag{6.3.10}$$

Hence, by (6.3.9) and (6.3.10), the radial Cauchy stress for the equilibrium state at t is equal to

$$\sigma_{rr}^{(0)}(r,t) = 2 \int \left(\beta_1 - \beta_{-1} \frac{r^2}{R^2}\right)\left(\frac{r^2}{R^2} - \frac{R^4}{r^4}\right) \frac{\mathrm{d}r}{r} + \psi(t), \tag{6.3.11}$$

where $\psi = \psi(t)$ is an arbitrary function of time. Substitution of (6.3.5) and (6.3.11) into (2.2.5) gives the following principal Cauchy stresses at time t;

$$\sigma_{rr}(r,t) = -\rho \left(\frac{a^2 \ddot{a} + 2a\dot{a}^2}{r} - \frac{a^4 \dot{a}^2}{2r^4}\right) + 2 \int \left(\beta_1 - \beta_{-1} \frac{r^2}{R^2}\right)\left(\frac{r^2}{R^2} - \frac{R^4}{r^4}\right)\frac{\mathrm{d}r}{r} +$$

$$+ \psi(t),$$

$$\sigma_{\theta\theta}(r,t) = \sigma_{rr}(r,t) + \left(\beta_1 - \beta_{-1}\frac{r^2}{R^2}\right)\left(\frac{r^2}{R^2} - \frac{R^4}{r^4}\right),$$

$$\sigma_{\phi\phi}(r,t) = \sigma_{\theta\theta}(r,t).$$

$$\tag{6.3.12}$$

In (6.3.12), the function $\beta_1 - \beta_{-1}\left(r^2/R^2\right)$ can be regarded as the following nonlinear

shear modulus [25, 127]

$$\widetilde{\mu} = \beta_1 - \beta_{-1}\frac{r^2}{R^2}, \tag{6.3.13}$$

corresponding to the combined deformation of infinitesimal shear superposed on finite axial stretch, defined by

$$x_1 = \alpha X_1 + k\frac{X_2}{\alpha^2}, \qquad x_2 = \frac{X_2}{\alpha^2}, \qquad x_3 = \alpha X_3, \tag{6.3.14}$$

with the shear parameter satisfying $k \to 0$ and the stretch parameter $\alpha = r/R$. This modulus is positive if the BE inequalities (3.1.1) hold [127]. In this case, the integrand in (6.3.12) is negative for $0 < r^2/R^2 < 1$ (i.e. when $0 < a^2/A^2 < 1$) and positive for $r^2/R^2 > 1$ (i.e. when $a^2/A^2 > 1$).

When $R^2/r^2 \to 1$, the nonlinear elastic modulus given by (6.3.13) converges to the shear modulus from linear elasticity;

$$\mu = \lim_{R^2/r^2 \to 1} \widetilde{\mu}. \tag{6.3.15}$$

In this case, the stress components given in (6.3.12) are equal.

For the spherical shell deforming by (6.3.1), the inner and outer radial pressures acting on the curvilinear surfaces, $r = a(t)$ and $r = b(t)$ at time t, are set as $\sigma_1(t)$ and $\sigma_2(t)$, respectively [209, pp. 217-219]. Evaluating $\sigma_1(t) = -\sigma_{rr}(a, t)$ and $\sigma_2(t) = -\sigma_{rr}(b, t)$, using (6.3.12), with $r = a$ and $r = b$, respectively, and

subtracting the results, then gives

$$
\begin{aligned}
\sigma_1(t) - \sigma_2(t) &= \rho \left[(a^2 \ddot{a} + 2a\dot{a}^2) \left(\frac{1}{a} - \frac{1}{b} \right) - \frac{a^4 \dot{a}^2}{2} \left(\frac{1}{a^4} - \frac{1}{b^4} \right) \right] + \\
&\quad + 2 \int_a^b \widetilde{\mu} \left(\frac{r^2}{R^2} - \frac{R^4}{r^4} \right) \frac{\mathrm{d}r}{r} \\
&= \rho \left[(a\ddot{a} + 2\dot{a}^2) \left(1 - \frac{a}{b} \right) - \frac{\dot{a}^2}{2} \left(1 - \frac{a^4}{b^4} \right) \right] + \\
&\quad + 2 \int_a^b \widetilde{\mu} \left(\frac{r^2}{R^2} - \frac{R^4}{r^4} \right) \frac{\mathrm{d}r}{r} \\
&= \rho A^2 \left[\left(\frac{a}{A} \frac{\ddot{a}}{A} + 2\frac{\dot{a}^2}{A^2} \right) \left(1 - \frac{a}{b} \right) - \frac{\dot{a}^2}{2A^2} \left(1 - \frac{a^4}{b^4} \right) \right] + \\
&\quad + 2 \int_a^b \widetilde{\mu} \left(\frac{r^2}{R^2} - \frac{R^4}{r^4} \right) \frac{\mathrm{d}r}{r}.
\end{aligned}
\tag{6.3.16}
$$

Setting the notation

$$
u = \frac{r^3}{R^3} = \frac{r^3}{r^3 - a^3 + A^3}, \qquad x = \frac{a}{A}, \qquad \gamma = \frac{B^3}{A^3} - 1, \tag{6.3.17}
$$

we can rewrite the terms in (6.3.16) as

$$
\begin{aligned}
\left(\frac{a}{A} \frac{\ddot{a}}{A} + 2\frac{\dot{a}^2}{A^2} \right) \left(1 - \frac{a}{b} \right) - \frac{\dot{a}^2}{2A^2} \left(1 - \frac{a^4}{b^4} \right) &= (\ddot{x}x + 2\dot{x}^2) \left[1 - \left(1 + \frac{\gamma}{x^3} \right)^{-1/3} \right] - \\
&\quad - \frac{\dot{x}^2}{2} \left[1 - \left(1 + \frac{\gamma}{x^3} \right)^{-4/3} \right] \\
&= \left(\ddot{x}x + \frac{3}{2}\dot{x}^2 \right) \left[1 - \left(1 + \frac{\gamma}{x^3} \right)^{-1/3} \right] - \\
&\quad - \frac{\dot{x}^2}{2} \frac{\gamma}{x^3} \left(1 + \frac{\gamma}{x^3} \right)^{-4/3} \\
&= \frac{1}{2x^2} \frac{\mathrm{d}}{\mathrm{d}x} \left\{ \dot{x}^2 x^3 \left[1 - \left(1 + \frac{\gamma}{x^3} \right)^{-1/3} \right] \right\}
\end{aligned}
\tag{6.3.18}
$$

and

$$
\begin{aligned}
\int_a^b \widetilde{\mu} \left(\frac{r^2}{R^2} - \frac{R^4}{r^4} \right) \frac{\mathrm{d}r}{r} &= \int_a^b \widetilde{\mu} \left[\left(\frac{r^3}{r^3 - a^3 + A^3} \right)^{2/3} - \left(\frac{r^3 - a^3 + A^3}{r^3} \right)^{4/3} \right] \frac{\mathrm{d}r}{r} \\
&= \frac{1}{3} \int_{\frac{x^3 + \gamma}{1 + \gamma}}^{x^3} \widetilde{\mu} \frac{1 + u}{u^{7/3}} \mathrm{d}u.
\end{aligned}
\tag{6.3.19}
$$

Hence, (6.3.16) can be written equivalently as follows;

$$2x^2 \frac{\sigma_1(t) - \sigma_2(t)}{\rho A^2} = \frac{\mathrm{d}}{\mathrm{d}x} \left\{ \dot{x}^2 x^3 \left[1 - \left(1 + \frac{\gamma}{x^3} \right)^{-1/3} \right] \right\} + \frac{4x^2}{3\rho A^2} \int_{\frac{x^3 + \gamma}{1 + \gamma}}^{x^3} \widetilde{\mu} \frac{1 + u}{u^{7/3}} \mathrm{d}u.$$

(6.3.20)

When the BE inequalities (3.1.1) hold, $\widetilde{\mu} > 0$, and the integral in (6.3.20) is
negative if $0 < x < 1$, and positive if $x > 1$.

In the static case, (6.3.16) reduces to

$$\sigma_1(t) - \sigma_2(t) = 2 \int_a^b \widetilde{\mu} \left(\frac{r^2}{R^2} - \frac{R^4}{r^4} \right) \frac{\mathrm{d}r}{r},$$

(6.3.21)

and (6.3.20) becomes

$$2 \frac{\sigma_1(t) - \sigma_2(t)}{\rho A^2} = \frac{4}{3\rho A^2} \int_{\frac{x^3 + \gamma}{1 + \gamma}}^{x^3} \widetilde{\mu} \frac{1 + u}{u^{7/3}} \mathrm{d}u.$$

(6.3.22)

For the dynamic spherical shell, we set

$$H(x, \gamma) = \frac{4}{3\rho A^2} \int_1^x \left(\zeta^2 \int_{\frac{\zeta^3 + \gamma}{1 + \gamma}}^{\zeta^3} \widetilde{\mu} \frac{1 + u}{u^{7/3}} \mathrm{d}u \right) \mathrm{d}\zeta,$$

(6.3.23)

and obtain that $H(x, \gamma)$ is monotonically decreasing when $0 < x < 1$, and increasing when $x > 1$.

A pressure impulse that is constant in time is also set;

$$2 \frac{\sigma_1(t) - \sigma_2(t)}{\rho A^2} = \begin{cases} 0 & \text{if } t \le 0, \\ p_0 & \text{if } t > 0. \end{cases}$$

(6.3.24)

Integrating (6.3.20) once then gives

$$\dot{x}^2 x^3 \left[1 - \left(1 + \frac{\gamma}{x^3} \right)^{-1/3} \right] + H(x, \gamma) = \frac{p_0}{3} \left(x^3 - 1 \right) + C,$$

(6.3.25)

with $H(x, \gamma)$ defined by (6.3.23), and

$$C = \dot{x}_0^2 x_0^3 \left[1 - \left(1 + \frac{\gamma}{x^3} \right)^{-1/3} \right] + H(x_0, \gamma) - \frac{p_0}{3} \left(x_0^3 - 1 \right), \qquad (6.3.26)$$

where $x(0) = x_0$ and $\dot{x}(0) = \dot{x}_0$ are the initial conditions. From (6.3.25), we obtain

$$\dot{x} = \pm \sqrt{\frac{\frac{p_0}{3} \left(x^3 - 1 \right) + C - H(x, \gamma)}{x^3 \left[1 - \left(1 + \frac{\gamma}{x^3} \right)^{-1/3} \right]}}. \qquad (6.3.27)$$

The analogy with the motion of a point mass in a potential still holds with appropriate modification. Hence, oscillatory motion of the spherical shell occurs if and only if the following equation,

$$H(x, \gamma) = \frac{p_0}{3} \left(x^3 - 1 \right) + C, \qquad (6.3.28)$$

has exactly two distinct solutions, representing the amplitudes of the oscillation, $x = x_1$ and $x = x_2$, such that $0 < x_1 < x_2 < \infty$. In this case, the minimum and maximum radii of the inner surface in the oscillation are given by $x_1 A$ and $x_2 A$, respectively, and the period of oscillation is equal to

$$T = 2 \left| \int_{x_1}^{x_2} \frac{\mathrm{d}x}{\dot{x}} \right| = 2 \left| \int_{x_1}^{x_2} \sqrt{\frac{x^3 \left[1 - \left(1 + \frac{\gamma}{x^3} \right)^{-1/3} \right]}{\frac{p_0}{3} \left(x^3 - 1 \right) + C - H(x, \gamma)}} \, \mathrm{d}x \right|. \qquad (6.3.29)$$

Here, the amplitude and the period of the oscillation are random variables characterised by probability distributions.

Next, the specific case of the radial oscillations of a spherical shell of stochastic neo-Hookean material will be presented.

6.3.2 Radial oscillations of a spherical shell of stochastic neo-Hookean material

For a spherical shell of stochastic neo-Hookean material, with $m = 1$, $\mu_1 = \mu > 0$ and $\mu_2 = 0$ in (3.1.2), evaluating the integral in (6.3.23) gives (see Appendix F for a detailed derivation)

$$H(x, \gamma) = \frac{\mu}{\rho A^2} \left(x^3 - 1 \right) \left[\frac{2x^3 - 1}{x^3 + x^2 + x} - \frac{2\frac{x^3 + \gamma}{1 + \gamma} - 1}{\frac{x^3 + \gamma}{1 + \gamma} + \left(\frac{x^3 + \gamma}{1 + \gamma} \right)^{2/3} + \left(\frac{x^3 + \gamma}{1 + \gamma} \right)^{1/3}} \right]. \tag{6.3.30}$$

Assuming that the nonlinear shear modulus μ is uniformly bounded from below, so

$$\mu > \eta, \tag{6.3.31}$$

for some constant $\eta > 0$, it follows that

$$\lim_{x \to 0} H(x, \gamma) = \lim_{x \to \infty} H(x, \gamma) = \infty. \tag{6.3.32}$$

(i) When $p_0 = 0$ and $C > 0$, equation (6.3.28) has exactly two solutions, $x = x_1$ and $x = x_2$, satisfying $0 < x_1 < 1 < x_2 < \infty$, for any positive constant C. In this case, by (6.3.12), if $\sigma_{rr}(r, t) = 0$ at $r = a$ and $r = b$, so that $\sigma_1(t) = \sigma_2(t) = 0$, then, $\sigma_{\theta\theta}(r, t) = \sigma_{\phi\phi}(r, t) \neq 0$ at $r = a$ and $r = b$, unless $r^3/R^3 \to 1$. That is, the oscillations cannot be considered as 'free' in general, due to the nonzero tractions.

In Figure 6.11, the stochastic function $H(x, \gamma)$ (6.3.30) is shown intersecting the line $C = 10$ to solve equation (6.3.28) when $p_0 = 0$, and the associated velocity (6.3.27), assuming that $\rho = 1$, $A = 1$, $\gamma = 1$, and μ follows the Gamma distribution (3.1.6) with hyperparameters $\rho_1 = 405$ and $\rho_2 = 0.01$ (see Figure 5.21).
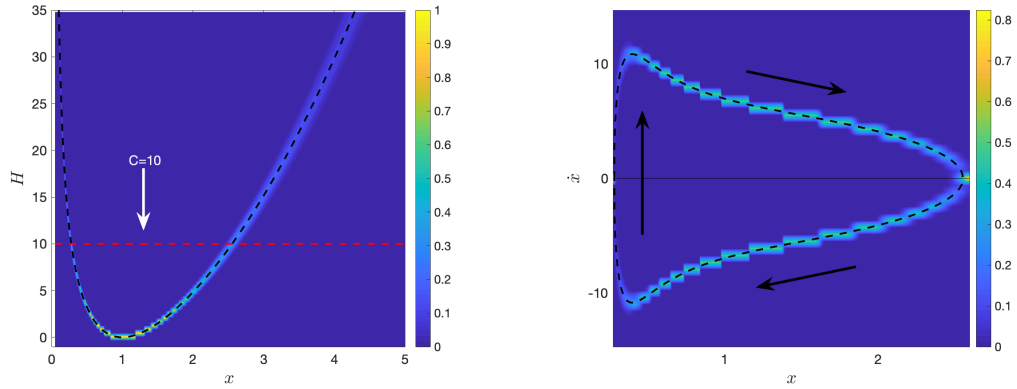
Figure 6.11: The function $H(x,\gamma)$, defined by (6.3.30), intersecting the (dashed red) line $C = 10$, when $p_0 = 0$ (left), and the associated velocity, given by (6.3.27) (right), for the spherical shell of stochastic neo-Hookean material, where $\rho = 1$, $A = 1$, $\gamma = 1$, and μ is drawn from the Gamma distribution (3.1.6) with $\rho_1 = 405$ and $\rho_2 = 0.01$. The dashed black lines correspond to the expected values based only on mean value, $\underline{\mu} = \rho_1\rho_2 = 4.05$. Each distribution was calculated from the average of 1000 stochastic simulations.

(ii) When $p_0 \neq 0$ and $C \geq 0$, substitution of (6.3.30) into (6.3.28) gives

$$p_0 = \frac{3\mu}{\rho A^2}\left[\frac{2x^3-1}{x^3+x^2+x} - \frac{2\frac{x^3+\gamma}{1+\gamma}-1}{\frac{x^3+\gamma}{1+\gamma}+\left(\frac{x^3+\gamma}{1+\gamma}\right)^{2/3}+\left(\frac{x^3+\gamma}{1+\gamma}\right)^{1/3}}\right] - \frac{3C}{x^3-1}. \quad (6.3.33)$$

The necessary and sufficient condition for the motion to be oscillatory is then that p_0 satisfies (see example in Figure 6.12)

$$-\infty = \lim_{x\to 0_+}\frac{3\mu}{\rho A^2}\left[\frac{2x^3-1}{x^3+x^2+x} - \frac{2\frac{x^3+\gamma}{1+\gamma}-1}{\frac{x^3+\gamma}{1+\gamma}+\left(\frac{x^3+\gamma}{1+\gamma}\right)^{2/3}+\left(\frac{x^3+\gamma}{1+\gamma}\right)^{1/3}}\right] - \frac{3C}{x^3-1} < p_0,$$

$$\quad (6.3.34)$$

and

$$p_0 < \sup_{0<x<\infty}\frac{3\mu}{\rho A^2}\left[\frac{2x^3-1}{x^3+x^2+x} - \frac{2\frac{x^3+\gamma}{1+\gamma}-1}{\frac{x^3+\gamma}{1+\gamma}+\left(\frac{x^3+\gamma}{1+\gamma}\right)^{2/3}+\left(\frac{x^3+\gamma}{1+\gamma}\right)^{1/3}}\right] - \frac{3C}{x^3-1}.$$

$$\quad (6.3.35)$$

In the static case, by (6.3.22) and (6.3.24), the applied pressure takes the form

$$p_0^{(s)} = \frac{\mu}{\rho A^2} \left[\left(\frac{1+\gamma}{x^3+\gamma} \right)^{4/3} + 4 \left(\frac{1+\gamma}{x^3+\gamma} \right)^{1/3} - \frac{1}{x^4} - \frac{4}{x} \right]. \tag{6.3.36}$$
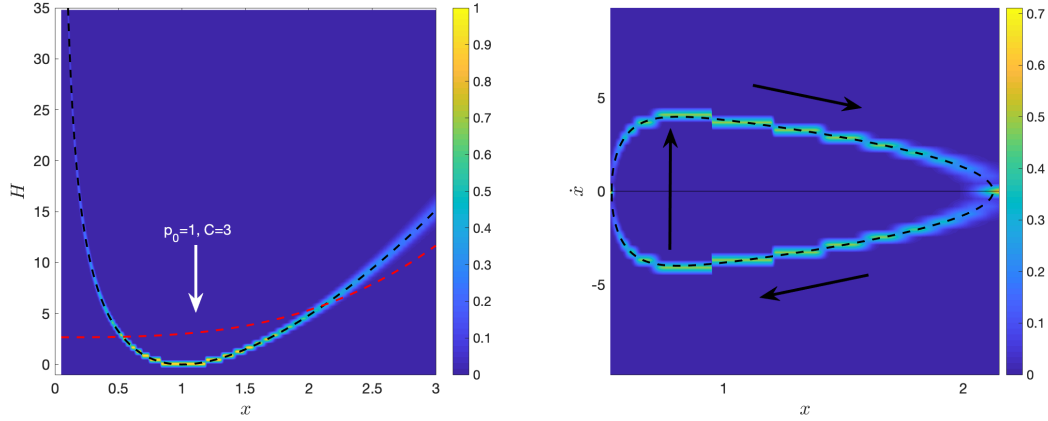
Figure 6.12: The function $H(x,\gamma)$ (6.3.30) intersecting the (dashed red) curve $p_0 \left(x^3 - 1 \right)/3 + C$, with $p_0 = 1$ and $C = 3$ (left), and the associated velocity (6.3.27) (right) for the spherical shell of stochastic neo-Hookean material, where $\rho = 1$, $A = 1$, $\gamma = 1$, and μ is drawn from the Gamma distribution (3.1.6) with $\rho_1 = 405$ and $\rho_2 = 0.01$. The dashed black lines correspond to the expected values based only on mean value $\overline{\mu} = \rho_1\rho_2 = 4.05$. Each distribution was calculated from the average of 1000 stochastic simulations.

In Figure 6.12, the stochastic function $H(x,\gamma)$ (6.3.30) is represented intersecting the curve $p_0 \left(x^3 - 1 \right)/3 + C$, with $p_0 = 1$ and $C = 3$, to obtain the solutions of equation (6.3.28) and the associated velocity (6.3.27), assuming that $\rho = 1$, $A = 1$, $\gamma = 1$, and μ follows the Gamma distribution with $\rho_1 = 405$ and $\rho_2 = 0.01$.

If the spherical shell has an infinitely thick wall [18, 108], then $\gamma \to \infty$, and the necessary and sufficient condition for the motion to be oscillatory becomes

$$\lim_{x \to 0} \left[\frac{3\mu}{\rho A^2} \left(\frac{2x^3 - 1}{x^3 + x^2 + x} - \frac{1}{3} \right) - \frac{3C}{x^3 - 1} \right] < p_0 <$$
$$< \lim_{x \to \infty} \left[\frac{3\mu}{\rho A^2} \left(\frac{2x^3 - 1}{x^3 + x^2 + x} - \frac{1}{3} \right) - \frac{3C}{x^3 - 1} \right], \tag{6.3.37}$$

that is

$$-\infty < p_0 < \frac{5\mu}{\rho A^2}. \tag{6.3.38}$$

Thus, for the oscillations to occur, the shear modulus must satisfy [108]

$$\mu > p_0 \frac{\rho A^2}{5} = \frac{2}{5} \left(\sigma_1(t) - \sigma_2(t) \right). \tag{6.3.39}$$

The probability distribution of oscillatory motions occurring is then

$$P_1 \left(\mu > p_0 \frac{\rho A^2}{5} \right) = 1 - \int_0^{p_0 \frac{\rho A^2}{5}} g(u; \rho_1, \rho_2) \mathrm{d}u, \tag{6.3.40}$$

and that of non-oscillatory motions, or monotonic inflation, is

$$P_2 \left(\mu < p_0 \frac{\rho A^2}{5} \right) = 1 - P_1 \left(\mu > p_0 \frac{\rho A^2}{5} \right) = \int_0^{p_0 \frac{\rho A^2}{5}} g(u; \rho_1, \rho_2) \mathrm{d}u. \tag{6.3.41}$$

For $\rho = 1$, $A = 1$, and $\widetilde{\mu} = \mu = \mu_1 + \mu_2$ drawn from the Gamma distribution (3.1.6) with $\rho_1 = 405$ and $\rho_2 = 0.01$, the probability distributions given by (6.3.40) and (6.3.41) are shown in Figure 6.13 (blue lines for P_1 and red lines for P_2). For the deterministic thin-walled shell, the critical value $p_0 = 5\underline{\mu} = 20.25$ strictly separates the cases of oscillations occurring or not. However, as in Section 6.2, in the stochastic case, there is competition between the two cases.
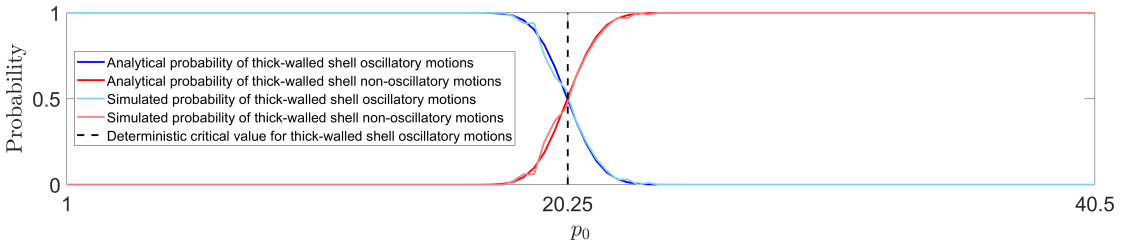
Figure 6.13: Probability distributions of whether oscillatory motions can occur or not for an infinitely thick-walled spherical shell of stochastic neo-Hookean material, with $\rho = 1$, $A = 1$, and the shear modulus, μ, following the Gamma distribution (3.1.6) with $\rho_1 = 405$, $\rho_2 = 0.01$. Dark coloured lines represent analytically derived solutions, given by equations (6.3.40)-(6.3.41), whereas the lighter versions represent stochastically generated data. The vertical line at the critical value $p_0 = 20.25$ separates the expected regions based only on mean value, $\underline{\mu} = \rho_1 \rho_2 = 4.05$. The probabilities were calculated from the average of 100 stochastic simulations.

If the spherical shell wall is thin [25, 211, 213], then $0 < \gamma \ll 1$, and setting

$C = 0$, for example, the necessary and sufficient condition for the oscillatory motions to occur becomes

$$-\infty = \lim_{x \to 0} \frac{\mu}{\rho A^2} \frac{(x+1)\left(2x^4 - x^2 - 1\right)}{x^3\left(x^3 + x^2 + x\right)} < \frac{p_0}{\gamma} < \sup_{0 < x < \infty} \frac{\mu}{\rho A^2} \frac{(x+1)\left(2x^4 - x^2 - 1\right)}{x^3\left(x^3 + x^2 + x\right)}$$
$$\approx 0.7414 \frac{\mu}{\rho A^2},$$
$$(6.3.42)$$

where "sup" denotes supremum. Hence, for the motion to be oscillatory, the shear modulus must be uniformly bounded from below as follows,

$$\mu > \frac{p_0}{\gamma} \frac{\rho A^2}{0.7414} \approx \frac{2.7}{\gamma} \left(\sigma_1(t) - \sigma_2(t)\right). \tag{6.3.43}$$

The probability distribution of oscillatory motions occurring is then

$$P_1\left(\mu > \frac{p_0}{\gamma} \frac{\rho A^2}{0.7414}\right) = 1 - \int_0^{\frac{p_0}{\gamma} \frac{\rho A^2}{0.7414}} g(u; \rho_1, \rho_2)\mathrm{d}u, \tag{6.3.44}$$

and that of non-oscillatory motions (or monotonic inflation) is

$$P_2\left(\mu < \frac{p_0}{\gamma} \frac{\rho A^2}{0.7414}\right) = 1 - P_1\left(\mu > \frac{p_0}{\gamma} \frac{\rho A^2}{0.7414}\right) = \int_0^{\frac{p_0}{\gamma} \frac{\rho A^2}{0.7414}} g(u; \rho_1, \rho_2)\mathrm{d}u. \tag{6.3.45}$$

For $\rho = 1$, $A = 1$, and $\widetilde{\mu} = \mu = \mu_1 + \mu_2$ drawn from the Gamma distribution (3.1.6) with $\rho_1 = 405$ and $\rho_2 = 0.01$, the probability distributions given by (6.3.44) and (6.3.45) are shown in Figure 6.14 (blue lines for P_1 and red lines for P_2). For the deterministic thin-walled tube, the critical value $p_0/\gamma = 0.7414\underline{\mu} = 3.0027$ strictly separates the cases of oscillations occurring or not. However, in the stochastic case, the two cases compete.

6.4 Summary

In this chapter, a synthesis on the analysis of finite amplitude oscillations resulting from dynamic finite deformations of given isotropic incompressible nonlinear hy-
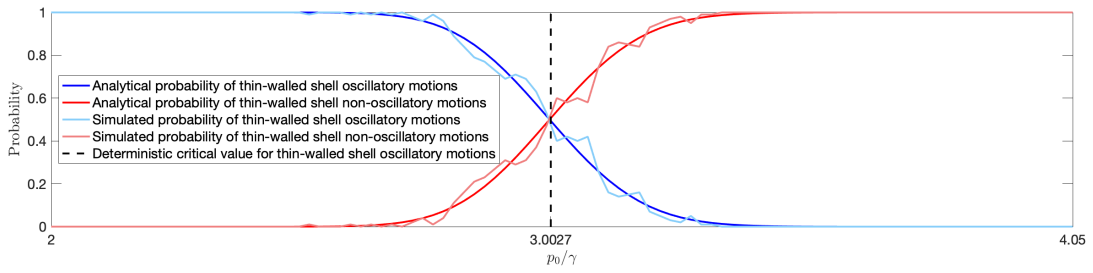
Figure 6.14: Probability distributions of whether oscillatory motions can occur or not for a thin-walled spherical shell of stochastic neo-Hookean material, with $\rho = 1$, $A = 1$, and the shear modulus, μ, following the Gamma distribution (3.1.6) with $\rho_1 = 405$, $\rho_2 = 0.01$. Dark coloured lines represent analytically derived solutions, given by equations (6.3.44)-(6.3.45), whereas the lighter versions represent stochastically generated data. The vertical line at the critical value, $p_0/\gamma = 3.0027$, separates the expected regions based only on mean value, $\underline{\mu} = \rho_1 \rho_2 = 4.05$. The probabilities were calculated from the average of 100 stochastic simulations.

perelastic solids was presented. This was then extended to non-deterministic oscillatory motions of stochastic isotropic incompressible hyperelastic solids with similar geometries. Specifically, the generalised shear motion of a cuboid of stochastic neo-Hookean material, and the radial motion of inflated cylindrical tubes and spherical shells, of stochastic Mooney-Rivlin or neo-Hookean material, respectively, were treated in a unified manner. For these finite dynamic problems, attention was focused on the periodic motion and the time-dependent stresses, while taking into account the stochastic model parameters, which are random variables described by given probability laws. In this case, it was observed that the amplitude and period of the oscillation of the stochastic bodies are also characterised by probability distributions, and, for cylindrical tubes and spherical shells, when an impulse surface traction is applied, there is a parameter interval where both the oscillatory and non-oscillatory motions can occur with a given probability. This is in contrast to the deterministic problem, where a single critical parameter value strictly separates the cases where oscillations can or cannot occur.

If the material is compressible (unconstrained), then the theorem on quasi-equilibrated dynamics recalled in Section 2.2, is not applicable [209, p. 209]. Here,

the notion of quasi-equilibrated motion was relied upon to derive the analytical results for incompressible cylindrical tubes and spherical shells. As such, the same approach cannot be used for the compressible case. Nevertheless, as seen from the generalised shear motion of a cuboid presented in Section 6.1, more general elastodynamic problems can still be formulated where the motion is not quasi-equilibrated. However, while stochastic versions of compressible hyperelastic materials can also be obtained, as shown in [195], there are very few theoretical results on the oscillatory motion of finitely deformed compressible hyperelastic solids (for example, see [4]) available.

The analysis presented here is appropriate because time-dependent finite elastic deformations, although relevant to the modelling of various physical systems, have seldom been considered in more recent studies, which have focused primarily on static elastic deformations or on dynamic viscoelasticity problems. Evidently, further numerical and experimental investigations of oscillatory finite deformations could aid to bridge the gap between these popular areas of research, and add some valuable insight into specific applications as well.

Chapter 7

Potential directions for future research

The stochastic analysis theoretically presented within this work could potentially be applied to many practical scenarios. For example, the inflation of cylinders and spheres presented in Section 5.2 could provide the foundations for gaining an enhanced insight into the circulatory system, as blood vessels could be treated in this way. The physics of growing biological tissues could also be explored from this stochastic angle [5], and there is the potential to mathematically model the behaviour of human organs stochastically [44, 71, 112]. Further, in engineering applications, aircraft fuselages could be treated in a similar manner. In this field, not only is there a need to understand uncertainties in materials or data, but there is also a requirement to reduce the uncertainties present to achieve repeatability between experiments, and for the material in question to obtain optimal performance. There are, of course, many further deformations of solid materials that could potentially be extended from being treated in the traditional deterministic sense, to being investigated from the stochastic perspective, taking into account the variability that occurs within the material parameters for each respective deformation, thus enhancing the understanding of the behaviour of these materials in every sense, both theoretical and practical.

Theoretically, the analysis presented in Chapter 5 could also be extended stochastically to the investigation of concentric tubes and spheres of solid materials. It would also then be possible to explore radially inhomogeneous tubes and spheres, building on the stochastic extension previously mentioned.

A further avenue of development using the presented stochastical analysis is that of machine learning and multiscale modelling, within the fields of biological, biomedical and behavioural sciences [5].

The finite dynamic analysis presented in Chapter 6 can be extended, albeit numerically, to other stochastic homogeneous hyperelastic materials. Examples of this are provided in [129], using the stochastic strain-energy functions derived from experimental data, and in [54], extending to inhomogeneous incompressible bodies similar to those considered deterministically. For incompressible bodies with inhomogeneous material parameters, the constitutive parameters of the stochastic hyperelastic models can be treated as random fields, as described in [198, 199]. The combination of knowledge from elasticity, statistics, and probability theories offers a richer set of tools compared to the elastic framework alone.

In terms of experimental data, there are numerous tests that can be performed on solid materials, and the variation within the obtained data can be observed. Following the approach laid out in Chapter 4, the mathematical model that best represents the experimental data can be determined, leading to a more accurate theoretical analysis of the behaviour of the material in question. As a specific example, indentation tests could be performed on a silicone material similar to that manufactured and used here, and the data could then be analysed and modelled analogously to the approach demonstrated in Section 4.3.4.

Once we have stochastic parameters, the potential arises to apply the techniques described here to the field of fracture analysis [29, 30]. By making the parameters in question within fracture analysis stochastic, an insight into the conditions under which a fracture occurs can be gained, thus leading to an enhanced

treatment of problems of this kind. Further, and particularly within the study of fracture path datasets [77], the enhancement of datasets could also be achieved by building on the standard assumptions associated with the stochastic representation of random media.

Chapter 8

Conclusion

In this thesis, the broad area of applying a stochastic approach to traditional deterministic material modelling problems to enhance the accuracy of the results obtained has been explored. Uncertainties in experimental observations can arise at many times during testing, such as from the inherent stiffness and inhomogeneity of the material in question, sample-to-sample intrinsic variability, or when the data extracted from viscoelastic mechanical tests is elastic, and can occur in both natural and engineered materials. The use of stochastic modelling techniques enables these inevitable uncertainties, which lead to the dispersion of the obtained data, to be accounted for. The approach presented here builds on the deterministic modelling that has been common practice for many years by incorporating at least one probabilistic element into the model, leading to an enhanced insight into the behaviours of materials during deformation.

The aim of this work was to devise an explicit method by which homogeneous isotropic hyperelastic models, whose random field parameters follow probability laws, could be calibrated to the mean values and standard deviation of either the stress-strain function, or the nonlinear shear modulus. Using a combination of finite elasticity and information theory, a calibration procedure for stochastic isotropic incompressible hyperelastic models was presented in Chapter 3. Firstly, a set of model assumptions was outlined in Section 3.1. These would prove fun-

damental in the analysis that was to follow in later chapters of this work. An example of an application of this calibration procedure was demonstrated in Section 3.2 with regard to rubberlike materials, using the data obtained in [170], to obtain the random shear modulus. A theoretical analysis then followed, with the development of a calibration procedure for models with multiple terms in Section 3.3. The calibration procedure for the more specific cases of models with two terms and models with one term was then presented in Sections 3.4 and 3.5, respectively.

Details of simple tests performed on manufactured silicone specimens in order to observe variations arising in experimental data were given in Chapter 4, with information given about the manufactured material in Section 4.2.1, and the experimental set up and techniques in Sections 4.2.2 and 4.2.3, respectively. Full details of the stochastic modelling procedure were presented in Section 4.3, with the assumptions that need to be made in order to use this procedure to represent the experimental data in Section 4.3.1, details of the statistical tests that were used to verify the treatment of the experimental data sets in terms of the material modelling in Section 4.3.2, information about the calibration of the random Piola-Kirchhoff shear stress of three material models, namely, the Mooney-Rivlin, Gent-Gent, and Ogden models, to the data obtained for the material under uniaxial stretch in Section 4.3.3, and a guide on how to use Bayes' theorem as a means of choosing the best performing model to represent the obtained experimental data in Section 4.3.4. The conclusion of this investigation was that the data obtained were more likely with the computations performed by the Ogden model than with either the Mooney-Rivlin or the Gent-Gent models, leading to the advocation of its use when mathematically modelling materials of this type.

Several specific theoretical examples of deformations of stochastic hyperelastic bodies were presented in Chapter 5. Extending further the general model calibration procedure demonstrated in Chapter 3, firstly, the conditions under which a necking instability occurs in materials represented by various different mathe-

matical models were determined in Section 5.1. Following this, a detailed account of the behaviour observed in the inflation of spherical shells and cylindrical tubes was presented in Section 5.2. In both of these cases, the deterministic approach was outlined first, followed by the extension to approaching the problem from the stochastic perspective. A limit-point criterion for both the spherical shells and cylindrical tubes was then determined. In contrast to the deterministic elastic problem where there is a critical value that strictly separates the cases where either the radially symmetric inflation is stable or a limit-point instability occurs, for the stochastic problem, it was established that there are probabilistic intervals for the model parameters, where there is a quantifiable chance for both the stable and unstable states to be found. This approach was applied once again in Section 5.3, to examine the cavitation problems of incompressible spheres of stochastic hyperelastic material under radial tensile dead loads. The stability of the cavitation in both the deterministic and stochastic cases is the main area of discussion within this section, the main difference between the respective cases being that, analogous to the results obtained in Section 5.2, in the deterministic case, there is a critical parameter value that strictly separates the cases where either stable or unstable cavitation occurs, whereas in the stochastic case, there is a probabilistic interval surrounding the deterministic critical value, in which both the stable and unstable states have a quantifiable chance of being found. In this case also, in relation to the onset of cavitation, there is a probabilistic interval where a cavity may form, with a given probability, under smaller or greater loads than the expected critical value.

Extending further the techniques presented in Chapter 3, in Chapter 6, the dynamic finite deformations of stochastic hyperelastic solids were discussed. Here, the likely oscillation of these solids was investigated, then applied, firstly to explore the generalised shear motion of stochastic hyperelastic cuboids in Section 6.1, before drawing on the idea of quasi-equilibrated motion introduced in Section

2.2 to consider the quasi-equilibrated radial-axial motion of a stochastic hyperelastic cylindrical tube (Section 6.2), and the quasi-equilibrated radial motion of a stochastic hyperelastic spherical shell (Section 6.3). In these respective sections, applications were made to a cylindrical tube made of a stochastic Mooney-Rivlin material, and a spherical shell made of a stochastic neo-Hookean material, with the dynamic radial-axial and radial deformations for the tubes and shells, respectively, also being presented. Ultimately, the analysis presented demonstrated that the amplitude and period of the oscillation of the respective stochastic bodies were characterised by probability distributions.

Overall, the work presented here aims to place an emphasis on the need for mathematical models to consider the variability in the mechanical responses of solid materials to deliver an enhanced representation of the material in question. The use of hyperelastic models in practical applications, from biological systems to engineering materials, demands the utmost precision of the models used to represent the experimental data obtained from these materials during testing, and so, by incorporating the inherent variability, an improvement in the quality of mathematical modelling can be achieved, leading to an enhanced insight into the behaviour of these, often complex, materials.

The analysis presented here is timely, since "Today, it is well understood that as soon as the probability theory can be used, then the probabilistic approach of uncertainties is certainly the most powerful, efficient and effective tool for modelling and for solving direct and inverse problems" [190].

Appendices

Appendix A

Measure theory prerequisites

Definition A.0.1 *A function $f : [a,b] \to \mathbb{R}$ is said to be **absolutely continuous** on $[a,b]$ if, given $\epsilon > 0$, there exists some $\delta > 0$ such that*

$$\sum_{i=1}^{n} |f(y_i) - f(x_i)| < \epsilon,$$

whenever $\{[x_i, y_i] : i = 1, \cdots, n\}$ is a finite collection of mutually disjoint subintervals of $[a,b]$ with $\sum_{i=1}^{n} |y_i - x_i| < \delta$.

Appendix B

Maximum Entropy Principle

First defined within the context of information theory by Shannon (1948) [179], the measure of uncertainty (or entropy) of a discrete probability distribution $(R_1, ..., R_n)$ is given by

$$H(R_1, ..., R_n) = -\sum_{p=1}^{n} R_p \log R_p \geq 0. \tag{B.0.1}$$

Equation (B.0.1) is known as Shannon's entropy. The Maximum Entropy Principle is concerned with the explicit construction of the probability distribution that maximises Shannon's entropy under the following $m+1$ equality constraints;

$$\sum_{p=1}^{n} R_p = 1, \qquad \sum_{p=1}^{n} R_p f_{pq} = f_q, \qquad q = 1, ..., m, \tag{B.0.2}$$

where f_q and f_{pq}, $p = 1, ..., n$, $q = 1, ..., m$, are given. The values of f_q and f_{pq} are usually given by data [187]. This is a constrained optimisation problem; solving such a problem is equivalent to finding the maximum of the Lagrangian function;

$$\mathcal{L}(R_1, ..., R_n) = H(R_1, ..., R_n) - \Lambda_0 \left(\sum_{p=1}^{n} R_p - 1 \right) - \sum_{q=1}^{m} \Lambda_q \left(\sum_{p=1}^{n} R_p f_{pq} - f_q \right), \tag{B.0.3}$$

where $\{\Lambda_q\}_{q=0,1,...,m}$ are the Lagrange multipliers associated with the constraints given in (B.0.2), respectively. The general form solution of this problem, first stated by Jaynes (1957) [94, 95], is

$$R_p = e^{-\Lambda_0 - \sum_{q=1}^{m} \Lambda_q f_{pq}}, \qquad p = 1, ..., n, \tag{B.0.4}$$

and provides the most unbiased probability model under the given information. Substituting expression (B.0.4) into (B.0.2) then yields

$$\Lambda_0 = \ln z, \qquad f_q = -\frac{\partial}{\partial \Lambda_q}(\ln z), \qquad q = 1, ..., m, \tag{B.0.5}$$

where

$$z(\Lambda_1, ..., \Lambda_m) = \sum_{p=1}^{n} e^{-\sum_{q=1}^{m} \Lambda_q f_{pq}}. \tag{B.0.6}$$

The uncertainty (entropy) of the discrete distribution (B.0.4) then reduces to

$$H_{\max} = \Lambda_0 + \sum_{q=1}^{m} \Lambda_q f_{pq}. \tag{B.0.7}$$

Appendix C

Further calculations corresponding to Section 3.4

The coefficient of variation for the two-term model presented in Section 3.4 can be calculated in detail as follows:

Rearrangement of (3.4.20) leads to the following expression;

$$\frac{\xi_2}{\xi_1(\xi_1 + \xi_2 + 1)} = \frac{\mathrm{Var}[R_1]}{\underline{R}_1^2} = \frac{\|R_1\|^2}{\underline{R}_1^2} = \left(\frac{\|R_1\|}{\underline{R}_1}\right)^2 = \delta_{R_1}^2, \quad \text{(C.0.1)}$$

and likewise, rearranging (3.4.21) yields, where $R_2 = 1 - R_1$,

$$\frac{\xi_1}{\xi_2(\xi_1 + \xi_2 + 1)} = \delta_{1-R_1}^2. \quad \text{(C.0.2)}$$

Dividing (C.0.1) by (C.0.2) then gives

$$\frac{\delta_{R_1}^2}{\delta_{1-R_1}^2} = \frac{\xi_2^2(\xi_1 + \xi_2 + 1)}{\xi_1^2(\xi_1 + \xi_2 + 1)} = \frac{\xi_2^2}{\xi_1^2}, \quad \text{(C.0.3)}$$

and so, after some rearrangement, we obtain

$$\xi_2 = \xi_1 \frac{\delta_{R_1}}{\delta_{1-R_1}}. \quad \text{(C.0.4)}$$

Substituting equation (C.0.4) into equation (C.0.2) yields

$$\delta_{1-R_1}^2 = \frac{\xi_1}{\xi_1 \frac{\delta_{R_1}}{\delta_{1-R_1}}\left(\xi_1 + \xi_1 \frac{\delta_{R_1}}{\delta_{1-R_1}} + 1\right)} = \frac{\delta_{1-R_1}}{\delta_{R_1}} \frac{1}{\left(\xi_1 + \xi_1 \frac{\delta_{R_1}}{\delta_{1-R_1}} + 1\right)}, \qquad \text{(C.0.5)}$$

which, after rearrangement, gives

$$\xi_1\left(1 + \frac{\delta_{R_1}}{\delta_{1-R_1}}\right) + 1 = \frac{1}{\delta_{R_1}\delta_{1-R_1}}. \qquad \text{(C.0.6)}$$

From the expression above, it is then possible to deduce a value for ξ_1;

$$\xi_1 = \frac{1 - \delta_{R_1}\delta_{1-R_1}}{\delta_{R_1}\delta_{1-R_1}\left(1 + \frac{\delta_{R_1}}{\delta_{1-R_1}}\right)} = \frac{1 - \delta_{R_1}\delta_{1-R_1}}{\delta_{R_1}(\delta_{R_1} + \delta_{1-R_1})}. \qquad \text{(C.0.7)}$$

Substitution of (C.0.7) into (C.0.4) allows an expression for ξ_2 to be deduced, namely;

$$\xi_2 = \left[\frac{1 - \delta_{R_1}\delta_{1-R_1}}{\delta_{R_1}(\delta_{R_1} + \delta_{1-R_1})}\right]\frac{\delta_{R_1}}{\delta_{1-R_1}} = \frac{1 - \delta_{R_1}\delta_{1-R_1}}{\delta_{1-R_1}(\delta_{R_1} + \delta_{1-R_1})}. \qquad \text{(C.0.8)}$$

Hence, we have obtained the following expressions for ξ_1 and ξ_2;

$$\xi_1 = \frac{1 - \delta_{R_1}\delta_{1-R_1}}{\delta_{R_1}(\delta_{R_1} + \delta_{1-R_1})} \qquad \text{and} \qquad \xi_2 = \frac{1 - \delta_{R_1}\delta_{1-R_1}}{\delta_{1-R_1}(\delta_{R_1} + \delta_{1-R_1})}. \qquad \text{(C.0.9)}$$

Since we have obtained expressions for ξ_1 and ξ_2, it is now possible to determine Var $[R_1]$, Var $[1 - R_1]$, $\|R_1\|$, $\|1 - R_1\|$, $E[R_1]$, $E[1 - R_1]$, $\underline{R}_1$ and $1 - \underline{R}_1$.

Beginning with the variance of R_p, $p = 1, 2$, from (3.4.20) and (3.4.21), we have

$$\text{Var}\,[R_1] = \frac{R_1^2 \xi_2}{\xi_1(\xi_1 + \xi_2 + 1)} \qquad \text{and} \qquad \text{Var}\,[1 - R_1] = \frac{(1 - \underline{R}_1)^2 \xi_1}{\xi_2(\xi_1 + \xi_2 + 1)}. \qquad \text{(C.0.10)}$$

For Var$[R_1]$, substituting in expressions (C.0.7) and (C.0.8) for ξ_1 and ξ_2, respec-

tively, we obtain

$$
\begin{aligned}
\mathrm{Var}\,[R_1] &= \frac{\underline{R}_1^2\left[\frac{1-\delta_{R_1}\delta_{1-R_1}}{\delta_{1-R_1}(\delta_{R_1}+\delta_{1-R_1})}\right]}{\left[\frac{1-\delta_{R_1}\delta_{1-R_1}}{\delta_{R_1}(\delta_{R_1}+\delta_{1-R_1})}\right]\left[\frac{1-\delta_{R_1}\delta_{1-R_1}}{\delta_{R_1}(\delta_{R_1}+\delta_{1-R_1})}+\frac{1-\delta_{R_1}\delta_{1-R_1}}{\delta_{1-R_1}(\delta_{R_1}+\delta_{1-R_1})}+1\right]} \\[2mm]
&= \frac{\frac{\underline{R}_1^2(1-\delta_{R_1}\delta_{1-R_1})}{\delta_{1-R_1}(\delta_{R_1}+\delta_{1-R_1})}}{\left[\frac{1-\delta_{R_1}\delta_{1-R_1}}{\delta_{R_1}^2\delta_{1-R_1}(\delta_{R_1}+\delta_{1-R_1})}\right]} \\[2mm]
&= \frac{\underline{R}_1^2(1-\delta_{R_1}\delta_{1-R_1})\delta_{R_1}^2\delta_{1-R_1}(\delta_{R_1}+\delta_{1-R_1})}{\delta_{1-R_1}(\delta_{R_1}+\delta_{1-R_1})(1-\delta_{R_1}\delta_{1-R_1})} \\[2mm]
&= \underline{R}_1^2\delta_{R_1}^2.
\end{aligned}
\tag{C.0.11}
$$

Thus, we have

$$
\mathrm{Var}\,[R_1] = \underline{R}_1^2\delta_{R_1}^2.
\tag{C.0.12}
$$

By symmetry, it is clear that

$$
\mathrm{Var}\,[1-R_1] = (1-\underline{R}_1)^2\delta_{1-R_1}^2.
\tag{C.0.13}
$$

By definition, the standard deviation of R_p, $p=1,2$, is given by

$$
\|R_p\| = \sqrt{\mathrm{Var}\,[R_p]}, \qquad p=1,2.
\tag{C.0.14}
$$

From equations (3.4.26) and (3.4.28), it can be observed that

$$
\|R_1\| = \sqrt{\mathrm{Var}\,[R_1]} = \underline{R}_1\delta_{R_1}
\tag{C.0.15}
$$

and

$$
\|1-R_1\| = \sqrt{\mathrm{Var}\,[1-R_1]} = (1-\underline{R}_1)\delta_{1-R_1}.
\tag{C.0.16}
$$

An expression for $\underline{R}_p$ was stated in (3.4.19). This expression can now be

developed using (C.0.7) and (C.0.8). Therefore;

$$
\begin{aligned}
\underline{R}_1 &= \frac{\xi_1}{\xi_1 + \xi_2} = \frac{\frac{1 - \delta_{R_1}\delta_{1-R_1}}{\delta_{R_1}(\delta_{R_1}+\delta_{1-R_1})}}{\left[\frac{1 - \delta_{R_1}\delta_{1-R_1}}{\delta_{R_1}(\delta_{R_1}+\delta_{1-R_1})} + \frac{1 - \delta_{R_1}\delta_{1-R_1}}{\delta_{1-R_1}(\delta_{R_1}+\delta_{1-R_1})} \right]} \\
&= \frac{\left[\frac{1 - \delta_{R_1}\delta_{1-R_1}}{\delta_{R_1}(\delta_{R_1}+\delta_{1-R_1})} \right]}{\left[\frac{(1 - \delta_{R_1}\delta_{1-R_1})(\delta_{R_1}\delta_{1-R_1})}{\delta_{R_1}\delta_{1-R_1}(\delta_{R_1}+\delta_{1-R_1})} \right]} \\
&= \frac{(1 - \delta_{R_1}\delta_{1-R_1})\delta_{R_1}\delta_{1-R_1}(\delta_{R_1}+\delta_{1-R_1})}{\delta_{R_1}(\delta_{R_1}+\delta_{1-R_1})(1 - \delta_{R_1}\delta_{1-R_1})(\delta_{R_1}\delta_{1-R_1})} \\
&= \frac{\delta_{1-R_1}}{\delta_{R_1}+\delta_{1-R_1}}.
\end{aligned}
\tag{C.0.17}
$$

Hence, we have

$$
\underline{R}_1 = \frac{\delta_{1-R_1}}{\delta_{R_1}+\delta_{1-R_1}},
\tag{C.0.18}
$$

and, by symmetry,

$$
\underline{R}_2 = 1 - \underline{R}_1 = \frac{\delta_{R_1}}{\delta_{R_1}+\delta_{1-R_1}}.
\tag{C.0.19}
$$

By definition, the mathematical expectations are given by

$$
E[R_1] = \underline{R}_1 \qquad \text{and} \qquad E[1 - R_1] = 1 - \underline{R}_1.
\tag{C.0.20}
$$

Therefore, using (C.0.18) and (C.0.19), the mathematical expectations (C.0.20) can be rewritten in terms of δ_{R_1} and δ_{1-R_1};

$$
E[R_1] = \frac{\delta_{1-R_1}}{\delta_{R_1}+\delta_{1-R_1}} \qquad \text{and} \qquad E[1 - R_1] = \frac{\delta_{R_1}}{\delta_{R_1}+\delta_{1-R_1}}.
\tag{C.0.21}
$$

Substituting (C.0.18) and (C.0.19) into (C.0.12) and (C.0.13), respectively, then yields expressions for the variance of R_p, in terms of δ_{R_1} and δ_{1-R_1};

$$
\text{Var}\,[R_1] = \underline{R}_1^2 \delta_{R_1}^2 = \left(\frac{\delta_{1-R_1}\delta_{R_1}}{\delta_{R_1}+\delta_{1-R_1}} \right)^2
\tag{C.0.22}
$$

and

$$\text{Var}\,[1 - R_1] = (1 - \underline{R}_1)^2 \delta^2_{1-R_1} = \left(\frac{\delta_{R_1} \delta_{1-R_1}}{\delta_{R_1} + \delta_{1-R_1}} \right)^2. \tag{C.0.23}$$

By definition, the expressions for the standard deviation of R_p, $p = 1, 2$, in terms of δ_{R_1} and δ_{1-R_1} are then

$$\|R_1\| = \frac{\delta_{1-R_1} \delta_{R_1}}{\delta_{R_1} + \delta_{1-R_1}} \qquad \text{and} \qquad \|1 - R_1\| = \frac{\delta_{R_1} \delta_{1-R_1}}{\delta_{R_1} + \delta_{1-R_1}}. \tag{C.0.24}$$

Hence,

$$\|R_1\| = \|1 - R_1\|. \tag{C.0.25}$$

Appendix D

Normal distribution as limiting distribution of the Gamma distribution

Theorem D.0.1 *The limiting distribution of the Gamma distribution with shape and scale parameters ρ_1 and ρ_2, respectively, such that $\rho_1 \to \infty$, is the Gaussian (normal) distribution with mean value $\rho_1 \rho_2$ and standard deviation $\rho_2 \sqrt{\rho_1}$.*

Proof: If μ is a random variable following a Gamma probability distribution with shape parameter $\rho_1 > 0$ and scale parameter $\rho_2 > 0$, then

$$\underline{\mu} = \rho_1 \rho_2, \qquad \|\mu\| = \sqrt{\rho_1}\rho_2, \tag{D.0.1}$$

where $\underline{\mu} = E[\mu]$ is the mean value and $\|\mu\|$ is the standard deviation of μ, defined as $\|\mu\| = \sqrt{\text{Var}[\mu]}$, with $\text{Var}[\mu]$ denoting the variance of μ.

The moment generating function of μ is

$$M_\mu(t) = E\left[e^{t\mu}\right] = (1 - \rho_2 t)^{-\rho_1}, \qquad t < \frac{1}{\rho_2}. \tag{D.0.2}$$

Subtracting the mean value $\underline{\mu}$ from μ and dividing by the standard deviation $\|\mu\|$

gives the following 1-1 transformation,

$$Y = \frac{\mu - \mu}{\|\mu\|}, \tag{D.0.3}$$

or equivalently,

$$Y = \frac{\mu}{\rho_2 \sqrt{\rho_1}} - \sqrt{\rho_1}. \tag{D.0.4}$$

The moment generating function of Y is then

$$
\begin{aligned}
M_Y(t) &= E\left[e^{tY}\right] \\
&= E\left[e^{t\left(\frac{\mu}{\rho_2\sqrt{\rho_1}} - \sqrt{\rho_1}\right)}\right], \\
&= e^{-t\sqrt{\rho_1}} E\left[e^{t\frac{\mu}{\rho_2\sqrt{\rho_1}}}\right], \\
&= e^{-t\sqrt{\rho_1}} M_\mu\left(\frac{t}{\rho_2\sqrt{\rho_1}}\right), \\
&= e^{-t\sqrt{\rho_1}}\left(1 - \frac{t}{\sqrt{\rho_1}}\right)^{-\rho_1}, \qquad t < \sqrt{\rho_1}.
\end{aligned}
\tag{D.0.5}
$$

Thus, the limiting moment generating function of Y when $\rho_1 \to \infty$ takes the form

$$\lim_{\rho_1 \to \infty} M_Y(t) = \lim_{\rho_1 \to \infty} e^{-t\sqrt{\rho_1}}\left(1 - \frac{t}{\sqrt{\rho_1}}\right)^{-\rho_1}, \qquad -\infty < t < \infty. \tag{D.0.6}$$

The above limit can be calculated as follows,

$$\lim_{\rho_1 \to \infty} e^{-t\sqrt{\rho_1}}\left(1 - \frac{t}{\sqrt{\rho_1}}\right)^{-\rho_1} = \lim_{y = 1/\sqrt{\rho_1} \to 0_+} e^{-(t/y)}\left(1 - ty\right)^{-1/y^2} = e^{\lim_{y \to 0_+} \frac{-ty - \ln(1 - ty)}{y^2}}, \tag{D.0.7}$$

where, applying L'Hôspital's rule [111],

$$\lim_{y \to 0_+} \frac{-ty - \ln(1 - ty)}{y^2} = \lim_{y \to 0} \frac{-t + t/(1 - ty)}{2y} = \lim_{y \to 0_+} \frac{t^2}{2(1 - ty)} = \frac{t^2}{2}. \tag{D.0.8}$$

Therefore,

$$\lim_{\rho_1 \to \infty} M_Y(t) = e^{\frac{t^2}{2}}, \qquad -\infty < t < \infty, \tag{D.0.9}$$

which is the moment generating function of a normal-distributed random variable. Thus, the limiting distribution of a Gamma distribution with $\rho_1 \to \infty$ is the normal distribution. This completes the proof. $\square$

Appendix E

Stability analysis

Here, a corrected version of Proposition 5.2 of [19] and its proof is provided. In particular, it is shown that, in the deterministic elastic case, both subcritical and supercritical behaviours close to the bifurcation are possible, depending on the material.

Proposition E.0.1 *Let $W(\lambda)$ be twice differentiable at $\lambda = 1$, and*

$$P(c) = (1 + c^n)^{(n-1)/n} \int_{(1+c^n)^{1/n}}^{\infty} \frac{\mathrm{d}W}{\mathrm{d}\lambda} \frac{\mathrm{d}\lambda}{\lambda^n - 1},$$

where $n > 1$. Then $\lim_{c \to 0_+} (\mathrm{d}P/\mathrm{d}c) = 0$, and if

$$\lim_{c \to 0_+} P(c) - \lim_{\lambda \to 1} \frac{1}{n(n-1)} \frac{\mathrm{d}^2 W}{\mathrm{d}\lambda^2} > 0, \tag{E.0.1}$$

then $\mathrm{d}P/\mathrm{d}c > 0$ for sufficiently small $c > 0$ (i.e. the bifurcation is supercritical), while if

$$\lim_{c \to 0_+} P(c) - \lim_{\lambda \to 1} \frac{1}{n(n-1)} \frac{\mathrm{d}^2 W}{\mathrm{d}\lambda^2} < 0, \tag{E.0.2}$$

then $\mathrm{d}P/\mathrm{d}c < 0$ for sufficiently small $c > 0$ (i.e. the bifurcation is subcritical).

These cases are illustrated, for the particular example of the material presented in Section 5.3, in Figures 5.23 and 5.24.

Proof. Denote $\theta = (1 + c^n)^{(n-1)/n}$ and define $\widehat{P}(\theta) = P(c)$. Then

$$\widehat{P}(\theta) = \theta \int_{\theta^{1/(n-1)}}^{\infty} \frac{\mathrm{d}W}{\mathrm{d}\lambda} \frac{\mathrm{d}\lambda}{\lambda^n - 1}$$

and

$$\frac{\mathrm{d}P}{\mathrm{d}c} = \frac{\mathrm{d}\widehat{P}}{\mathrm{d}\theta} \frac{\mathrm{d}\theta}{\mathrm{d}c},$$

where

$$\frac{\mathrm{d}\widehat{P}}{\mathrm{d}\theta} = \int_{\theta^{1/(n-1)}}^{\infty} \frac{\mathrm{d}W}{\mathrm{d}\lambda} \frac{\mathrm{d}\lambda}{\lambda^n - 1} - \frac{\theta^{1/(n-1)}}{n-1} \left(\frac{\mathrm{d}W}{\mathrm{d}\lambda} \frac{1}{\lambda^n - 1} \right) |_{\lambda = \theta^{1/(n-1)}} .$$

It follows that

$$
\begin{aligned}
\lim_{\theta \to 1} \frac{\mathrm{d}\widehat{P}}{\mathrm{d}\theta} &= \lim_{\theta \to 1} \int_{\theta^{1/(n-1)}}^{\infty} \frac{\mathrm{d}W}{\mathrm{d}\lambda} \frac{\mathrm{d}\lambda}{\lambda^n - 1} - \lim_{\theta \to 1} \frac{\theta^{1/(n-1)}}{n-1} \frac{\mathrm{d}W}{\mathrm{d}\lambda} \frac{1}{\lambda^n - 1} |_{\lambda = \theta^{1/(n-1)}} \\
&= \lim_{c \to 0_+} P(c) - \lim_{\theta \to 1} \frac{\theta^{1/(n-1)}}{n-1} \left(\frac{\mathrm{d}W}{\mathrm{d}\lambda} \frac{1}{\lambda^n - 1} \right) |_{\lambda = \theta^{1/(n-1)}} \\
&= \lim_{c \to 0_+} P(c) - \lim_{\lambda \to 1} \frac{1}{n(n-1)} \frac{\mathrm{d}W}{\mathrm{d}\lambda} \frac{1}{\lambda - 1} \\
&= \lim_{c \to 0_+} P(c) - \lim_{\lambda \to 1} \frac{1}{n(n-1)} \frac{\mathrm{d}^2 W}{\mathrm{d}\lambda^2}.
\end{aligned}
\tag{E.0.3}
$$

Provided that the above limit is finite (since cavitation is assumed), it follows that

$$\lim_{c \to 0_+} \frac{\mathrm{d}P}{\mathrm{d}c} = 0,$$

since

$$\lim_{c \to 0_+} \frac{\mathrm{d}\theta}{\mathrm{d}c} = \lim_{c \to 0_+} (n-1) \frac{c^{n-1}}{(1 + c^n)^{\frac{1}{n}}} = 0.$$

This concludes the proof.

Note that the difference between this result and Proposition 5.2 of [19] comes from the (correct) minus sign between the two terms on the right-hand side of (E.0.3) (whereas a plus sign is found in the corresponding unlabelled expression

appearing between equations (5.25) and (5.26) of [19]).

Appendix F

Additional detailed calculations

to Sections 6.2 and 6.3

For the stochastic cylindrical and spherical shells discussed in Sections 6.2 and 6.3, respectively, detailed derivations of the general functions $G(x, \gamma)$, defined by (6.2.30), and $H(x, \gamma)$, defined by (6.3.30), are provided, and calculations of the limits of these functions, in the particular cases of thin-walled and infinitely thick-walled shells, are given.

(I) For a Mooney-type model, the function $G(x, \gamma)$ is defined by (6.2.22), where

$\widetilde{\mu} = \mu_1 + \mu_2\alpha^2 t$. In this case, we obtain

$$
\begin{aligned}
G(x,\gamma) &= \frac{1}{\rho A^2} \int_{1/\sqrt{\alpha}}^{x} \left(\zeta \int_{\frac{\zeta^2+\frac{\gamma}{\alpha}}{1+\gamma}}^{\zeta^2} \widetilde{\mu}\frac{1+\alpha u}{\alpha^2 u^2}du \right) d\zeta \\
&= \frac{\widetilde{\mu}}{\rho A^2} \int_{1/\sqrt{\alpha}}^{x} \left(\zeta \int_{\frac{\zeta^2+\frac{\gamma}{\alpha}}{1+\gamma}}^{\zeta^2} \frac{1+\alpha u}{\alpha^2 u^2}du \right) d\zeta \\
&= \frac{\widetilde{\mu}}{\rho A^2} \int_{1/\sqrt{\alpha}}^{x} \left\{ \frac{1}{\alpha^2}\left[(1+\gamma)\frac{\zeta}{\zeta^2+\frac{\gamma}{\alpha}} - \frac{1}{\zeta} \right] + \frac{1}{\alpha}\left[\zeta\log\zeta^2 - \zeta\log\frac{\zeta^2+\frac{\gamma}{\alpha}}{1+\gamma} \right] \right\} d\zeta \\
&= \frac{\widetilde{\mu}}{2\alpha\rho A^2}\left(\frac{1+\gamma}{\alpha}\log\frac{x^2+\frac{\gamma}{\alpha}}{\frac{1}{\alpha}+\frac{\gamma}{\alpha}} - \frac{1}{\alpha}\log x^2 + \frac{1}{\alpha}\log\frac{1}{\alpha} \right) \\
&\quad + \frac{\widetilde{\mu}}{2\alpha\rho A^2}\left(x^2\log x^2 - x^2 - \frac{1}{\alpha}\log\frac{1}{\alpha} + \frac{1}{\alpha} \right) \\
&\quad - \frac{\widetilde{\mu}}{2\alpha\rho A^2}\left(x^2\log\frac{x^2+\frac{\gamma}{\alpha}}{1+\gamma} - x^2 + \frac{\gamma}{\alpha}\log\frac{x^2+\frac{\gamma}{\alpha}}{\frac{1}{\alpha}+\frac{\gamma}{\alpha}} - \frac{1}{\alpha}\log\frac{1}{\alpha} + \frac{1}{\alpha} \right) \\
&= \frac{\widetilde{\mu}}{2\alpha\rho A^2}\left(x^2 - \frac{1}{\alpha} \right)\log\frac{1+\gamma}{1+\frac{\gamma}{\alpha x^2}}.
\end{aligned}
$$

$$\text{(F.0.1)}$$

For the thin-walled tube [107,175], $\alpha = 1$ and $0 < \gamma \ll 1$, and approximating $\log(1+\gamma)$ by γ and $\log\left[1 + \gamma/\left(\alpha x^2\right)\right]$ by $\gamma/\left(\alpha x^2\right)$, we find

$$
G(x,\gamma) = \gamma\frac{\widetilde{\mu}}{2\rho A^2}\left(x^2 - 1 \right)\left(1 - \frac{1}{x^2} \right). \tag{F.0.2}
$$

For the cylindrical cavity [176], $\gamma \to \infty$, hence

$$
G(x,\gamma) = \frac{\widetilde{\mu}}{2\alpha\rho A^2}\left(x^2 - \frac{1}{\alpha} \right)\log\left(\alpha x^2 \right). \tag{F.0.3}
$$

(II) For a neo-Hookean-type model, the function $H(x,\gamma)$ is defined by (6.3.23), where $\widetilde{\mu} = \mu$. Following [108], the corresponding strain-energy density is set in the form

$$
W_0(u) = \frac{\mu}{2}\left(u^{-4/3} + 2u^{2/3} - 3 \right), \tag{F.0.4}
$$

and denote by $W_0'(u)$ its first derivative with respect to u. By standard calculations (involving integration by parts and change of variables), we

then obtain

$$H(x,\gamma) = \frac{4}{3\rho A^2}\int_1^x \left(\zeta^2 \int_{\frac{\zeta^3+\gamma}{1+\gamma}}^{\zeta^3} \widetilde{\mu}\,\frac{1+u}{u^{7/3}}\,du\right)d\zeta$$

$$= \frac{2}{\rho A^2}\int_1^x \left(\zeta^2 \int_{\frac{\zeta^3+\gamma}{1+\gamma}}^{\zeta^3} \frac{W_0'(u)}{u-1}\,du\right)d\zeta$$

$$= \frac{2}{\rho A^2}\int_1^x \left\{\zeta^2\left[\frac{W_0(\zeta^3)}{\zeta^3-1} - \frac{W_0\left(\frac{\zeta^3+\gamma}{1+\gamma}\right)}{\frac{\zeta^3+\gamma}{1+\gamma}-1} + \int_{\frac{\zeta^3+\gamma}{1+\gamma}}^{\zeta^3}\frac{W_0(u)}{(u-1)^2}\,du\right]\right\}d\zeta$$

$$= \frac{2}{\rho A^2}\left\{\int_1^x \zeta^2\left[\frac{W_0(\zeta^3)}{\zeta^3-1} - \frac{W_0\left(\frac{\zeta^3+\gamma}{1+\gamma}\right)}{\frac{\zeta^3+\gamma}{1+\gamma}-1}\right]d\zeta\right.$$

$$\left. + \int_1^x \left[\zeta^2 \int_{\frac{\zeta^3+\gamma}{1+\gamma}}^{\zeta^3}\frac{W_0(u)}{(u-1)^2}\,du\right]d\zeta\right\}$$

$$= \frac{2}{3\rho A^2}\left[\int_1^{x^3}\frac{W_0(u)}{u-1}\,du + x^3\int_1^{x^3}\frac{W_0(u)}{(u-1)^2}\,du - \int_1^{x^3}\frac{uW_0(u)}{(u-1)^2}\,du\right]$$

$$+ \frac{2}{3\rho A^2}\left[\int_{\frac{x^3+\gamma}{1+\gamma}}^1 (1+\gamma)\frac{W_0(u)}{u-1}\,du + x^3\int_{\frac{x^3+\gamma}{1+\gamma}}^1\frac{W_0(u)}{(u-1)^2}\,du\right.$$

$$\left. - \int_{\frac{x^3+\gamma}{1+\gamma}}^1\frac{[u(1+\gamma)-\gamma]\,W_0(u)}{(u-1)^2}\,du\right]$$

$$= \frac{2}{3\rho A^2}\left[x^3\int_1^{x^3}\frac{W_0(u)}{(u-1)^2}\,du - \int_1^{x^3}\frac{W_0(u)}{(u-1)^2}\,du\right]$$

$$+ \frac{2}{3\rho A^2}\left[x^3\int_{\frac{x^3+\gamma}{1+\gamma}}^1\frac{W_0(u)}{(u-1)^2}\,du - \int_{\frac{x^3+\gamma}{1+\gamma}}^1 (1+\gamma)\frac{W_0(u)}{(u-1)^2}\,du\right.$$

$$\left. + \int_{\frac{x^3+\gamma}{1+\gamma}}^1 \gamma\frac{W_0(u)}{(u-1)^2}\,du\right]$$

$$= \frac{2}{3\rho A^2}\left(x^3-1\right)\int_{\frac{x^3+\gamma}{1+\gamma}}^{x^3}\frac{W_0(u)}{(u-1)^2}\,du$$

$$= \frac{\mu}{3\rho A^2}\left(x^3-1\right)\int_{\frac{x^3+\gamma}{1+\gamma}}^{x^3}\frac{2u^{4/3}+4u+3u^{2/3}+2u^{1/3}+1}{u^{2/3}(u+u^{2/3}+u^{1/3})^2}\,du$$

$$= \frac{\mu}{\rho A^2}\left(x^3-1\right)\left[\frac{2x^3-1}{x^3+x^2+x} - \frac{2\frac{x^3+\gamma}{1+\gamma}-1}{\frac{x^3+\gamma}{1+\gamma}+\left(\frac{x^3+\gamma}{1+\gamma}\right)^{2/3}+\left(\frac{x^3+\gamma}{1+\gamma}\right)^{1/3}}\right].$$

<div style="text-align:right">(F.0.5)</div>

For the thin-walled shell [25, 211, 213], $0 < \gamma \ll 1$, and

$$
\begin{aligned}
H(x, \gamma) &= \gamma \frac{4\mu}{3\rho A^2} \int_1^x \frac{u^6 - 1}{u^5} du \\
&= \gamma \frac{\mu}{\rho A^2} \frac{(x + 1)\left(2x^4 - x^2 - 1\right)}{x^3 \left(x^3 + x^2 + x\right)}.
\end{aligned}
\tag{F.0.6}
$$

For the spherical cavity [18, 108], $\gamma \to \infty$, hence

$$
H(x, \gamma) = \frac{\mu}{3\rho A^2} \left(x^3 - 1\right) \frac{5x^3 - x^2 - x - 3}{x^3 + x^2 + x}.
\tag{F.0.7}
$$

Bibliography

[1] M. Abramowitz, I.A. Stegun. 1964. Handbook of Mathematical Functions with Formulas, Graphs and Mathematical Tables, National Bureau of Standards, Applied Mathematics Series, Vol. 55, Washington.

[2] J.E. Adkins, R.S. Rivlin. 1952. Large elastic deformations of isotropic materials. IX. The deformation of thin shells, Philosophical Transactions of the Royal Society of London A 244, 505-531.

[3] T. Ahamed, R.A. Peattie, L. Dorfmann, E.M. Cherry-Kemmerling. 2018. Pulsatile flow measurements and wall stress distribution in a patient specific abdominal aortic aneurysm phantom, Zeitschrift für Angewandte Mathematik und Mechanik (ZAMM) 98, 2258-2274.

[4] U. Akyüz, A. Ertepinar. 1998. Stability and asymmetric vibrations of pressurized compressible hyperelastic cylindrical shells, International Journal of Non-Linear Mechanics 34, 391-404.

[5] M. Alber, A. Buganza Tepole, W. Cannon, S. De, S. Dura-Bernal, K. Garikipati, G. Karniadakis, W. Lytton, P. Perdikaris, L. Petzold, E. Kuhl. 2019. Integrating Machine Learning and Multiscale Modeling: Perspectives, Challenges, and Opportunities in the Biological, Biomedical, and Behavioral Sciences, arXiv:1910.01258.

[6] F. Alijani, M. Amabili. 2014. Non-linear vibrations of shells: A literature review from 2003 to 2013, International Journal of Non-Linear Mechanics 58, 233-257.

[7] M. Amabili. 2008. Nonlinear Vibrations and Stability of Shells and Plates, Cambridge University Press, Cambridge, 2008.

[8] M. Amabili, M.P. Païdoussis. 2003. Review of studies on geometrically nonlinear vibrations and dynamics of circular cylindrical shells and panels, with and without fluidstructure interaction, Applied Mechanics Reviews 56, 349-381.

[9] D. Aranda-Iglesias, G. Vadillo, J.A. Rodríguez-Martnez. 2015. Constitutive sensitivity of the oscillatory behaviour of hyperelastic cylindrical shells, Journal of Sound and Vibration 358, 199-216.

[10] D. Aranda-Iglesias, C. Ram'on-Lozano, J.A. Rodríguez-Martnez. 2017. Nonlinear resonances of an idealized saccular aneurysm, International Journal of Engineering Science 121, 154-166.

[11] D. Aranda-Iglesias, J.A. Rodríguez-Martnez, M.B. Rubin. 2018. Nonlinear axisymmetric vibrations of a hyperelastic orthotropic cylinders, International Journal of Non-Linear Mechanics 99, 131-143.

[12] J.D. Arregui-Mena, L. Margetts, P.M. Mummery. 2016. Practical application of the stochastic finite element method, Archives of Computational Methods in Engineering 23, 171-190.

[13] B. Audoly, J. Hutchinson. 2015. Analysis of necking based on a one-dimensional model. Journal of the Mechanics and Physics of Solids 97.

[14] I. Babuška, R. Tempone, G.E. Zouraris. 2005. Solving elliptic boundary value problems with uncerain coefficients by the finite element method: the stochastic formulation, Computer Methods in Applied Mechanics and Engineering 194, 1251-1294.

[15] I. Babuška, F. Nobile, R. Tempone. 2007. Reliability of computational science, Numerical Methods for Partial Differential Equations 23, 753-784.

[16] I. Babuška, F. Nobile, R. Tempone. 2008. A systematic approach to model validation based on Bayesian updates and prediction related rejection criteria, Computer Methods in Applied Mechanics and Engineering 197, 2517-2539.

[17] M. Baker, J.L. Ericksen. 1954. Inequalities restricting the form of stress-deformation relations for isotropic elastic solids and Reiner-Rivlin fluids, Journal of the Washington Academy of Sciences 44, 24-27.

[18] R. Balakrishnan, M. Shahinpoor. 1978. Finite amplitude oscillations of a hyperelastic spherical cavity, International Journal of Non-Linear Mechanics 13, 171-176.

[19] J.M. Ball. 1982. Discontinuous equilibrium solutions and cavitation in non-linear elasticity, Philosophical Transactions of the Royal Society of London A: Mathematical, Physical and Engineering Sciences 306, no. 1496, 557-611.

[20] J.M. Ball, R.D. James. 2002. The scientific life and influence of Clifford Ambrose Truesdell III, Archive for Rational Mechanics and Analysis 161, 1-26.

[21] D. Balzani, P. Neff, J. Schröder, G.A. Holzapfel. 2006. A polyconvex framework for soft biological tissues. Adjustment to experimental data, International Journal of Solids and Structures 43, 6052-6070.

[22] T. Bayes. 1763. An essay toward solving a problem in the doctrine of chances, Philosophical Transactions of the Royal Society 53, 370-418.

[23] M.F. Beatty. 2007. On the radial oscillations of incompressible, isotropic, elastic and limited elastic thick-walled tubes, International Journal of Non-Linear Mechanics 42, 283-297.

[24] M.F. Beatty. 2010. Small amplitude radial oscillations of an incompressible, isotropic elastic spherical shell, Mathematics and Mechanics of Solids 16(5), 492-512.

[25] M.F. Beatty. 2011. Infinitesimal stability of the equilibrium states of an incompressible, isotropic elastic tube under pressure, Journal of Elasticity 104, 7190.

[26] M. Ben Amar, P. Nassoy, L. LeGoff. 2019. Physics of growing biological tissues: the complex cross-talk between cell activity, growth and resistance. Philosophical transactions. Series A, Mathematical, physical, and engineering sciences. 377. 10.1098/rsta.2018.0070.

[27] J.O. Berger, W.H. Jefferys. 1992. The application of robust Bayesian analysis to hypothesis testing and Occam's razor, Journal of the Italian Statistical Society 1, 17-32.

[28] P. Biscari, C. Omati. 2010. Stability of generalized Knowles solids, IMA Journal of Applied Mathematics 75, 479-491.

[29] M. Buze, T. Hudson, C. Ortner. 2019. Analysis of an atomistic model for anti-plane fracture, Mathematical Models and Methods in Applied Sciences, 10.1142/S0218202519500520.

[30] M. Buze, T. Hudson, C. Ortner. 2019. Analysis of cell size effects in atomistic crack propagation, arXiv:1905.13328 .

[31] I. Breslavsky, M. Amabili. 2018. Nonlinear vibrations of a circular cylindrical shell with multiple internal resonances under multi-harmonic excitation, Nonlinear Dynamics 93, 53-62.

[32] I. Breslavsky, M. Amabili, M. Legrand. 2016. Static and dynamic behaviors of circular cylindrical shells made of hyperelastic arterial materials, Journal of Applied Mechanics, American Society of Mechanical Engineers 83, 051002.

[33] P.T. Brewick, K. Teferra. 2018. Uncertainty quantification for constitutive model calibration of brain tissue, Journal of the Mechanical Behavior of Biomedical Materials 85, 10.1016/j.jmbbm.2018.05.037.

[34] A. Bucchi, E.H. Hearn. 2013. Predictions of aneurysm formation in distensible tubes: Part A - Theoretical background to alternative approaches, International Journal of Mechanical Sciences 71, 1-20.

[35] A. Bucchi, E.H. Hearn. 2013. Predictions of aneurysm formation in distensible tubes: Part B - Application and comparison of alternative approaches, International Journal of Mechanical Sciences 70, 155-170.

[36] S. Budday, G. Sommer, C. Birkl, C. Langkammer, J. Haybäch, J. Kohnert, M. Bauer, F. Paulsen, P. Steinmann, E. Kuhl, G.A. Holzapfel. 2017. Mechanical characterization of human brain tissue, Acta Biomaterialia 48, 319-340.

[37] C. Calderer. 1983. The dynamical behaviour of nonlinear elastic spherical shells, Journal of Elasticity 13, 17-47.

[38] M.M. Carroll. 1987. Pressure maximum behaviour in inflation of incompressible elastic hollow spheres and cylinders, Quarterly of Applied Mathematics 1 45, 141-154.

[39] I. Caylak, E. Penner, A. Dridger, R. Mahnken. 2018. Stochastic hyperelastic modeling considering dependency of material parameters, Computational Mechanics 62, 1273-1285.

[40] G. Chagnon, M. Rebouah, D. Favier. 2014. Hyperelastic energy densities for soft biological tissues: a review, Journal of Elasticity 120, 129-160.

[41] M.S. Chou-Wang, C.O. Horgan. 1989. Void Nucleation and growth in a class of incompressible nonlinearly elastic materials, International Journal of Solids and Structures, Volume 25, Issue 11, 1239-1254.

[42] A. Corona, M. Marchesi, C. Martini, S. Ridella. 1987. Minimizing Multimodal Functions of Continuous Variables with the "Simulated Annealing" Algorithm, ACM Transactions on Mathematical Software (TOMS) 13, 262-280.

[43] J.C. Criscione, J.D. Humphrey, A.S. Douglas, W.C. Hunter. 2000. An invariant basis for natural strain which yields orthogonal stress response terms in isotropic hyperelasticity, Journal of the Mechanics and Physics of Solids 48, 2445-2465.

[44] M. Croci, V. Vinje, M. Rognes. 2019. Uncertainty quantification of parenchymal tracer distribution using random diffusion and convective velocity fields. Fluids and Barriers of the CNS. 16. 10.1186/s12987-019-0152-7.

[45] G. deBotton, R. Bustamante, A. Dorfmann. 2013. Axisymmetric bifurcations of thick spherical shells under inflation and compression, International Journal of Solids and Structures, Volume 50, Issue 2, 403-413.

[46] R. De Pascalis, W.J. Parnell, I.D. Abrahams, T. Shearer, D.M. Daly, D. Grundy. 2018. The inflation of viscoelastic balloons and hollow viscera, Proceedings of the Royal Society A 474, 20180102.

[47] M. Destrade, A. Goriely, G. Saccomandi. 2011. Scalar evolution equations for shear waves in incompressible solids: a simple derivation of the Z, ZK, KZK and KP equations, Proceedings of the Royal Society A 467, 1823-1834.

[48] M. Destrade, J.G. Murphy, G. Saccomandi. 2012. Simple shear is not so simple, International Journal of Non-Linear Mechanics 47, 210-214.

[49] M. Destrade, G. Saccomandi, I. Sgura. 2017. Methodical fitting for mathematical models of rubber-like materials, Proceedings of the Royal Society A 473, 20160811.

[50] Y.H. Dong, B. Zhu, Y. Wang, Y.H. Li, J. Yang. 2018. Nonlinear free vibration of graded graphene reinforced cylindrical shells: Effects of spinning motion and axial load, Journal of Sound and Vibration 437, 79-96.

[51] A.W.F. Edwards. 1974. The History of Likelihood, International Statistical Review 42.

[52] W. Edwards, H. Lindman, L.J. Savage. 1963. Bayesian Statistical Inference for Psychological Research, Psychological Review, 70(3), 193242.

[53] I. Elishakoff, C. Soize. 2012. Nondeterministic Mechanics, Springer, New York.

[54] A. Ertepinar, H.U. Akay. 1976. Radial oscillations of nonhomogeneous, thick-walled cylindrical and spherical shells subjected to finite deformations, International Journal of Solids and Structures 12, 517-524.

[55] S.L. Evans, C.A. Holt. 2009. Measuring the mechanical properties of human skin in vivo using digital image correlation and finite element modelling, The Journal of Strain Analysis for Engineering Design 44, 337-345.

[56] C.L. Farmer. 2017. Uncertainty quantification and optimal decisions, Proceedings of the Royal Society of London A: Mathematical, Physical and Engineering Sciences, 473 2200, 1364-5021.

[57] D. Fitt, H. Wyatt, T.E. Woolley, L.A. Mihai. 2019. Uncertainty quantification of elastic material responses: testing, stochastic calibration and Bayesian model selection, Mechanics of Soft Materials 1, 13.

[58] C. Fond. 2001. Cavitation criterion for rubber materials: A review of void-growth models, Journal of Polymer Science Part B: Polymer Physics 39 17, 2081-2096.

[59] D. Freedman, R. Pusani, R. Perves. Statistics, 4th ed, W.W. Norton & Company, New York.

[60] C. Freiling. 1986. Axioms of symmetry: Throwing darts at the real number line, The Journal of Symbolic Logic 51(1), 190-200.

[61] Y.B. Fu, C.K. Chui, C.L. Teo. 2013. Liver tissue characterization from uniaxial stress-strain data using probabilistic and inverse finite element methods, Journal of the Mechanical Behaviour of Biomedical Materials 20, 105-112.

[62] Y.B. Fu, J.L. Liu, G.S. Francisco. 2016. Localized bulging in an inflated cylindrical tube of arbitrary thickness - the effect of bending stiffness, Journal of the Mechanics and Physics of Solids 90, 45-60.

[63] A.N. Gent, R.S. Rivlin. 1952. Experiments on the Mechanics of Rubber II: The Torsion, Inflation and Extension of a Tube, Proceedings of the Physical Society, Section B 65, 487.

[64] A.N. Gent, A.G. Thomas. 1958. Forms for the stored (strain) energy function for vulcanized rubber, Journal of Polymer Science 28, 625-628.

[65] A.N. Gent, P.B. Lindley. 1959. Internal rupture of bonded rubber cylinders in tension, Proceedings of the Royal Society of London A: Mathematical, Physical and Engineering Sciences 249 1257, 195-205.

[66] A.N. Gent. 1996. A new constitutive relation for rubber, Rubber Chemistry & Technology, 69, 59-61.

[67] R. Ghanem, D. Higdon, H. Owhadi (Eds.). 2017. Handbook of Uncertainty Quantification, Springer, New-York, 2017.

[68] P.B. Goncalves, D. Pamplona, S.R.X. Lopes. 2008. Finite deformations of an initially stressed cylindrical shell under internal pressure, International Journal of Mechanical Sciences 50, 92-103.

[69] A. Goriely, M. Destrade, M. Ben Amar. 2006. Instabilities in elastomers and in soft tissues. Quarterly Journal of Mechanics and Applied Mathematics, Vol. 59, no. 4, 615-630.

[70] A. Goriely. 2017. The Mathematics and Mechanics of Biological Growth 45, Springer-Verlag, New York.

[71] A. Granados, M. Schweiger, V. Vakharia, A. Mcevoy, A. Miserocchi, J. Duncan, R. Sparks, S. Ourselin. 2019. A Generative Model of Hyperelastic Strain Energy Density Functions for Real-Time Simulation of Brain Tissue Deformation.

[72] A.E. Green, R.T. Shield. 1950. Finite elastic deformation of incompressible isotropic bodies, Proceedings of the Royal Society of London A: Mathematical, Physical and Engineering Sciences 202 1070, 407-419.

[73] A.E. Green, J.E. Adkins. 1970. Large Elastic Deformations (and Non-linear Continuum Mechanics), 2nd ed, Oxford University Press, Oxford.

[74] G.R. Grimmett, D.R. Stirzake. 2001. Probability and Random Processes, 3rd ed, Oxford University Press, Oxford.

[75] J. Guilleminot, C. Soize C. 2012. Generalised stochastic approach for constitutive equation in linear elasticity; a random matrix model, International Journal for Numerical Methods in Engineering 90, 613-635.

[76] J. Guilleminot, C. Soize. 2013. On the statistical dependence for the components of random elasticity tensors exhibiting material symmetry properties, Journal of Elasticity 111, 109-130.

[77] J. Guilleminot, J.E. Dolbow. 2019. Data-Driven Enhancement of Fracture Paths in Random Composites, Mechanics Research Communications.

[78] Z.H. Guo, R. Solecki. 1963. Free and forced finite amplitude oscillations of an elastic thick-walled hollow sphere made of incompressible material. Arch. Mech. Stos. 15, 427-433.

[79] P.A. Haas, R.E. Goldstein. 2015. Elasticity and Glocality: Initiation of Embryonic Inversion in Volvox, Journal of the Royal Society Interface 12, 112, p. 20150671.

[80] P.A. Haas, S.S.M.H. Höhn, A.R. Honerkamp-Smith, J.B. Kirkegaard, R.E. Goldstein. 2017. Mechanics and variability of cell sheet folding in the embryonic inversion of Volvox. arXiv 1708.07765.

[81] P.A. Haas, R.E. Goldstein. 2019. Nonlinear and nonlocal elasticity in coarse-grained differential-tension models of epithelia, Physical Review E 99, 022411.

[82] S. Hartmann. 2001. Parameter estimation of hyperelasticity relations of generalized polynomial-type with constraint conditions, International Journal of Solids and Structures 38, 7999-8018.

[83] H. Haslach, J. Humphrey. 2004. Dynamics of biological soft tissue and rubber: internally pressurized spherical membranes surrounded by a fluid, International Journal of Non-Linear Mechanics 39, 399-420.

[84] P. Hauseux, J.S. Hale., S.P.S. Bordas. 2017. Accelerating Monte Carlo estimation with derivatives of high level finite element models, Computer Methods in Applied Mechanics and Engineering 318, 917-936.

[85] P. Hauseux, J.S. Hale, S. Cotin, S.P.S. Bordas. 2018. Quantifying the uncertainty in a hyperelastic soft tissue model with stochastic parameters, Applied Mathematical Modelling 62, 86-102.

[86] G.Z. Heng, R. Solecki. 1963. Free and forced finite amplitude oscillations of an elastic thick-walled hollow sphere made of incompressible material, Archiwum Mechaniki Stosowanej 3, 427-433.

[87] C.O. Horgan, T.J. Pence. 1989. Void nucleation in tensile dead-loading of a composite incompressible nonlinearly elastic sphere. Journal of Elasticity, 21(1), 61-82.

[88] C.O. Horgan, D.A. Polignone. 1995. Cavitation in Nonlinearly Elastic Solids: A Review, ASME, Applied Mechanics Reviews 48 8, 471-485.

[89] I. Hughes, T.P.A. Hase. 2010. Measurements and their uncertainties: A practical guide to modern error analysis, Oxford University Press, Oxford.

[90] C. Huet. 1990. Application of variational concepts to size effects in elastic heterogeneous bodies, Journal of the Mechanics and Physics of Solids 38, 813-841.

[91] R.R. Huilgol. 1967. Finite amplitude oscillations in curvilinearly aeolotropic elastic cylinder, Quarterly of Applied Mathematics 25, 293-298.

[92] A.T. Il'ichev, Y.B. Fu. 2014. Stability of an inflated hyperelastic membrane tube with localized wall thinning, International Journal of Engineering Science 80, 53-61.

[93] P.A. Janmey, M.E. McCormick, S. Rammensee, J.L. Leight, P.C. Georges, F.C. MacKintosh. 2006. Negative normal stress in semiflexible biopolymer gels, Nature Materials 6, 48-51.

[94] E.T. Jaynes. 1957. Information theory and statistical mechanics i, Physical Review 108, 171-190.

[95] E.T. Jaynes. 1957. Information theory and statistical mechanics ii, Physical Review 106, 620-630.

[96] E.T. Jaynes. 2003. Probability Theory: The Logic of Science, Cambridge University Press.

[97] H. Jeffreys. 1935. Some Tests of Significance, Treated by the Theory of Probability, Mathematical Proceedings of the Cambridge Philosophical Society 31, 203-222.

[98] H. Jeffreys. 1961. Theory of Probability, 3rd ed, Oxford University Press, Oxford, UK.

[99] W.H. Jefferys, J.O. Berger. 1992. Ockham's razor and Bayesian analysis, American Scientist 80, 64-72.

[100] N.L. Johnson, S. Kotz, N. Balakrishnan. 1994. Continuous Univariate Distributions, Vol 1, 2nd edition, John Wiley & Sons, New York.

[101] O. Jones, R. Maillardet, A. Robinson. 2014. Introduction to Scientific Programming and Simulation Using R. Chapman & Hall/CRC The R Series. Chapman & Hall/CRC.

[102] P. Junker, J. Nagel. 2019. Modeling of viscoelastic structures with random material properties using timeseparated stochastic mechanics, International Journal for Numerical Methods in Engineering, 10.1002/nme.6210.

[103] M. Kaminski, B. Lauke. 2018. Probabilistic and stochastic aspects of rubber hyperelasticity, Meccanica 53, 2363-2378.

[104] E.A. Kearsley, L.J. Zapas. 1980. Some Methods of Measurement of an Elastic Strain-Energy Functionof the Valanis-Landel Type, Journal of Rheology 24, 483-500.

[105] A. Kloczkowski. 2002. Application of statistical mechanics to the analysis of various physical properties of elastomeric networks - a review. Polymer 43 4, 1503-1525.

[106] J.K. Knowles. 1960. Large Amplitude Oscillations of a Tube of Incompressible Elastic Material, American Mathematical Society.

[107] J.K. Knowles. 1962. On a Class of Oscillations in the Finite-Deformation Theory of Elasticity, Journal of Applied Mechanics, Americal Society of Mechanical Engineers 29(2), 283-286.

[108] J.K. Knowles, M.T. Jakub. 1965. Finite dynamic deformations of an incompressible elastic medium containing a spherical cavity, Archive for Rational Mechanics and Analysis 18, 367-378.

[109] H. Krauss. 1967. Thin Elastic Shells, John Wiley & Sons, New York - London - Sydney.

[110] N. Kumar, A. DasGupta. 2013. On the contact problem of an inflated spherical hyperelastic membrane, International Journal of Non-Linear Mechanics 57, 130-139.

[111] G.F.A. de L'Hospital. 1696. Analyse des infiniment petits, pour l'intelligence des lignes courbes, A Paris, de l'Imprimerie royale, 145-146.

[112] G. Limbert. 2019. Constitutive Modelling of Skin Mechanics, Springer International Publishing, 10.1007/978-3-030-13279-8_2.

[113] O. Lopez-Pamies, M.I. Idiart, T. Nakamura. 2011. Cavitation in elastomeric solids: I - A defect-growth theory. Journal of the Mechanics and Physics of Solids, 59 8, 1464-1487.

[114] O. Lopez-Pamies, T. Nakamura, M.I. Idiart. 2011. Cavitation in elastomeric solids: II - Onset-of-cavitation surfaces for Neo-Hookean materials. Journal of the Mechanics and Physics of Solids, 59 8, 1488-1505.

[115] A.E.H. Love. 1888. On the small free vibrations and deformations of thin elastic shells, Philosophical Transactions of the Royal Society A 179, 491-546.

[116] A.E.H. Love. 1944. A Treatise on the Mathematical Theory of Elasticity, 4th ed, Diver Publications, New York.

[117] S. Madireddy, B. Sista, K. Vemaganti. 2015. A Bayesian approach to selecting hyperelastic constitutive models of soft tissue, Computer Methods in Applied Mechanics and Engineering 291, 102-122.

[118] S. Madireddy, B. Sista, K. Vemaganti. 2016. Bayesian calibration of hyperelastic and constitutive models of soft tissue, Journal of the Mechanical Behavior of Biomedical Materials 59, 108-127.

[119] R. Mangan, M. Destrade. 2015. Gent models for the inflation of spherical balloons, International Journal of Non-Linear Mechanics 68, 52-58.

[120] M. Marzano. 1983. An interpretation of Baker-Ericksen inequalities in uniaxial deformation and stress, Meccanica 18, 233-235.

[121] J.J. McCoy. 1973. A Statistical Theory for Predicting Response of Materials that Possess a Disordered Structure, AD, 768-790.

[122] S.B. McGrayne. 2012. The Theory That Would Not Die: How Bayes' Rule Cracked the Enigma Code, Hunted Down Russian Submarines, an Emerged Triumphant from Two Centuries of Controversy, Paperback ed., Yale University Press, New Haven.

[123] M. Mestre, J.P. Roselot. 2002. Least-Square best fit of a Deterministic Model to Experimental Data using Linear Prediction: Estimating Confidence of the RMS with Prediction and Application to Dimensional Metrology of Mirrors, Journal of Optics A: Pure and Applied Optics 4, 145.

[124] L.A. Mihai, A. Goriely. 2011. Positive or negative Poynting effect? The role of adscititious inequalities in hyperelastic materials, Proceedings of the Royal Society A 467, 3633-3646.

[125] L.A. Mihai, A. Goriely. 2013. Numerical simulation of shear and the Poynting effects by the finite element method: An application of the generalised empir-

ical inequalities in non-linear elasticity, International Journal of Non-Linear Mechanics 49, 1-14.

[126] L.A. Mihai, K. Alayyash, A. Goriely. 2015. Paws, pads, and plants: the nehanced elasticity of cell-filled load-bearing structures, Proceedings of the Royal Society A 471, 20150107.

[127] L.A. Mihai, S. Budday, G.A. Holzapfel, E. Kuhl, A. Goriely. 2017. A family of hyperelastic models for human brain tissue, Journal of Mechanics and Physics of Solids 106, 60-79.

[128] L.A. Mihai, A. Goriely. 2017. How to characterize a nonlinear elastic material? A review on nonlinear constitutive parameters in isotropic finite elasticity, Proceedings of the Royal Society A 473, 20170607.

[129] L.A. Mihai, T.E. Woolley, A. Goriely. 2018. Stochastic isotropic hyperelastic materials: constitutive calibration and model selection, Proceedings of the Royal Society A 474, 20170858.

[130] L.A. Mihai, D. Fitt, T.E. Woolley, A. Goriely. 2018. Likely equilibria of stochastic hyperelastic spherical shells and tubes, Mathematics and Mechanics of Solids 24(7), 2066-2082.

[131] L.A. Mihai, D. Fitt, T.E. Woolley, A. Goriely. 2018. Likely cavitation in stochastic elasticity, Journal of Elasticity 137(1), 27-42.

[132] L.A. Mihai, T.E. Woolley, A. Goriely. 2019. Likely chirality of stochastic anisotropic hyperelastic tubes, International Journal of Non-Linear Mechanics 114, 9-20.

[133] L.A. Mihai, T.E. Woolley, A. Goriely. 2019. Likely equilibria of the stochastic Rivlin cube, Philosophical Transactions of the Royal Society A 377, 20180068.

[134] L.A. Mihai, D. Fitt, T.E. Woolley, A. Goriely. 2019. Likely oscillatory motions of stochastic hyperelastic solids, Transactions of Mathematics and Its Applications 3(1), 1-42.

[135] S. Misra, K.T. Ramesh, A.M. Okamura. 2010. Modelling of non-linear elastic tissues for surgical simulation, Computer Methods in Biomechanics and Biomedical Engineering 13, 811-818.

[136] H. Moon, C. Truesdell. 1974. Interpretation of adscititious inequalities through the effects pure shear stress produces upon an isotropic elastic solid, Archive for Rational Mechanics and Analysis 55, 1-17.

[137] M. Mooney. 1940. A theory of large elastic deformation, Journal of Applied Physics 11, 582-592.

[138] R.D. Moser, T.A. Oliver. 2017. Validation of Physical Models in the Presence of Uncertainty, Handbook of Uncertainty Quantification, 129-156.

[139] I. Müller, H. Struchtrup. 2002. Inflation of rubber balloon, Mathematics and Mechanics of Solids 7, 569-577.

[140] D. Mumford. 2000. The dawning of the age of stochasticity, Mathematics: Frontiers and Perspectives, V. Arnold, M. Atiyah, P. Lax, B. Mazur (eds.), American Mathematical Society, 197-218.

[141] A.N. Natali, L.C. Emanuele, P.G. Pavan, P. Dario, I. Izzo. 2006. Hyperelastic models for the analysis of soft tissue mechanics: definition of constitutive parameters, 188-196.

[142] N. Nörenberg, R. Mahnken. 2015. Parameter identification for rubber materials with artificial spatially distributed data, Computational Mechanics 56, 353-370.

[143] J.L. Nowinski. 1966. On a dynamic problem in finite elastic shear, International Journal of Engineering Science 4, 501-510.

[144] J.L. Nowinski, A.R. Schultz. 1964. Note on a class of finite longitudinal oscillations of thick-walled cylinders, Proceedings of the Indian National Congress of Theoretical and Applied Mechanics, 31-44.

[145] L.C.S. Nunes, D.C. Moreira. 2013. Simple shear under large deformation: Experimental and theoretical analyses, European Journal of Mechanics - A/Solids 42, 315-322.

[146] J.T. Oden, R. Moser, O. Ghattas. 2010. Computer predictions with quantified uncertainty, part I. SIAM News 43 9, 1-3.

[147] J.T. Oden, R. Moser, O. Ghattas. 2010. Computer predictions with quantified uncertainty, part II. SIAM News 43 10, 1-4.

[148] J.T. Oden, E.E. Prudencio, A. Hawkins-Daarud. 2013. Selection and assessment of phenomenological models of tumor growth, Mathematical Models and Methods in Applied Sciences 23, 1309-1338.

[149] J.T. Oden. 2018. Adaptive multiscale predictive modelling. Acta Numerica 27, 353-450.

[150] R.W. Ogden. 1972. Large deformation isotropic elasticity - on the correlation of theory and experiment for incompressible rubberlike solids, Proceedings of the Royal Society of London A 326, 565-584.

[151] R.W. Ogden. 1997. Non-Linear Elastic Deformations, 2nd ed, Dover, New York.

[152] R.W. Ogden, G. Saccomandi, I. Shura. 2004. Fitting hyperelastic models to experimental data, Computational Mechanics 34, 484-502.

[153] M. Ostoja-Starzewski. 2008. Microstructural Randomness and Scaling in Mechanics of Materials, Chapman and Hall/CRC, New York.

[154] S.P. Pearce, Y.B. Fu. 2010. Characterization and stability of localized bulging/necking in inflated membrane tubes, IMA Journal of Applied Mathematics 75, 581-602.

[155] R.W. Penn, E.A. Kearsley. 1976. The Scaling Law for Finite Torsion of Elastic Cylinders, Journal of Rheology 20, 227-238.

[156] A.D. Polignone, C. Horgan. 1993. Cavitation for incompressible anisotropic nonlinearly elastic spheres, Journal of Elasticity 33, 27-65.

[157] W.B. Powell. 2014. Clearing the Jungle of Stochastic Optimisation, Bridging Data and Decisions, Chapter 4, 109-137.

[158] J.H. Poynting. 1909. On pressure perpendicular to the shear-planes in finite pure shears, and on the lengthening of loaded wires when twisted, Proceedings of the Royal Society A 82, 546-559.

[159] X. Poulain, V. Lefévre, O. Lopez-Pamies, K. Ravi-Chandar. 2017. Damage in elastomers: nucleation and growth of cavities, micro-cracks, and macro-cracks, International Journal of Fracture 205, 1-21.

[160] X. Poulain, O. Lopez-Pamies, K. Ravi-Chandar. 2018. Damage in elastomers: Healing of internally nucleated cavities and micro-cracks, Soft Matter 14, 4633-4640.

[161] E. Pucci, G. Saccomandi. 2002. A note on the Gent model for rubber-like materials, Rubber Chemistry and Technology 75, 839-852.

[162] F.M. Rabinowitz. 1995. Algorithm 744: A Stochastic Algorithm for Global Optimisation with Constraints, ACM Transactions on Mathematical Software 21 2, 194-213.

[163] K.R. Rajagopal, A.S. Wineman. 1987. New universal relations for nonlinear isotropic elastic materials, Journal of Elasticity 17, 75-83.

[164] H. Rappel, L.A.A. Beex, J.S. Hale, S.P.A. Bordas. 2016. Bayesian inference for the stochastic identification of elastoplastic material parameters: Introduction, misconceptions and insights, arXiv:1606.02422.

[165] E. Reissner. 1941. A new derivation of the equations for the deformation of elastic shells, American Journal of Mathematics 63, 177-184.

[166] J.S. Ren. 2008. Dynamical response of hyper-elastic cylindrical shells under periodic load, Applied Mathematics and Mechanics 29, 1319-1327.

[167] J.S. Ren. 2009. Dynamics and destruction of internally pressurized incompressible hyper-elastic spherical shells, International Journal of Engineering Science 47, 745-753.

[168] R.S. Rivlin. 1948. Large elastic deformations of isotropic materials. IV. Further developments of the general theory, Philosophical Transactions of the Royal Society of London. Series A, Mathematical and Physical Sciences 241, 379-397.

[169] R.S. Rivlin. 1949. Large elastic deformations of isotropic materials VI. Further results in the theory of torsion, shear and flexure, Philosophical Transactions of the Royal Society of London A: Mathematical, Physical and Engineering Sciences 242, 173-195.

[170] R.S. Rivlin, D.W. Saunders. 1951. Large elastic deformations of isotropic materials VII. Experiments on the deformation of rubber, Philosophical Transactions of the Royal Society of London A: Mathematical, Physical and Engineering Sciences 243, 251-288.

[171] R.S. Rivlin. 1953. The solution of problems in second order elasticity theory, Journal of Rational Mechanics and Analysis 2, 53-81.

[172] C.P. Robert. 2007. The Bayesian Choice: From Decision-Theoretic Foundations to Computational Implementation, 2nd ed, Springer, New York.

[173] J.A. Rodriíguez-Martiínez, J. Fernández-Sáaez, R. aera. 2015. The role of constitutive relation in the stability of hyper-elastic spherical membranes subjected to dynamic inflation, International Journal of Engineering Science 93, 31-45.

[174] M. Schrodt, G. Benderoth, A. Kühhorn, G. Silber. 2005. Hyperelastic description of polymer soft foams at finite deformations, Technische Mechanik 25, 3-4162.

[175] M. Shahinpoor, J.L. Nowinski. 1971. Exact solution to the problem of forced large amplitude radial oscillations of a thin hyperelastic tube, International Journal of Non-Linear Mechanics 6, 193-207.

[176] M. Shahinpoor. 1973. Combined radial-axial large amplitude oscillations of hyperelastic cylindrical tubes, Journal of Mathematical and Physical Sciences 7, 111-128.

[177] M. Shahinpoor. 1974. Exact solution to finite amplitude oscillation of an anisotropic thin rubber tube, The Journal of the Acoustical Society of America 56, 477-480.

[178] M. Shahinpoor, R. Balakrishnan. 1978. Large amplitude oscillations of thick hyperelastic cylindrical shells, International Journal of Non-Linear Mechanics 13, 295-301.

[179] C.E. Shannon. 1948. A mathematical theory of communication, Bell System Technical Journal 27, 379-423, 623-659.

[180] R.T. Shield. 1971. Deformations possible in every compressible, isotropic, perfectly elastic material, Journal of Elasticity 1, 91-92.

[181] R.T. Shield. 1972. On the stability of finitely deformed elastic membranes. II: Stability of inflated cylindrical and spherical membranes, Zeitschrift für Angewandte Mathematik und Physik (ZAMP) 23, 16-34.

[182] J. Sivaloganathan. 1992. Cavitation, the incompressible limit, and material inhomogeneity, Quarterly of Applied Mathematics Volume XLIX, no. 3, 521-541.

[183] J. Sivaloganathan. 1999. On cavitation and degenerate cavitation under internal hydrostatic pressure, Proceedings of the Royal Society of London A: Mathematical, Physical and Engineering Sciences 455 1990, 3645-3664.

[184] G.W. Snedecor, W.G. Cochran. 1989. Statistical Methods, Eighth Edition, Iowa State University Press.

[185] R.M. Soares, P.F.T. Amaral, F.M.A. Silva, P.B. Gonçalves. 2019. Nonlinear breathing motions and instabilities of a pressure-loaded spherical hyperelastic membrane, Nonlinear Dynamics 1-22.

[186] J. Soni, R. Goodman. 2017. A Mind at Play: How Claude Shannon Invented the Information Age, Simon & Schuster, New York.

[187] C. Soize. 2000. A nonparametric model of random uncertainties for reduced matrix models in structural dynamics, Probabilistic Engineering Mechanics 15, 277-294.

[188] C. Soize. 2001. Maximum entropy approach for modeling random uncertainties in transient elastodynamics, Journal of the Acoustical Society of America 109, 1979-1996.

[189] C. Soize. 2006. Non-Gaussian positive-definite matrix-valued random fields for elliptic stochastic partial differential operators, Computer Methods in Applied Mechanics and Engineering 195, 26-64.

[190] C. Soize. 2013. Stochastic modeling of uncertainties in computational structural dynamics - Recent theoretical advances, Journal of Sound and Vibration 332, 2379-2395.

[191] C. Soize. 2017. Uncertainty Quantification: An Accelerated Course with Advanced Applications in Computational Engineering, Interdisciplinary Applied Mathematics Book 47, Springer, New York.

[192] G. Sommer, M. Eder, L. Kovacs, H. Pathak, L. Bonitz, C. Mueller, P. Regitnig, G.A. Holzapfel. 2013. Multiaxial mechanical properties and constitutive modeling of human adipose tissue: a basis for preoperative simulations in plastic and reconstructive surgery, Acta Biomaterialia 9, 9036-9048.

[193] A.J.M. Spencer. 1971. Theory of invariants. In: Eringen, A.C. (ed.) Continuum Physics 1, 239-253, Academic Press, New York.

[194] B. Staber, J. Guilleminot. 2015. Stochastic modelling of a class of stored energy functions for incompressible hyperelastic materials with uncertainties, Comptes Rendus Mécanique 343, 503-514.

[195] B. Staber, J. Guilleminot. 2016. Stochastic modelling of the Ogden class of stored energy functions for hyperelastic materials: the compressible case, Journal of Applied Mathematics and Mechanics/Zeitschrift für Angewandte Mathematik und Mechanik 97, 273-295.

[196] B. Staber, J. Guilleminot. 2017. Stochastic hyperelastic constitutive laws and identification procedure for soft biological tissues with intrinsic variability, Journal of the Mechanical Behaviour of Biomedical Materials 65, 743-752.

[197] B. Staber, J. Guilleminot. 2017. Stochastic modeling and generation of random fields of elasticity tensors: A unified information-theoretic approach, Comptes Rendus Mcanique 345, 399-416.

[198] B. Staber, J. Guilleminot. 2018. A random field model for anisotropic strain energy functions and its application for uncertainty quantification in vascular mechanics, Computer Methods in Applied Mechanics and Engineering 333, 94-113.

[199] B. Staber, J. Guilleminot, C. Soize, J. Michopoulos, A. Iliopoulos. 2019. Stochastic modeling and identification of an hyperelastic constitutive model for laminated composites, Computer Methods in Applied Mechanics and Engineering 347, 425-444.

[200] P. Steinmann, M. Hossain, G. Possart. 2012. Hyperelastic models for rubber-like materials: consistent tangent operators and suitability for Treloar's data, Archive of Applied Mechanics 82, 1183-1217.

[201] Student. 1908. The Probable Error of a Mean. Biometrika, 6(1), 1-25.

[202] T.J. Sullivan. 2015. Introduction to Uncertainty Quantification, Springer-Verlag, New York.

[203] M. Sutton, J.J. Orteu, H.W. Schreire. 2009, Image correlation for shape, motion and deformation measurements: basic concepts, theory and applications, Springer, New York.

[204] W.M. Thorburn. 1918. The myth of Occam's razor, Mind 27, 345-353.

[205] L.R.G. Treloar. 1944. Stress-strain data for vulcanized rubber under various types of deformation, Transactions of the Faraday Society 40, 59-70.

[206] L.R.G. Treloar. 2005. The physics of rubber elasticity, Clarendon Press, Oxford, UK.

[207] C.A. Truesdell. 1952. A programme of physical research in classical mechanics, Zeitschrift für Angewandte Mathematik und Physik (ZAMP) 3, 79-95.

[208] C. Truesdell. 1962. Solutio generalis et accurata problematum quampluri-morum de motu corporum elasticorum incomprimibilium in deformationibus valde magnis, Archive of Rational Mechanics and Analysis 11, 106-113.

[209] C. Truesdell, W. Noll. 2004. The Non-Linear Field Theories of Mechanics, 3rd ed, Springer-Verlag, New York.

[210] E.H. Twizell, R.W. Ogden. 1983. Non-linear optimization of the material constants in Ogden's stress-deformation function for incompressible isotropic elastic materials, The ANZIAM Journal 24, 424-434.

[211] E. Verron, R.E. Khayat, A. Derdouri, B. Peseux. 1999. Dynamic inflation of hyperelastic spherical membranes, Journal of Rheology 43, 1083-1097.

[212] S. Vogel. 1998. Cat's Paws and Catapults, W.W. Norton and Company, New York, London.

[213] C.C. Wang. 1965. On the radial oscillations of a spherical thin shell in the finite elasticity theory, Quarterly of Applied Mathematics 23, 270-274.

[214] A.S.D. Wang. 1969. On free oscillations of elastic incompressible bodies in finite shear, International Journal of Engineering Science 7, 1199-1212.

[215] A. Wang, A. Ertepinar. 1972. Stability and vibrations of elastic thick-walled cylindrical and spherical shells subjected to pressure, International Journal of Non-Linear Mechanics.

[216] H.L. Wyatt, R. Pullin, T.H.J. Yang, S.L. Evans. 2016. Deformation during the electrosurgical vessel sealing process, Strain 52, 372-379.

[217] H. Wyatt, A. Safar, A. Clarke, S.L. Evans, L.A. Mihai. 2019. Nonlinear scaling effects in the stiffness of soft cellular structures, Royal Society Open Science 6, 181361.

[218] Y. Ye, Y. Liu, Y. Fu. 2020. Weakly nonlinear analysis of localized bulging of an inflated hyperelastic tube of arbitrary wall thickness, Journal of the Mechanics and Physics of Solids 135.

[219] O.H. Yeoh. 1993. Some forms of the strain energy function for rubber, Rubber Chemistry & Technology 66, 754-771.

[220] X. Yuan, R. Zhang, H. Zhang. 2008. Controllability conditions of finite oscillations of hyperelastic cylindrical tubes composed of a class of Ogden material models, Computers, Materials and Continua 7, 155-166.

[221] V. Zamani, T.J. Pence. 2017. Swelling, Inflation and a Swelling-Burst Instability in Hyperelastic Spherical Shells, International Journal of Solids and Structures.

[222] L. Zanelli, A. Montanaro, E.L. Carniel, P.G. Pavan, A.N. Natali. 2017. The study of equivalent material parameters in a hyperelastic model, International Journal of Nonlinear Mechanics 89, 142-150.

[223] G. Zhong-Heng, R. Solecki. 1963. Free and forced finite-amplitude oscillations of a thick-walled hollow sphere made of incompressible material, Arch. Mech. Stosow 15, 427-433.